UNIVERSITY OF COPENHAGEN

Ph.D. Thesis

Magnetic structure and dynamics of cuprate superconductors studied by neutron scattering
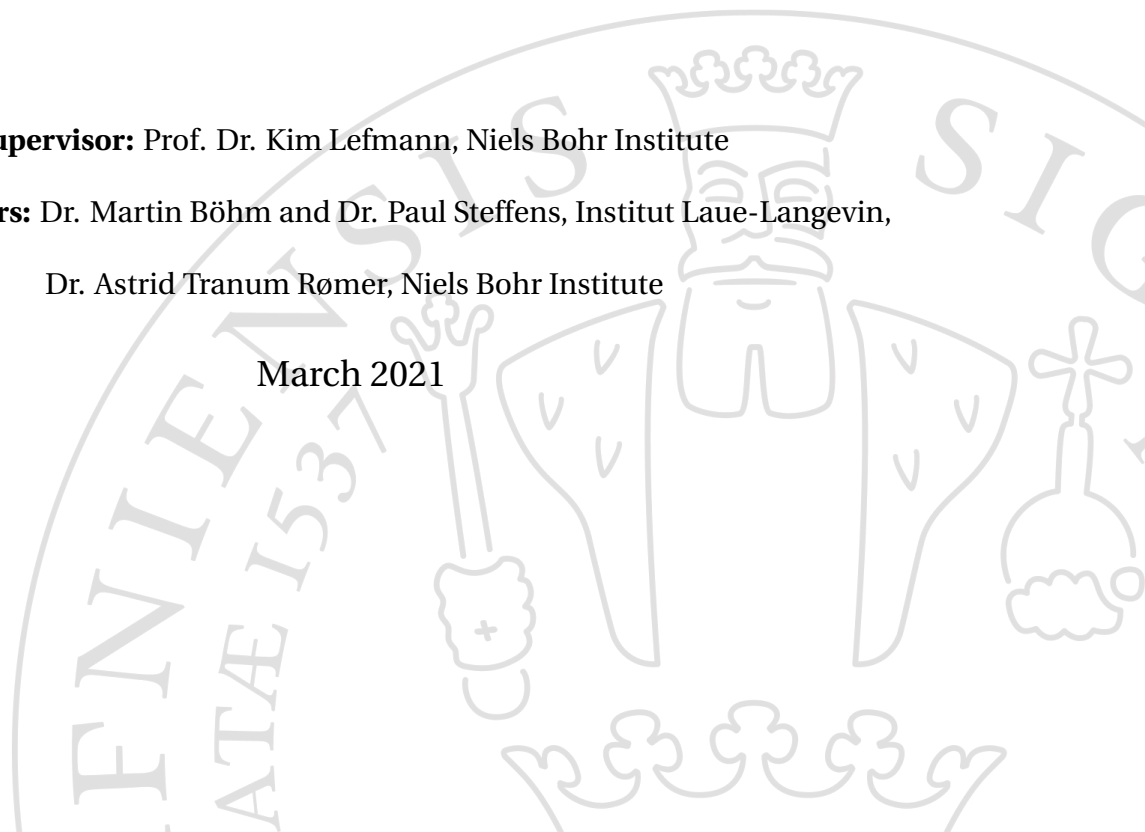
Ana-Elena Țuțueanu

Supervisor: Prof. Dr. Kim Lefmann, Niels Bohr Institute

Co-supervisors: Dr. Martin Böhm and Dr. Paul Steffens, Institut Laue-Langevin,

Dr. Astrid Tranum Rømer, Niels Bohr Institute

March 2021

ABSTRACT

The research presented in this thesis is centred around two compounds of the cuprates family. In both cases the aim has been to understand the relationship between magnetism and superconductivity by means of neutron scattering experiments.

The main focus of my experimental investigations has been the underdoped region of the $La_{2-x}Sr_xCuO_4$ (LSCO) phase diagram around the doping dependent transition from an insulator to a superconductor. The consistent study of crystals with different levels of strontium doping has revealed a number of similarities and differences between superconducting and non-superconducting samples. Our experiments revealed a spectral weight shift from low-energy spin fluctuations towards the elastic or quasi-elastic magnetic signals. This, corroborated with a lack of spin gap in all our samples, regardless of conduction properties, and a drastic decrease of both elastic and inelastic signals at the onset of superconductivity as a function of doping led us to propose a model composed of several coexisting electronic orders. We argue that the phase diagram of LSCO displays coexisting pair density wave and uniform d-wave superconducting regions the ratio of which can be tuned by adjusting the doping concentration.

In addition to the studies of the magnetic structure we have also investigated the doping distribution in one of our superconducting LSCO single crystals by means of polarised neutron imaging. The temperature dependence of the trapped magnetic flux inside our sample revealed a doping variation in the growth direction of our crystals also confirmed by means of magnetic susceptibility measurements. Finally, we have identified the origin of an incommensurate signal appearing at the same position in reciprocal space as the spin stripes signal. Calculations have revealed the signal to be a spurious double scattering event.

The second compound that we focused on was the oxygen doped La_2CuO_{4+y} (LCO+O). A significant amount of data has been acquired on these samples by our group over the years. I have gathered and combined the data and performed additional measurements which led to an improved general understating of the magnetism in this type of compounds. Through polarisation analysis we showed that charged stripes run along both tetragonal a and b axis and that magnetic fluctuations are most probably isotropic in nature. Furthermore, the lack of a spin gap or a significant applied magnetic field effect on low-energy magnetic excitations have

been interpreted as manifestations of a microscopical co-existence between superconductivity and spin fluctuations. In this picture we argue that magnetic order originates from a separate electronic phase competing with with superconductivity.

Besides the details of each conclusion we draw, our study also reveals that seemingly similar samples, which have the emergence of superconductivity in common, also exhibit significantly different magnetic structures. This points to a fairly complex interplay between superconductivity and magnetism that needs to be further investigated and understood in order to explain the pairing mechanism in these compounds.

RESUMÉ

Forskningen præsenteret i denne afhandling er centreret omkring to materialer som er medlemmer af kuprat-familien. I begge tilfælde har målet været at forstå forholdet mellem magnetisme og superledning ved hjælp af neutronspredningseksperimenter.

Hovedfokus for mine eksperimentelle undersøgelser har været den underdotede region i $La_{2-x}Sr_xCuO_4$ (LSCO) fasediagrammet omkring den doteringsafhængige overgang fra en isolator til en superleder. Undersøgelserne af krystaller med forskellige niveauer af strontiumdotering har afsløret en række ligheder og forskelle mellem superledende og ikke-superledende prøver. Vores eksperimenter viste en forskydning af den spektrale vægt fra spinfluktuationer med lav energi mod endnu lavere energier, dvs. til den elastiske eller kvasi-elastiske kanal. Desuden finder vi intet spin gap i nogen af vores prøver uanset ledningsegenskaber og et drastisk fald i både elastiske og uelastiske magnetiske signaler for superledende krystaller førte os til at foreslå en model sammensat af flere sameksisterende elektroniske ordener. Vi argumenterer for, at fasediagrammet for LSCO udviser moduleret superledning i form af en såkaldt par-densitets-bølge samtidig med homogen d-bølge superledende regioner, og forholdet mellem disse kan justeres ved hjælp af doteringsgraden.

Ud over studierne af den magnetiske struktur har vi også undersøgt doteringsfordelingen i en af vores superledende LSCO-enkeltkrystaller ved hjælp af polariseret neutronbilleddannelse. Temperaturafhængigheden af den indfangede magnetiske flux i vores prøve viste en doteringsvariation i vækstretningen af vores krystaller, der også blev bekræftet ved hjælp af magnetiske susceptibilitets målinger. Endelig har vi identificeret oprindelsen til et inkommensurabelt magnetisk signal, der findes i samme position i det reciprokke rum som spin-stripesignalet. Beregninger har vist, at signalet er en falsk dobbeltspredningshændelse.

Den anden kuprat-forbindelse, som vi fokuserede på, var ilt-doteret La_2CuO_{4+y} (LCO+O). En betydelig mængde data er blevet indsamlet for disse prøver af vores gruppe gennem årene. Jeg har samlet og kombineret data og udført yderligere målinger, som førte til en uddybende forståelse af magnetismen i denne type forbindelser. Ved hjælp af polarisationsanalyse viste vi, at ladningsstriber løber langs både den tetragonale a og b akse, og at magnetiske fluktuationer sandsynligvis er isotrope. Desuden er manglen på et spin gab eller en signifikant effekt ved

påtrykkelse af et magnetfelt på lav-energistiske magnetiske fluktuationer blevet fortolket som en manifestation af en mikroskopisk sameksistens mellem superledning og spin fluktuationer. Vi argumenterer for, at magnetisk orden stammer fra en separat elektronisk fase, der konkurrerer med superledning.

Udover de konklusioner, vi har draget ovenfor, viser vores undersøgelser at lignende materialer, der har superledning til fælles, kan udvise store forskelle ved angår de magnetiske strukturer. Dette peger på et meget komplekst samspil mellem superledning og magnetisme yderligere forskning er nødvendig for at forklare mekanismen bag pardannelsen i disse materialer.

ACKNOWLEDGEMENTS

I have entered the PhD program with an idyllic and probably naive view of how science is produced, what it takes and how long it takes. The reality of the job has been a bit more hectic and confusing than what I had expected but it has undoubtedly been the most rewarding and fun professional experience I have had so far.

The past three years have been enjoyable largely thanks to the people I have encountered and with whom I got to work. I am indebted to many people who have been instrumental in getting this thesis to completion. Some deserve a special mention:

My supervisors - Kim Lefmann, Martin Böhm, Paul Steffens and Astrid Tranum Rømer who inspired me and very kindly supported me all along the project.

Tim - for stimulating discussions and all the fun moments we spent together during the late-running beamtimes.

Henrik - for the many *good learning experiences* and pushing and helping me to go further

All my collaborators and co-authors - for their constructive critique and comments

All the scientists that published papers on high temperature superconductors - who have brought confusion, frustration but also enlightenment into my life

The ILL PhD community - for all the special moments we shared in what became an enlarged family

The students from KU - who have always been extremely welcoming and made me feel part of the group even though I was away most of these years

My family and my husband - for their unconditional love and support.

CONTENTS

LIST OF FIGURES

LIST OF TABLES

NOMENCLATURE

Physical Constants

Symbol	Description	Value
$\hbar$	Reduced Planck constant	$1.054571800(13) \times 10^{34}$ Js
μ_0	Magnetic permeability of free space	$4\pi \times 10^7$ TmA^{-1}
μ_B	Bohr magneton	$9.274009994(57) \times 10^{24}$ JT^{-1}
e	Electron charge	$1.6021766208 \times 10^{19}$ C
h	Planck constant	$6.626070040(81) \times 10^{34}$ Js
k_B	Boltzmann constant	$1.38064852(79) \times 10^{23}$ JK^1
m_e	Electron mass	$9.10938356 \times 10^{31}$ kg

Physical Symbols

Symbol	Description
χ	Magnetic susceptibility
δ	Incommensurability
λ_L	London penetration depth
Φ	Magnetic flux
ρ	Resistivity
ε	Electric field
ξ	Coherence length
B	Magnetic flux density
H	Magnetic field strength
j	Electrical current density

M	Magnetisation
T^*	Pseudo gap closing temperature
T_g	Magnetic freezing temperature/ Onset of spin glass phase
T_N	Néel temperature
T_s	Phase transition temperature (from HTT to LTO)
T_c	Superconductivity critical temperature
a_T, b_T, c_T	Tetragonal crystal lattice parameters
a, b, c	Orthorhombic crystal lattice parameters
x	Strontium doping content
y	Additional oxygen doping content

Abbreviations

μSR	Muon spin rotation
AC	Alternating current
AFM	Antiferromagnetic
CDW	Charge density wave
FL	Fermi liquid
FM	Ferromagnetic
HTSC	High temperature superconductors
HTT	High temperature tetragonal
IC	Incommensurate
ILL	Institute Laue Langevin in Grenoble, France
LCO	La_2CuO_4
LCO+O	La_2CuO_{4+y}
LSCO	$La_{2-x}Sr_xCuO_4$

LSCO+O	$La_{2-x}Sr_xCuO_{4+y}$
LTO	Low temperature orthorhombic
LTT	Low temperature tetragonal
NMR	Nuclear magnetic resonance
PDW	Pair density wave
PG	Pseudo gap
SC	Superconductor
SCVF	Superconducting volume fraction
SDW	Spin density wave
TSFZ	Traveling solvent float zone
VSM	Vibrating sample magnetometry
XPD	X-ray powder diffraction
ZFC	Zero field cooled

LSCO+O $La_{2-x}Sr_xCuO_{4+y}$

Part I

INTRODUCTION AND THEORY

INTRODUCTION TO THE PROJECT

1.1 MOTIVATION

Solving the long-standing question of the origin of high temperature superconductivity will undoubtedly be one of the most celebrated achievements of, hopefully, this century. The discovery will not only be exceptional in itself but also through the remarkable amount of research that will lead up to it. The field already counts tens of thousands of publications [1] making it difficult to navigate and keep up with the new developments. Still today, high temperature superconductivity remains one of the most active research fields thanks to improved experimental techniques and sample preparation methods as well as theoretical and modelling advances.

In the cuprates family of high temperature superconductors, there is ample evidence supporting the idea that the complex magnetism, exhibited by these materials, is strongly connected to superconductivity. For this reason we have decided to study the interplay between these two by means of elastic and inelastic neutron scattering. To address this issue we have focused on a very specific region of the phase diagram of the archetypal cuprate $La_{2-x}Sr_xCuO_4$. These samples exhibit a zero-temperature phase transition between an insulating and a superconducting phase around strontium doping $x = 0.055$. This boundary can be crossed not only by doping but also by applying a magnetic field perpendicular to the CuO_2 layers. We have thus set out to make a detailed study of this phase transition by analysing samples on both sides of the of the boundary ($x = 0.05$, 0.06, 0.07 and 0.08), as a function of varying temperature and applied magnetic field. Part of the motivation comes from the fact that this region of the phase diagram has been sparsely studied up to now. However, we believe it holds important information about the conditions which make superconductivity possible. Through this comparative experimental analysis we aimed to discover which characteristics are essential for the emergence of superconductivity and which are not.

Another essential aspect in developing a unified theory to explain high temperature superconductivity is the universality of the observed traits across all the compounds of this class of materials. One of the most interesting and challenging compounds to test is the oxygen doped La_2CuO_{4+y}. Even though crystallographically it is very similar to the other constituents of the family the mobility of the doped ions gives rise to new intriguing phenomena. Part of this research work has been dedicated to performing a detailed study of this sample. Elastic and inelastic neutron scattering have been used to analyse the magnetic field and temperature dependence of both static and dynamic stripes. Polarisation analysis was also employed in order to determine the orientation of the two signals.

1.2   READING GUIDE

This thesis is divided into three main parts depending on the type of content.

Part i aims to introduce the general concepts used thought the rest of the manuscript. Chapter 2 is a brief basic introduction into the field of magnetism. In Chapter 3 I go through the most important properties of superconductivity in general and highlight some basic characteristics of the particular class of superconductors of interest in this work, the cuprates. A detailed description of the latest developments concerning each sample of interest is included in the beginning of each chapter in Part ii. Finally, Chapter 4 introduces concepts of neutron scattering focusing on scattering from crystalline materials. It also includes descriptions of the neutron instruments used in this research.

Part ii includes the experimental data, analysis and discussions undertaken in this project. The division mirrors the articles we have published or are in preparation. Chapter 5 encompasses most of the experimental work which I have performed. It focuses on measurements performed in the underdoped region of the LSCO phase diagram. This chapter is further divided into sections according to sample doping and ends with an overall discussion and conclusion. Chapter 6 presents a detailed study for the oxygen doped compound of the cuprates family LCO+O. In Chapter 7 I present the results of a polarised neutron imaging experiments which revealed a doping distribution in one of our crystals. Chapter 8 comes as a continuation of my Master's thesis and displays the analysis that led to the unveiling the origin of an apparent magnetic signal as a spurious double scattering event. Chapter 9 consists of an overview of the different conclusions drawn in each subsection of the project.

Finally, the appendices include detailed guides on data conversion and normalisation, additional relevant data plots as well as a complete list of all the publications that I have been part of together with a brief description of my contribution to each of them.

MAGNETISM

The first observation of magnetism dates back to 585 B. C. when Thales (a name which will be recurrent throughout this manuscript) of Miletus observed that loadstone attracts iron and concluded that the former must have a soul [2]. Knowledge evolved of course from this initial explanation and many civilisations in the Middle Ages were making use of magnetism for travel purposes. However, it wasn't until the 16th century that another important breakthrough was to take place. This was the time when W. Gilbert postulated that the Earth itself is a giant magnet [3]. But what is maybe an even more important contribution is the paradigm shift in how to approach science which Gilbert stood for. He advocated for a challenge of absolute authority through individual experimentation. This upsurge in investigations lead to a number of important discoveries such as the development of the voltaic cell and the realisation, by Oersted, that electrical currents and magnetism are connected [4]. The latter constitutes the groundwork of what we call today the field of electromagnetism. On this foundation, over the next centuries, numerous physicists have built theories that made possible the transition from empirical knowledge to a thorough understanding of the properties of magnetic materials and magnetic effects.

In this chapter a brief introduction into the vast field of magnetism is provided. The main focus is on the interactions between magnetic moments which eventually lead to the formation of various ordered states. Finally we will briefly look into the emergence of these ordered states through different types of phase transitions. The text and structure are inspired by S. Blundell's well-known book on magnetism in condensed matter [5].

2.1 MAGNETIC MOMENTS AND SUSCEPTIBILITY

The elementary units of magnetism are the magnetic moments defined as $\boldsymbol{\mu} = g\mu_B \boldsymbol{s}$, which includes the g-factor, the Bohr magneton $\mu_B = \frac{e\hbar}{2m_e} = 9.274 \times 10^{-24}$ J/T (e being the elementary charge, $\hbar$ the Planck constant and m_e the mass of the electron) and the spin, $\boldsymbol{s}$. Since in materials magnetism is caused by unpaired electrons, it is interesting to look at this particular case. Knowing that the g-factor is ~ 2 for a free electron and that it's spin is $1/2$ we deduce that the magnetic moment of one free electron is given by the Bohr magneton.

If we are now to place our electron in a magnetic field ($\boldsymbol{B}$) the Hamiltonian or energy associated with the interaction between the two will depend on the relative orientation of the magnetic moment and field and is given by

$$\mathcal{H}_Z = -g\mu_B \boldsymbol{B} \cdot \boldsymbol{s}.$$

This is also named the Zeeman splitting pointing to the fact that the energy levels of an electron are split in the presence of a magnetic field. However, real materials are composed of atoms with more than one electron orbiting the nucleus. The atom's magnetic moment (associated with the total angular momentum $\boldsymbol{J}$) is thus the sum of spin $\boldsymbol{S}$ and orbital $\boldsymbol{L}$ angular momenta: $\boldsymbol{J} = \boldsymbol{S} + \boldsymbol{L}$. The manner in which the electrons occupy the atom's energy levels (shells) dictates the value of the total angular momentum. In order to minimise the energy, most electrons will fill inner shells of the atom and, owing to Pauli's exclusion principle, will have no net contribution to the angular momentum. As it has been mentioned before, it is the unpaired electrons from the unfilled shells that give materials their magnetic character by combining in ways that result in non-zero spin and orbital angular momentum. To determine the electronic ground state the empirical Hund's rules provide a fairly accurate prediction especially for 3d[1] and 4f ions. They are however limited to materials in which interactions between the atoms (such as crystals fields which will be explained in the following section) are not dominant. In total there are 3 rules which tell us to:

- maximise the total spin $\boldsymbol{S} = \sum_i \boldsymbol{s}_i$,

- maximise the orbital momentum, $\boldsymbol{L}$,

- if the shell is more than half filled, maximise the total angular momentum $\boldsymbol{J} = |\boldsymbol{L} + \boldsymbol{S}|$. Otherwise, minimise $\boldsymbol{J}$ ($\boldsymbol{J} = |\boldsymbol{L} - \boldsymbol{S}|$).

The underlying physical interactions behind Hund's rules are Coulomb interaction (rules 1 and 2) and spin orbit coupling (rule 3).

Knowing the magnetic moment we can move one step further and also define the magnetisation ($\boldsymbol{M}$) of a material as the magnetic moment per unit volume. Using the magnetisation it is now possible to differentiate between various categories of materials as a function of their response to an applied magnetic field. For this purpose we can define an additional property, namely the magnetic susceptibility (χ):

$$\boldsymbol{M} = \chi \boldsymbol{H},$$

where $\boldsymbol{H}$ is the magnetic field (and it is related to the above mentioned $\boldsymbol{B} = \mu_0 \boldsymbol{H}$, where $\mu_0 = 4\pi \times 10^{-7}$ Hm^{-1} is the permeability of free space). This relationship is valid in the limit of small H. Judging by the value of the magnetic susceptibility two main classes of materials are defined: (1) diamagnetic materials which have negative susceptibility indicating that the applied magnetic field induces a magnetic moment in the opposite direction (all materials exhibit a certain degree of diamagnetism) and (2) paramagnetic materials exhibiting positive susceptibility which reveals that the magnetic moments align parallel with the applied magnetic field.

---

1 It should be noted that Hund's rules predictions for 3d ions are often less accurate than for 4f ions. The reason for that is the fact that d-orbitals extend out too far from the nucleus and are thus more sensitive to environment, while the f-electrons are closer to the nucleus and less perturbed by the surroundings.

2.2 MAGNETIC INTERACTIONS AND ORDER

So far we have mostly considered the properties of free electrons and their interaction with an external magnetic field. In real materials however, the interplay between magnetic atoms, their environment and their neighbouring magnetic atoms can play a crucial role.

The local symmetry of the environment will influence the distribution of the atom's energy levels through the so-called crystal fields. The origin of a crystal field is the electrostatic interaction which arises from the overlap of the orbitals of the magnetic atom and those of the surrounding atoms. A splitting of the energy levels can thus be induced by the environment with levels corresponding to a high overlap being raised in energy and conversely the ones with lower or no overlap being lowered in energy. In some cases however, it might be more energetically favourable for the environment to distort as a consequence of the magnetic properties of the magnetic atoms. This is known as the Jahn-Teller effect.

The most interesting phenomena, such as the emergence of magnetic order or frustration, arise from the magnetic interactions between spins. There are several types of interactions some more important in certain materials than others. For example, one such interaction is the dipolar interaction which depends on the separation and degree of alignment between two magnetic dipoles. While it is usually too weak to be considered a driving factor in magnetic ordering of most materials, it can become important in understanding the ones that order at sub-kelvin temperatures.

When discussing long-range magnetic order it is however the exchange interaction that plays the most important role. The microscopic origin of the exchange interaction is the Coulomb repulsion (in concert with Pauli's exclusion principle) and the fermionic wavefunction anti-symmetry. The total wavefunction of a system comprising two electrons must be anti-symmetric with respect to the exchange of the two particles. However, the wavefunction involves the product of a spin part and a spatial part. Therefore, the spatial part must be symmetric if the spin part is anti-symmetric (a singlet state) and vice-versa for a symmetric spin triplet state:

$$\Psi_S = \frac{1}{\sqrt{2}}[\psi_a(\boldsymbol{r}_1)\psi_b(\boldsymbol{r}_2) + \psi_a(\boldsymbol{r}_2)\psi_b(\boldsymbol{r}_1)]\chi_S, \tag{2.1}$$
$$\Psi_T = \frac{1}{\sqrt{2}}[\psi_a(\boldsymbol{r}_1)\psi_b(\boldsymbol{r}_2) - \psi_a(\boldsymbol{r}_2)\psi_b(\boldsymbol{r}_1)]\chi_T.$$

According to the Pauli's exclusion principle the particles will have a different spatial separation depending on their spin symmetry. This means that states with different spin symmetry will also have different energies (E_S and E_T). Hence the Hamiltonian can be expressed in terms of the singlet and triplet energies and parametrized using the spins of the two particles $\boldsymbol{S_1} \cdot \boldsymbol{S_2}$:

$$\mathcal{H} = \frac{1}{4}(E_S + 3E_T) - (E_S - E_T)\boldsymbol{S_1} \cdot \boldsymbol{S_2}.$$

The spin part of this Hamiltonian can be written as:

$$\mathcal{H}^{spin} = -2J\boldsymbol{S_1} \cdot \boldsymbol{S_2},$$

where we define the exchange constant $J = \frac{E_s - E_T}{2}$. This can of course be generalised to a system of many particles (it is however not a trivial task) and use the so-called Heisenberg Hamiltonian to describe the exchange interactions between neighbouring atoms:

$$\mathcal{H} = -2 \sum_{i>j} J_{ij} \boldsymbol{S_i} \cdot \boldsymbol{S_j}.$$

Depending on the sign of the exchange constant different types of magnetic order emerge. If $J > 0$, meaning $E_S > E_T$, the triplet state is favoured and thus the energy is minimised when spins are parallel. Therefore, below a certain critical temperature (the Curie temperature) a ferromagnetic (FM) order will become the ground state. Similarly, for $J < 0$ the ground state (below the so-called Néel temperature) will be antiferromagnetic (AFM). Other more complicated types or order, such as spin glasses or helical order, are also possible. Figures 2.2.1(a)-(c) exemplify three such types of magnetic order. What is of interest, especially for the particular case of neutron scattering experiments which are the main probing technique of this thesis, is the relationship between the crystallographic unit cell size and the length of the magnetic structure (the period L). The associated magnetic ordering vector $\boldsymbol{Q}$ is related to the latter as $|\boldsymbol{Q}| = 2\pi/L$ [6]. This means that in a neutron scattering experiment (simulated in Figure 2.2.1(d)) the FM signal will be visible at the same position as the structural one (since $L = a$), the AFM signal will appear at $(1/2, 1/2)$ of that distance (since it requires two crystal unit cells to make up one magnetic unit cell and the magnetic unit cell is also tilted by 45°) and, similarly, the helical one will require 12 crystal unit cells for one full period (in the particular case represented here).
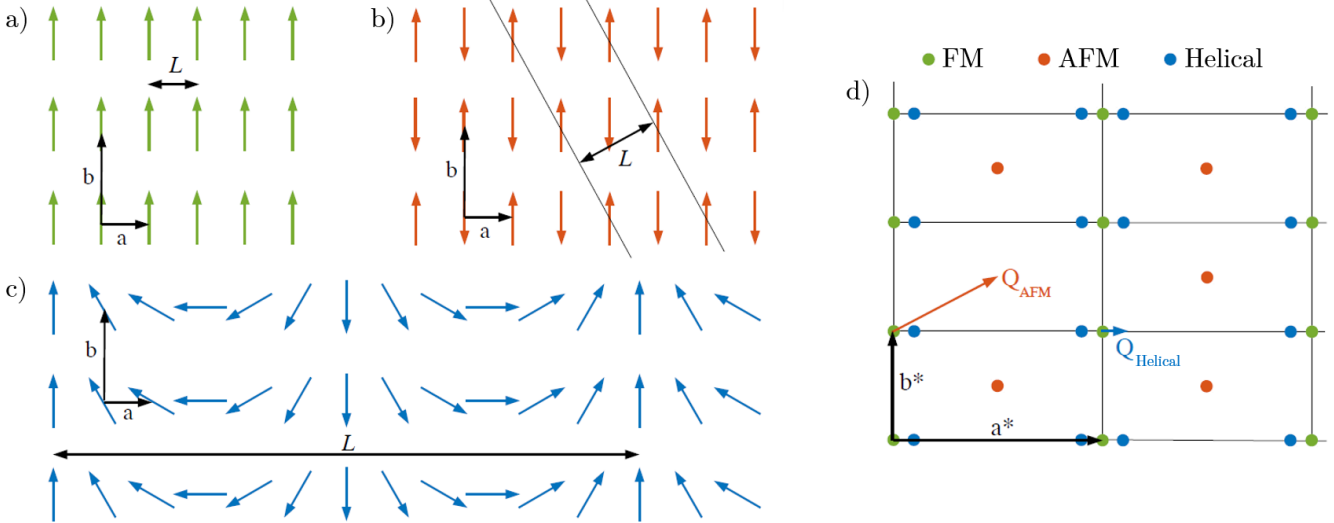
Figure 2.2.1: Various types of magnetic orders depicted in real space: **(a)** ferromagnetic (FM), **(b)** antiferromagnetic (AFM), **(c)** helical order. The crystallographic unit cell vectors a and b are kept the identical for all examples. The length of the magnetic period is denoted by L in each image. **(d)** Graphical representation of the expected positions, in reciprocal space, of the neutron scattering signal generated by each type of magnetic structure. Images taken from [6].

Unmediated direct exchange in most materials is not effective enough to account for the formation of magnetic order due to insufficient overlap between the magnetic orbitals of neighbouring ions. In many magnetically ordered materials it is the indirect exchange that plays the most important role. One such type of interaction is the superexchange where the interaction

between non-neighbouring magnetic ions is mediated by intercalated non-magnetic ones (such as oxygen). In this case the exchange constant balances the costs in Coulomb energy (U) induced by the proximity of charges of the same type (electrons for example) and the energetic gain if charges are free to move from one orbital to another (quantified by a so-called hopping constant, t), $J \approx -t^2/U$. Other types of indirect exchange interactions include: the RKKY interaction mediated by the conduction electrons in metals or the double exchange which may arise in oxides containing ions with mixed valencies.

2.3 MAGNETIC PHASE TRANSITIONS

As it has been mentioned in the previous section, magnetic order sets in below a certain critical temperature (more generally named a critical point) which marks the transition from a disordered state to an ordered one. When talking about magnetic order we implicitly assume the existence of an order parameter that defines the state. For example, for a ferromagnet the order parameter is the magnetisation $\boldsymbol{M}$ while for an antiferromagnet the order parameter is the staggered magnetisation $\boldsymbol{M}_\uparrow - \boldsymbol{M}_\downarrow$ (where the two define the magnetisation of the two sublattices with magnetic moments pointing up or down) [6]. The order parameter arises as a consequence of a broken symmetry. Thus above the critical point the order parameter is zero while below the critical point the spin rotation symmetry will be broken and the order parameter will have a non-zero value [7].

Phase transitions can be classical first or second order phase transitions or quantum phase transitions. The order of the classical transitions is given by the lowest derivative of the free energy which exhibits a discontinuity at the critical point. For first order transition, as the name suggests, the first derivative of the energy (magnetisation, entropy or volume) will show discontinuous jumps. Abrupt changes in entropy will manifest as absorption or release of heat. This is not the case for a second order phase transition (also called a continuous phase transition) where discontinuities occur in the second derivative of the free energy. One such transition is the ferromagnetic and antiferromagnetic transitions for which the order parameter follows a power law decay near the critical temperature, T_c, characteristic to second order transition:

$$M \propto (T_\text{c} - T)^\beta.$$

This power law behaviour is also exemplified in Figure 2.3.1.

On the other hand, a quantum phase transition is a transition driven by a non-temperature parameter (such as magnetic field, pressure or chemical composition) taking place at 0 K. The generic phase diagram depicted in Figure 2.3.2 shows the difference between the temperature driven classical phase transition and the quantum phase transition characterised by the tuning parameter p. At the quantum critical point (QCP) the system transitions from an ordered state to another one with a different ground state or to a disordered phase. Even though absolute zero cannot be achieved in experiments, traits of a quantum phase transition are observable close to the QCP at low temperature. In this quantum critical region (highlighted in blue in the figure) quantum fluctuations (with an energy scale $\hbar\omega$, where ω is the frequency of quantum fluctuations) dominate over classical thermal fluctuations (of energy scale $k_B T$).
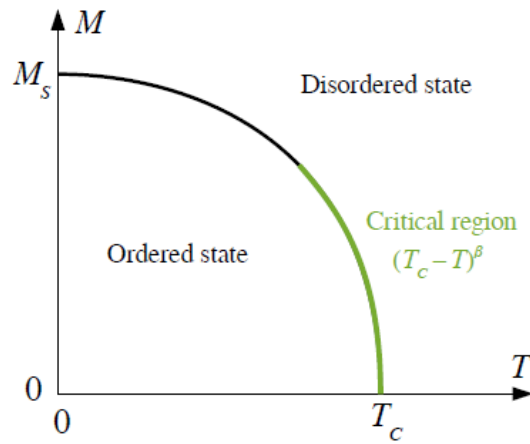
Figure 2.3.1: Generic phase diagram of a second order phase transition. M_S denotes the saturation magnetisation while the critical region is highlighted in green. Image taken from [6].
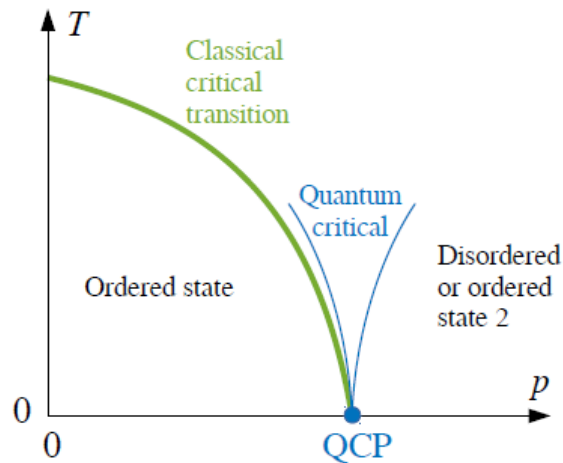
Figure 2.3.2: Generic phase diagram of a quantum phase transition. The representation shows the transition from an ordered phase to a disordered/differently ordered one as a function of varying tuning parameter p. In blue the quantum critical point and region are depicted. Image adapted from [8] by S. Holm [6].

SUPERCONDUCTIVITY

The very first observation of one of the properties that define superconductors (SC), namely zero electrical resistance, dates back to 1911 when Heike Kamerlingh Onnes measured the, by now famous, resistivity curve of pure mercury as a function of decreasing temperature [9] (see Figure. 3.0.1).
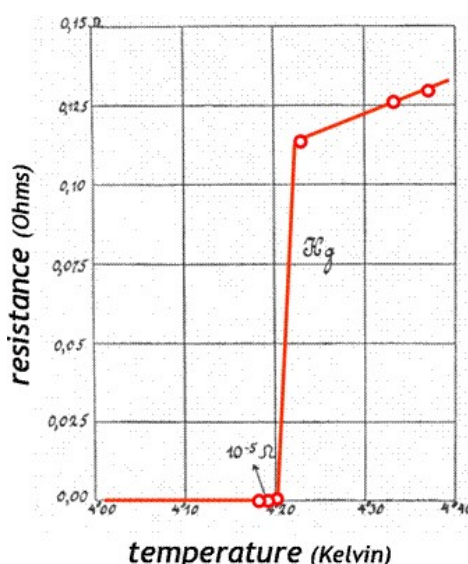
Figure 3.0.1: Electrical resistivity measured as a function of temperature by H. K. Onnes in 1911 [9].

Even though the result was unexpected it does not mean that the phenomenon was discovered by chance. Some decades before in the 1860s a new type of thermometer was proposed by William Siemens, the so-called resistance thermometers. These proved to be an excellent complementary tool to the classical gas thermometers. As a consequence one of the most asked scientific question at the time was how does the electrical resistance of a metal behave in the proximity of absolute zero. To answer this, two main theories were circulating [10]. One, proposed by William Thomson (Lord Kelvin), was speculating that the resistivity will become infinite as a consequence of electrons freezing upon cooling. The second, put forward by Paul Drude, argued that electrical resistance will decrease linearly with temperature down to zero. The opportunity to settle this matter arrived when H. K. Onnes managed to liquefy helium for the first time in history in 1908 thus making experiments under extremely low temperatures possible. Once the cooling system based on liquid helium was in place, Onnes began to measure the resistivity of metals as a function of decreasing temperature starting with platinum which was commonly

used in resistance thermometers. The experiment revealed that below 4.25 K platinum exhibits a constant resistivity thus disproving Lord Kelvin's theory of freezing electrons. This meant that the second proposal could be correct one and the observed residual resistivity, which prevented the reach of perfect conductivity as predicted, was caused by impurities in the material. To prove the theory beyond doubt a pure metal was needed. Hence the next experiments were performed on double distilled mercury and resulted in the historical graph shown in Figure 3.0.1. However, the discovery deviates from prediction in that mercury has a sharp transition, and not linear, to zero resistivity at 4.2 K. Onnes understood that a new state of matter emerges below this critical temperature and decided to name it supraconductivity. Only one year later supraconductivity was achieved in both tin and lead below 3.8 and 6 K respectively. At this point, the phenomenon was validated and universally recognised.

However challenging this discovery might seem, it is only the beginning of a research field which has been enchanting the curiosity of numerous scientists ever since. 113 years later, the phenomenon still holds great enigmas that need to be understood. This chapter contains a short review of both the understood as well as the ununderstood properties of superconductors inspired by J. F. Annett's [11] and C. Kittel's [12] books. The final sections focus of the family of cuprate superconductors which are the main focus of this thesis.
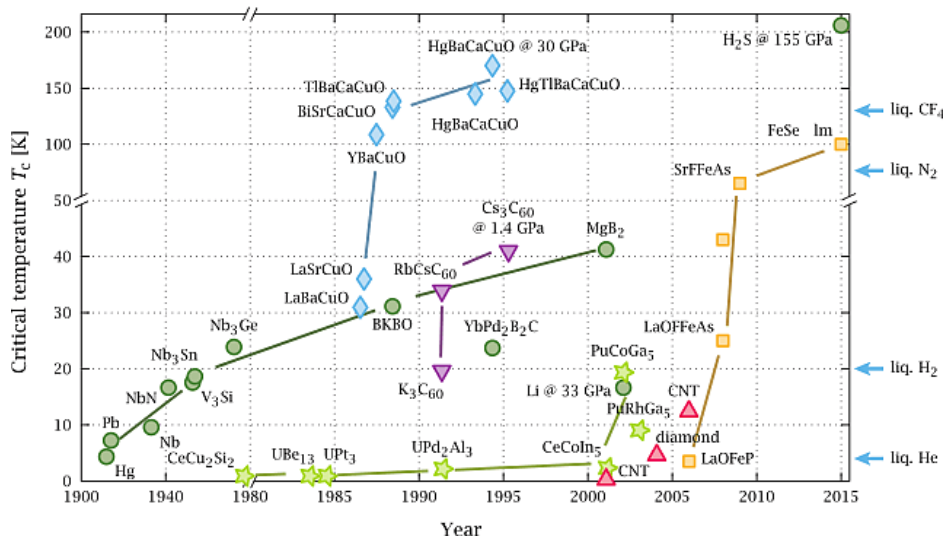
Figure 3.0.2: Timeline of superconductivity. Different classes of superconductors are denoted by different symbols. Green circles represent the type I (or conventional) superconductors explained by BCS theory. The records in this class are held by H_2S, under extremely high pressure (155GPa), with $T_c = 203$ K [13], while in ambient pressure only a modest $T_c = 39$ K is achieved in MgB_2. The next discovered family of superconductors are the heavy fermion ones depicted by light green stars. The blue diamonds are the cuprate superconductors which have in common layers of copper-oxide. In purple and red triangles are depicted the organic and carbon structure superconductors respectively. Finally, the orange squares denote iron based superconductors. Various liquefying temperatures are highlighted on the right-hand side y-axis. Note that both x and y-axis exhibit one change of scale each. Image taken from [14].

3.1 TYPE I SUPERCONDUCTORS

Over the years, many different types of superconducting materials with different properties have been discovered. Figure 3.0.2 presents the timeline of these discoveries including the critical

superconducting temperature, T_c. The main focus of this chapter are however only the type I SC which include the first discovered mercury (these are often called conventional superconductors as there exists a theory in place to explain the details of the SC phase) and the family of cuprate superconductors which belong to the type II class (sometimes called unconventional, partly due to a lack of full understanding of the SC phase, or high temperature superconductors). One of the subsections of this chapter explains the differences between these two types of superconductivity.

3.1.1 *Resistivity*

The first property used to define superconductivity has been the transition to the unforeseen zero electrical resistivity below a specific critical temperature. In practice it is rather difficult to measure a parameter with a value of exactly zero as it is complicated to distinguish it from very small finite values. We are however certain that the resistivity is exactly zero and probably one of the most conclusive manifestations of this phenomenon is the observation of persistent currents [11].

The experiment goes as follows. Let us consider a superconducting ring. The flux (Φ) of magnetic field ($\boldsymbol{B}$) through the centre of the ring will be defined by:

$$\Phi = \int \boldsymbol{B} \cdot d\boldsymbol{S},$$

where $d\boldsymbol{S}$ is a vector perpendicular to the surface of the ring of length equal to an infinitesimal portion of the area confined by the ring.

In order to include the resistivity, which is the property of interest for us, we must make use of the Maxwell equation:

$$\nabla \times \boldsymbol{\varepsilon} = -\frac{\partial \boldsymbol{B}}{\partial t}.$$

and Stokes's theorem:

$$\int (\nabla \times \boldsymbol{\varepsilon})\, d\boldsymbol{S} = \oint \boldsymbol{\varepsilon} \cdot d\boldsymbol{r}$$

This leads us to:

$$-\frac{d\Phi}{dt} = \oint \boldsymbol{\varepsilon}\, d\boldsymbol{r}, \tag{3.1}$$

where the integral is taken along a path enclosed by the ring. The resistivity, ρ, is related to the electrical field, $\boldsymbol{\varepsilon}$, through the electrical current density, $\boldsymbol{j}$, as $\boldsymbol{\varepsilon} = \rho \boldsymbol{j}$. If a path well inside [1] the superconducting ring is considered where $\rho = 0$ and therefore $\boldsymbol{\varepsilon} = 0$ Equation 3.1 will become:

$$\frac{d\Phi}{dt} = 0, \tag{3.2}$$

meaning that the magnetic flux through the ring is constant in time. To test this experimentally a magnetic flux is trapped inside the superconducting ring by cooling it through its critical

---

1 It will be explained in the following sections why a path at the surface is not optimal.

temperature inside an applied magnetic field. When the ring is in the superconducting phase and the external field is turned off in order to obey Equation 3.2 the superconductor must generate a circulating current I which will induce the appearance of a magnetic field through the centre of the ring. Since the flux must be kept constant then the current must also be constant. This requires the absence of any energy dissipation meaning the resistivity of the ring must be zero. The phenomenon was first observed by Onnes and subsequent experiments have shown that the decay time of the current is more than 100.000 years [15]. This makes resistivity practically zero in the reference system any experiment.

3.1.2 *Meissner-Ochsenfeld Effect*

The second and most used property in describing superconductors, for the practical reason that it is easier to demonstrate experimentally, was brought to light 22 years after Onnes' initial discovery by W. Meissner and R. Ochsenfeld hence the naming [16]. In a nutshell the Meissner-Ochsenfeld effect describes the ability of superconducting materials to expel magnetic fields. This means that as temperature is decreased below the superconducting critical one, the sample transitions to a state in which $B = 0$ inside the material as exemplified in Figures 3.1.1(a) and (b). In order to create the expulsion effect, the material will create so-called shielding currents at the surface (highlighted in orange in Figure 3.1.1(b)) which in turn will generate a magnetic field inside the superconductor in the opposite direction of the applied one such that the two exactly cancel out. In the previous chapter it has been mentioned that all materials exhibit diamagnetic behaviour to some extent. Superconductors are one of the few examples where it is dominant. In fact SC are perfect diamagnets below the critical temperature meaning that magnetic susceptibility χ abruptly drops to -1 when the sample becomes superconducting. This is related to the null value of the magnetic field inside the sample:

$$\boldsymbol{B} = \mu_0(\boldsymbol{H} + \boldsymbol{M}) = 0, \tag{3.3}$$

which is accomplished when

$$\boldsymbol{M} = -\boldsymbol{H}. \tag{3.4}$$

In turn this implies:

$$\chi = \frac{|\boldsymbol{M}|}{|\boldsymbol{H}|} = -1. \tag{3.5}$$

In practice, the magnetic field does penetrate the superconductor at the surface over a length called the London penetration depth (λ_{L}) after its discoverers the German brothers Fritz and Heinz London [18]. As exemplified in Figure 3.1.1(c), the applied magnetic field ($H_x = B_0$) will decay exponentially after entering the superconductor [12]:

$$B = B_0 \exp\left(-\frac{x}{\lambda_{\mathrm{L}}}\right), \tag{3.6}$$
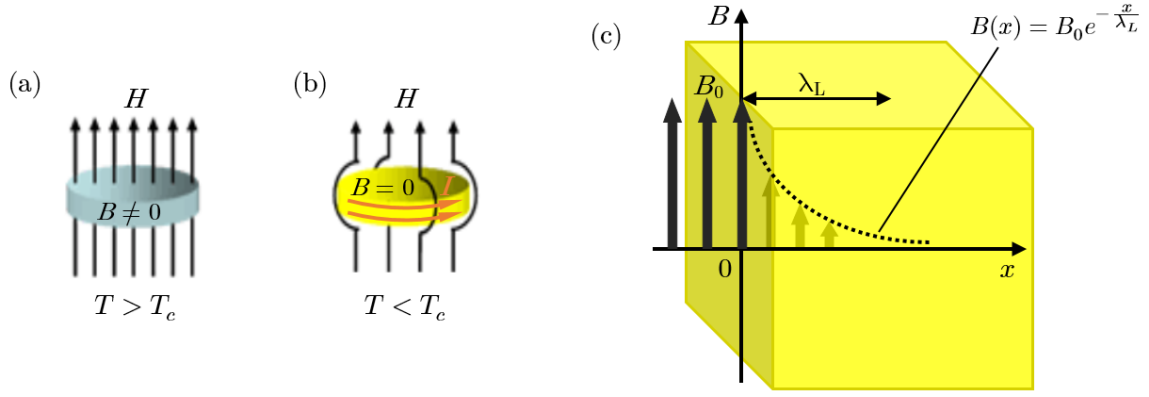
Figure 3.1.1: (a)-**(b)**Graphical representation of the Meissner-Ochsenfeld effect: in blue the normal state, ($T > T_c$) is presented with the applied magnetic field lines penetrating inside the SC, while in yellow we observe a sample which has transitioned into the superconducting state ($T < T_c$) and is expelling the magnetic field lines. **(c)** Penetration of an applied magnetic field inside a superconducting material. The exponential decay on a length scale given by the London penetration depth is depicted. Images adapted from [6] and [17].

where the penetration depth is defined as:

$$\lambda_{\mathrm{L}} = \sqrt{\frac{m_e}{\mu_0 n_s e^2}},$$
(3.7)

and includes the electron mass (m_e) and charge (e), the number density of superconducting carriers (n_s) and the magnetic permeability of free space (μ_0). Typically the penetration depth takes values between 50 and 500 nm [19].

3.1.3   *BCS Theory*

Type I superconductors are often called conventional in part because we now have a microscopic theory to explain the phenomenon. The breakthrough was made by J. Bardeen, L. N. Cooper, and J. R. Schrieffer mode than 40 years after the initial discovery [20]. In very simple terms, the theory explains how the lattice vibrations, phonons, enable the electrons to form so-called Cooper pairs. The process is sketched in Figure 3.1.2.

BCS theory was based on a number of important observations and assumptions. One such insight is the possibility that the forces between electrons can be attractive and not only repulsive. This makes possible the formation of pairs of electrons with opposite spin and momentum. The newly formed pair will have a bosonic behaviour and the collection of all pairs in the material will result in a Bose-Einstein-like condensate.

The nature of the electron pairing interaction was postulated based on the prior observation that the superconducting critical temperature is isotope dependent. E. Maxwell was the first to observe that heavier mercury isotopes exhibit a lower superconducting critical temperature compared to the lighter ones [21]. At the same time C. A. Reynolds *et al.* [22] have performed magnetic susceptibility measurements on different isotopes of mercury with the average mass number varying from 199.7 to 203.4 and have shown that there is a linear dependence between T_c
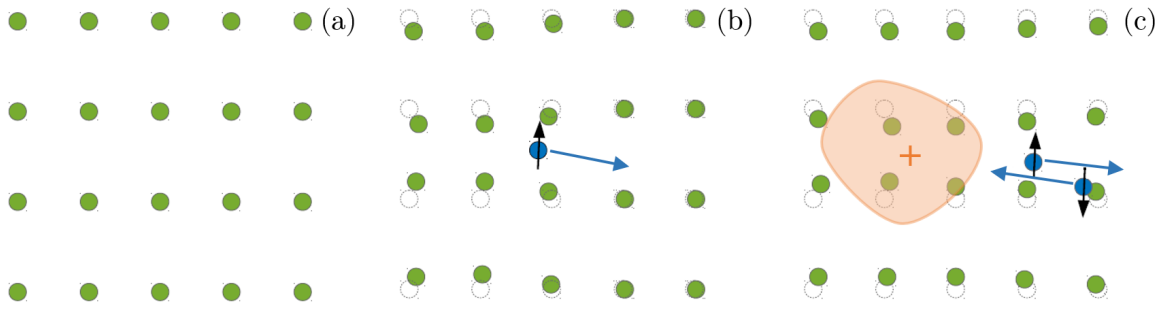
Figure 3.1.2: Graphical representation of phonon mediated Cooper pairing in the BCS theory framework. The undisrupted lattice **(a)** gets disturbed by the passing of an electron (blue circle) **(b)**. The positive ions of the lattice will be attracted by the negative charge of the electron creating, for a short period, an area of increased positive charge (highlighted in orange). **(c)** A second electron will then be attracted by this area. The two electrons thus continue to interact with each other through the distortion of the lattice as they continue their movement. The black arrows represent the spins of the electrons while the blue arrows indicate their trajectory. Images adapted from [6] and [14].

and the average atomic mass number (see Figure 3.1.3). This realisation was fundamental in the development of the theory relating the attractive potential of electrons and the lattice vibrations frequencies.
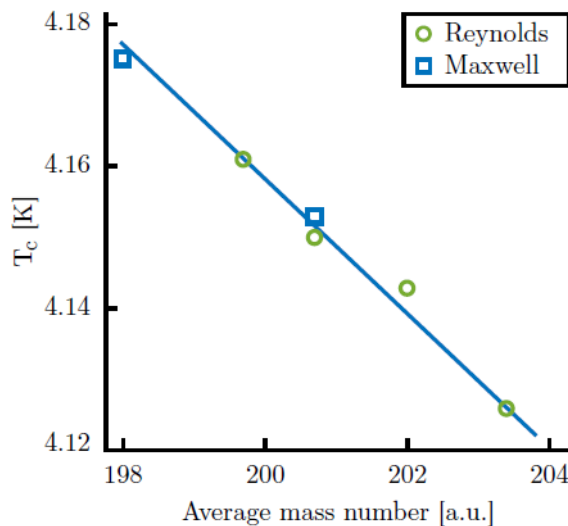
Figure 3.1.3: Superconducting critical temperature as a function of the average atomic mass number of different mercury isotopes. Image adapted by [6] from [22].

Another remarkable feature of BCS theory is the fact that it predicted a number of testable properties such as: (1) a ~ 30 K upper limit for the superconducting critical temperature (in ambient pressure[2]) imposed by the requirement of having materials with a low enough atomic mass that can accommodate high frequency phonons while in crystalline phase; or (2) the existence of a temperature dependent energy gap ($\Delta(T)$) which relates to T_c as: $2\Delta(T=0) = 3.52 k_B T_c$ (where k_B is the Boltzmann constant).

---

2 Under high applied pressure (155 GPa) H_2S, which cannot be crystallise in ambient pressure, exhibits the highest critical temperature known so far $T_c = 203$ K [13]

3.1.4   *Type II superconductors*

A second type of superconducting materials differs from conventional BCS superconductors mainly by their behaviour in an applied magnetic field (H). Type I SC expel magnetic magnetic field lines up to a so-called critical field (H_c) above which superconductivity is destroyed. As exemplified in Figure 3.1.4(a),in this case the magnetisation follows $M = -H$ for fields below H_c and then drops to zero as the applied field continues to increase. For low enough fields fields the two types of SC behave in the same manner as they can be found in the Meissner state. However, type II materials enter a special regime upon exiting the Meissner state at the lower critical field denoted H_{c1}. As sketched in Figure 3.1.4(b), in this phase the applied magnetic field penetrates the sample, and not only its surface, in the form of quantized vortices as predicted by A. A. Abrikosov [23]. As the number of vortices increases with increasing magnetic field so does the magnetisation which eventually becomes zero at fields higher than the upper critical one H_{c2}.
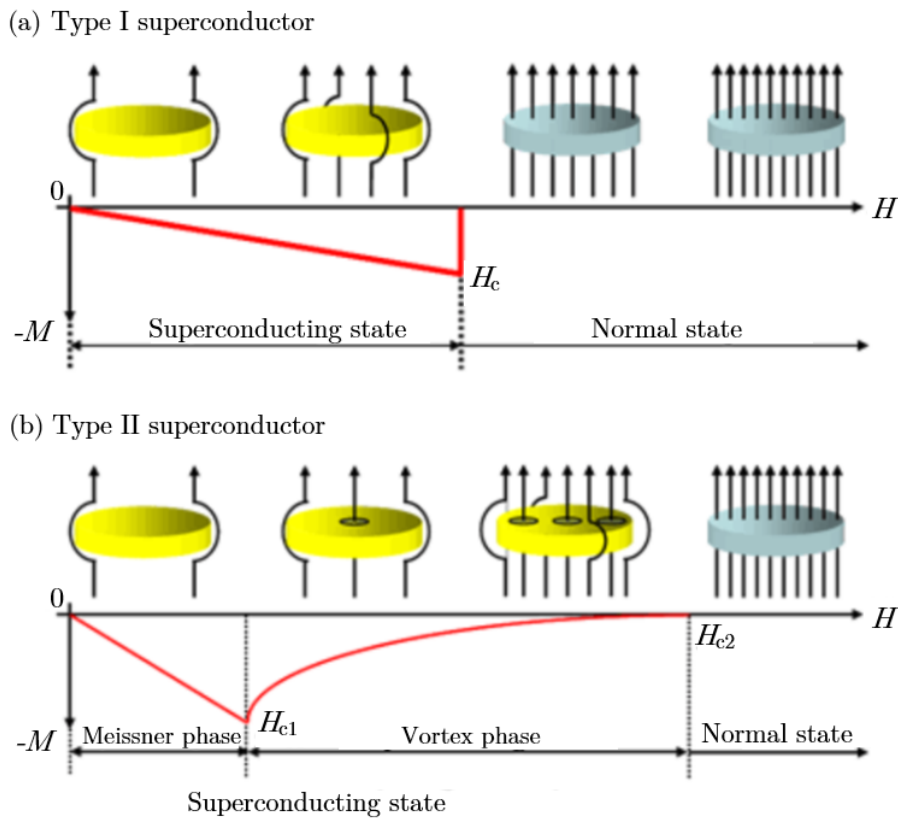
Figure 3.1.4: Magnetisation curves for **(a)** type I and **(b)** type II superconductors presented along graphical representations of the interaction between the applied magnetic field and the SC material. Image taken from [17].

An even more precise distinction can be made, between these two types of superconductors, by using two length scales. One is the above defined London penetration depth, λ_L. The second is called the coherence length ξ and, similarly to the penetration depth, it defines the distance from the surface of the material necessary for the superconducting order parameter (Ψ defined in the Ginzburg-Landau theory framework) to reach its bulk value as represented in Figure 3.1.5. For elemental metals the coherence length takes values in the micrometer range (for example 3.8 μm

for niobium or 160 μm for aluminium [12]) while for cuprates, which are the main focus of this thesis, it typically takes values on the nanometre scale (for example ~ 1 nm in $YBa_2Cu_3O_{6.9}$ [24] or ~ 2 nm $Bi_2Sr_2CaCu_2O_8$ [25]). The ratio of the two lengths, $\kappa = \lambda_L / \xi$, indicates how the order parameter behaves near the critical field. For type I superconductors $\kappa < 1/\sqrt{2}$ pointing towards a first order phase transition in which the order parameter jumps to a finite value at H_c. On the other hand, if $\kappa > 1/\sqrt{2}$ we are dealing with a type II SC which exhibits a second order phase transition with a continuous variation of the order parameter as a function of field.

However, what is probably the most fascinating difference between the two classes is the fact that type II superconductors cannot be explained by the conventional BCS theory. There are several characteristics that dismiss the possibility of a phonon mediated pairing mechanism such as the increased critical temperatures (above 30 K) or the lack of a significant isotope effect [26]. A consensus has not been reached yet as to the involvement of the phonons in the electron pairing or the origin of the "glue" that keeps the electrons bound. These unanswered questions have held the attention of many scientists over the last decades.
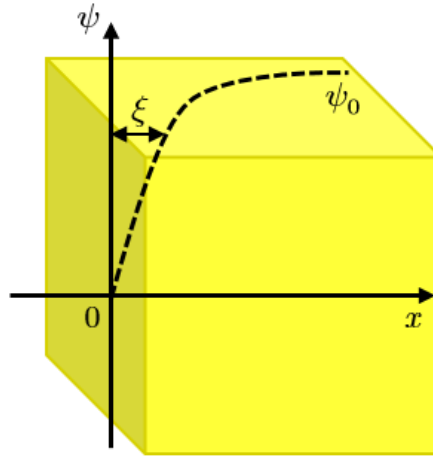
Figure 3.1.5: Evolution of the superconducting order parameter, Ψ, as a function of position in the material. The bulk value, Ψ_0, is recovered over a distance ξ (the coherence length) from the surface. Image adapted from [11].

3.2 CUPRATES

The discovery that the ceramic material $La_{2-x}Ba_xCuO_4$ is superconducting at temperatures above the recognised limit of the time ($T_c = 35$ K) came as a big surprise to the scientific community of the moment. It was two German physicists, J. G. Bednorz and K. A. Müller, who, in 1986 [27], opened the door to the fascinating field of so-called high temperature superconductivity which continues to hold great mysteries even today. Only one year later $YBa_2Cu_3O_{7\delta}$ was discovered to superconduct at temperatures as high as 93 K [28]. This realisation was remarkable not only for its unexpectedly high critical temperature, but also for the fact that liquid nitrogen (77 K) was enough to cool the samples into their superconducting phase giving the opportunity to many more laboratories in the world, which did not have access to liquid helium, to study this new class of materials and making everyday application foreseeable. What followed are thousands

of publications which add different pieces of information and create a field difficult to navigate without a specific focus. For this reason the following sections aim to briefly introduce the family of cuprate superconductors and present characteristics which are, to some extent, universal to these compounds. Detailed introductions of the up-to-date knowledge on the particular samples studied in this research, namely strontium doped $La_{2-x}Sr_xCuO_4$ (LSCO) and oxygen doped La_2CuO_{4+y} (LCO+O), are presented in the begining of each chapter that make up Part ii.

3.2.1 *Crystal structure and doping*

The common trait that defines this family of ceramic superconductors is their layered structure composed of CuO_2 planes separated by so-called charge reservoirs[3]. Figure 3.2.1 shows the crystal structure of some representative, both hole and electron doped, cuprates. Cuprates are typically characterised as a layered perovskite type of structure with copper atoms bond to both in-plane and apical oxygen in an octahedral coordination as represented in the LSCO compound in Figure 3.2.1. Due to different thermal expansion of the Cu-O and A-O bonds, where A stands for the other cations present in the charge reservoir (such as La in the case of LSCO) the oxygen octahedra will tilt as a function of temperature which in turn will induce a doping dependent phase transition typically from a high temperature tetragonal phase to a low temperature orthorhombic one. Twinning of the crystal lattice is one of the side effects of this transition. A special characteristic of certain cuprates, such as $La_{2-x}Ba_xCuO_4$ and $La_{1.48}Nd_{0.4}Sr_{0.12}CuO_4$, is the suppression of the superconducting critical temperatures at certain doping simultaneous with yet another phase transition to a low temperature tetragonal (LTT) phase. Other compounds, such as LSCO, show a less significant suppression of T_c at particular doping accompanied by a softening of certain phonon branches which suggests an instability towards the LTT phase [29] that is however never achieved. This surprising correlation with T_c has been taken as evidence that the crystal lattice symmetry is not completely uninvolved in the emergence of superconductivity though its precise role is still a matter of debate [30, 31].
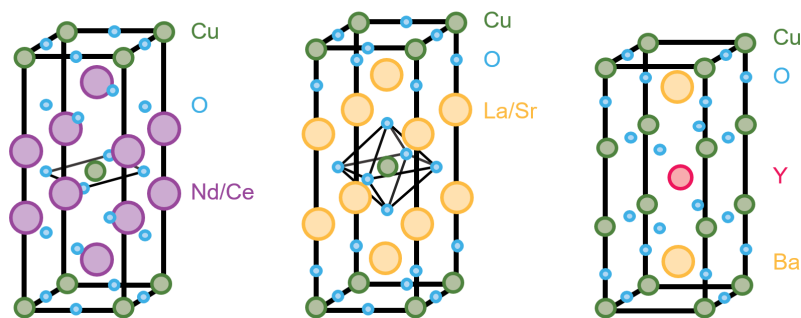
Figure 3.2.1: Unit cells of three representative cuprate superconductors. From left to right: electron doped $Nd_{2-x}Ce_xCuO_{4\pm y}$ (NCCO), the monolayer $La_{2-x}Sr_xCuO_4$ and the bilayer $YBa_2Cu_3O_6$. Image adapted from [14] and [32].

This thesis deals with the La-214 branch of the cuprates family which all have a common parent compound La_2CuO_4 (LCO). LCO is a Mott insulator that becomes superconducting upon

---

3 The name points to the role this additional layers play in the doping process by providing extra electrons or holes to the CuO_2 layers which in turn alters the behaviour of the conduction electrons.

hole doping (electron removal from the CuO_2 planes). There are two types of doping processes: (1) chemical substitution in which La is exchanged for another element such as Sr to obtain LSCO. This results in a quenched disorder as the Sr atoms are randomly distributed on the La sites and fixed after crystallisation of the sample during the growth process; or (2) addition of a new atom to the parent compound such as intercalated oxygen through electrochemical methods resulting in LCO+O. This type of doping is annealed meaning that the oxygen atoms sit on interstitial sites and are mobile at high enough temperatures. There is of course a third possibility of doping by combining the two methods and obtaining so-called co-dopped samples such as $La_{2-x}Sr_xCuO_{4+y}$ (LSCO+O). Chapters 5 and 6 present in detail the structural and magnetic particularities of LSCO and LCO+O respectively.

3.2.2 *Phase diagram*

The generic phase diagram of cuprate SC is shown in Figure 3.2.2. The first aspect to notice is the qualitative symmetry in the distribution of the different electronic phases on the two sides of the doping axis, the electron and hole-doping. The electron-doped side is much less studied in comparison to the hole-doped one mainly due to the small doping range in which the material is superconducting and the lower critical temperature.

Hole-doped samples form, as a function of doping, a so-called superconducting dome spanning from $x = 0.055$ to $x = 0.28$ which reaches a maximum critical temperature typically around $x = 0.15$. With this in mind the dome is usually divided into three sections: (1) the underdoped region $0.055 \lessapprox x \lessapprox 0.14$, (1) the optimally doped region $0.14 \lessapprox x \lessapprox 0.17$ and (3) the overdoped region $0.17 \lessapprox x \lessapprox 0.28$. Throughout this thesis I might sometimes refer to a fourth section, namely the *highly* underdoped regime which we have focused on $0.055 \lessapprox x < 0.12$.

It is interesting to notice that the superconducting dome is confined between two very different electronic states. On one side we have the magnetic insulator parent compound and on the other side we find highly overdoped samples which are typically metallic in nature. This clash of antithetic phases gives rise not only to the unconventional superconducting phase but also to two other, up to now, poorly understood regions that make up the normal state[4] of the SC, namely the pseudo-gap and the strange metal phase.

Understanding the strange metal phase is possibly one of the most significant open issues in the field of quantum materials as it has already been observed in various other strongly correlated electron materials [33]. A number of known properties have awarded this phase its naming as a strange or bad metal. For example the resistivity varies linearly with temperature in contrast with the quadratic dependence in a normal Fermi liquid [34, 35].

In the immediate vicinity of the upper border of the SC dome we can observe the so-called pseudo-gap phase. It is the second most studied, if not equally intensely studied phase as the SC one, as many believe that it is a crucial precursor of superconductivity. One theory argues the Cooper pairs are already present in the pseudo-gap phase at temperatures beyond T_c but long-range superconductivity is not established due to the uncorrelated nature of the pairing field fluctuations [36]. The naming is suggestive of the gap observed in the electronic density

---

4 By normal state is meant the region in the phase diagram spanning the same doping range as the superconducting dome but for temperatures above the superconducting critical ones.

of states through angle-resolved photoemission spectroscopy (ARPES) measurements [37, 38]. Signatures of the pseudo-gap have also been observed in nuclear magnetic resonance (NMR) [39, 40], resistivity [41, 42] or specific heat spectra [43]. Interestingly enough these different methods yield different values for the onset temperature of the pseudo-gap (T^*) making it difficult to define the microscopic origin of this intriguing phase.

The phase diagram of oxygen doped samples shows additional interesting features induced by the mobile nature of the dopant. See Section 6.1 for a detailed overview of these particularities.
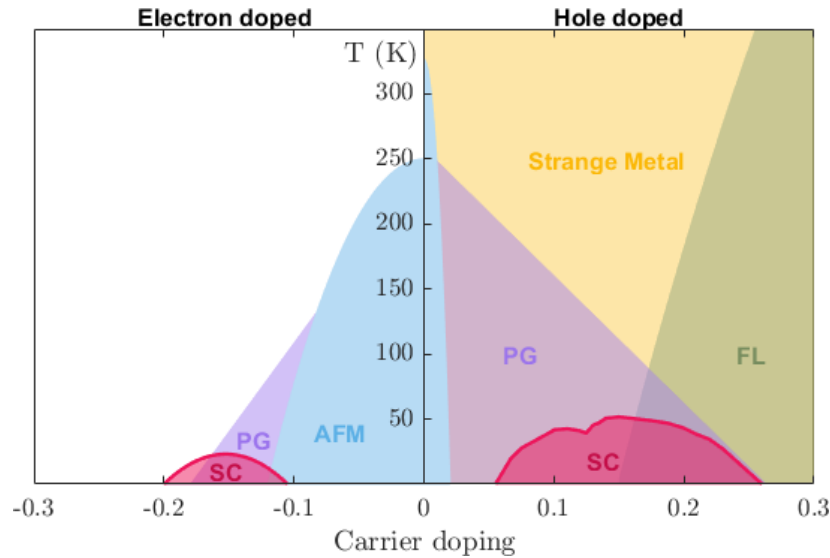
Figure 3.2.2: Generic doping versus temperature phase diagram of both electron and hole doped cuprates superconductors. The hole doped side is better defined by numerous measurements presented in the literature. It contains the antiferromagnetic phase (AFM - in light blue) spanning from 325 K at $x = 0$ to 0 K at $x = 0.02$ [44], the pseudo gap phase (PG - in purple) [45], the the strange metal phase (in yellow) which transitions, at higher doping, to a normal metal, or Fermi liquid, phase (FL - in green) [46] and the superconducting phase (SC in pink) [47]. It should be noted that the pseudogap represented on the electron doped side is a magnetic field induced one [48]. Image adapted from [49] and [48].

3.2.3 *Magnetic correlations*

The doping affects not only the crystal structure or the behaviour of conduction electrons but also the magnetism of cuprate compounds. As a function of increased doping these materials transition from an antiferromagnetic parent compound to a spin stripe structure [50, 51]. As little as $x = 0.02$ doping is enough to destroy long range antiferromagnetic order. In the stripes picture, the newly introduced holes will arrange themselves in so-called charge rivers separating domains of insulating antiferromagnetic order. The particular case depicted in Figure 3.2.3 shows a period eight magnetic stripe phase. However, the periodicity does not have to, and most often it doesn't, match that of the crystal lattice and thus it is routinely called incommensurate magnetic order. The periodicity or incommensurability (δ) varies with doping as $\delta = x$ up to $x = 0.12$ (which corresponds to the period eight stripes structure). For higher doping the incommensurability has a constant $\delta = 1/8$ value [52]. Magnetic order is generally observed in underdoped samples ($x < 0.14$) [47] with the possibility for it to be induced in optimally doped crystals (up to $x \sim 0.145$) by applying a magnetic field parallel to the c-axis (perpendicular to the CuO_2 planes) [53–55].

Magnetic order is thus thought to be incompatible with optimal d-wave superconductivity [56]. An applied magnetic field parallel to the c-axis is known to enhance the static stripe order also in underdoped samples [55, 57], yet another piece of evidence supporting the competition scenario since that same field is known to locally destroy superconductivity by causing the appearance of a vortex lattice.
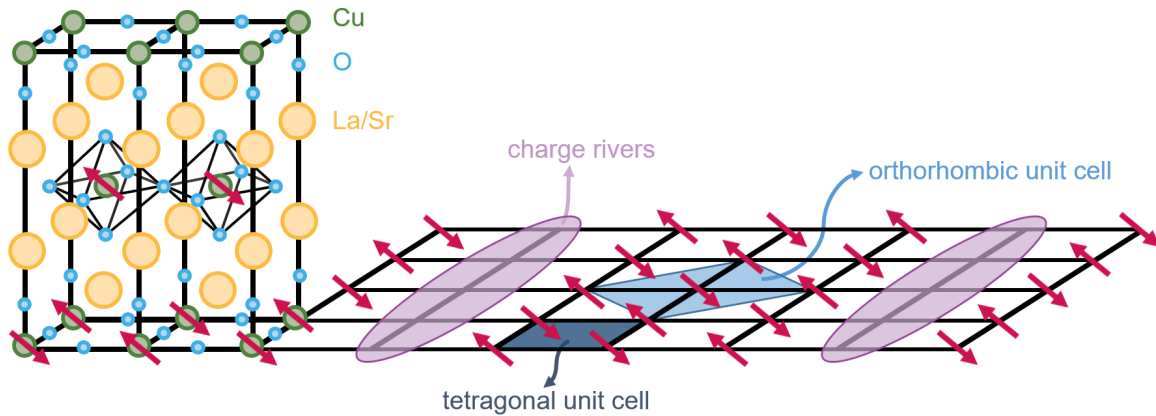
Figure 3.2.3: Graphical representation of spin in charge stripes in LSCO superconductor. The crystallographic unit cell is shown in tetragonal notation with the Cu spins aligned along the orthorhombic b-axis, orientation preserved from the parent compound. The tetragonal and orthorhombic unit cell conventions are highlighted in dark and light blue respectively. The two are rotated by 45° with respect to each other. The particular case of magnetic spin stripes with a period 8 and charge stripes with period 4 is represented here. Image adapted from [6].

Spin excitations are also present in numerous cuprates over a large doping range (in both superconducting and non-superconducting samples) and are often referred to as dynamic stripes in connection with the static stripes described previously. Elastic and inelastic neutron scattering measurements revealed a very similar positioning, in reciprocal space, of the elastic and low-energy fluctuations signals. This led to the interpretation that low-energy dynamic stripes are the Goldstone modes of the static stripes related to the breakdown of the spin-rotational symmetry of the latter. The dispersion of excitations typically takes the shape of an hourglass (as depicted in Figure 3.2.4) with low-energy fluctuations dispersing sharply towards the antiferromagnetic $\mathbf{Q}$ vector $(1, 0, 0)$ and high-energy ones dispersing outwards. The crossing energy (E_{cross}) between these two regimes is generally called the superconducting or neutron resonance. In optimally doped samples the dispersion is disrupted by a spin gap at low energies (usually below 10 meV) [58, 59]. In-gap states can be induced either by increasing the temperature above T_{c} or by an applied a magnetic field in the c-direction.

In recent years, however, the universality of these properties has been challenged. For example, in certain compounds of the family, such as LCO+O, a subtle mismatch in incommensurability of the elastic and inelastic magnetic signals was taken as evidence for a different, though related, origin of the static and dynamic spin stripes [61]. LSCO with doping around $x = 0.13$ is another interesting case where a magnetic phase separation picture has been proposed in order to explain the observation of both a spin gap and elastic and quasi-elastic fluctuations [47].

The neutron resonance feature is also no stranger to scrutiny. Due to the proximity in energy of the highly dispersive spin excitations and low-lying weakly dispersive optic phonons, a spin-phonon hybridisation has been proposed as a more plausible origin for the enhanced intensity
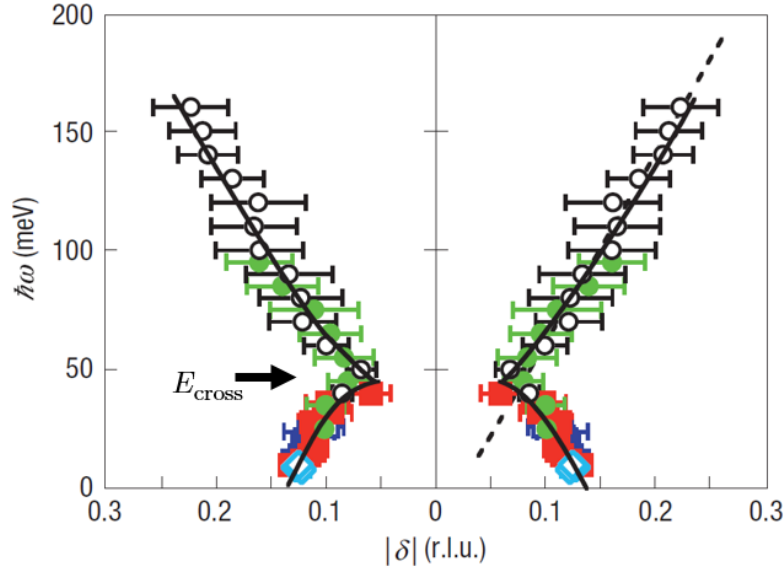
Figure 3.2.4: Hourglass dispersion of spin excitations in optimally doped $La_{1.84}Sr_{0.16}CuO_4$ represented as the energy dependence of the incommensurability (δ). The different symbols depict data taken with different incident energies. Image taken from [60].

around E_{cross} compared to a purely magnetic effect [62, 63]. Furthermore, in underdoped LBCO, the lack of a resonance corroborated with the absence of a spin gap has been taken as evidence for a different type of superconducting phase namely a pair density wave [64]. Such a phase differs from the classical uniform d-wave in that superconducting wave function is modulated throughout the unit cell. Figure 3.2.5 illustrates the spatial variation of the superconducting order parameter in both types of order. While the uniform d-wave is not modulated, the PDW order parameter changes sign with a periodicity equal to that of the charge stripes. As it will be described in greater detail in the following chapters, this variation is related to the perpendicular arrangement of charge stripes in adjacent planes which in turn causes the frustration of the interlayer Josephson coupling. Both types of order show a spatial modulation of the order parameter amplitude with different wavelength though, while the uniform d-wave follows the periodicity of charge stripes ($\lambda = 4a$, where a is the the lattice parameter), the PDW exhibits a wavelength double in size ($\lambda = 8a$) [65].
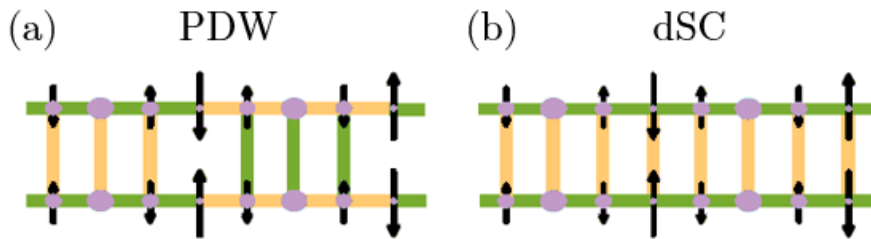
Figure 3.2.5: Graphical illustration of the superconducting order parameter distribution inside a unit cell in **(a)** a pair density wave phase and **(b)** a uniform d-wave superconducting phase. A positive order parameter is represented in green while a negative one takes the colour yellow. The size of the arrows and purple circles indicates the magnitude of the magnetisation and hole density respectively. Image taken from [66].

It has been common to distinguish, in rough terms, two types of cuprates according to their magnetic behaviour: (1) materials which do not exhibit magnetic order in zero field and have gapped excitations and (2) samples that show magnetic order, ungapped excitations and a reduced superconducting critical temperature. The following chapters will show that the reality is more nuanced than this. There have been observed numerous exceptions that need to be understood before a universal theory, that explains superconductivity of the cuprates family, can be established.

NEUTRON SCATTERING

The field of neutron scattering has changed dramatically in the last 80 years since the first neutron diffraction experiments which took place in 1936 and aimed to study the neutron itself, more precisely its wave-particle duality [67]. Nowadays neutrons scattering experiments tackle questions from various fields ranging from particle physics to art or archaeology. The reason for this is the high versatility of neutrons as a probe which can be summarised as a few key properties [68]:

- The cross section of neutrons (this property describes the strength of the interaction between neutrons and the studied elements and shall be defined more precisely in the following sections) varies in a seemingly random fashion as a function of the atomic number of the material. This is often compared to the complementary technique: X-ray scattering. As exemplified in Figure 4.0.1 the irregular variation of the cross section across different elements and their isotopes makes neutrons an ideal probe to study for example light elements which are practically invisible for X-rays.
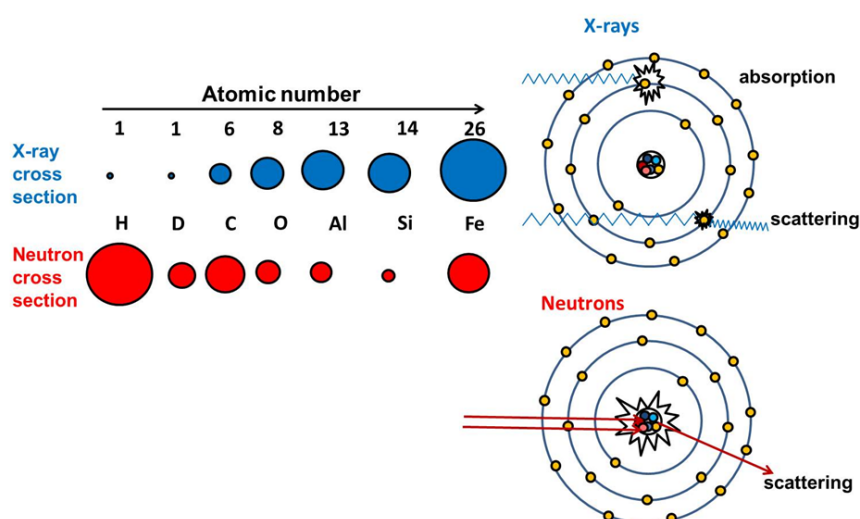
Figure 4.0.1: Sketch of neutron and X-ray scattering cross sections presented in parallel for different elements or isotopes. On the right hand-side a graphical representation of the interaction of these two probes and matter is shown. While X-rays with the electrons of one atom the neutrons will interact with its nucleus. This gives rise to a almost linear variation of the X-ray cross section as a function of atomic number which is clearly not the case for the nuclear interaction. Image adapted from [69].

- The scattering length (another property describing the interaction between neutrons and matter which shall be defined in the following sections) can take positive and negative values for different isotopes of the same element. A textbook example, which has been intensively employed in the study of biological samples, is the use of various ratios of water and heavy water so as to obtain mixtures that match the scattering length of different components of the sample. This allows the experimenters to chose which parts of the sample to make visible for neutrons.

- The weak interaction neutron have with matter (in comparison with other probes such as X-rays) can be regarded both as a quality as well as a shortcoming. For one thing, it allows the probing of the entire bulk of the sample in various environments such inside furnaces, magnets, pressure cells etc. On the flip side, neutron scattering experiments generally require larger samples in order to obtain adequate signals.

- The energy (in the milli-electron-Volt range) and wavelength (in the angstrom range) of neutrons matches those of the fundamental excitations and inter-atomic distances making neutrons very well adapted for studying a variety of fluctuations in materials (see Figure 4.0.2) as well as structural properties.
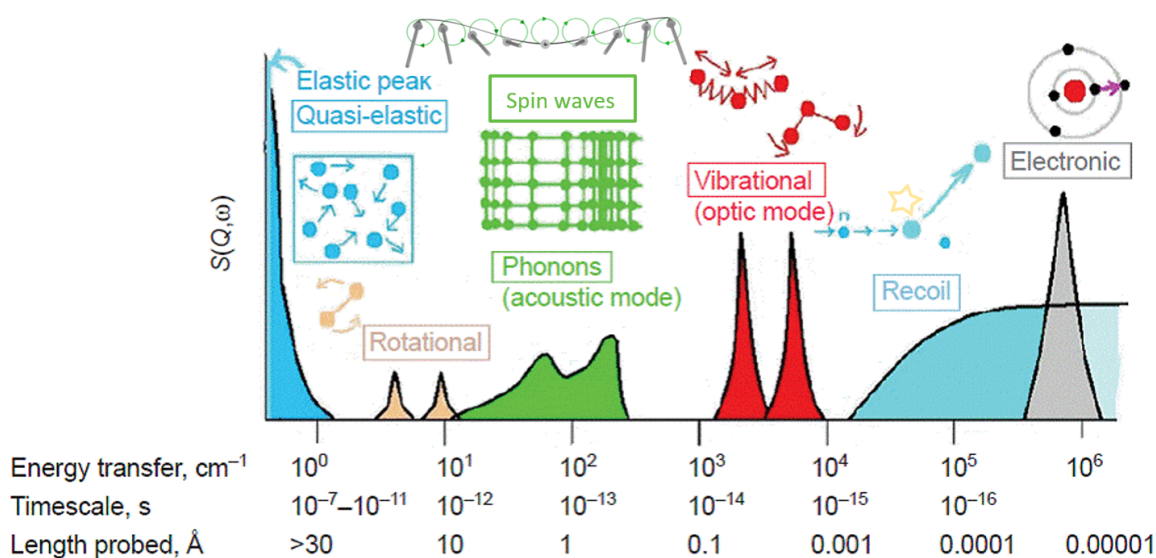
Figure 4.0.2: Sketch of different phenomena that can be probed by neutron scattering. Image adapted from [70].

- Neutrons posses a magnetic moment which can interact with various magnetic structures. This makes them one of the few techniques capable of probing magnetic order and excitations.

This chapter aims to introduce the basics of neutron scattering with a focus on the techniques used thought this thesis. For a complete treatment of this vast field the reader is referred to the following writings which have inspired this chapter: A. T. Boothroyd's newly published book [71], the well-known book by G. L. Squires [72] and the course notes of K. Lefmann [68].

4.1   BASICS NEUTRON PROPERTIES

In order to be able to perform neutron scattering experiments one needs to extract neutrons from a nucleus. There are two processes which can be used in this scope: (1) fission which uses a chain reaction as shown in Figure 4.1.1 or (2) spallation which makes use of a proton accelerator to excite heavy nuclei which will afterwards expel neutrons upon deexcitation.
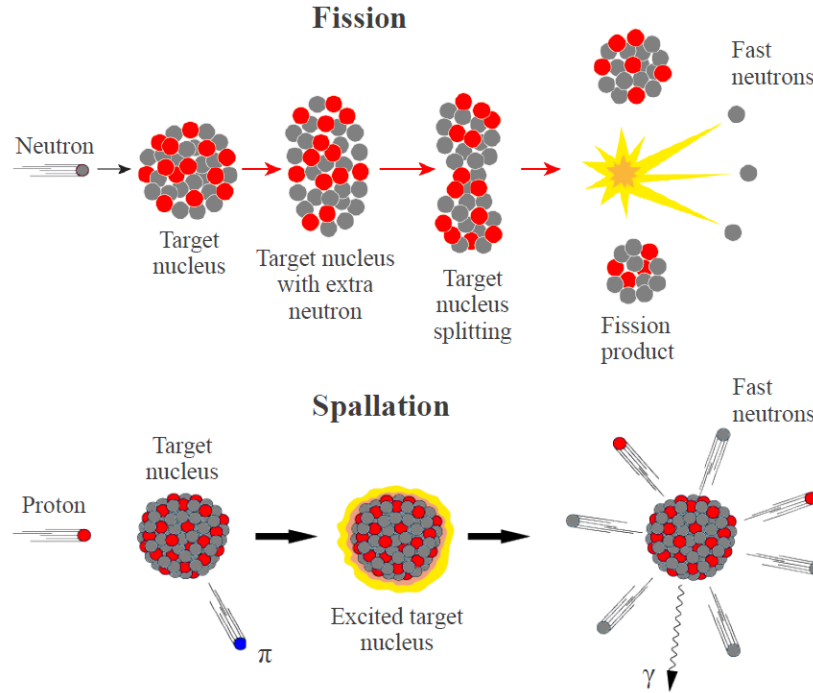
Figure 4.1.1: Sketch of the two different neutron production processes. During fission the target nucleus (which is generally uranium) will split and release on average 2.45 neutrons. Out of these some will continue to participate in other fission processes keeping the chain reaction going and other will be collected and transported to the experimental station. The spallation procedure requires a proton source which will bombard a heavy metal target causing the dislocation of a greater number of neutrons (up to 30 per nucleus [73]). Image taken from [6].

Table 1 summarises a number of the properties of neutrons. Due to its dual wave-particle character we can describe a neutron and its direction of propagation by a wavevector k which relates to the wavelength as $k = \frac{2\pi}{\lambda}$. Since in condensed matter we can consider neutrons as non-relativistic particles we define its energy as $E = \frac{p^2}{2m_n} = \frac{\hbar^2 k^2}{2m_n}$, where p is the neutron's momentum. Depending on their energy tree different categories of neutrons can be defined as exemplified in Table 1. This distinction is quite helpful since in practice neutron instruments and experimental methods are often defined with respect to the temperature/energy of the incoming neutron beam.

Property	Value
Mass (m_n)	1.675×10^{27} kg
Electric charge(q_n)	0
Spin (s)	$1/2$
Magnetic moment (μ_n)	$-1.913\,\mu_N = -0.0010\,\mu_B$
Energy (E)	0.1-10 meV (cold neutrons)
	5-100 meV (thermal neutrons)
	100-500 meV (hot neutrons)
Temperature (T)	1-120 K (cold neutrons)
	60-1000 K (thermal neutrons)
	1000-6000 K (hot neutrons)
Wavelength (λ)	30-3 Å (cold neutrons)
	4-1 Å (thermal neutrons)
	1-0.4 Å (hot neutrons)

Table 1: Various basic neutron properties. Here μ_N is the nuclear magneton $\mu_N = 5.051 \times 10^{-27}$ J/T

4.2 ELASTIC SCATTERING

The simplest way to visualise a scattering event is by drawing the so-called scattering triangle depicted in Figure 4.2.1. This allows us to define the scattering vector as a function of the incoming and outgoing wavevectors: $\mathbf{Q} = \mathbf{k}_i - \mathbf{k}_f$. It is thus straightforward to distinguish between elastic ($k_i = k_f$) and inelastic events. In general from trigonometrical considerations we can write:

$$Q = k_i^2 + k_f^2 - 2k_i k_f \cos(2\theta). \tag{4.1}$$

While in the particular case of elastic scattering this is reduced to:

$$Q = 2k \sin(\theta) = \frac{4\pi}{\lambda} \sin(\theta). \tag{4.2}$$

In the special case of scattering from crystalline materials, the scattering vector is related to the lattice spacings (d) through the Laue condition as: $Q = \frac{2\pi}{d}$.

In practice a scattering event is influenced not only by the studied material and its ability to scatter neutrons but also by the properties of the neutron beam such as the flux (Ψ measured in neutrons/cm^2/s) which measures the number of neutrons generated per area. The above mentioned scattering cross section (σ measured in m^2) is then defined in relation to the flux as
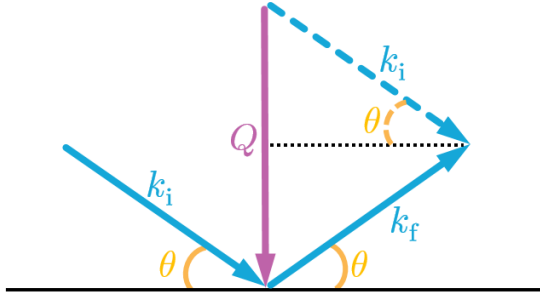
Figure 4.2.1: Graphical representation of a scattering triangle corresponding to an elastic scattering event ($k_i = k_f$). Image adapted from [6].

the ratio between the number of neutrons scattered by the sample per second and the flux. As we have seen above the direction in which the neutrons are scattered holds information about the structure of the sample. In order to take this into account we can define the differential scattering cross section for a system of nuclei which are fixed in position:

$$\frac{d\sigma}{d\Omega} = \frac{1}{\Psi} \frac{\text{no. of neutrons scattered per second into the solid angle } d\Omega}{d\Omega}, \qquad (4.3)$$

where $d\Omega$ is the solid angle in which the neutrons are scattered. In practice there are two scattering processes that contribute to the measured signal:

(1) coherent scattering:

$$\left(\frac{d\sigma}{d\Omega}\right)_{\text{coh}} = \left| \sum_j \bar{b}_j \exp(i\mathbf{Q} \cdot \mathbf{r}_j) \right|^2, \qquad (4.4)$$

where b is the nuclear scattering length mentioned in the previous section and similar to the cross section it varies as a function of element but also isotope. $\bar{b}$ is the average of b, r denotes the position of the scattering atoms. Since the coherent cross section depends on the relative position of the atoms it contains important information about the structure of the material.

(2) incoherent scattering:

$$\left(\frac{d\sigma}{d\Omega}\right)_{\text{inc}} = \sum_j (\overline{b_j^2} - \bar{b}_j^2). \qquad (4.5)$$

In contrast with the coherent component the incoherent scattering cross section is only dependent on the species of atoms present in the sample.

In most experiments one aims to maximise the coherent component while minimising the incoherent one which generates a flat background as depicted in Figure 4.2.2. There are however cases where incoherent scattering, especially inelastic incoherent scattering, is of interest as it provides information on the dynamical properties of materials.
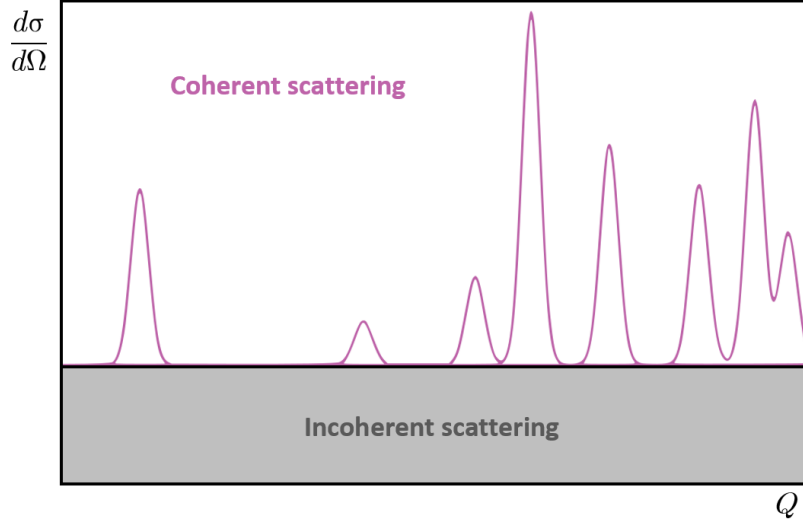
Figure 4.2.2: Schematic graphical representation of the coherent and incoherent scattering components which contribute to the differential cross section. Image taken from [71].

Most often in experiments, as it is the case of the current study, we are interested in characterising the nuclear elastic scattering of crystalline materials. For this some correction to Equation 4.4 are in order. For example we need to discard the imposed restriction of immobile nuclei in order to model scattering from vibrating nuclei. This comes as a correction by a so-called Debye-Waller factor: $\exp(-2W) = \exp(-\langle \mathbf{Q} \cdot \boldsymbol{u} \rangle^2)$. Here $\boldsymbol{u}$ is the mean displacement from the average nuclear position which leads to scattering from an apparent diffuse object rather than an ideal point point-like scatterer. The potential lack of phase coherence between waves interacting with different sectors of the diffuse object causes a reduction of the scattered beam amplitude. Thus, the Debye–Waller factor takes values between zero and unity and varies as a function of temperature and scattering vector $\mathbf{Q}$.

Next we can define another term which holds information about the arrangement of atoms inside a unit cell, namely the nuclear structure factor: $F_N(\mathbf{Q}) = \sum_i b_i \exp(i \mathbf{Q} \cdot \boldsymbol{\Delta}_i)$. The sum is taken over all atoms of one unit cell. Being dependent on the scattering length, the structure factor indicates whether certain reflections are visible or not from a neutron scattering perspective even if the reflection is an allowed one in the crystallographic space group of the sample.

Finally we need to extrapolate to all N unit cells of the sample taking into account the volume of a Brillouin zone $\frac{(2\pi)^3}{V_0}$. So we obtain the differential cross section for crystal neutron diffraction:

$$\left(\frac{d\sigma}{d\Omega} \right)_{\text{nucl.el}} = N \frac{(2\pi)^3}{V_0} \exp(-2W) |F_N(\mathbf{Q})|^2 \sum_\tau \delta(\mathbf{Q} - \tau). \tag{4.6}$$

4.3 INELASTIC SCATTERING

In an inelastic scattering process we are interested to define and control the energy transfer between the neutron and the sample. For this reason we shall define the partial differential scattering cross section which takes into account the energy of the outgoing neutrons E_f:

$$\frac{d^2\sigma}{d\Omega\,dE_f} = \frac{1}{\Psi} \frac{\text{no. of neutrons scattered per second into the solid angle } d\Omega}{d\Omega\,dE_f}. \tag{4.7}$$
$$\text{with energies } [E_f; E_f + dE_f]$$

A scattering event can be described by the probability to reach a final state $|\psi_f\rangle$ from an initial state $|\psi_i\rangle$ also known as Fermi's Golden Rule [6, 74]. The partial differential cross section can thus be rewritten as:

$$\frac{d^2\sigma}{d\Omega\,dE_f} = \frac{k_f}{k_i}\left(\frac{m_n}{2\pi\hbar^2}\right)^2 \left|\langle\lambda_i\psi_i|\hat{V}|\lambda_f\psi_f\rangle\right|^2 \delta(\hbar\omega - (E_{\lambda_f} - E_{\lambda_i})), \tag{4.8}$$

where $\hat{V}$ is the nuclear scattering potential: $\hat{V} = \frac{2\pi\hbar^2}{m_n}\sum_j b_j \delta(\boldsymbol{r} - \boldsymbol{R}_j)$ and $\boldsymbol{R}_j$ indicates the position of each nucleus of the sample. $|\lambda_i\rangle$ and $|\lambda_f\rangle$ denote the initial and final states of the sample while the delta function ensured that the energy conservation law is obeyed, meaning that the energy loss or gain of the sample $\hbar\omega$ is equal to that of the neuron beam $E_{\lambda_f} - E_{\lambda_i}$.

In practice inelastic neutron scattering is predominantly used in condensed matter to measure lattice vibrations, phonons (and magnetic fluctuations as it will be explained in the next section). We can distinguish two classes of lattice vibrations: acoustic in which case atoms move in-phase with each other and optical in which case the movement is out-of-phase [12]. Since the atoms have three degrees of freedom determined by the three directions in space x, y and z, we can also distinguish between so-called longitudinal modes where the wave propagated in the same direction as the individual atom displacement or, on the contrary, transverse modes in which the displacement is perpendicular to the wave propagation direction. Figure 4.3.1 shows a graphical representation of these vibration modes together with their dispersion in energy-momentum space. In a typical neutron scattering experiment performed on a triple-axis type of instrument one would perform a varying energy scan across the phonon branches.
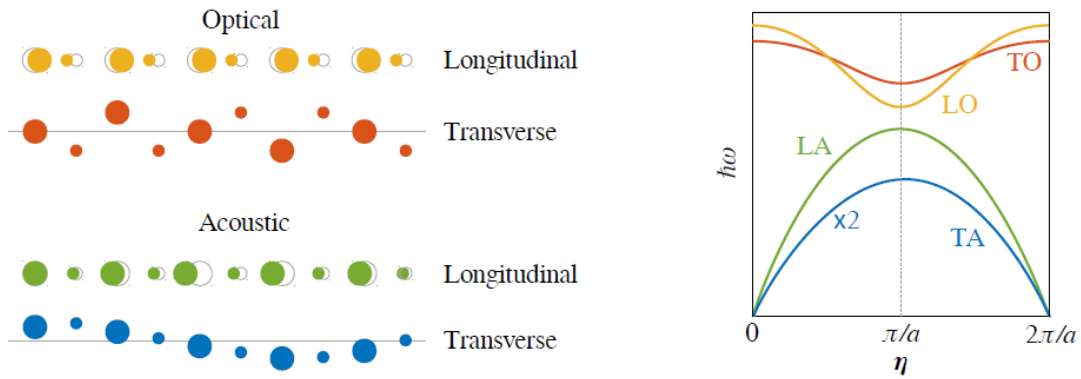
Figure 4.3.1: Graphical representation of the different vibration modes exemplified on a diatomic linear lattice. On the right-hand side the typical dispersions are plotted in momentum-energy space. Image taken from [6].

The characteristic scattering cross section describing the creation or absorption of one phonon can be written as a sum of two terms:

$$\left(\frac{d^2\sigma}{d\Omega dE_{\mathrm{f}}}\right)_{1ph} = \frac{k_{\mathrm{f}}}{k_{\mathrm{i}}}\frac{|F_{\mathrm{N}}(\mathbf{Q})|^2(2\pi)^3}{2MV_0}\exp(-2W)\sum_{Q,p,\tau}\frac{(\mathbf{Q}\cdot\boldsymbol{e}_{Q,p})^2}{\omega_{Q,p}}\times$$
$$\times[(n_{Q,p}+1)\delta(\omega-\omega_{Q,p})\delta(\mathbf{Q}-\mathbf{Q}'+\boldsymbol{\tau})+$$
$$+n_{Q,p}\delta(\omega+\omega_{Q,p})\delta(\mathbf{Q}+\mathbf{Q}'+\boldsymbol{\tau})]. \tag{4.9}$$

The two added terms enclosed by the square brackets correspond to the creation and absorption of a phonon and indicate that during the creation the neutron looses a certain amount of energy ($\hbar\omega_{Q,p}$) to the lattice and vice-versa, the neutron gains the same amount of energy when the phonon is annihilated. The sum also contains the population factors of phonons $n_{Q,p}$ described by Bose-Einstein statistics $n_{Q,p} = \frac{1}{\exp(\hbar\omega\beta)}$ where $\beta = \frac{1}{k_{\mathrm{B}}T}$. These pre-factors $n_{Q,p}+1$ and $n_{Q,p}$ indicate that in the absence of any lattice vibrations $n_{Q,p} = 1$ at $T\rightarrow 0$ K phonons can only be created but not absorbed. Another important term is $(\mathbf{Q}\cdot\boldsymbol{e}_{Q,p})^2$ which implies that neutrons are only sensitive to the components of the lattice vibrations parallel to $\mathbf{Q}$. Here p is the phonon polarisation index, $\mathbf{Q}'$ is the phonon wavevector and M is the nuclear mass of the sample's atoms.

4.4 MAGNETIC SCATTERING

Analogous to nuclear scattering, due to the fact that neutrons posses a magnetic moment, one is able to probe the magnetic fields generated by the unpaired electrons of materials.

4.4.1 *Elastic magnetic scattering*

The magnetic differential scattering cross section is rather similar to that of nuclear elastic scattering (Equation 4.6):

$$\left(\frac{d\sigma}{d\Omega}\right)_{\mathrm{mag.el}} = N\frac{(2\pi)^3}{V_0}\exp(-2W)|F_{\mathrm{M}}(\mathbf{Q})|^2\sum_{\tau}\delta(\mathbf{Q}-\boldsymbol{\tau}-\mathbf{Q}'). \tag{4.10}$$

As the magnetic unit cell might differ in size from the structural one a magnetic ordering vector, $\mathbf{Q}'$, needs to be defined. Similarly, N and V_0 describe the magnetic unit cell. The main difference between the magnetic and nuclear cross sections is contained in the structure factor:

$$F_{\mathrm{M}}(\mathbf{Q}) = \sum_{mag.cell}\underbrace{\left[\gamma r_0\frac{g_j}{2}F_j(\mathbf{Q})\langle\boldsymbol{s}_{j,\perp}\rangle\right]}_{b_j}\exp(-i\mathbf{Q}\cdot\boldsymbol{R}_j). \tag{4.11}$$

The equivalent magnetic scattering length, b_j, includes the magnetogyric ratio of neutrons (γ), the gyromagnetic ratio of the studied magnetic ion (g_j), the radius of an electron (r_0), the magnetic form factor ($F_j(\mathbf{Q})$) as well as the thermal average of the spin components perpendicular to the scattering wavevector $\mathbf{Q}$ ($\langle\boldsymbol{s}_{j,\perp}\rangle$) indicating that neutrons are only sensitive to these perpendicular spin components. The magnetic and nuclear scattering lengths are usually

comparable in size (both taking values in the femtometer range) resulting in scattering intensities of similar magnitudes. The exception to this are magnetic materials with large spin numbers (such as rare-earth compounds or iron oxides) where magnetic scattering is the dominant signal.

4.4.2 *Inelastic magnetic scattering*

Similar to the previously described phonons, spin fluctuations called magnons are at the core of inelastic magnetic scattering. As depicted in Figure 4.4.1 for the particular case of a ferromagnetic one dimensional chain a magnon represents a net spin reduction which manifests itself as a precession of spins around their equilibrium position. A collective movement is then generated due to the coupling between the spins. In this case as well neutron experiments focus on mapping the momentum and energy dependent dispersion.
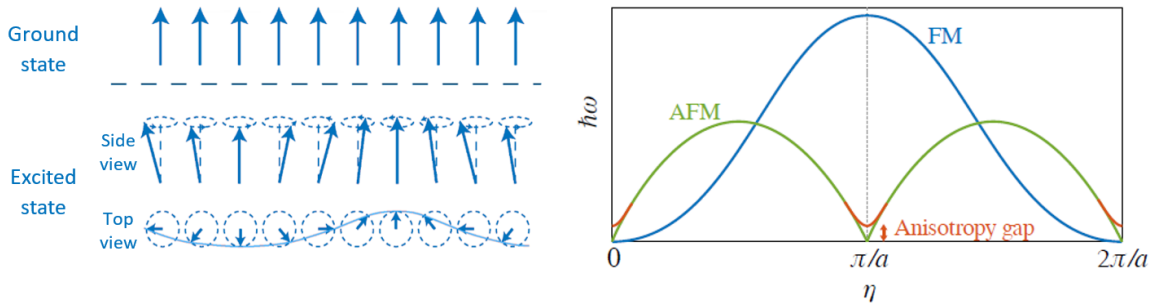
Figure 4.4.1: Graphical representation of a one dimensional ferromagnetic structure and its excited state. A magnon is formed as spins are precessing around their equilibrium position. On the right-hand side typical magnon dispersions of a ferromagnetic (FM) and antiferromagnetic one dimensional systems are plotted in momentum-energy space. A gap in the dispersion is induced by any anisotropy present in the AFM system. Images taken from [6] and [75].

The magnetic partial differential scattering cross section of a ferromagnet, as the one depicted in Figure 4.4.1, is very similar to that describing lattice vibrations (Equation 4.9):

$$
\left(\frac{d^2\sigma}{d\Omega\, dE_f} \right)_{mag} = \frac{k_f}{k_i} \left[\gamma r_0 \frac{g}{2} F(\mathbf{Q}) \right]^2 \frac{(2\pi)^3}{V_0} \exp(-2W)(1 + \hat{q}_z^2)\frac{\langle S^z \rangle}{2} \times
$$

$$
\times \sum_{Q,\tau} [(n_B\left(\frac{\hbar\omega_Q}{k_B T} \right) + 1)\delta(\hbar\omega_{Q'} - \hbar\omega)\delta(\mathbf{Q}' - \mathbf{Q} - \boldsymbol{\tau}) + \qquad (4.12)
$$

$$
+ n_B\left(\frac{\hbar\omega_{Q'}}{k_B T} \right)\delta(\hbar\omega_{Q'} + \hbar\omega)\delta(\mathbf{Q}' + \mathbf{Q} - \boldsymbol{\tau})].
$$

Here as well the energy and momentum conservation is obeyed for both the creation (the second line of the equation) and the annihilation (third line) of a magnon. In the particular case of FM systems the spin wave is purely transverse (perpendicular to the spin direction) meaning that, knowing that spins are only sensitive to spin components perpendicular to $\mathbf{Q}$, the intensity of the signal will be highest when $\mathbf{Q}$ and the direction of the ordered moment (z in this case) are parallel.

4.5 XYZ POLARISATION ANALYSIS

As mentioned previously, one of the most unique features of employing neutrons as a probe is the possibility to make use of their spin in order to extract information about the magnetic structure of a particular sample. In this respect, polarised neutron diffraction and scattering are essential tools in separating nuclear from magnetic contributions to scattering as well as in resolving the orientation of the studied magnetic structure. Throughout this section, I will focus on describing the type of information that can be extracted from the simplest type of polarisation analysis which can be performed on a triple axis instrument, namely longitudinal polarisation analysis. This simplified derivation follows closely explanations provided by G. Ehlers *et al.* [76] and A. Boothroyd [71]. The formalism can be expanded to more complex multi-detection systems (such as the D7 - diffuse scattering spectrometer at the ILL [77]), but it can also be further simplified (as shown at the end of this section) to account for the particularities of a triple-axis spectrometer in polarisation analysis configuration employing Helmholtz coils.

In any scattering event, one measures simultaneously the nuclear and magnetic scattering (each with their respective coherent and incoherent components). The scope of polarisation analysis is to disentangle all these contributions in order to paint an accurate picture of the magnetic structure of our chosen sample. Thus, the total differential scattering cross section is written as the following sum:

$$\left(\frac{\partial \sigma}{\partial \Omega}\right)_{\text{total}} = \left(\left(\frac{\partial \sigma}{\partial \Omega}\right)_{\text{coh}} + \left(\frac{\partial \sigma}{\partial \Omega}\right)_{\text{incoh}}^{\text{isotope}}\right) + \left(\frac{\partial \sigma}{\partial \Omega}\right)_{\text{incoh}}^{\text{spin}} + \left(\frac{\partial \sigma}{\partial \Omega}\right)_{\text{mag}} \tag{4.13}$$
$$= N + I + M,$$

where the terms are divided according to their influence on the neutron spin. N stands for nuclear scattering, both coherent [1] and isotope incoherent, which does not affect the neutron spin. This means that the entire nuclear scattering will show up in the non spin flip channel:

$$\left(\frac{\partial \sigma}{\partial \Omega}\right)_{N,\uparrow}^{(t)} = N, \tag{4.14}$$

$$\left(\frac{\partial \sigma}{\partial \Omega}\right)_{N,\downarrow}^{(t)} = 0. \tag{4.15}$$

Here t denotes the incoming neutron spin direction ($t = x, y, z$ in the specific case of XYZ polarisation analysis discussed here). In the current chosen convention, the incoming neutron spin is aligned along one of the three axis of the chosen coordinate system (see Figure 4.5.1), meaning that the up arrow will indicate the non spin flip channel (NSF) while the down arrow corresponds to the spin flip channel (SF).

Regardless of the initial neutron polarisation, there is a $2/3$ probability that the interaction with the nuclear spin of the sample will flip the spin of the neutron. Thus the spin incoherent scattering, I, has the following NSF and SF components respectively:

---

1 Nuclear Bragg scattering, phonons or other more complex lattice fluctuations.
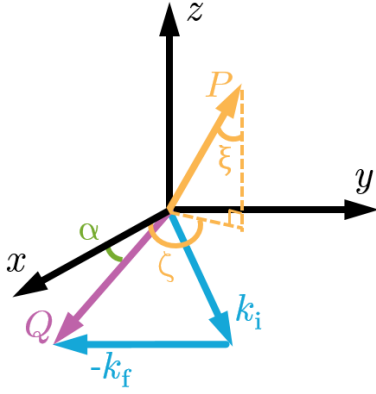
Figure 4.5.1: The so-called Blume–Maleev coordinate system including the scattering triangle. It should be noted that the polarisation of the incoming neutron beam, in yellow here, can be oriented in any direction. However, in the particular case of the XYZ polarisation analysis method, it will lie along one of the three axis of the coordinate system. Another particularity of this representation is the fact that all scattering is constrained to the xy-plane (all k_i, k_f and $\mathbf{Q}$ vector will then lie in the plane as shown here). Image adapted from [76].

$$\left(\frac{\partial\sigma}{\partial\Omega}\right)^{(t)}_{I,\uparrow} = \frac{1}{3}I, \tag{4.16}$$

$$\left(\frac{\partial\sigma}{\partial\Omega}\right)^{(t)}_{I,\downarrow} = \frac{2}{3}I. \tag{4.17}$$

Lastly, with respect to the magnetic scattering term (M), it is important to remember that neutrons are only sensitive to the components of the magnetisation perpendicular to the scattering vector $\mathbf{Q}$ [78]. Thus, the final polarisation of the beam $(\mathbf{P}'_M)$, after the sample, relates to the initial one $(\mathbf{P}_M)$ as:

$$\mathbf{P}'_M = -(\hat{\mathbf{Q}} \cdot \mathbf{P}_M)\hat{\mathbf{Q}}, \tag{4.18}$$

where $\hat{\mathbf{Q}}$ is the unit vector along $\mathbf{Q}$. In the particular case considered here, where scattering originates entirely in the x-y plane, the momentum transfer and polarisation vector can be written as:

$$\mathbf{P}_M = [\cos\zeta\sin\xi, \sin\zeta\sin\xi, \cos\xi], \tag{4.19}$$

$$\hat{\mathbf{Q}} = [\cos\alpha, \sin\alpha, 0]. \tag{4.20}$$

All the angles are represented in Figure 4.5.1. By rewriting Equation 4.18, we obtain the component of $\mathbf{P}'_M$ parallel to $\mathbf{P}_M$ (since this is the component measured in practice [70]):

$$\begin{aligned} p^{(t)}_M = \mathbf{P}'_M \cdot \mathbf{P}_M &= -(\hat{\mathbf{Q}} \cdot \mathbf{P})^2 \\ &= -(\cos\alpha\cos\zeta\sin\xi + \sin\alpha\sin\zeta\sin\xi)^2 \\ &= -[\sin\xi(\cos\alpha\cos\zeta + \sin\alpha\sin\zeta)]^2 \\ &= -(\sin\xi\cos(\alpha-\zeta))^2. \end{aligned} \tag{4.21}$$

As previously mentioned, for the XYZ polarisation analysis, three directions of $\mathbf{P}_M$ are employed each giving rise to an associated component of $p^{(t)}$:

$$
\begin{aligned}
\mathbf{P}_M \parallel x &\quad [\xi = \pi/2,\ \zeta = 0] &\qquad p^{(x)} &= -\cos^2(\alpha), &\qquad (4.22)\\
\mathbf{P}_M \parallel y &\quad [\xi = \pi/2,\ \zeta = \pi/2] &\qquad p^{(y)} &= -\sin^2(\alpha),\\
\mathbf{P}_M \parallel z &\quad [\xi = 0] &\qquad p^{(z)} &= 1.
\end{aligned}
$$

We need to further use two definitions:

$$
p_M^{(t)} = \frac{\left(\frac{\partial \sigma}{\partial \Omega}\right)_{\mathrm{M},\uparrow}^{(t)} - \left(\frac{\partial \sigma}{\partial \Omega}\right)_{\mathrm{M},\downarrow}^{(t)}}{\left(\frac{\partial \sigma}{\partial \Omega}\right)_{\mathrm{M},\uparrow}^{(t)} + \left(\frac{\partial \sigma}{\partial \Omega}\right)_{\mathrm{M},\downarrow}^{(t)}}, \tag{4.23}
$$

$$
\left(\frac{\partial \sigma}{\partial \Omega}\right)_{\mathrm{M},\uparrow}^{(t)} + \left(\frac{\partial \sigma}{\partial \Omega}\right)_{\mathrm{M},\downarrow}^{(t)} = M. \tag{4.24}
$$

Combining these two definitions with Equations 4.22, one can calculate the contributions to the magnetic cross section corresponding to both neutron spin up (NSF) and down (SF) along all three directions in space. For example in the case of spin polarisation along x we have:

$$
\begin{aligned}
p_M^{(x)} = -\cos^2(\alpha) &= \frac{\left(\frac{\partial \sigma}{\partial \Omega}\right)_{\mathrm{M},\uparrow}^{(x)} - \left(\frac{\partial \sigma}{\partial \Omega}\right)_{\mathrm{M},\downarrow}^{(x)}}{\left(\frac{\partial \sigma}{\partial \Omega}\right)_{\mathrm{M},\uparrow}^{(x)} + \left(\frac{\partial \sigma}{\partial \Omega}\right)_{\mathrm{M},\downarrow}^{(x)}}; \tag{4.25}\\
-\cos^2(\alpha) &= \frac{M - 2\left(\frac{\partial \sigma}{\partial \Omega}\right)_{\mathrm{M},\downarrow}^{(x)}}{M};\\
\left(\frac{\partial \sigma}{\partial \Omega}\right)_{\mathrm{M},\downarrow}^{(x)} &= \frac{M\left(1 + \cos^2(\alpha)\right)}{2}.
\end{aligned}
$$

After calculating in the same manner all six components we are now able to write out the total differential scattering cross sections [2] along the x-, y- and z-directions for both the spin flip and non spin flip channels:

---

2 I would like to remind the reader that this derivation is only valid the particular case in which all scattering originates in the x-y plane. The formulas can easily be extended to the general case by adding an extra component to the scattering vector $\mathbf{Q}$ in the form of an angle γ spanning between $\mathbf{Q}$ and the x-y plane. Of course in the specific case considered here $\gamma = \pi/2$.

$$\left(\frac{\partial\,\sigma}{\partial\,\Omega}\right)^{(x)}_{\downarrow} = \frac{2}{3}I + \frac{1}{2}M(1 + \cos^2(\alpha)), \tag{4.26}$$

$$\left(\frac{\partial\,\sigma}{\partial\,\Omega}\right)^{(x)}_{\uparrow} = N + \frac{1}{3}I + \frac{1}{2}M(1 - \cos^2(\alpha)),$$

$$\left(\frac{\partial\,\sigma}{\partial\,\Omega}\right)^{(y)}_{\downarrow} = \frac{2}{3}I + \frac{1}{2}M(1 + \sin^2(\alpha)),$$

$$\left(\frac{\partial\,\sigma}{\partial\,\Omega}\right)^{(y)}_{\uparrow} = N + \frac{1}{3}I + \frac{1}{2}M(1 - \sin^2(\alpha)),$$

$$\left(\frac{\partial\,\sigma}{\partial\,\Omega}\right)^{(z)}_{\downarrow} = \frac{2}{3}I + \frac{1}{2}M,$$

$$\left(\frac{\partial\,\sigma}{\partial\,\Omega}\right)^{(z)}_{\uparrow} = N + \frac{1}{3}I + \frac{1}{2}M.$$

It is possible now to further separate the magnetic, incoherent and nuclear contributions to the scattering cross sections [79]:

$$\frac{1}{2}M = \left(\frac{\partial\,\sigma}{\partial\,\Omega}\right)^{(x)}_{\downarrow} + \left(\frac{\partial\,\sigma}{\partial\,\Omega}\right)^{(y)}_{\downarrow} - 2\left(\frac{\partial\,\sigma}{\partial\,\Omega}\right)^{(z)}_{\downarrow}, \tag{4.27}$$

$$\frac{2}{3}I = 3\left(\frac{\partial\,\sigma}{\partial\,\Omega}\right)^{(z)}_{\downarrow} - \left(\frac{\partial\,\sigma}{\partial\,\Omega}\right)^{(x)}_{\downarrow} - \left(\frac{\partial\,\sigma}{\partial\,\Omega}\right)^{(y)}_{\downarrow},$$

$$6N = 2\left(\left(\frac{\partial\,\sigma}{\partial\,\Omega}\right)^{(x)}_{\uparrow} + \left(\frac{\partial\,\sigma}{\partial\,\Omega}\right)^{(y)}_{\uparrow} + \left(\frac{\partial\,\sigma}{\partial\,\Omega}\right)^{(z)}_{\uparrow}\right) - \left(\left(\frac{\partial\,\sigma}{\partial\,\Omega}\right)^{(x)}_{\downarrow} + \left(\frac{\partial\,\sigma}{\partial\,\Omega}\right)^{(y)}_{\downarrow} + \left(\frac{\partial\,\sigma}{\partial\,\Omega}\right)^{(z)}_{\downarrow}\right).$$

In the particular case of a triple-axis experiment, which is of interest for this thesis the coordinate system depicted in Figure 4.5.1 is always aligned such that the scattering wavevector **Q** lies along x. This implies that information about the magnetisation along x is lost (since the measurement is only sensitive to components of the magnetisation perpendicular to **Q**). At the same time, this choice makes it easier to distinguish between magnetic and non magnetic scattering. Following Equations 4.26 we have set the α angle (between **Q** and x) to zero. If we assume that the isotope and spin incoherent scattering are featureless and we treat them as a constant background to our signal, we can very easily distinguish between magnetic and coherent nuclear scattering by only measuring the total differential scattering cross section along the x direction ($x \parallel \mathbf{P} \parallel \mathbf{Q}$). If we further measure the other two polarisation directions ($y \parallel \mathbf{P} \perp \mathbf{Q}$ and $z \parallel \mathbf{P} \perp \mathbf{Q}$), Equations 4.26 reduce to:

$$\left(\frac{\partial \sigma}{\partial \Omega}\right)^{(x)}_{\downarrow} = M, \tag{4.28}$$

$$\left(\frac{\partial \sigma}{\partial \Omega}\right)^{(x)}_{\uparrow} = N_{\text{coh}},$$

$$\left(\frac{\partial \sigma}{\partial \Omega}\right)^{(y)}_{\downarrow} = \frac{1}{2}M,$$

$$\left(\frac{\partial \sigma}{\partial \Omega}\right)^{(y)}_{\uparrow} = N_{\text{coh}} + \frac{1}{2}M,$$

$$\left(\frac{\partial \sigma}{\partial \Omega}\right)^{(z)}_{\downarrow} = \frac{1}{2}M,$$

$$\left(\frac{\partial \sigma}{\partial \Omega}\right)^{(z)}_{\uparrow} = N_{\text{coh}} + \frac{1}{2}M.$$

What is also remarkable about such a set-up is its capability to further distinguish between the different magnetisation direction. For this one needs to make use of the Moon-Riste- Koehler equations [70] which dictate that the components of the magnetisation (M_x, M_y or M_z) parallel to the neutron spin will show up in the non spin flip channel while the perpendicular components will be measured in the spin flip channel. This translates into the equations which we ultimately use in the following Chapter 6:

$$\left(\frac{\partial \sigma}{\partial \Omega}\right)^{(x)}_{\downarrow} = M_y + M_z, \tag{4.29}$$

$$\left(\frac{\partial \sigma}{\partial \Omega}\right)^{(x)}_{\uparrow} = N_{\text{coh}},$$

$$\left(\frac{\partial \sigma}{\partial \Omega}\right)^{(y)}_{\downarrow} = M_z,$$

$$\left(\frac{\partial \sigma}{\partial \Omega}\right)^{(y)}_{\uparrow} = N_{\text{coh}} + M_y,$$

$$\left(\frac{\partial \sigma}{\partial \Omega}\right)^{(z)}_{\downarrow} = M_y,$$

$$\left(\frac{\partial \sigma}{\partial \Omega}\right)^{(z)}_{\uparrow} = N_{\text{coh}} + M_z.$$

Notice that information about the x component of the magnetisation is lost and we are only able to distinguish the other two components. Sample realignment is necessary in order to characterise the magnetisation in all three directions of the sample.

4.6 INSTRUMENTATION

4.6.1 *Triple-axis spectrometers*

Most of the data presented in this thesis has been acquired on a triple-axis spectrometer. Figure 4.6.2 shows the layout of such an instrument, namely the low-energy spectrometer ThALES at the ILL. The naming comes from the three transformations that the neutron beam undergoes during a scattering event which can be tuned by adjusting three different angles. Firstly, the angle between the monochromator and the incoming polychromatic neutron beam (θ_M) is used to select specific wavelengths by means of Bragg scattering. After the beam hits the sample it will be scattered in all directions with different wavelengths and intensities. A second monochromating crystal, the analyser, is then placed in a certain position, defined by the θ angle, so as to pick up neutrons with a certain energy depending on the energy transfer which is to be studied. Finally the beam is again monochromatised at the analyser by means of Bragg scattering through the analyser angle (θ_A) and sent into the detector for the final neutron count.

In practice, due to the imperfect nature of the beam-shaping components, the incoming and outgoing beams are usually defined by a distribution of wavevectors rather than a single one. This gives rise to a limited instrumental resolution which will have a broadening effect on the signal. In many cases, the low neutron flux available combined with weak signals create the need to relax the resolution in order to obtain good quality data in a reasonable amount of time.

The resolution can be represented as a four dimensional ellipsoid in reciprocal space with the fourth dimension being the energy axis. When projected on the energy vs Q plane the ellipsoid is generally tilted. This feature can, and should, be used to the advantage of the experimenters as it creates a focusing and a defocusing mode when measuring dispersing signals. Figure 4.6.1 shows a textbook example of the effect of the ellipsoid inclination with respect to the measured dispersion. When scanning on the defocusing side (represented in green) a clearly broader less intense signal is obtained compared to the focusing side.
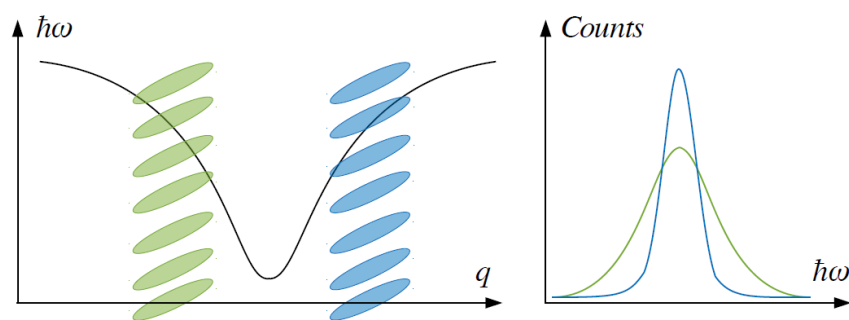
Figure 4.6.1: Illustration of a typical dispersion mapping method on a triple-axis spectrometer. The blue and green ellipsoids indicate the direction of two constant Q scans. On the right-hand side we can observe the difference in the measured signal arising from the position of the resolution ellipsoid with respect to the dispersion. Image taken from [6].
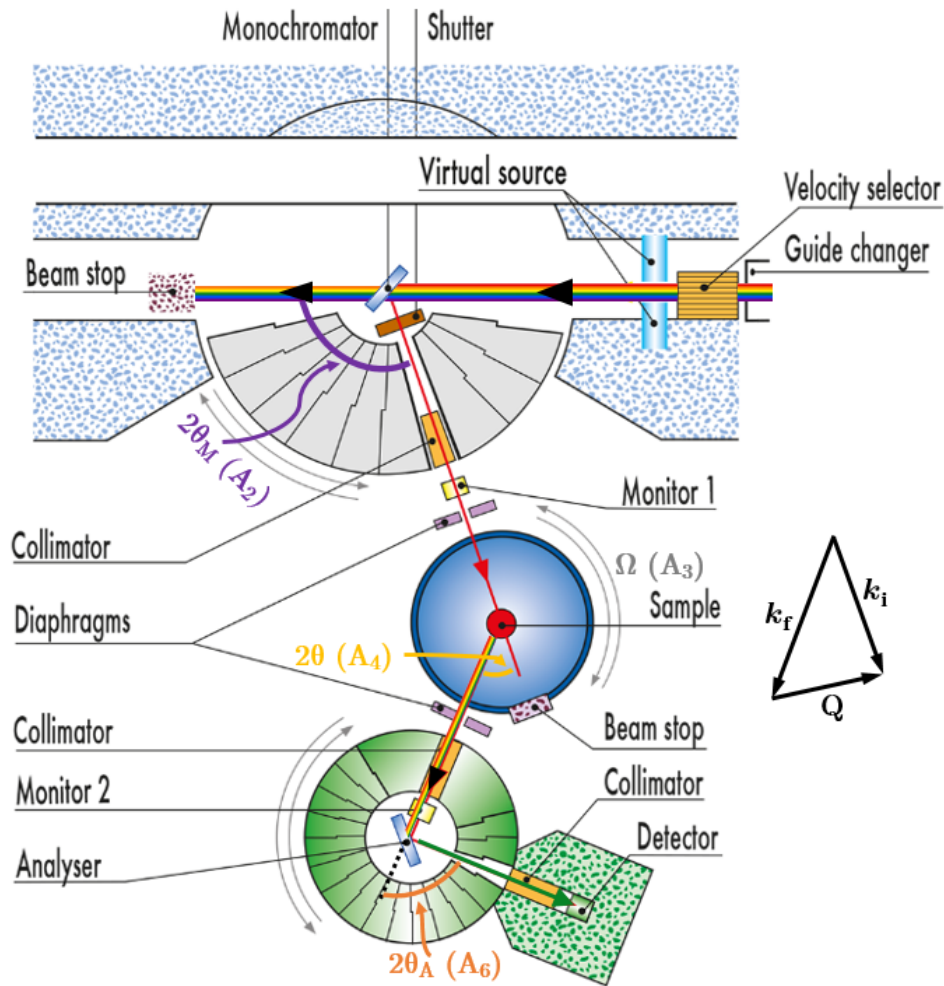
Figure 4.6.2: Illustration of the ThALES triple-axis spectrometer layout. The drawing includes the most optical components that shape the neutron beam throughout its path. Besides the shown ones additional filters can be used in order to minimise the undesired effects oh higher order scattering. The angles that define the experimental conditions are also represented along the neutron path. The insert shows the scattering triangle for the specific instrument configuration represented. Image adapted from [80].

4.6.2 *Imaging*

Imaging is the second neutron scattering technique used in this research. Neutron as well as X-ray imaging make use of the fact that the attenuation coefficients vary as a function of material and this creates an absorption contrast. The advantage of neutrons over X-rays is again the random variation (unrelated to the atomic number) of the attenuation factors throughout the periodic table. Light elements have high scattering and absorption rates in contrast with numerous metals which are more penetrable by neutrons. This complementarity between neutrons and X-rays makes the use of both techniques necessary in many cases in order to obtain a complete picture of the studied materials.

The typical layout of an imaging instrument includes very few components (see Figure 4.6.3). After exiting the guide the neutron beam is collimated with the help of so-called pinholes. The diameter of the aperture influences the spatial resolution but also the neutron flux and ultimately the counting time. Afterwards the beam encounters the studied object. The placing of the

sample as a function of the pinhole and the detector unit is another factor which affects the spatial resolution of the recorded images. The detection usually consists of a conversion process of the neutrons into visible light by a scintillator. The light is further recorded by a CCD (charge-couple-device) camera.

As shown in Figure 4.6.3, other elements can be added to this basic setup. Most notably a spin analysis system can be introduced. This way one is able to make use of the fact that neutrons posses a magnetic moment in order to perform so-called polarised neutron imaging which allows us to map magnetic fields in real space. We have employed this particular technique in order to study the temperature dependence of a trapped magnetic flux inside of a superconducting LSCO single crystal. The experimental details and results are presented in Chapter 7.
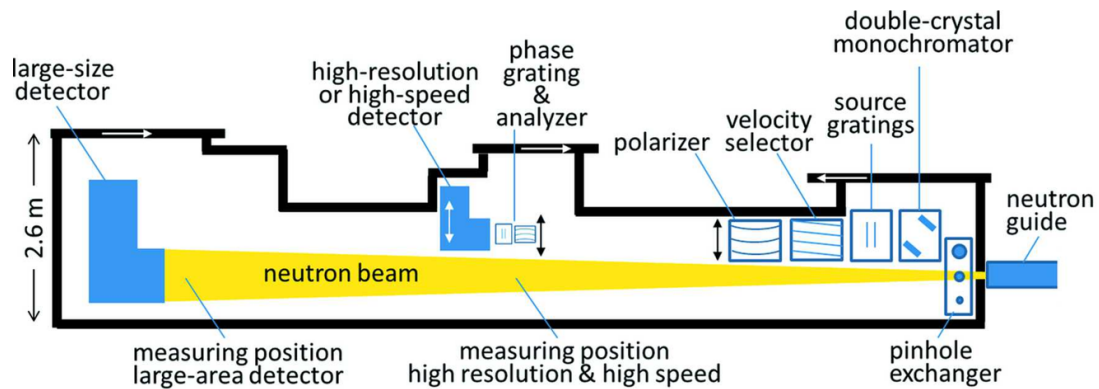
Figure 4.6.3: Instrument layout of CONRAD-2 imaging station at the Helmholtz-Zentrum Berlin (HZB). Image taken from [81].

Part II

EXPERIMENTS, ANALYSIS AND RESULTS

MAGNETISM IN $La_{2-x}Sr_xCuO_4$ CUPRATE SUPERCONDUCTORS AT THE UNDERDOPED QUANTUM CRITICAL POINT

5.1 LITERATURE REVIEW

As previously mentioned in the introduction section of this thesis, in broad terms, the main aim of this research has been to understand the differences and similarities, with respect to the magnetism, between the underdoped superconducting and non-superconducting LSCO samples. To this end we have performed numerous neutron scattering experiments in which different parameters (such as temperature, energy of excitations or applied magnetic field) have been varied in order to establish which traits are tied to the emergence of superconductivity and which are not. Throughout this section I will introduce part of the vast literature on cuprates. The main focus will be to present similar effects to the ones studied in this research, which have been observed across the phase diagram of $La_{2-x}Sr_xCuO_4$. This will also make our choice of doping evident as the underdoped regime of LSCO has been sparsely studied so far.

Looking at the phase diagram of LSCO, depicted in Figure 5.1.1(a), it becomes evident that superconductivity emerges in a very particular electronic environment balancing between two antithetical electronic phases. On one hand, the parent undoped compound is an antiferromagnetic Mott insulator with localised electrons while at the opposite overdoped end of the spectrum we find a metallic phase with itinerant electrons. This clash of very different behaviours gives rise not only to the still puzzling superconducting phase at low temperatures, but also to other insufficiently understood states at higher temperatures such as the pseudogap or the strange metal regimes. It comes thus as no surprise that the study of the electronic structure and the associated magnetism of samples across the phase diagram has claimed a significant portion of the research in this field.

Throughout this section I will divide the phase diagram into three main regions, according to doping, which will be discussed by comparison. One is the underdoped regime which spans from $x = 0.02$ to $x \sim 0.14$ and includes the highly underdoped non-superconducting samples ($0.02 \leq x \leq 0.055$), the superconducting ones with decreased superconducting critical temperature as well as the so-called anomalous doping ($x = 0.12$). The other two regions are the optimally doped one, exhibiting maximum critical temperature ($0.14 \leq x \leq 0.16$) and the overdoped region where the system moves away from optimal superconductivity ($0.16 < x \leq 0.26$).
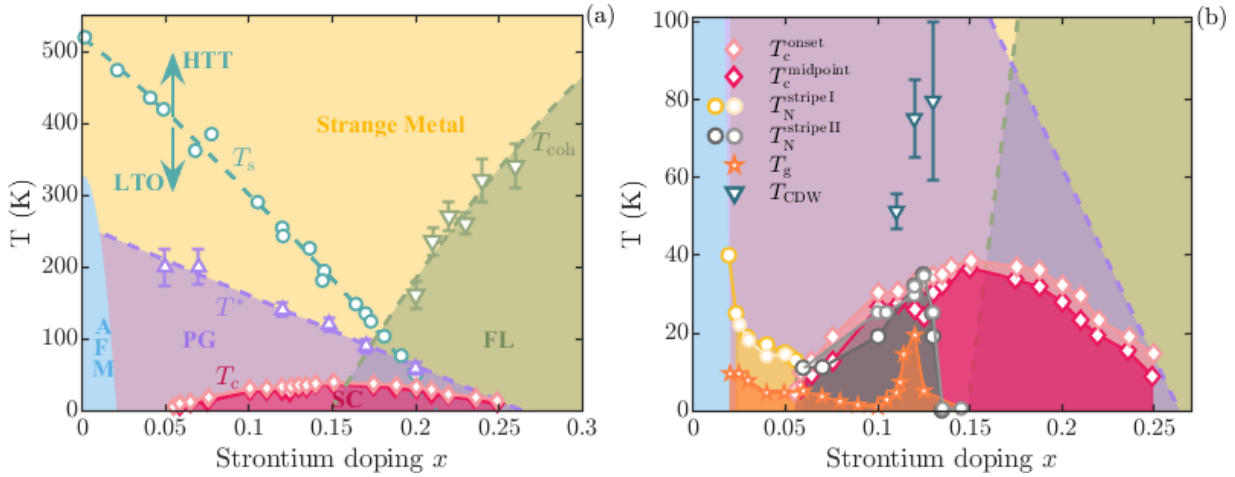
Figure 5.1.1: (a) Temperature vs doping phase diagram of $La_{2-x}Sr_xCuO_4$. The schematic representation includes the antiferromagnetic phase (AFM - in light blue) spanning from 325 K at $x = 0$ to 0 K at $x = 0.02$ [44], the pseudogap phase (PG - in purple) delimited by the gap opening temperature T^* [45], the normal metal, or Fermi liquid, phase (FL - in green) demarcated from the strange metal phase (in yellow) by the T_{coh} critical temperature [46], the superconducting phase (SC in pink) defined from the onset (in light pink diamonds) and midpoint critical temperatures (in dark pink diamonds) T_c [47] and the structural phase transition temperature (T_s), in dark green circles, from the high-temperature tetragonal phase to a low-temperature orthorhombic one [82]. **(b)** Zoom into the superconducting region of the phase diagram. The circles denote the onset of spin-density-wave order (elastic spin stripes) as measured by neutron scattering outside (stripe I phase in yellow) and inside (stripe II phase in grey) the superconducting dome. The light shades depict data taken from Ref [45] while the darker shades are data from Ref [47]. Orange squares indicate the onset temperature of magnetic order (spin-glass phase) as measured by μSR and NMR, while the dark blue triangles depict the onset temperature of charge-density-wave as measured by x-ray diffraction [45].

Figure 5.1.1(b) compiles a number of different measurements delimiting various electronic phases. It becomes quickly evident that the underdoped region is the most rich in coexisting (or competing as we shall see) phases. One such phase, relevant for this study, is the magnetically ordered one which has been analysed by means of: (1) elastic neutron scattering, represented in yellow and grey in Figure 5.1.1(b) as well as (2) truly low-energy[1] probes such as μSR and NMR, represented in orange in the phase diagram. The two types of probes have very different energy (or time) resolution with cold neutrons typically exhibiting a resolution of approximately 0.2 meV (or 50 GHz) while muons can achieve resolutions three orders of magnitude lower (in the MHz regime). This difference is the reason for the discrepancy in onset temperatures (T_N and T_g respectively). On the other hand, bulk magnetisation measurements have revealed that, samples with doping outside the superconducting dome ($0.02 < x \leqslant 0.05$), show numerous traits of a canonical spin-glass [84] such as remnant slow decaying magnetisation and irreversible behaviour below the glass transition temperature or scaling behaviour (for example the divergence of magnetic susceptibility at the glass transition temperature in the absence of applied magnetic field) [83, 85, 86]. Later on, additional magnetisation measurements, performed on detwinned non-superconducting LSCO samples, exposed an in-plane[2] spin anisotropy which led to the proposal of a spin-glass in the form of phase-separated antiferromagnetic domains with random

---

1 This is also supported by the great agreement in magnetic order critical temperatures obtained from magnetic susceptibility measurements, which are almost static [56], and μSR for example [83].

2 In the a-b-plane defined by the copper oxide layers.

orientation [87]. Additional evidence for such a picture in a wider doping range ($0.02 \leqslant x \leqslant 0.08$), came from ^{139}La nuclear quadrupole resonance (NQR) measurements [88] which were able to probe the intradomain coupling and anisotropy. It was thus proved that the ordered magnetic phase is not a traditional spin-glass but rather that, as a function of decreasing temperature, the mesoscopic antiferromagnetic domains freeze in a disordered fashion, due to the weak long range dipolar coupling between domains. This has motivated its naming as a cluster spin-glass state [89]. Within this picture, elastic spin stripes measured through neutron scattering are merely a signature of a cluster spin-glass state with correlated antiferromagnetic domains [56].

In terms of doping dependence, both the cluster spin-glass phase measured by µSR, NMR and NQR, as well as the elastic spin stripe phase measured by neutron diffraction, span across the entire underdoped region of the phase diagram ($x < 0.14$) and seem to be in competition with superconductivity. This hypothesis of a competing superconducting phase, without magnetic order, and a magnetically ordered phase is supported by two empirical observations: (1) the complete suppression of magnetic order at optimal doping and (2) the increase in magnetic order critical temperature (both T_N and T_g) concomitant with a decrease of the superconducting critical temperature at the anomalous $x = 0.12$ doping (see Figure 5.1.1(b)). Alternatively, the anticorrelation between the two critical temperatures might also be explained by structural defects [56]. The drastic increase in magnetic order critical temperature at $x = 0.12$, could be a result of local pinning of spin stripes by lattice distortions induced by a phase transition to a low-temperature tetragonal (LTT) phase. This is even more evident in LBCO where T_c is drastically suppressed while at the same time the crystal transitions to the LTT phase [90]. Moreover, the effect (suppression of T_c) disappears under uniaxial strain, proving the relation to the structural phase transition [91]. In LSCO, the effect is more subtle as the structure only shows signs of local LTT distortions [92, 93]. Consequently, samples such as superconducting $Bi_{2.1}Sr_{1.9}Ca_{1-x}Y_xCu_2O_{8+y}$, which do not exhibit instabilities towards an LTT phase, also do not display the anomalous behaviour at $x = 0.12$ doping level [94]. The interplay between the superconducting and magnetically ordered phases is still a matter of great debate and research [95].

In terms of the extent of the magnetic domains, S. Wakimoto *et al.* [96] have shown, through elastic neutron scattering measurements, that the size of the ordered magnetic moment per Cu site decreases from $\sim 0.18\mu_B/$Cu at $x = 0.03$ to $\sim 0.06\mu_B/$Cu at $x = 0.07$. It should also be noted that no significant modification has been observed at the onset of superconductivity ($x \sim 0.055$) and that the incommensurate magnetic phase exhibits a small correlation length of $\xi \sim 20$ Å in this doping regime. At higher doping the moment increases sharply again and reaches $\sim 0.1\mu_B/$Cu at $x = 0.12$ with a much higher correlation length of $\xi \geqslant 200$ Å. This can be indicative of the presence of two distinct magnetic phases as a function of doping (one below $x = 0.07$ and another above) which might affect superconductivity in different manners.

To aid the understanding of the interplay between superconductivity and magnetic order, neutron scattering experiments have been performed under applied magnetic field, which is known to locally destroy superconductivity. As it can be observed in Figure 5.1.2(a), in underdoped samples, where magnetic order is already present in zero field at low temperatures, the applied magnetic field tends to increase the ordered magnetic moment up to values specific to the 1/8 ground state. The linear-logarithmic dependence exhibited at low fields by the static incommensurate magnetic order is in great agreement with the phenomenological Ginzburg-

Landau model proposed by E. Demler *et al.* [97]. According to this theoretical phase diagram the sample can transition between three phases by tuning its doping and/or the strength of the applied magnetic field: (1) a purely magnetic phase (SDW) at very low doping or high applied magnetic fields, (2) a mix superconducting and magnetic (SDW + SC) phase in an intermediate doping regime and at applied fields much lower than the upper critical field (H_{c2}) or (3) a purely superconducting (SC) phase at higher doping and under a wide range of applied magnetic field strengths. Clearly the underdoped LSCO samples ($x \leqslant 0.13$) belong to the second phase and are driven into the first one by an applied magnetic field. On the other hand, optimally doped samples belong to the third phase having no observable magnetic order in zero field. However, as predicted by the above-mentioned model of competing phases, experimental observations have confirmed that magnetic order can be induced by as small applied magnetic field with the lowest transition detected at 3 T (see Figure 5.1.2(b)[3]). The agreement between experimental observations and theoretical predictions led B. Lake *et al.* [55] to explain the field effect as inducing additional magnetic order around the vortex cores. It is worth noting though that even if induced locally around the vortex cores, the incommensurate antiferromagnetic order is still long range ($\xi > 400$ Å).
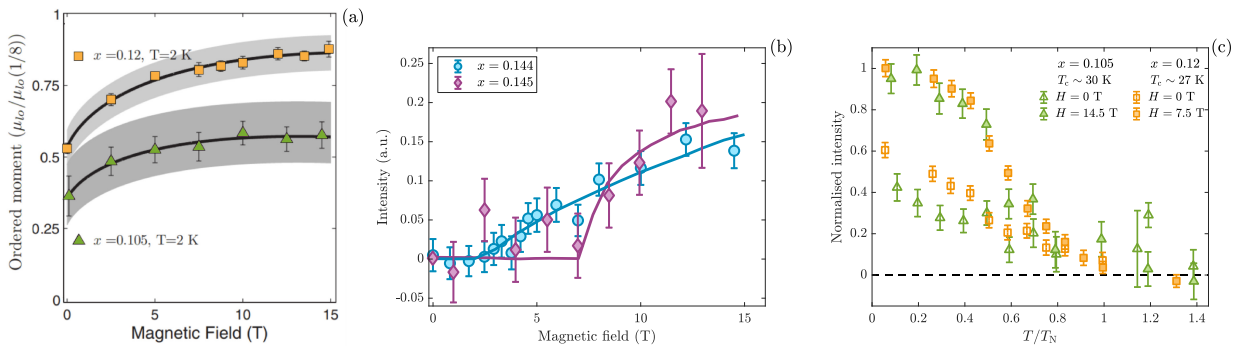
Figure 5.1.2: Applied magnetic field dependence of elastic spin stripes in **(a)** underdoped and **(b)** optimally doped samples. **(a)** The ordered moment is plotted as a function of increasing magnetic field. The solid lines represent linear-logarithmic fits to the data of the form $\mu = \sqrt{I(H)} \propto \sqrt{(H/H_c)\ln(H_c/H)}$. The shaded grey areas indicate the magnetic moments as determined from zero field μSR and have the purpose to demonstrate the extent of the neutron measurement error. Image taken from [53]. **(b)** The intensity of the incommensurate signal is plotted as a function on applied magnetic field. The $x = 0.145$ data is reproduced from [53] and the associated fit is the same as in subfigure (a). The $x = 0.144$ data is reproduced from [54]. The solid blue line is a power law fit to the data of the form $I(H) = I_0 + A(H - H_c)^{2\beta}$. Both fitting routines are inspired by the phenomenological Ginzburg-Landau model proposed by E. Demler *et al.* [97]. **(c)** Temperature dependence of the neutron scattering intensity corresponding to static spin stripes of LSCO samples with $x = 0.105$ and $x = 0.12$. The filled and empty symbols denote measurements acquired with and without applied magnetic field respectively. x and y-axis are normalised to the magnetic order onset temperature ($T_N^{x=0.105} = 25$ K and $T_N^{x=0.12} = 30$ K) and to the value of the intensity at 2 K respectively. Data reproduced from [53].

The next logical step has been to look into the corresponding vortex phase diagram [98]. The fact that the field effect on the incommensurate AFM order arises in the region of the phase diagram corresponding to 2D disordered vortex structures led J. Chang [82] to conclude that the effect cannot be directly related to vortex physics. Consequently, he proposes a scenario of

---

3 The rather significant difference between the two data sets presented for seemingly very similar samples could be the result of an imprecise determination of doping. It should also be noticed that the difference between the to fits lies in one point (at 7 T for the $x = 0.145$ data) which has a rather high errorbar.

competing order parameters the balance of which is sensitive to applied magnetic fields. To add to the competition picture, the temperature dependence of the incommensurate AFM signal, reproduced in Figure 5.1.2(c), shows that the field enhancement takes place only at temperature within the superconducting dome[4].

A consensus regarding the type of competition between magnetic order and superconductivity is a crucial step in understanding the phase diagram of cuprates. As it can be inferred, from the data presented thus far, the highly underdoped region of the phase diagram ($x < 0.10$), where magnetic order has indeed been observed in zero field [99–102], has not been analysed as intensively as other doping regimes. This adds to our motivation to focus on this doping region in particular as we believe it might hold the answer to some of these very interesting debates.
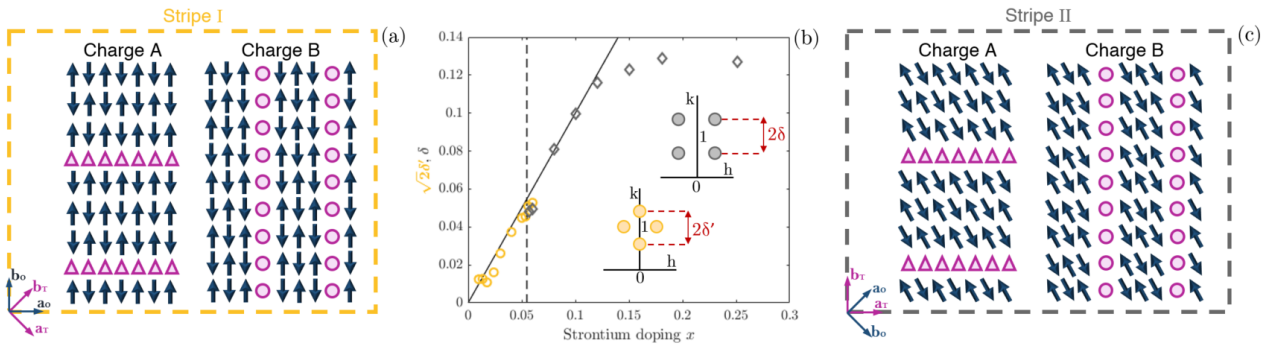
Figure 5.1.3: (a) and **(c)** Graphical representation of stripes arrangement in both stripe I and stripe II phases respectively. In each case, the spin direction, along the orthorhombic b-axis, of the parent compound (LCO) is preserved [103, 104]. The purple triangles and circles depict the doped charge rivers. The corresponding neutron scattering patterns are represented in the inset of subfigure (b), stripe I in yellow and stripe II in grey. The yellow points have been multiplied by a factor $\sqrt{2}$ in order to correct for the difference in symmetry so that, in both cases, the half difference in Q between two neighbour IC peaks is plotted in the y-axis. Note that in both illustrations a $1/8$ periodicity is presented which is valid for $x \geqslant 0.12$. **(b)** Doping dependence of the incommensurability over the entire phase diagram of LSCO. Yellow circles depict the highly underdoped and non-superconducting region in which stripes run along the orthorhombic a/b-axis (stripe I) while grey diamonds represent the superconducting region in which stripes run along the tetragonal a/b-axis (stripe II). Note that the insets showing the expected neutron pattern follow the orthorhombic notation with h/k reciprocal space directions superimposed on the orthorhombic a/b-axis. Solid line indicates the linear dependence $\delta = x$ while the dashed line marks the onset of superconductivity. Data reproduced from [105].

Another phenomenon occurring at $x = 0.12$ doping in LSCO, which contributed to it being known as the so-called anomalous $1/8$ doping, is the saturation of the incommensurability as seen by neutron scattering experiments, discovered early on by K. Yamada *et al.* [52]. As it can be observed in Figure 5.1.3(b) in the low doping regime the dependence is almost linear $\delta = x$ while at doping $x \geqslant 0.12$ it saturates to $\delta \sim 0.12$. The doping dependence of the incommensurability presented in Figure 5.1.3(b) contains predominantly low-energy inelastic measurements ($<$ 5 meV) of spin stripes although, specifically at very low doping ($x < 0.02$), some of the data has been acquired from elastic scans. This mixture is however not problematic since, as we shall see next, the magnetic excitations dispersion is very steep at such low energies and, taking into

---

4 It should be noted though that the two doping values presented here exhibit very similar critical temperatures $T_c \sim T_N$ making it very difficult to establish a true correlation with T_c

account the limited $\mathbf{Q}$ resolution of neutron scattering experiments[5], the incommensurability of elastic and inelastic signals is virtually the same.

Another aspect to notice is the transition from a stripe I phase, with charge stripes running along the orthorhombic a/b-axis, to a stripe II phase, with charge stripes running along the tetragonal a/b-axis at the onset of superconductivity (see Figures 5.1.3(a) and (c) for graphical representations of these two magnetic structures). The corresponding neutron patterns, depicted in the inset of Figure 5.1.3(b), are 45° rotated with respect to one another equivalent to the angle between the tetragonal and orthorhombic coordinate systems (note that the local coordinate system is included in each panel). The stability of the stripe I phase in the non-superconducting regime (the weak-coupling region) and stripe II phase in the superconducting one has been predicted early on by calculations of the Hubbard model [106, 107]. Neutron experiments on LSCO samples with strontium doping across the insulator-superconductor phase transition have confirmed the universality of such a rotation of the spin and charge modulation [99, 100, 108–110]. We have also been able to map out the magnetic signal around the antiferromagnetic reflection in our LSCO $x = 0.05$ sample and observed a stripe I type of modulation as it shall be revealed in the next sections.

Charge stripes (or charge-density-wave - CDW) have also been observed, through X-ray diffraction measurements, only around the anomalous $x = 0.12$ doping as shown in Figure 5.1.1(b). There are a few aspects of these measurements that support the hypothesis of spatially modulated charge and spin order parameters in a stripe pattern in LSCO[6]. Firstly, as predicted by the stripe model and exemplified in the graphical representation in Figures 5.1.3(a) and (c), the relationship between the wavevectors of the two forms of correlation follows the $\delta_{\mathrm{CDW}} = 2\delta_{\mathrm{SWD}}$ relationship [45]. Secondly, both applied magnetic field [111] and temperature [45] dependencies of CDW and SDW are remarkably similar. A magnetic field applied along the c-axis (perpendicular to the CuO_2 layers) induces an enhancement of similar magnitude of spin and charge-density-wave orders (see Figure 5.1.4(b)). On the other hand, a magnetic field parallel to the in-plane a-axis produces no detectable effect on charge stripes. Likewise, a magnetic field has an anisotropic influence on spin stripes with in-plane components being much more inefficient in disturbing magnetic order or superconductivity [55]. In terms of temperature effect, again CDW mimics very well the behaviour of very low-energy spin fluctuations ($\hbar = 0.3$ meV) having the same temperature onset and evolution (suppression below the superconducting critical temperature) as shown in Figure 5.1.4(a). At the same time both CDW and SDW exhibit the strongest signal at the anomalous $x = 0.12$ doping. Lastly, both charge and spin orders are rotated away from the Cu-O bond direction by very similar amounts: 3° in the case of SDW [112] and 2.7° in the case of CDW [113].

To explain the relationship between these three main electronic orders, SDW, CDW and superconductivity, two main pictures have been put forward. The first is a competition picture in which the spatially modulated SDW and CDW orders are in competition with a uniform d-wave superconducting phase. Evidence for such a phase can be found in optimally doped LSCO samples where, as discussed above, magnetic order can be induced by applying a magnetic field

---

5 It should be noted though that a careful analysis of the peaks position, measured in an instrument configuration adapted for improved $\mathbf{Q}$ resolution, has revealed a mismatch in incommensurability in LCO+O samples [61] which is discussed in detail in Chapter 6.

6 This might not be universal to all cuprates as for example YBCO does not exhibit some of these features [45].
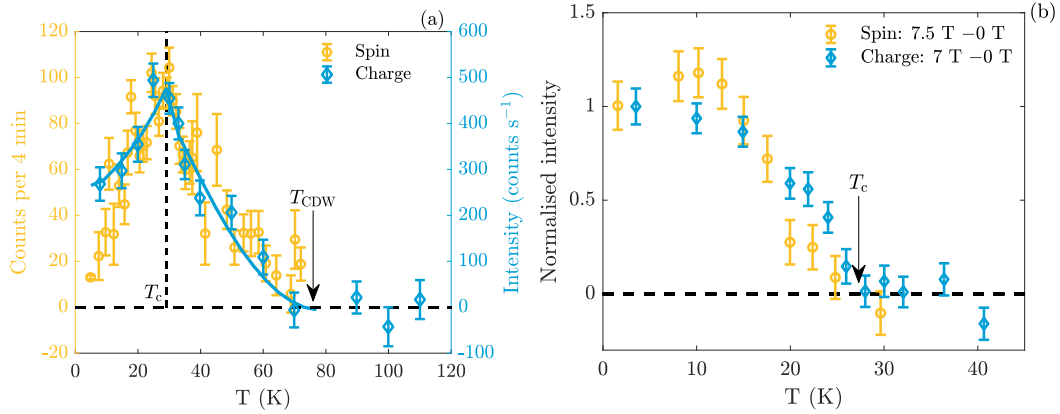
Figure 5.1.4: (a) Temperature dependence of x-ray diffraction intensity probing the charge stripe order (in blue diamonds) and of the neutron scattering intensity corresponding to spin fluctuations with $\hbar\omega = 0.3$ meV (in yellow circles) in LSCO with $x = 0.12$. The indicated superconducting critical temperature ($T_c \sim 29$ K) corresponds to the sample used for measurements of CDW. A sample of the same doping, with $T_c \sim 27$ K, was used in the SDW excitations measurement. The solid line is a power law fit to the 'charge' data. Data reproduced from [45, 114]. **(b)** Comparison of the magnetic field effect on spin and charge stripe orders. The plot has been obtained by subtracting the zero field intensity of the neutron and x-ray signal respectively from the rest of the measurements recorded in applied magnetic field. Additionally, all points have been normalised to the values at base temperature. The superconducting critical temperature indicated in the figure ($T_c \sim 27$ K) is valid for both measurements. Data reproduced from [111].

which is known to locally destroy superconductivity. On the other hand, for samples that exhibit magnetic order in zero field, such as underdoped LSCO or LBCO, a pair density wave (PDW) picture has been put forward to account for the coexistence of SDW and superconducting order parameters [115]. In a PDW superconducting state the order parameter varies as a function of position and is intertwined with the SDW and CDW order parameters. Evidence for this intertwined scenario comes from measurements of in-plane (ρ_{ab}) and out-of-plane (ρ_c) resistivity [116]. In LBCO at the anomalous $x = 1/8$ doping, the in-plane resistivity has a significant drop at the onset of SDW ($T_N > T_c$) concomitant with an increase of the out-of-plane resistivity. This points towards the emergence of a two dimensional in-plane superconducting phase, at temperatures above T_c, which is prevented to act as a coherent superconductor by the weakened interlayer Josephson coupling that in turn is caused by the perpendicular arrangement of charge stripes in adjacent CuO_2 layers. Besides the absence of a spin gap, theoretical calculations also predict the lack of a resonance in the excitation spectrum for a PDW superconductor [66].

As previously mentioned, magnetic fluctuations have also been extensively studied in LSCO samples across the phase diagram especially by means of neutron scattering. One of the most important experimental findings is the universality of an hourglass dispersion of spin excitations across the cuprates family [95, 117]. As exemplified in Figure 5.1.5(a), LSCO is no different and exhibits incommensurate excitations that disperse towards the antiferromagnetic Q-value at low energies and at the Q-value of the antiferromagnetic order for the parent compound (at the crossing energy of the hourglass E_{cross} - neutron resonance peak). This is followed, at higher energies, by an outwards dispersion similar to that of the AFM parent compound, in the same energy range, but with a reduced slope which points towards a lower nearest neighbour super-exchange constant (J) in superconducting doped compounds ($J = 81 \pm 9$ meV in LSCO with $x = 0.16$ [60]). In the underdoped regime it has been observed that the slope of the dispersion at low energies

is almost doping independent [118]. Given that, as we know, the incommensurability is highly doping dependent in this region of the phase diagram, it is expected that the resonance energy E_{cross} would depend linearly on the incommensurability δ and implicitly on the doping x [119, 120]. Indeed, the experimental neutron scattering results are consistent with the predicted linear relationship between E_{cross} and x at doping values $x \leqslant 0.12$ (see Figure 5.1.5(b)). It should also be noted that the 45° rotation of stripes, discussed earlier, does not influence this trend. This correlation implies a fully magnetic origin of the resonance which defines yet another characteristic energy scale, in these systems, that is not a direct consequence of the emergence of superconductivity [120]. The fact that the resonance energy does not scale with the superconducting critical temperature indicates that it is not directly related to the superconducting pairing mechanism [121, 122].

In optimally doped LSCO ($x = 0.16$), a two-component structure of the hourglass dispersion (above and below $E_{cross} \sim 50$ meV) has been proposed in order to account for the observed abrupt broadening of excitations above E_{cross} and the sharp increase in spectral weight at energies below the resonance (~ 20 meV) [60]. Similar features have also been encountered in underdoped LSCO with $x = 0.10$ ($T_c = 28.6$ K) [123]. It should also be mentioned that in LBCO samples a similar peak in the dynamic spin susceptibility appearing at ~ 18 meV has been attributed to spin-phonon hybridisation [64]. Later on this has been confirmed in a wide range of LSCO ($x = 0.08$ and $x = 0.11$) and LBCO ($0 \leqslant x \leqslant 0.095$) samples and it is thought to have the origin in the crossing between the magnetic dispersion and an optical phonon branch [62, 63].
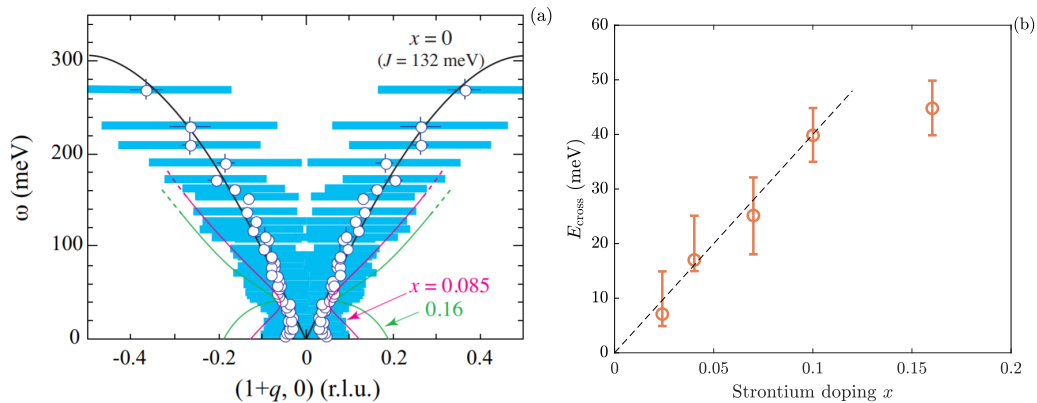
Figure 5.1.5: **(a)** Magnetic hourglass dispersion as measured in LSCO with strontium doping $x = 0.05$ (white circles). The blue horizontal bars indicate the with of the peaks in constant energy scans. Additional pink, green and black curves show the measured dispersion of LSCO underdoped ($x = 0.085$), optimally ($x = 0.16$) and the antiferromagnetic LCO parent compound respectively. The inset also shows the value of the nearest neighbour super exchange constant (J) of undoped samples. **(b)** Doping dependence of the hourglass crossing energy in LSCO. The dashed line is a guide to the eye. Images taken from [118].

Even though the precise relationship between spin fluctuations and superconductivity still needs to find consensus in the scientific community, one thing can be stated without doubt and that is that there must be an interplay between the two. One of the most cited evidence for this is the opening of a spin gap at the onset of superconductivity [58]. Full spin gaps have been observed to open in LSCO optimally doped with $x = 0.163$ below $\Delta_{SG} \sim 6.7$ meV [58, 124], with $x = 0.15$ below $\Delta_{SG} \sim 3.5$ meV [125, 126], with $x = 0.145$ below $\Delta_{SG} \sim 4$ meV [127] and underdoped with $x = 0.135$ below $\Delta_{SG} \sim 4$ meV [47] and overdoped with $x = 0.18$ below

$\Delta_{SG} \sim 4.5$ meV [126]. Other samples on the other hand have shown signs of a so-called incomplete spin gap. Suppressed dynamic susceptibility, at temperatures within the superconducting dome, has been measured in LSCO samples with strontium doping $x = 0.184$ ($\Delta_{SG} \sim 5$ meV) [128], $x = 0.14$ ($\Delta_{SG} \sim 6$ meV) [129], $x = 0.105$ ($\Delta_{SG} \sim 6$ meV) [130]. In most of the above-mentioned cases (with the exception of the $x = 0.135$, $x = 0.14$, $x = 0.15$ and $x = 0.18$ where applied magnetic field effects have not been reported) additional sub-gap states are induced in the presence of an applied magnetic field, perpendicular to the CuO$_2$ layers, of the order 7.5-10 T. Similar to the explanation for field-induced magnetic order, the vortex lattice or other impurities are thought to favour low-energy spin fluctuations [124, 127], a hypothesis which is also supported by theoretical calculations [131]. Equivalently, a continuous spectrum of excitations is recovered, at all doping concentrations, above the superconducting critical temperature (with the exception of overdoped $x = 0.25$ samples where no significant temperature effects have been observed [126, 132]). The lack of a field effect, at temperatures greater than T_c, is yet another argument for a correlation between the opening of the spin gap and superconductivity [128]. In the anomalous $x = 0.12$ doping, the suppression of magnetic fluctuations below ~ 0.75 meV, corroborated with the lack of an applied magnetic field effect, has been interpreted as an out-of-plane spin gap co-existing with a smaller in-plane gap which could not be resolved [114]. In other slightly higher doping values $x = 0.125$ and $x = 0.13$, a small increase in spectral weight at energy transfers < 4 meV concomitant with sharp decrease of dynamic spin correlation length has been taken as evidence for the existence of two types of magnetic fluctuations: quasi-elastic fluctuations associated with static stripes and a fluctuation spectrum similar to that of optimally doped samples gapped below ~ 4 meV [47].

Spin fluctuations have also been observed in the highly underdoped region of the phase diagram ($x < 0.10$), both inside and outside the superconducting dome, [99, 108, 133], though, as in the case of magnetic order, much less explored beyond the determination of incommensurability. The temperature dependence of excitations of various energies has been measured in $x = 0.07$ LSCO [101] (a doping which is also considered in the current study, the data is thus presented for comparison in Figure 5.1.6(c)). The spectrum shows no clear spin gap to the lowest energy measured (2 meV). However, the signal is significantly suppressed at low energies ($\lesssim 25$ meV), below the resonance, as a function of increased temperature. The fact that the lower energy spectrum is much more sensitive to the onset of superconductivity adds to our motivation for exploring this region of the dispersion. Figures 5.1.6(a) and (b) show the corresponding magnetic order as a grid scan covering all four incommensurate peaks and confirming their orientation along the orthorhombic a/b-axis [99].

As it can be inferred from this review of the literature up to date, there is a significant lack of information on highly underdoped LSCO samples and their associated magnetic structure, in comparison with other doping regimes of the phase diagram. This motivated our quest for a better understanding of the interplay between magnetism and superconductivity by performing a detailed study of magnetic order and excitations under different conditions (such as applied magnetic field or varying temperature). In the next sections each doping ($x = 0.05, 0.06, 0.07$ and 0.08) will be discussed individually followed by an overall conclusion describing how our results fit into the already intricate picture of the cuprates family.
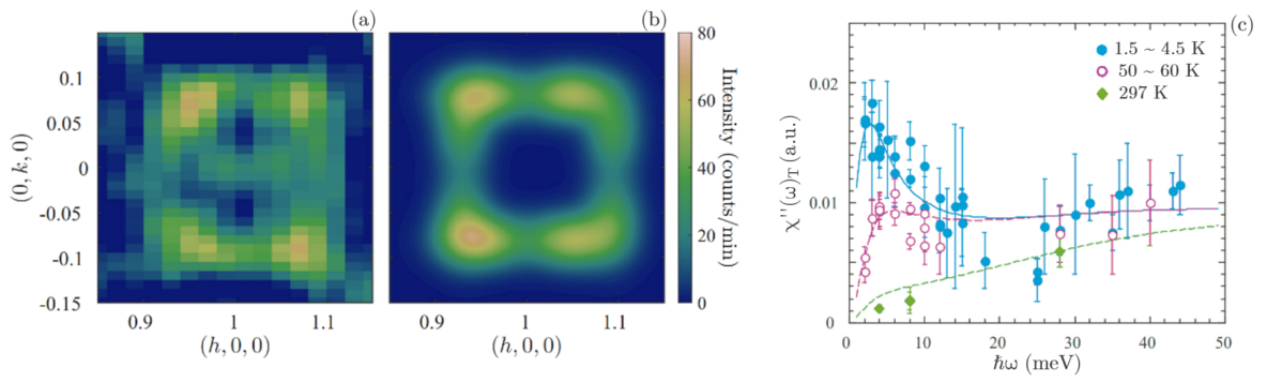
Figure 5.1.6: (a) Elastic stripe pattern measured in LSCO with $x = 0.07$ at 1.5 K recorded in the absence of applied magnetic field and **(b)** 2D Gaussian fit to the data. The data are presented in orthorhombic notation. Images taken from [99]. **(c)** Energy and temperature dependence of the dynamic spin susceptibility of LSCO with $x = 0.07$ ($T_c = 17$ K). Image taken from [101].

5.2   LSCO 5%

5.2.1   *Experimental method and sample*

The LSCO crystal with strontium doping $x = 0.05$ is the only non-superconducting sample of the series which has been studied. As all the rest of the samples, a large stoichiometric $La_{1.95}Sr_{0.05}CuO_4$ (LSCO5) crystal has been grown, by members of our group, inside a mirror furnace using the travelling solvent float zone technique (TSFZ) [134]. In order to make it possible to perform measurements inside cryomagnets, which have limited space within the sample chamber, smaller pieces have been cut. The piece used in this study, presented in Figure 5.2.1(a), measures 1.9 cm in length and 0.6 cm in diameter and weighs ~ 3.5 g. In preparation for the experiments, the sample has been placed in an aluminium sample holder and aligned such that the a-b plane is the scattering plane (parallel to the aluminium cylindrical base shown in Figure 5.2.1(a)). This allowed us to apply a magnetic field perpendicular to the a-b plane (the CuO_2 layers) by making use of the vertical field cryomagnets available at the ILL. The precise alignment has been carried out on the Laue backscattering neutron diffractometer Orient Express at the ILL. Magnetic susceptibility measurements, performed on small pieces resulted from cutting the crystal, confirm that the sample shows no signs of a transition to diamagnetism (see Figure 5.2.1(b)), to the lowest temperature measured (4.7 K). In order to identify the exact doping of the sample we resorted to determining the transition temperature between the high-temperature tetragonal (HTT) and the low-temperature orthorhombic (LTO) phases which, as mentioned before, is doping dependent. For this, the intensity of reflections only allowed in the LTO phase, such as $(0, 1, 4)$ or $(0, 3, 2)$, has been measured as a function of increased temperature in a neutron scattering experiment performed on the thermal triple axis spectrometer IN3. The data, discussed in detail in my Masters thesis [135], revealed a transition temperature for this particular crystal $T_s = 416 \pm 5$ K corresponding to a doping level $x = 0.050 \pm 0.002$ [82].
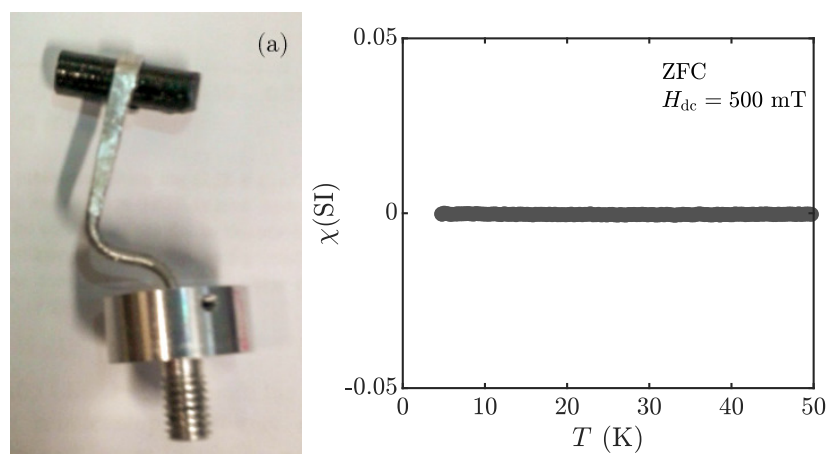
Figure 5.2.1: (a) $La_{1.95}Sr_{0.05}CuO_4$ single crystal sample placed inside an aluminium sample holder. This is the exact configuration used throughout all the neutron scattering experiments. **(b)** Magnetic (volume) susceptibility measured while heating the sample in a 500 mT applied magnetic field preceded by zero field cooling (ZFC).

Three neutron scattering experiments have been performed on this sample, two on the cold triple axis spectrometer ThALES, inside 10 T and 15 T vertical magnets respectively, and another on the thermal triple axis spectrometer IN8 in the 10 T vertical magnet. In all of the experiments performed at ThALES and presented in this chapter the standard instrument configuration has been used:

VELOCITY SELECTOR - PYROLYTIC GRAPHITE MONOCHROMATOR - SLITS - CRYOMAGNET - SLITS - BERYLLIUM FILTER - PYROLYTIC GRAPHITE ANALYSER - ^{3}HELIUM NEUTRON DETECTOR

The outgoing wavevector, $k_f = 1.55\,\text{Å}^{-1}$, has been kept constant across the different experiments since this value was found to be free of unwanted double scattering events (see Chapter 8). At the beginning of each experiment, the sample has always been slow cooled with a 1 K/min rate down to 100 K and afterwards fast cooled. There is no evidence for a cooling-rate dependent electronic ground state in these samples, as it is the case of oxygen-doped La_2CuO_{4+y} [136]. The reason for employing this cooling method is to ensure consistency over different experiments and samples. At ThALES, the energy resolution (ΔE) is on average $\sim 3\%$ of the incoming neutron energy [137], meaning $\Delta E \sim 0.15$ meV in elastic condition and increases up to ~ 0.3 meV depending on the energy transfer employed. In the standard focusing condition, which we have used, the momentum resolution $\Delta \sim 0.02\,\text{Å}^{-1}$ [80].

Low-energy fluctuations have been studied under different conditions by performing constant k scans around the $(0, 1, 0)$ reciprocal space position. Even though the incommensurability of the peaks is very small in this doping regime, we were able to distinguish two peaks in our patterns. All data has been fitted with the same Gaussian model with constrained equal amplitudes and widths for the two peaks. The data has then been normalised using the procedure proposed by G. Xu *et al.* [138] and explained in great detail in Appendix A. This normalisation allowed us not only to combine data from different experiments but also to make a direct quantitative comparison between magnetic susceptibilities of samples of different doping.

High-energy magnetic excitations have been studied under applied magnetic field at IN8. The instrument configuration used during this experiment has been the following:

SILICON111 MONOCHROMATOR - SLITS - CRYOMAGNET - SLITS - PYROLYTIC GRAPHITE FILTER - PYROLYTIC GRAPHITE ANALYSER - ^{3}HELIUM NEUTRON DETECTOR

Note that, in this configuration, Beryllium filters are not necessary since the Si111 monochromator does not allow second order contamination of the signal [139]. Additionally, the choice of monochromator is justified by the increased energy resolution and access to a broader incident energy range [140]. All of this was essential in our case as we set out to map the influence of an applied magnetic field on high-energy magnetic fluctuations, and a variation in energy resolution (induced by a change of the monochromator or the outgoing wavevector during the experiment) would make it difficult, if not impossible, to distinguish such small effects. Spatial constraints in the experimental zone forced us to measure the magnetic signal in the second Brillouin zone around $(1, 2, 0)$ as exemplified in Figure 5.2.2(a). We were able to use one single

outgoing wavevector, $k_f = 4.1 \, \text{Å}^{-1}$, for all the scans performed with energy transfer between 5 and 50 meV. The energy resolution for this outgoing wavevector is however considerably high (~ 6 meV) meaning that at low-energy transfers the signal is contaminated by the tail of the elastic line. As it can be observed in Figures 5.2.2(b) and (c), when a smaller $k_f = 2.662 \, \text{Å}^{-1}$ is used, reducing thus the resolution ellipsoid, the field effect apparent at the higher $k_f = 4.1 \, \text{Å}^{-1}$ disappears. The lowest energies 5 and 7.5 meV have thus been measured with the smaller k_f as well.

At IN8, due to additional spurious scattering and poorer Q-resolution, the incommensurate peaks are not distinguishable. For this reason the data has not been fitted but rather a point by point subtraction between high field and zero field scans has been used in the analysis. We found this method to be more appropriate as we made sure the subtraction pattern was featureless and no single model could be used to consistently fit all the scans (all the scans are presented in Appendix B). Additionally, the acoustic phonon (which we map through constant-energy scans) used in the normalisation process to determine the resolution volume could not be measured on the thermal spectrometer. At 2 meV, the energy at which we have consistently recorded the two phonon branches in all ThALES experiments, and also at 5 meV, on IN8, due to a high resolution volume, the two branches are indistinguishable. We have also tried to measure at higher energies, such as 10 meV, but with no success as it seemed that the phonon branches have already flattened.
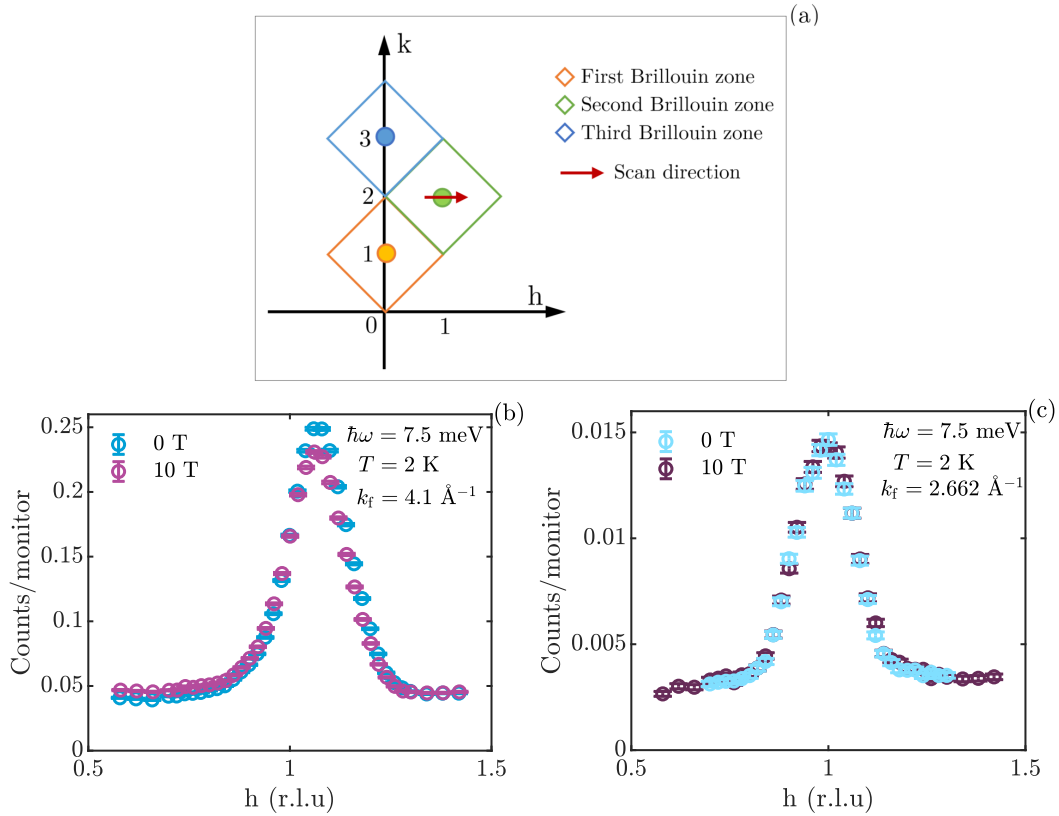
Figure 5.2.2: (a) Graphical representation of the three first Brillouin zones in reciprocal space including the scan direction employed during the IN8 experiment. **(b)** Inelastic scans as a function of applied magnetic field taken in the second Brillouin zone at 2 K and with $k_f = 4.1 \, \text{Å}^{-1}$. **(b)** The same inelastic scans as in subfigure (b) only this time recorded with $k_f = 2.662 \, \text{Å}^{-1}$.

5.2.2   *Results and discussion*

The first task has been to confirm the 45° rotation of the stripe signal outside the superconducting dome. For this reason we have performed a grid scan around the antiferromagnetic $(0,1,0)$ reflection. Indeed, the data shown in Figure 5.2.3(a) indicates that the signal is elongated h and k orthorhombic axis. Cuts through the grid further confirm the higher probability of distinguishing a two-peaks pattern along $(0,1\pm\delta,0)$ than along $(\pm\delta,1\pm\delta,0)$ (see Figure 5.2.3(b)). All the rest of the scan have been performed along the first direction.
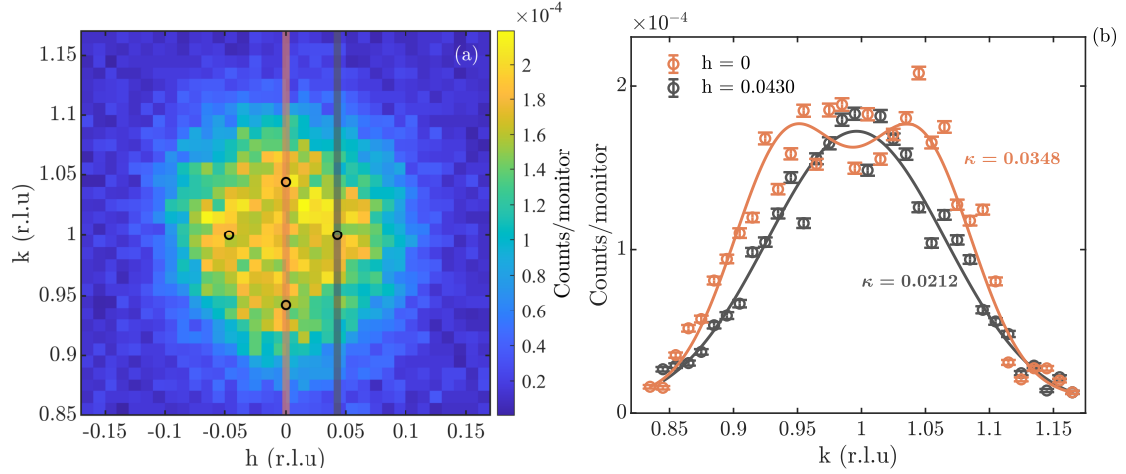
Figure 5.2.3: (a) Constant energy map of the inelastic magnetic signal with $\hbar\omega = 0.8$ meV measured at 40 K in the absence of applied magnetic field. The vertical lines show the direction of the two-dimensional scans presented in subfigure (b). The circles indicate centres of the four incommensurate peaks obtained through Gaussian fitting of scans along $(0,k,0)$ and $(h,1,0)$. **(b)** Two-dimensional cuts though the grid along $(0,k,0)$ (in orange) and $(0.43,k,0)$ (in grey). The solid lines represent the Gaussian fits to the data (single Gaussian in grey and double Gaussian with constrained equal amplitudes and widths in purple). The half width value at half maximum (HWHM $= \kappa$) in r.l.u. is also included in the figure for both directions.

As explained before in the introduction of this chapter, one of the signs of the emergence of superconductivity is the opening of a spin gap in the magnetic excitation spectrum. The effect of an applied field is then to create a vortex lattice in the sample which favours low-energy fluctuations, thus filling the gap. One of our main aims has been to study and understand the influence of an applied magnetic field on the magnetic structure of a non-superconducting sample without a SC phase to be destroyed in the core region of the vortices. For this purpose we have measured low-energy (≤ 5 meV) magnetic excitations at low (2 K) and high (40 K) temperature both in the absence and presence of a 10 T applied magnetic field. The data is summarised in Figure 5.2.4(a). Interestingly enough we have discovered that an applied magnetic field tends to suppress very low-energy fluctuations (< 2 meV) at low temperature (2 K). Even more intriguing is maybe the fact that the field has no effect at higher temperatures (40 K). At the same time, the only known change taking place in between is the onset of the spin-glass phase ($T_{\mathrm{g}} \sim 4.6$ K as measured by μSR [45] and $T_{\mathrm{N}} \sim 15$ K as measured by neutron scattering [47]). From the temperature dependence of the field effect, depicted in Figure 5.2.5(b), we can see that indeed the suppression of low-energy fluctuations seems to correlate with the onset of magnetic order below ~ 20 K. However, unlike the case of superconducting samples, where fluctuations are slowed down in the presence of an applied magnetic field, no additional increase of spectral weight has been observed in the elastic channel. Figure 5.2.6 shows the clear suppression of the 0.8 meV fluctuation under applied magnetic field concomitant with an unaffected magnetic order signal. However, it should be noted though that, from the same figure, it is also clear that this sample has a very well-developed magnetic order (the strongest we have measured in the highly underdoped region as it will become evident in the following sections) and the field effect reduction in low-energy spectral weight is of small magnitude in comparison with the strength of the elastic signal. It is thus possible that the small change might be concealed by the errorbars or it might occur in the quasi-elastic channel. Another possibility, though somewhat unlikely since the interaction energy of the spins with field is only about 2 meV, is that the spectral weight shifts to higher energies. For this reason we have also explored the field dependence of fluctuations below and above the resonance ($E_{\mathrm{cross}} \sim 20$ meV [118]). Figure 5.2.4(c) confirms that no significant field effect occurs at higher energies. As noted before the lowest energy measurements are more accurate when performed with a lower k_{f} value since this reduces the contamination of the signal, by the elastic line, by decreasing the size of the resolution ellipsoid.

In terms of correlation length, the half width at half maximum, presented in Figure 5.2.4(b), which is inversely proportional to the dynamic spin correlation length [47] indicates that magnetic excitations and the associated magnetic order are long range with *the lower bound of the resolution limited* correlation length $\xi \sim 50$ Å.

Another consequence of the absence of a superconducting phase is of course the lack of an upper critical magnetic field. When following the inelastic signal as function of varying applied magnetic field we observed that the suppression effect saturates already at ~ 5 T (see Figure 5.2.5(a)). This value is consistent with our findings on other superconducting samples as we shall see next. The question then arises, what exactly happens at this field value? In order to begin to formulate an answer we first need to look into whether this is a particularity of non-superconducting samples or if doped crystals withing the superconducting dome present similar behaviours.
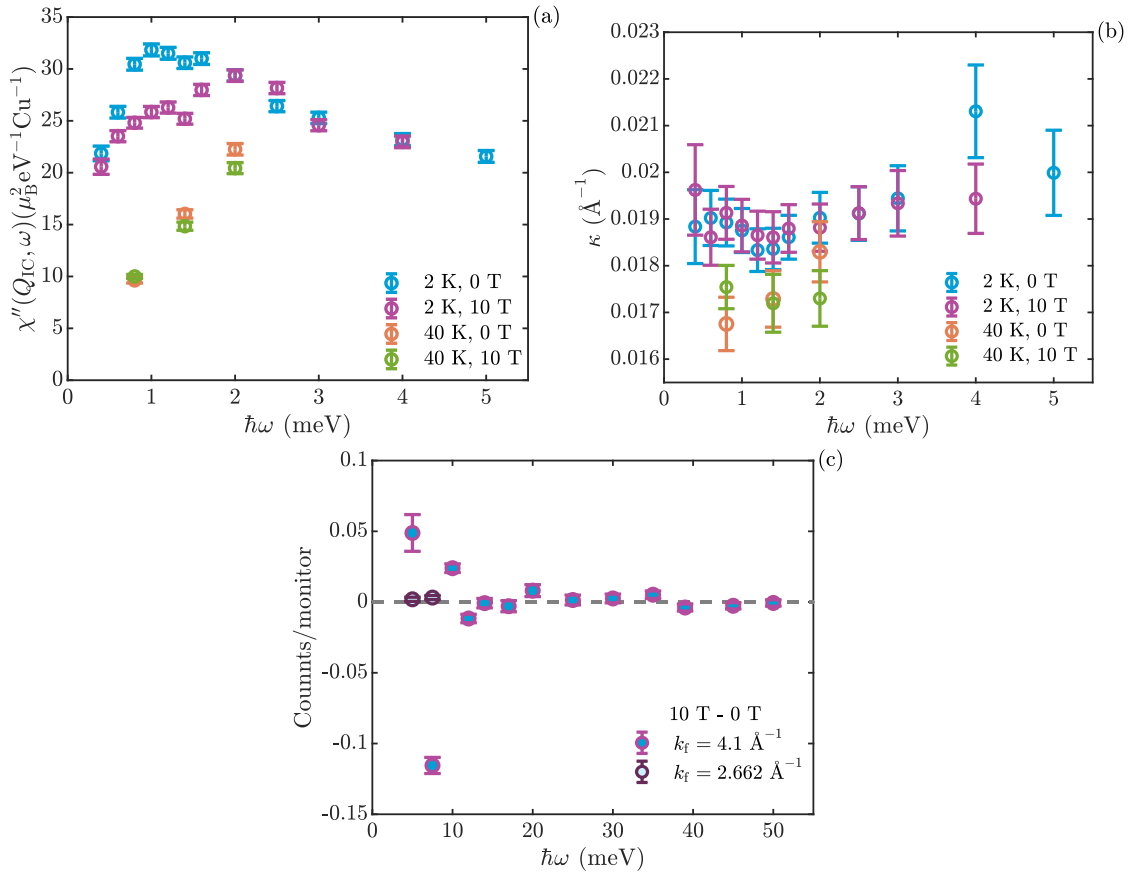
Figure 5.2.4: (a) Dynamic susceptibility $\chi''(Q_{IC}, \omega)$ measured at 2 K (circles in blue at zero field and purple in 10 T applied magnetic field) and at 40 K (circles in orange at zero field and green in 10 T applied magnetic field). **(b)** Half width at half maximum of the magnetic peaks at $(0, 1 \pm \delta, 0)$ as a function of energy transfer, varying temperature and applied magnetic field. The parameters are obtained from the Gaussian fits with constrained equal amplitude and widths in for the two measured peaks. **(c)** Variations of the intensity of high-energy fluctuations as a function of applied magnetic field measured at 2 K. A point by point subtraction of scans taken in 10 T applied magnetic field and zero field has been employed.

Figure 5.2.5: (a) Dynamic susceptibility $\chi''(Q_{IC}, \omega)$ of 0.8 meV magnetic fluctuations measured in the superconducting phase as a function of increased magnetic field. **(b)** Temperature dependence of 0.8 meV magnetic fluctuations with and without applied magnetic field.
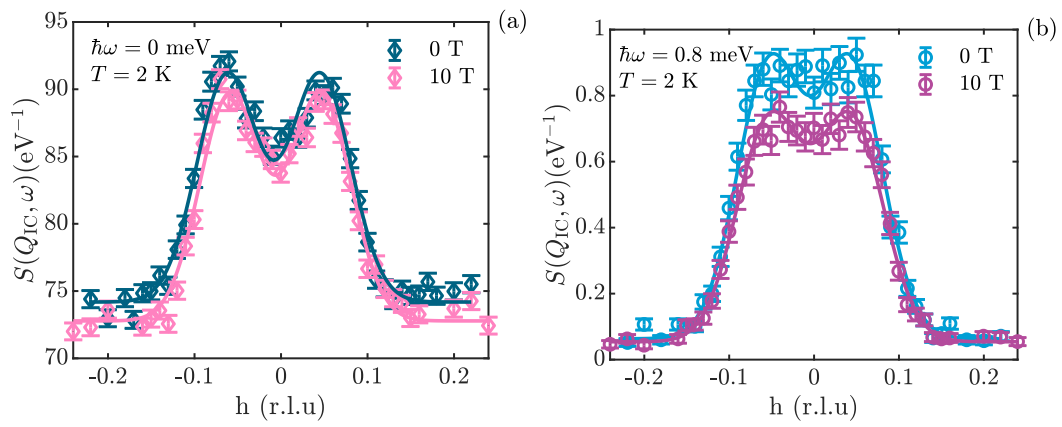
Figure 5.2.6: Dynamic spin correlation[a] $S(Q_{IC}, \omega)$ of both **(a)** elastic and **(b)** inelastic signals measured at 2 K with and without applied magnetic field. The solid lines are Gaussian fits explained in the text.

---

[a] Dynamic susceptibility $\chi''(Q_{IC}, \omega)$ is obtained by Bose normalisation of the dynamic spin correlation $S(Q_{IC}, \omega)$.

5.3 LSCO 6%

5.3.1 *Experimental method and sample*

In the case of our $La_{1.94}Sr_{0.06}CuO_4$ (LSCO6) crystal the main aim of the research has been to study the magnetic structure across the phase transition from the superconducting to the normal state by applying a magnetic field higher than the upper critical one (H_{c2}). This is our only sample of the series where such an experiment is possible with the current sample environments available as $H_{c2} = 16$ T for a similarly doped $x = 0.063$ LSCO samples [141]. We have thus performed a neutron scattering experiment on ThALES using the 15 T vertical field cryomagnet. The instrument configuration and fitting routine are exactly the same as the ones described above for the LSCO5 sample. Contrary to the LSCO5 experiments where we have performed constant h scans though the antiferromagnetic point due to the 45° rotation of the pattern, in the case of this crystal and the following superconducting samples we have employed diagonal scans through the peaks of the form $(1 \pm \delta, 0 \pm \delta, 0)$ or $(1 \pm \delta, 0 \mp \delta, 0)$. The reason for choosing this type of scan is the fact that diagonal peaks originate from the same twin domain (see Chapter 6 for a detailed description and graphical representation, in Figure 6.5.1, of the twinning pattern). Since the sample may have twin domains of different sizes, exploring only one of them allows for a fitting routine with less parameters. We are thus able to constrain the amplitudes and widths to equal values for the two peaks which would not have been necessarily true if we were to perform constant h or k scans.
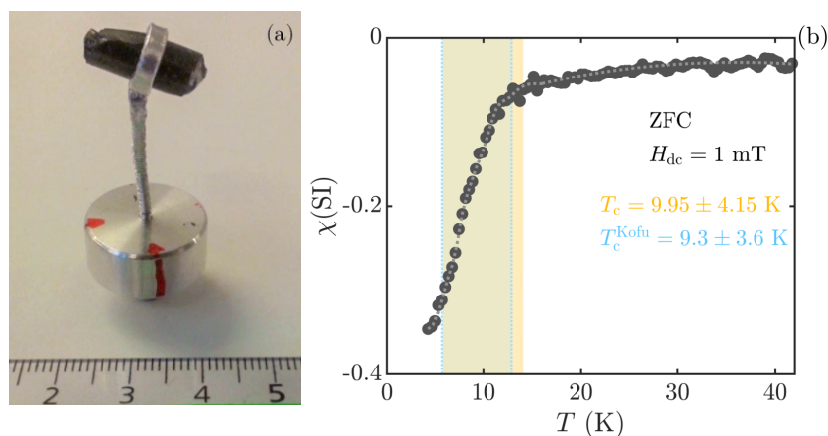
Figure 5.3.1: (a) $La_{1.94}Sr_{0.06}CuO_4$ single crystal sample placed inside an aluminium sample holder. This is the exact configuration used throughout all the neutron scattering experiments. **(b)** Magnetic (volume) susceptibility measured while heating the sample in a 1 mT applied magnetic field preceded by zero field cooling (ZFC). The shaded yellow area indicates the width of the superconducting transition spanning from 90% to 10% of the normal state susceptibility. The superconducting critical temperature is then defined as the mid value within this width. The blue shaded area indicates the superconducting transition of a $x = 0.065$ LSCO sample [47]. In this case the critical temperature is the mid value between the normal and superconducting state extrapolated to $T = 0$ K. The width is then defined by the onset temperature, meaning the temperature corresponding to the first point, in the susceptibility measurements, drifting away from the zero value expected in the normal state. The dotted light grey line is only a guide to the eye.

The crystal used is pictured in Figure 5.3.1(a), measures 1.5 cm in length and 0.5 cm in diameter and weighs $\sim$ 2.36 g. Previous measurements of the phase transition temperature between the

high-temperature tetragonal and the low-temperature orthorhombic one revealed a transition temperature $T_s = 382 \pm 1$ K corresponding to a doping level $x = 0.0664 \pm 0.0006$ [142]. Magnetic susceptibility measurements display as well a superconducting critical temperature very similar to other samples from the literature with strontium doping $x = 0.065$ (see Figure 5.3.1(b)). The critical temperature of our sample is $T_c = 9.95 \pm 4.15$ K, where the uncertainty is defined by the 10%-90% criterion [143] as spanning between 10% and 90% normal state susceptibility.

5.3.2 *Results and discussion*

Low-energy fluctuations have been measured in the superconducting phase, at 2 K, without applied magnetic field and in a field of 14.9 T very close to the upper critical field value. The data is shown in Figure 5.3.2(a). The first feature to remark is that, similar to other underdoped superconducting samples [130] and unlike optimally doped LSCO [124], the fluctuation spectrum is not gapped to the lowest energy measured 0.4 meV. Additionally, just like LSCO5, the effect of an applied magnetic field is to suppress low-energy fluctuations. Even though we have used the highest magnetic field value available the influence is already saturating at ~ 10 T as the field dependence of 0.8 meV excitations suggests (see Figure 5.3.3(a)). Nonetheless, it is clear from the temperature vs field comparison, shown in Figures 5.3.3(a) and (b) as individual scans, that 14.9 T is probably not enough of a magnetic field to drive the sample outside the superconducting state. A temperature higher than T_c has a greater suppression effect than a 14.9 T applied magnetic field. It should be noted though that the temperature dependence of magnetic fluctuations in the cuprates shows some interesting features that are still to be understood. For example an increase in intensity at temperatures around 30 K has been observed in LSCO samples with $x = 0.12$ [114] and in oxygen-doped LCO+O samples [144, 145]. What we can infer from our data is that the magnetic states reached by field or temperature are not the same. *One possible cause for the discrepancy could be the presence of a vortex lattice under* 14.9 *T field and its absence at temperatures above* T_c.

Figure 5.3.2: (a) Dynamic susceptibility $\chi''(Q_{IC}, \omega)$ measured in the superconducting phase, circles in blue at zero field and purple in 14.9 T applied magnetic field. **(b)** Half width at half maximum as a function of energy transfer and applied magnetic field. The parameters are obtained from the Gaussian fits with constrained equal amplitude and widths for the two measured peaks.
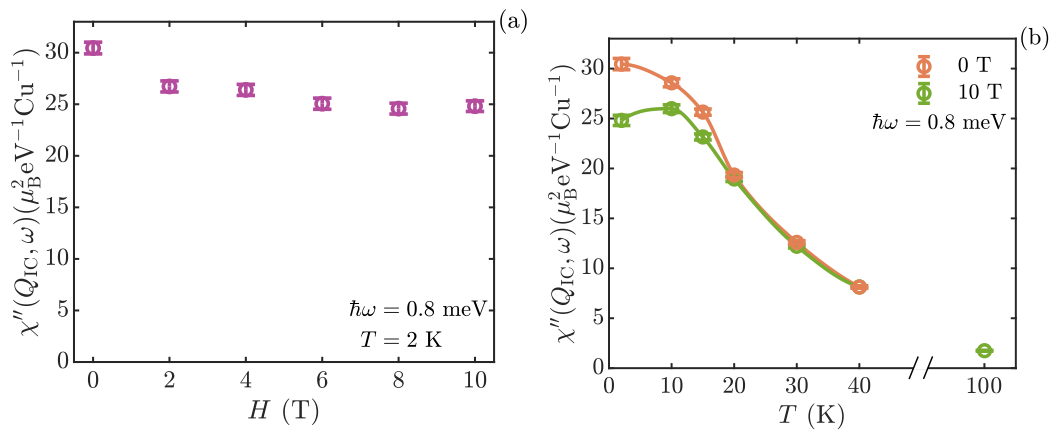
Figure 5.3.3: (a) Dynamic susceptibility $\chi''(Q_{IC}, \omega)$ of 0.8 meV magnetic fluctuations measured in the superconducting phase as a function of increased magnetic field but also outside the superconducting dome at 20 K without applied magnetic field. **(b)** Q-scan through the incommensurate peaks with constant energy transfer 0.8 meV. The data was acquired under different conditions inside the superconducting phase without (in blue) and with (in purple) an applied magnetic field and outside the superconducting phase in zero field (in orange). The solid lines are Gaussian fits with constrained equal amplitude and widths for the two peaks.
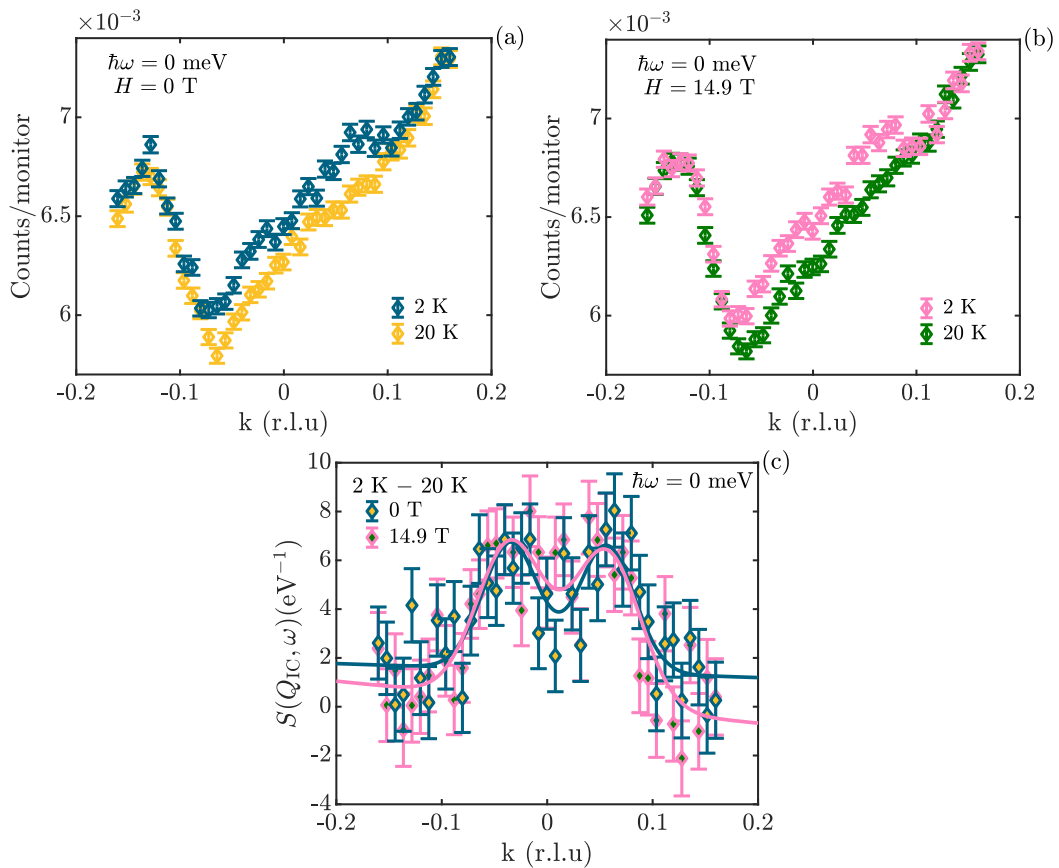
Figure 5.3.4: Q-scans through the incommensurate peaks in elastic condition. The data was recorded both inside and outside the superconducting dome in **(a)** zero applied magnetic field and **(b)** under 14.9 T applied magnetic field. **(c)** The subtracted high and low temperature scans are presented as a function of applied magnetic field. The solid lines are Gaussian fits to the data explained in the text.

The elastic signal has proven more difficult to measure due to additional spurious signal. Figures 5.3.4(a) and (b) show the raw data scans performed both with and without applied magnetic field. Because the elastic signal is expected to persist only up to $T_{\mathrm{N}} \sim 11$ K [45] we have used the measurements performed at 20 K as the background of our genuine elastic stripes signal. Figure 5.3.4(c) depicts the purely elastic signal obtained by a point by point subtraction of the data recorded at 20 K from the ones recorded at 2 K. No clear sign of a field effect can be distinguished in our data. We are thus once again, as in the case of LSCO5, in doubt whether magnetic fluctuations slow down in the presence of an applied magnetic field in this doping regime as it is the case of higher doping.

In terms of the extent of magnetic order and the associated fluctuations we observe a similar correlation length to LSCO5 $\xi \sim 60$ Å (see Figure 5.3.2(b)). The absolute normalisation of the data also allows us to compare the intensity of the signals across different samples. In comparison to the non-superconducting LSCO5 sample, the LSCO6 displays spectral weights reduced by approximately one half in both the elastic and inelastic channels. This could be a indication that the emergence of superconductivity claims half of the electrons which were otherwise involved in the magnetic order. At the same time, the fact that both the elastic and inelastic channels are reduced by a similar magnitude points to a common electronic origin of the two signals.

5.4 LSCO 7%

5.4.1 *Experimental method and sample*

In order to study the magnetic order and associated low-energy fluctuations, two neutron scattering experiments have been performed at ThALES on our $La_{1.93}Sr_{0.07}CuO_4$ sample. The sample, depicted in Figure 5.4.1, measures 1.7 cm in length and 0.6 cm in diameter and weighs ~ 3.4 g. Previous measurements on the transition temperature between the HTT phase and the LTO phase revealed a $T_s = 362 \pm 1$ K corresponding to a doping level $x = 0.0753 \pm 0.0003$ [142]. Magnetic susceptibility measurements confirmed the emergence of a superconducting phase with a critical temperature $T_c = 9.75 \pm 3.75$ K (see Figure 5.4.4(f)). In this case as well the width of the transition was determined using the 10%-90% criterion.
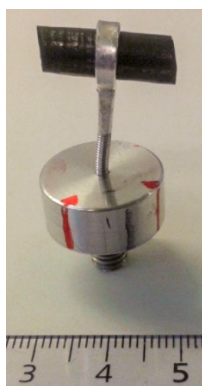
Figure 5.4.1: $La_{1.93}Sr_{0.07}CuO_4$ single crystal sample placed inside an aluminium sample holder. This is the exact configuration used throughout all the neutron scattering experiments.

The two scattering experiments have been performed inside a 10 T vertical field cryomagnet in the same configuration as described above. For consistency, the same fitting routine and normalisation procedure have been applied to the data in this case as in the above-mentioned analysis. The only exception is the field and temperature dependence of the elastic signal, displayed in Figure 5.4.4(a). As in the case of our LSCO6 sample, the elastic signal was covered by an increased spurious background. This made it necessary to perform scans with high statistics (high counting times) and subtract the measurements taken at $T = 40$ K $> T_N$ (as exemplified in Figure 5.4.4(b)). However, time constraints did not allow us to perform such detailed scans at all temperature and we have thus chosen to only measure the intensity on top of one of the incommensurate peaks as a function of increased temperature and applied magnetic field. Afterwards, the background level intensity at 40 K has been subtracted from each measurement.

5.4.2 *Results and discussion*

The applied magnetic field and temperature effects on low-energy magnetic fluctuations are summarised in Figure 5.4.2(a). We again observe a field suppression of excitations of energy $\hbar\omega < 2$ meV in the superconducting phase. This is again accompanied by a lack of a field effect at temperatures $T > T_c$ as we have observed for the other samples. The data presented in Figure 5.4.2(a) has been recorded over two separate beamtimes as indicated in the legend. Even though the normalisation process is performed consistently in the same way, small errors, arising

for example from the fitting of the data or the acoustic phonon used to account for the sample mass in the beam and possible misalignment, make it very difficult to account for such small effects in data acquired at different times. For this reason it was necessary to further normalise one of the data sets, the one recorded during the second experiment including mainly measurement of magnetic excitations under 2.5 T applied magnetic field. Because we have remeasured the zero field and 10 T applied field in the second experiment (shown in the figure in dark blue and pink circles respectively), we have used the zero field data point as a benchmark and used a multiplication by a constant value (0.87 to be precise) in order to force it overlap to the same data point recorded in the first experiment. Afterwards the same constant was used to multiply all the rest of the data. By doing this we were able to confirm that fluctuations are gradually suppressed by an increased value of a magnetic field even though the rate of suppression seems to be energy dependent. For example, at 0.6 meV, 2.5 T and 10 T applied magnetic fields have the same effect while this is clearly not the case at higher energies such as 0.8 meV. However, given the fact that the data was not acquired at the same time in fully identical conditions it is safer to refrain from drawing any conclusions when it comes to such small variations (see Figure 5.4.4(d) for an example of constant energy Q-scans which exemplify the magnitude of the effect). Nonetheless, the more complete field dependence of 0.8 meV excitations, depicted in Figure 5.4.3, does indeed exhibit a gradual suppression as a function of increased applied magnetic field data saturates at ~ 5 T.
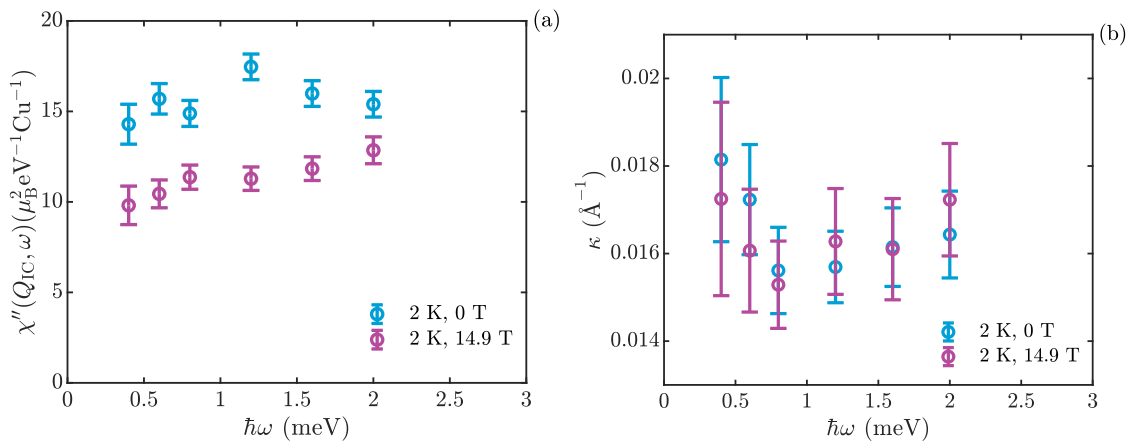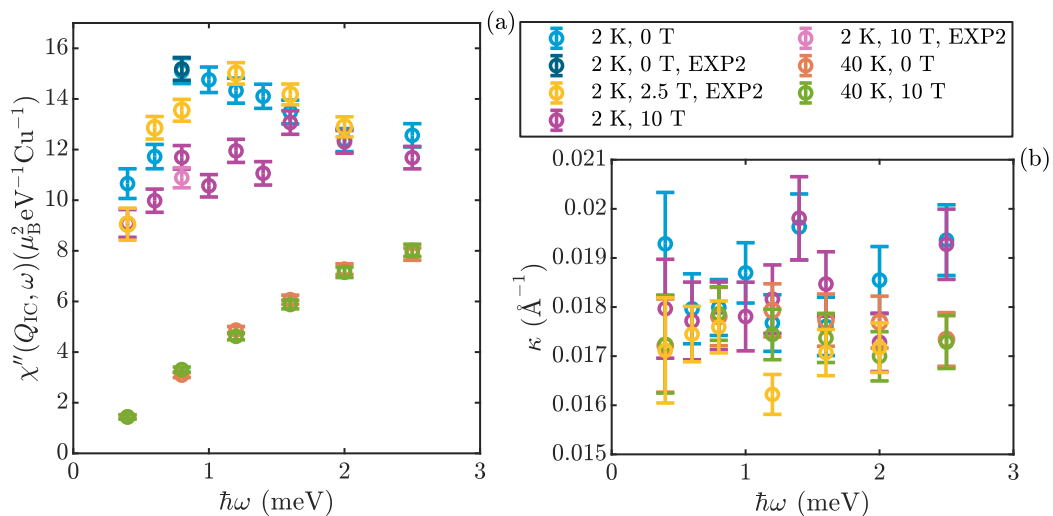

Figure 5.4.2: (a) Dynamic susceptibility $\chi''(Q_{\mathrm{IC}}, \omega)$ measured in the superconducting phase (circles in blue at zero field, yellow in 2.5 T and purple in 10 T applied magnetic field) and in the normal non-superconducting state (circles in orange at zero field and yellow in 10 T applied magnetic field). The data has been acquired over two separate beamtimes as indicated in the legend. All data points corresponding to the second experiment (EXP2) have been normalised such that the points measured at 0.8 meV without applied magnetic field (light and dark blue circles) overlap. **(b)** Half width at half maximum as a function of energy transfer, varying temperature and applied magnetic field. The parameters are obtained from the Gaussian fits with constrained equal amplitude and widths for the two measured peaks.
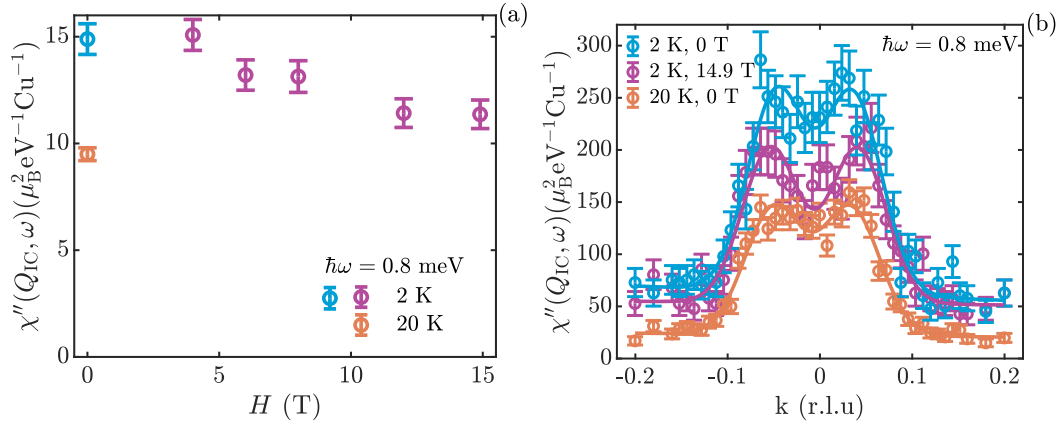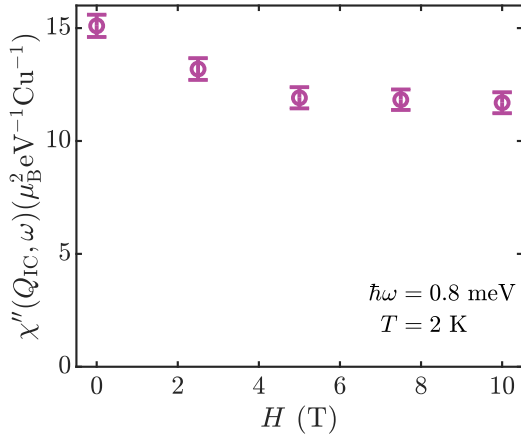
Figure 5.4.3: Dynamic susceptibility $\chi''(Q_{IC}, \omega)$ of 0.8 meV magnetic fluctuations measured in the superconducting phase as a function of increased magnetic field.

What is particular to this sample, in contrast to LSCO5 and LSCO6, is the fact that we have observed a concomitant field-induced enhancement of the magnetic order signal. Figure 5.4.4(b) shows a clear increase of the signal as a function of applied magnetic field. One indication that the same spectral weight is transferred from low-energy fluctuations to even lower ones would be if the two effects would present the same onset temperature. In Figures 5.4.4(a) and (c) we plot the temperature dependence of both the elastic and inelastic with $\hbar\omega = 0.8$ meV channels as a function of applied magnetic field together with the estimation of the superconducting critical temperature as obtained from magnetic susceptibility measurements also shown in Figure 5.4.4(f). Within errorbars the two effects seem to have very similar temperature dependence. This is maybe even more clear in Figure 5.4.4(e) where the difference between the data acquired under 10 T magnetic field and zero field data is plotted against temperature.

Because the elastic data was measured as one point scans it is difficult to accurately estimate the onset temperature of magnetic order. On top of that, estimates from the literature place $T_N \sim 11.2$ K [47] very close to $T_c = 9.75 \pm 3.75$ K making it virtually impossible to conclude whether the transfer of spectral weight correlates with the emergence of superconductivity or magnetic order. Nonetheless, we speculate that the phenomenon we detect is very similar to what happens in optimally doped samples at the formation of the vortex lattice. Namely, we observe a slowing down of low-energy magnetic fluctuations towards the elastic line, which as we know in the case of neutron scattering it is rather quasi-elastic also demonstrated by the difference in onset temperature measured by neutrons versus the one measured by μSR. The only thing that differs, as a function of doping, is the energy range of excitations which are involved.

In terms of the extent of magnetic order and the associated fluctuations, we observe similarly long range order as the other samples discussed so far, with a dynamic spin correlation length $\xi \sim$ 56 Å(see Figure 5.4.2(b)). Interestingly enough the spectral weight of both static and dynamic spin stripes is very similar to that of LSCO6 and once again only half of that of the non-superconducting compound of the series LSCO5.
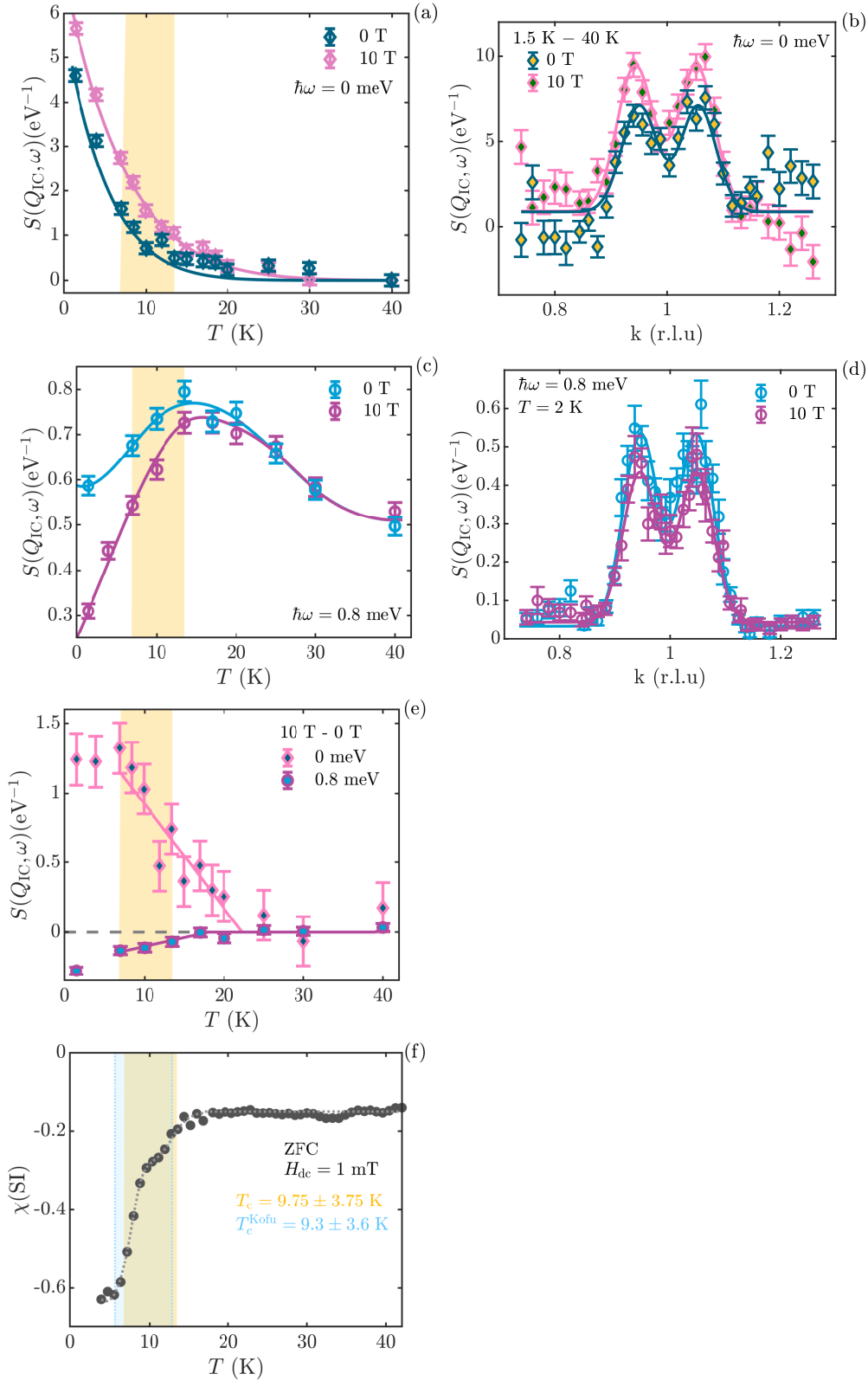
Figure 5.4.4: (a) Dynamic spin correlation $S(Q_{IC}, \omega)$ of magnetic order measured a function of applied field and temperature. The data has been recorded as 1 point scans on the top of the peak at reciprocal space position $(0.93, 0.07, 0)$. Solid lines are guides to the eye. All data has been normalised to the respective values at 40 K. **(b)** Q-scans obtained from the subtraction of high and low temperature scans recorded with and without applied magnetic field. The solid lines are Gaussian fits to the data explained in the text. **(c)** Dynamic spin correlation $S(Q_{IC}, \omega)$ of 0.8 meV magnetic fluctuations measured a function of applied field and temperature. The data was acquired from fitting of full scans to a Gaussian model as exemplified in subfigure (d). The solid lines are guides to the eye. **(d)** Q-scans through the incommensurate peaks with constant energy transfer 0.8 meV as a function of applied magnetic field. The solid lines are Gaussian fits explained in the text. **(e)** Point by point subtraction of 10 T and 0 T presented in subfigures (a) and (c). **(f)** Magnetic (volume) susceptibility measured while heating the sample in a 1 mT applied magnetic field preceded by zero field cooling (ZFC). ΔT_c is determined by the 10% - 90% criterion. The blue shaded area indicates the superconducting transition of a $x = 0.065$ LSCO sample [47]. The dotted light grey line is only a guide to the eye.

5.5   LSCO 8%

5.5.1   *Experimental method and sample*

Our final sample of the series is a $La_{1.92}Sr_{0.08}CuO_4$ (LSCO8) single crystal, pictured in Figure 5.5.1(a), measuring 2.3 cm in length, 0.5 cm in diameter and weighing ~ 5 g. From all the samples analysed in this study, this one exhibits the sharpest transition to diamagnetism as measured by magnetic susceptibility (see Figure 5.5.1(b)). This points to a very high quality sample with a superconducting critical temperature $T_c = 18.1 \pm 1.8$ K. However, since susceptibility measurements are only performed on small pieces cut from the crystals which have been used afterwards in neutron scattering experiments, is it difficult to draw any conclusions on the overall quality of the bulk sample.
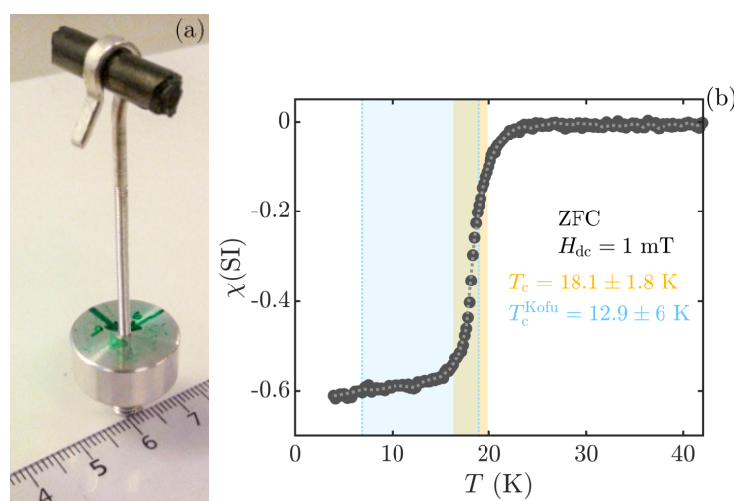
Figure 5.5.1: (a) $La_{1.92}Sr_{0.08}CuO_4$ (LSCO8) single crystal sample placed inside an aluminium sample holder. This is the exact configuration used throughout all the neutron scattering experiments. **(b)** Magnetic (volume) susceptibility measured while heating the sample in a 1 mT applied magnetic field preceded by zero field cooling (ZFC). The shaded yellow area indicates the width of the superconducting transition spanning from 90% to 10% of the normal state susceptibility. The superconducting critical temperature is then defined as the mid value within this width. The blue shaded area indicates the superconducting transition of a $x = 0.076$ LSCO sample [47]. In this case the critical temperature is the mid value between the normal and superconducting state extrapolated to $T = 0$ K. The width is then defined by the onset temperature, meaning the temperature corresponding to the first point, in the susceptibility measurements, drifting away from the zero value expected in the normal state. The dotted light grey line is only a guide to the eye.

Unlike the rest of the data discussed so far, the measurements presented in this section have been performed during my Masters and presented in detail at that time as well [135]. The data is included here as well in order to create a complete picture of the underdoped region of the LSCO phase diagram. Additionally, the data analysis has been redone in order to follow the same procedure as the rest of the experiments.

In contrast with the other superconducting samples, LSCO6 and LSCO7 where diagonal scans thorough the peaks have been preferred, in the case of LSCO8 the data has been acquired through constant h-scans. Figure 5.5.2(a) shows the expected stripes pattern as determined in the literature on a similarly doped LSCO7 sample [99]. One thing to notice is that, due to

the low incommensurability in this doping regime and the resolution limited widths, the stripe pattern appears as a square around the antiferromagnetic reflection rather than four individual well-separated peaks. By performing scans at the two indicated h positions we observe a similar behaviour in our sample. Figure 5.5.2(b) shows a better peak separation at the expense of a small decrease in intensity when the scan is performed through the antiferromagnetic point $(-1, k \pm \delta, 0)$ (in blue) compared to the one passing though the incommensurate position $(-1-\delta, k \pm \delta, 0)$ (in grey). For this reason, all the scans throughout this experiment have been performed in the first configuration. The experiment was performed inside a 15 T vertical field cryomagnet and the same fitting routine employing Gaussians with constrained equal widths and amplitudes used before proved to be most appropriate in this case as well. The reason for that was the slightly lower data quality which benefited from a fitting routine that allows for less fitting parameters. Figure 5.5.4(b) shows an example of fitted inelastic Q-scans.
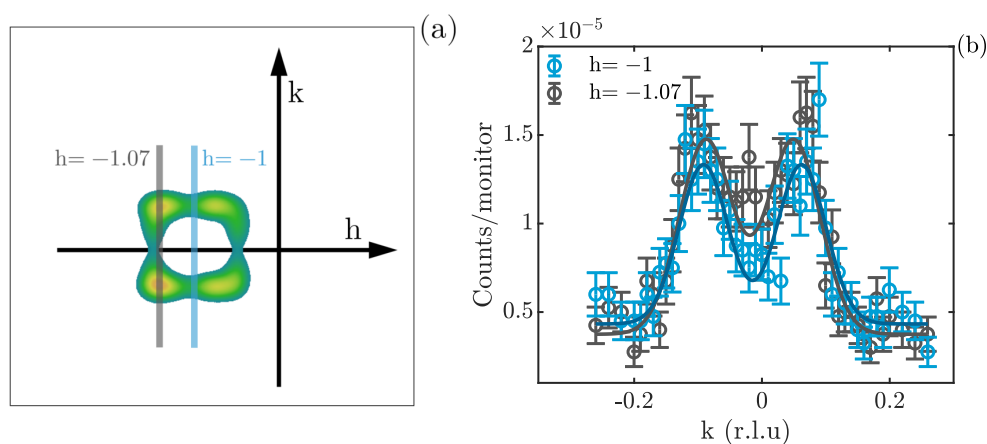
Figure 5.5.2: (a) Graphical representation of the reciprocal space position on which we have focused during the experiment. The signal pattern is reproduced from the literature on a similarly doped LSCO sample with nominal strontium doping $x = 0.07$ [99]. The grey and blue lines indicate the directions of the scans shown in the adjacent subfigure. **(b)** Constant h-scans performed with 0.6 meV energy transfer in the superconducting phase at 1.7 K. The corresponding h values are indicated in the legend. Solid lines are Gaussian fits with constrained equal amplitudes and widths for the two peaks.

5.5.2 *Results and discussion*

It comes as no surprise by now that, in agreement with the other samples discussed so far, the effect of an applied magnetic field in LSCO8 is to suppress the very low-energy fluctuations. In this case excitations below 1 meV are affected as it can be observed in Figure 5.5.3(a). The dynamic spin correlation length is, as well, very similar to previous observations: $\xi \sim 50$ Å(see Figure 5.5.3(b)). The magnitude of the spectral weight of magnetic fluctuation falls in the same regime as the rest of the superconducting samples. This gives us confidence that the reduction in spectral weight by one half is an intrinsic property of samples within the superconducting dome.

The evolution of magnetic fluctuations as a function of increased applied magnetic field, depicted in Figure 5.5.4(a), on the other hand, does not show any clear trend as it has been the case with the other LSCO samples. It should however be noted that a lower energy transfer has been followed in this experiment making a direct comparison difficult.
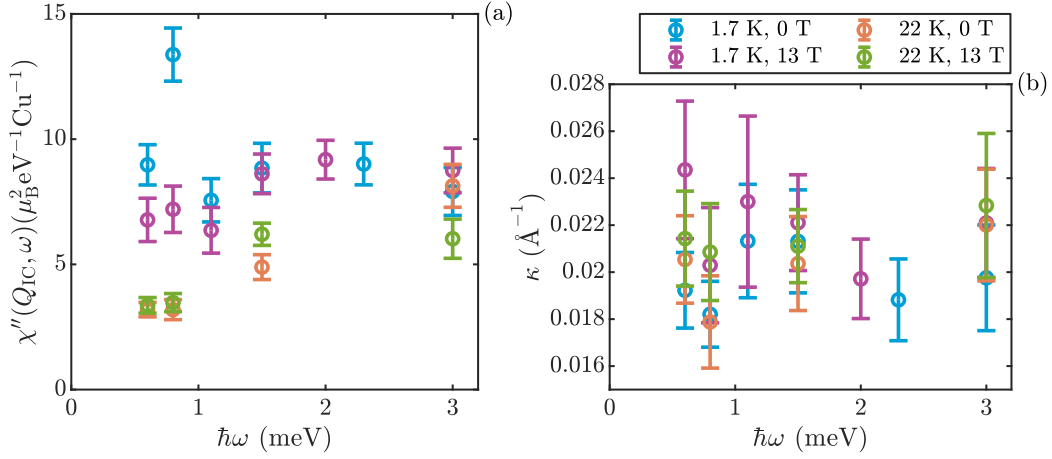
Figure 5.5.3: (a) Dynamic susceptibility $\chi''(Q_{\text{IC}}, \omega)$ measured in the superconducting phase (circles in blue at zero field and purple in 13 T applied magnetic field) and in the normal non-superconducting state (circles in orange at zero field and green in 13 T applied magnetic field). **(b)** Half width at half maximum as a function of energy transfer, varying temperature and applied magnetic field. The parameters are obtained from the Gaussian fits with constrained equal amplitude and widths for the two measured peaks.
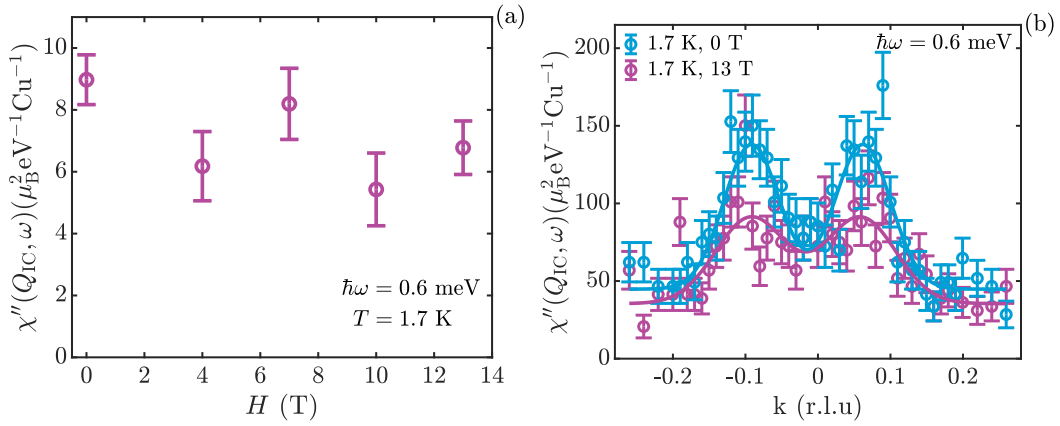
Figure 5.5.4: (a) Dynamic susceptibility $\chi''(Q_{\text{IC}}, \omega)$ of 0.6 meV magnetic fluctuations measured in the superconducting phase as a function of increased magnetic field. **(b)** Q-scans through the incommensurate peaks with constant energy transfer 0.6 meV as a function of applied magnetic field. The solid lines are Gaussian fits explained in the text.

The elastic signal has proven strenuous to distinguish in this sample as well. Unfortunately, in this early experiment, scans at temperatures inside and outside the superconducting dome have not been recorded in a consistent manner. As exhibited in Figure 5.5.5, scans below and above T_c have been performed only with and without applied magnetic field respectively. Consequently, the method of subtracting the high-temperature data, considered to be the spurion-containing background, cannot be applied in this case. This makes it impossible to rule out the possibility of the co-existence of the genuine elastic stripes signal with the spurious signal we have observed before as well. We have thus no clue whether the LSCO8 sample behaves similar to LSCO7 and shows signs of spectral weight shifting towards the elastic channel as a function of applied magnetic field, or on the contrary if elastic stripes are unperturbed by field as it is the case of LSCO6 and LSCO5.
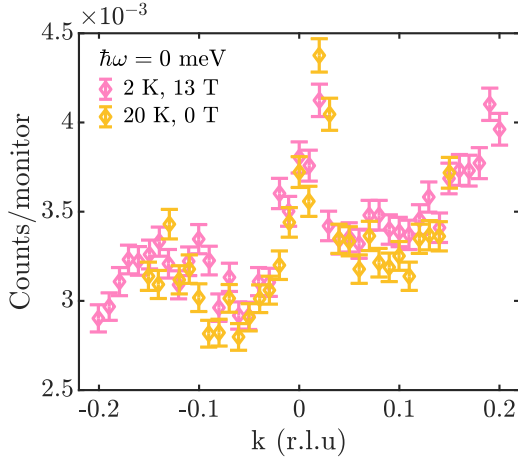
Figure 5.5.5: *Q*-scans through the incommensurate peaks in elastic condition. The data was recorded inside the superconducting dome under 13 T applied magnetic field (pink diamonds) and outside the superconducting phase in zero applied magnetic field (yellow diamonds.)

5.6 CONCLUSIONS AND OUTLOOK

Owing to the normalisation of the data to absolute units we are now able to make a quantitative comparison between the magnetic structures of all our LSCO samples presented in detail in this chapter. Table 2 summarises, as a function of doping, the most important findings of this study. In the second column of the table the superconducting volume fraction of each sample is presented as measured by the magnetic susceptibility measurements. An increase as a function of increased doping can be observed. One should however keep in mind that susceptibility measurements are performed on small sample pieces which are not always representative for the entire bulk of the crystal. The dynamic spin correlation is presented in the third column for measurements performed in elastic condition. The values are obtained as the amplitude of the largest of the incommensurate peaks, background subtracted. The final three columns present the energy integrated dynamic spin susceptibility of magnetic fluctuations measured at 2 K in zero field, high field (10 T for LSCO5 and LSCO7 and 14.9 T for LSCO6) and the difference between the two respectively. The energy integration consisted of the addition of *Q*-integrated susceptibilities measured at specific energies ($\hbar\omega = 0.4$, 0.6, 0.8, 1.2, 1.6 and 2.0 meV).

The first aspect to be noticed is the fact that, both elastic and inelastic signals are drastically suppressed at the onset, as a function of doping, of superconductivity pointing towards a competition between the magnetic and superconducting phases. Secondly, the magnitude of the decrease in spectral weight is very similar when comparing elastic and inelastic channels. Across the transition from a non-superconducting sample (LSCO5) to superconducting ones (LSCO6 and LSCO7) the elastic spectral weight is reduced by $\sim 2/3$ while the inelastic signal decreases by $\sim 1/2$. This is an indication that the magnetic order and fluctuations probably originate from the same phase, which competes with superconductivity, with the possibility that magnetic excitations are the Goldstone modes of the incommensurate AFM order.

In terms of the effect of an applied magnetic field, we have observed very similar field induced suppression, at low temperature, of the low-energy fluctuations regardless of the crystal doping. The fact that the LSCO5 sample exhibits such a behaviour in the presence of magnetic field, without displaying signs of a coherent superconducting phase, has been one of the most puzzling findings of our study. The magnitude of the field induced suppression, shown in the last column

of Table 2, seems to decrease as a function of increased doping (one should keep in mind that the LSCO6 data was collected under a higher applied magnetic field of 14.9 T).

Doping	SCVF	$S(Q_{IC})$ $\hbar\omega = 0$ meV	Energy integrated $\chi''(Q_{IC}, \omega)$ for $\hbar\omega = 0.4-2$ meV		
			0 T	high field (10 T or 14.9 T)	no field−high field
$x = 0.05$	0	~ 17.05	170.03 ± 1.44	152.53 ± 1.41	17.50 ± 2.01
$x = 0.06$	35%	~ 5.64	93.72 ± 1.99	67.59 ± 1.89	26.13 ± 2.74
$x = 0.07$	63%	~ 6.24	77.66 ± 1.22	68.08 ± 1.16	9.58 ± 1.68

Table 2: The superconducting volume fraction (SCVF) is extracted from the magnetic susceptibility measurements and corresponds to the value of the susceptibility extrapolated to $T = 0$ K. The elastic dynamic spin correlation ($S(Q_{IC}, \omega = 0)$) measured at 0 T is calculated as the amplitude of the highest of the two incommensurate peaks in the scan background subtracted. It should be noted that the measurements on LSCO6 and LSCO7 are obtained by subtracting the data collected outside the superconducting phase at 20 K and 40 K respectively. The values of the dynamic susceptibility ($\chi''(Q_{IC}, \omega)$) at 2 K under different applied magnetic field conditions have been determined as point by point addition of the values measured at $\hbar\omega = 0.4, 0.6, 0.8, 1.2, 1.6$ and 2 meV. The LSCO5 and LSCO7 high field data was measured under 10 T field while for LSCO6 a 14.9 T field was used.

Similar to the last column of the table, the spectral weight loss at 2 K is also represented in Figure 5.6.1 for all measured energies. What can be observed additionally is the fact that the onset of the field effect, for LSCO5 and LSCO7, is the same ~ 1.5 meV. All these similarities point to a picture in which all samples, superconducting or not, exhibit a common electronic phase at low temperatures which is at the origin of the applied magnetic field effect in underdoped LSCO.
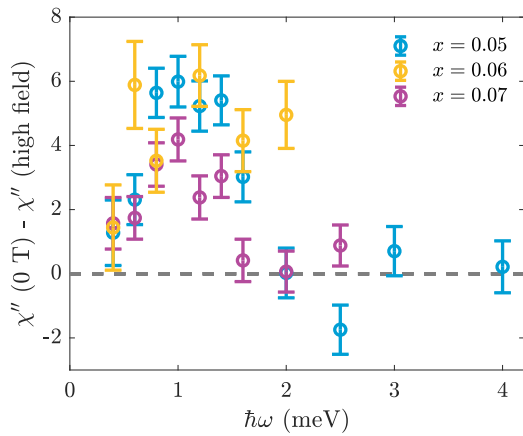
Figure 5.6.1: Calculated spectral weight loss induced by an applied magnetic field presented as a function of energy and sample doping. The dynamic susceptibility measured at 10 T (in LSCO5 and LSCO7) and at 14.9 T (in LSCO6) has been subtracted from the zero field measurements. All the data has been measured at 2 K and has been presented in the Results section above.

Measurements performed at high temperature (40 K) reveal however some differences between non-superconducting LSCO5 and superconducting LSCO7. Figure 5.6.2(a) shows the intensity of magnetic fluctuations measured at 40 K for various energies in the two samples with and without applied magnetic field. While both samples show no sign of a field effect at this temperature, the magnitude of fluctuations is rather distinct. In the absence of superconductivity, the reduced spectral weight in the LSCO7 sample is intriguing. However, as we have seen before, at base temperature the two exhibit different magnitudes of low-energy fluctuations spectral weight with an approximate ratio of 1:2 (LSCO7:LSCO5) which is preserved at high temperature. We have also looked into the relative variation of magnetic fluctuations as a function of temperature and field. Figure 5.6.2(b) shows the point by point subtraction of high temperature data from the low temperature one with and without applied magnetic field. Since there is no significant field effect at high temperature this data mimics the field induced suppression observed at 2 K.

It comes then as no surprise that in order to conserve the 1:2 ratio the decrease of LSCO5 as a function of temperature is twice as large as that of LSCO7. This is what Figure 5.6.2(b) reflects.
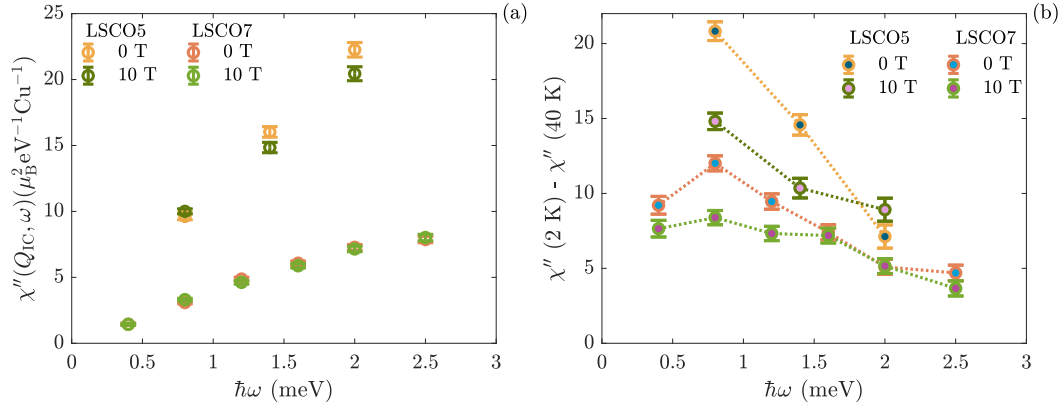
Figure 5.6.2: (a) Dynamic susceptibility $\chi''(Q_{IC}, \omega)$ of magnetic fluctuations measured at 40 K as a function of increased magnetic field in both non-superconducting LSCO5 and superconducting LSCO7 samples. **(b)** Point by point subtraction of high temperature (40 K) dynamic susceptibility from the low temperature data (2 K) as a function of energy and applied magnetic field measured in LSCO5 and LSCO7. The dashed lines are guides to the eye.

As exposed in the introduction of this chapter, two types of order have been proposed in order to explain the relationship between magnetic order, and associated fluctuations, and superconductivity. Certain cuprates form a uniform d-wave superconducting phase that co-exists with a magnetic phase which exhibits gapped excitations. In this scenario the effect of an applied magnetic field is to locally destroy superconductivity by creating a vortex lattice which in turn favours the emergence of sub-gap fluctuations and even magnetic order. The incompatibility between magnetic order and low energy fluctuations (which are pair-breaking in nature) and uniform d-wave superconductivity has also been predicted theoretically [146]. The optimally doped LSCO samples are the perfect example for such a phase.

The second interpretation focuses on superconductors which exhibit magnetic order already in zero field, such as underdoped LSCO or LBCO. In this picture magnetic order, and the associated low-energy fluctuations, and superconductivity are spatially intertwined forming the so-called pair density wave. Some trademarks of PDW are the absence of both a spin gap and the neutron resonance. As a consequence, the spin excitation spectrum is remarkably similar to that of a non-superconducting sample in the presence of striped spin and charge order [66]. Underdoped LBCO has been at the centre of this theory [64, 147].

The data we have presented so far seems to support the pair density wave scenario for a number of reasons. First of all, the puzzling very similar field effect on low energy fluctuations in superconducting and non-superconducting samples can be explained as an effect taking place within the CuO$_2$ planes. It has previously been shown, in LBCO, that in-plane two-dimensional superconductivity sets in at the same time as SDW order at temperatures higher than T_c [147]. We therefore speculate that, since the LSCO5 sample exhibits magnetic order, two-dimensional superconductivity is already present at a doping outside the superconducting dome. Following the PDW interpretation, bulk three-dimensional superconductivity is not achieved in LSCO5 due to the frustrated nature of the interlayer Josephson coupling induced by the change of sign of the superconducting order parameter with the same period as the SDW. On the other hand,

this also implies that the stripes have an orthogonal orientation in adjacent planes similar to LBCO when in the low-temperature-tetragonal phase. It would thus be worth determining the stripe orientation in both superconducting and non-superconducting samples in the future by means of, for example, high-energy–photon diffraction [148]. In the case of orthogonal stripes in consecutive CuO_2 layers, a sinusoidal signal with a period c should be observed.

Within this proposed picture, the effect of an applied magnetic field perpendicular to the CuO_2 layer would be to locally destroy the 2D superconducting phase. But how would one be able to observe such an effect by measuring the magnetic structure? Similar to uniform d-wave superconductivity, we argue for a spectral weight shift, as a function of field, from very low fluctuations (< 1.5 meV) towards the elastic or quasi-elastic order. We have unfortunately not been able to distinguish spectral weight increase in the elastic channel of our measurements probably due to a combination of very intense magnetic order signal and small field suppression of the inelastic signal (amounting to a modest spectral weight transferred in comparison to the strength of the elastic signal). One particularity of the spectral weight shift which we have observed in our experiments and associate with a PDW scenario is the fact that the onset of the field effect (~ 15 K see Figure 5.2.5(b)) coincides with the onset of SDW-order (~ 15 K [47]). In contrast, the field induced spin gap filling in a uniform d-wave SC phase correlates with the onset of superconductivity.

On the same note, recent μSR and magnetic susceptibility measurements performed under stress on an underdoped LBCO crystal with $x = 0.115$ [91] have revealed an interesting interplay between magnetic order and superconductivity. In the superconducting sample used in that study the onset of the diamagnetic response, as measured by AC susceptibility, was correlated with the emergence of 2D superconductivity while the mid point of the measurement was associated with the emergence of 3D superconductivity. Our magnetic susceptibility measurements performed in the absence of applied stress on the LSCO5 sample do not show such features. It should however be mentioned that no particular sample and field orientation has been used in the experiment as no superconducting traits were expected to be observed at that moment. A more careful study of the diamagnetic response for better aligned fields both in-plane and along the c-axis would be required. Alternatively, a study of the in-plane resistivity in comparison to out-of-plane measurements has the potential to reveal the presence of 2D SC in our sample.

The authors of the above-mentioned study [91] argue that PDW order co-exits with patches of uniform d-wave superconductivity due to a stress induced suppression of the 3D SC ordering temperature of smaller magnitude than expected by a perfect stripe phase. Stress has thus the potential to disrupt the orthogonal arrangement of stripes favouring the uniform d-wave superconducting patches. When the uniform patches reach a critical spread, the 2D and 3D superconductivity will have the same critical temperature. This is consistent with the observed, by means of μSR, decrease of magnetic order volume fraction (corroborated with a much less significant reduction of T_N), as a function of stress, which is incompatible with uniform d-wave SC. The same effect could not be obtained only by a rearrangement of stripes within the planes. The authors also speculate that the pairing mechanisms in both the 2D and 3D SC phases are the same pointing to the fact that the presence of a significant magnetic order volume inhibits locally the emergence of 3D superconductivity. It would be very interesting to study the effect of stress

on our LSCO5 sample and determine whether the 2D superconductivity, which we speculate is present in our sample, could evolve into 3D uniform d-wave SC.

Following the same logic, we argue that the pair density wave phase present in LSCO5 persists in superconducting underdoped LSCO samples where it is joined by patches of uniform d-wave superconductivity. Such a co-existence phase has been previously proposed [149] and would also imply the emergence of an additional type of order such as charge density wave [116]. One of the main observations supporting this scenario is the drastic reduction of magnetic spectral weight at the onset of superconductivity as a function of doping. A simple reduction of the interlayer Josephson coupling frustration, that would make possible the emergence of 3D superconductivity, can not explain such a suppression. On the other hand, it is possible that part of the electrons at the Fermi level leave the PDW phase in order to form uniform d-wave superconductivity. This could also explain the slight discrepancy in spectral weight reduction between the elastic and inelastic channels in LSCO5 and LSCO7. One would expect a reduction by the same amount, however the additional inelastic spectral weight could possibly have the origin in the uniform d-wave SC phase (taking into account the limited energy resolution and the lack of knowledge about the exact magnitude of the spin gap) which cannot accommodate magnetic order.

In terms of the effect of an applied magnetic field the data acquired on LSCO7 and presented in Figure 5.4.4 indicates that the observed suppression correlates with the onset of SDW order rather than with T_c. Since the onset of SDW order is associated with the emergence of in-plane superconductivity this correlation implies that the field effect observed concerns only the suppression of two-dimensional superconductivity present in the PDW phase. Furthermore, Z. Guguchia *et al.* [91] define the onset of 2D superconductivity as coinciding with the onset of the diamagnetic response (as measured by magnetic susceptibility) which is in agreement with our observations and further supports the hypothesis of an in-plane field effect. The great agreement between the onset of the field effect in the elastic and inelastic channels, observable in Figure 5.4.4(e) indicates that, similar to LSCO5, the spectral weight is shifted from energies < 1.5 meV towards the elastic channel. Quantitatively, in units of dynamic spin correlation $S(Q_{\mathrm{IC}}, \omega)$ magnetic fluctuations up to 2.5 meV lost, as a function of applied magnetic field at 2 K, 0.53 ± 0.08 eV^{-1} (obtained by point by point subtraction of data taken with and without field at different energies, see Figure 5.4.2(a)). At the same time, the magnetic order signal gained 2.41 ± 1.01 eV^{-1} (obtained as the difference in peak amplitude between data taken in field and in zero field, see Figure 5.4.4(b)). This discrepancy is to be expected since, as a function of applied magnetic field, additional low-energy fluctuations will also be induced in the uniform d-wave superconducting phase.

As a function of increased doping we speculate that the uniform d-wave superconducting order will grow continuously to the detriment of the PDW phase up to the anomalous 12% doping. The lack of a field effect on low-energy fluctuations, corroborated with a significant enhancement of the static signal, observed at this particular doping in both LSCO and LBCO samples [114, 150] could then be the result of balanced cancellation of spectral weight shift towards the elastic line in the PDW phase and the sub-gap states induced in the uniform d-wave SC phase. Above this doping the uniform d-wave becomes the dominant phase. It is probably worth noting that CDW order, which is supposed to emerge in the co-existence phase has only been observed in underdoped cuprates and only around 12% doping in LSCO.

If sufficiently good cleaving of LSCO crystals can be achieved in the future, scanning tunnelling microscopy (STM) measurements have the potential to not only confirm the existence of distinct PDW and uniform d-wave SC phases but they can also reveal what type of coexistence the two exhibit in LSCO samples. Are the two phases spatially separated or are we rather in a local coexistence scenario, as it is the case of $Bi_2Sr_2CaCu_2O_{8+x}$ [151, 152]? Additionally, a rather similar, to our LSCO samples, spectral weight reduction observed in Bi2201 [153] as a function of increased doping can be taken as a hint for a PDW - uniform d-wave SC co-existence scenario.

In conclusion, we propose a picture of coexisting pair density wave and uniform d-wave superconducting regions throughout the phase diagram of LSCO. We argue that the ratio between the two phases can be tuned by varying the strontium doping of the samples. In highly underdoped non-superconducting samples the PDW is the dominant phase which differs from uniform d-wave SC by the development of ungapped magnetic fluctuations and magnetic order in zero applied magnetic field. There we speculate that three-dimensional superconductivity is prohibited by the frustrated nature of the interlayer Josephson coupling. This does not however inhibit the appearance of two-dimensional superconductivity simultaneously with incommensurate magnetic order. As in classical d-wave SC in the presence of an applied magnetic field perpendicular to the CuO_2 layers superconductivity is locally destroyed which becomes evident in the magnetic spectrum as a spectral weight shift from very low energy fluctuations (< 1.5 meV) most probably towards the elastic and quasi-elastic signal. Besides the difference in energy scale of the fluctuations affected by the field, in comparison with uniform d-wave SC, the onset temperature of the field effect coincides with the onset of magnetic order rather than T_c.

As doping is increased and we enter the superconducting dome, regions of classical uniform d-wave superconductivity claim part of the electrons in the sample. This is evident in our data as a drastic suppression of both elastic and inelastic signals at the onset of SC. In the highly underdoped region, of which our crystals are a part, the PDW remains the dominant phase and thus we observe a very similar field effect as our non-superconducting sample. We also speculate that the anomalous $x = 1/8$ doping exhibits a particular balance between the two phases where sub-gap induced states in the d-wave SC regions exactly cancel out the field induced suppression of low-energy fluctuations in the PDW regions. The latter also makes its mark by spectral weight transfer towards the elastic line as a function of field. As doping is further increased into the optimally and over doped regions of the phase diagram the uniform d-wave superconducting phase become predominant exhibiting well-known features which have been intensively studied since the discovery of the LSCO compound.

SPECTRUM OF THE INCOMMENSURATE MAGNETIC FLUCTUATIONS IN FULLY OXYGENATED La_2CuO_{4+y}

This chapter is heavily based on our article submitted for publication in Physical Review B [154]. Parts of the text have been included in the manuscript as well. The data has been collected by various members of our group over the past seven years. Even though I was not part of all the beamtimes, I have done the data analysis presented in this chapter.

The central aim of this study has been to develop a better understanding of static and dynamic magnetic stripes in an optimally oxygen-doped cuprate superconductor, La_2CuO_{4+y}. For this a number of triple-axis experiments have been performed under different conditions such as varying temperature and applied magnetic field or polarisation analysis. The main findings are that both static magnetic order as well as low-energy fluctuations are fully developed in zero applied magnetic field and the low-energy spin fluctuations at $\hbar\omega = 0.3$-10 meV intensify upon cooling. We interpret this as an indication that superconductivity and low-energy spin fluctuations co-exist microscopically in spatial regions which are separated from domains with static magnetic order. Furthermore, polarisation analysis revealed that the magnetic stripe structure is equally represented along both of the tetragonal crystal axes and that the fluctuating stripes display significant weight for in-plane as well as out-of-plane spin components.

6.1 LITERATURE REVIEW

The parent compound of the cuprates family, La_2CuO_4 (LCO), is known to be a Mott insulator [155]. Nonetheless, in 1987 three groups in the US, France and Japan have reported observations of ~ 40 K superconductivity in this compound [156–158]. A deficiency of lanthanum was initially regarded as a more probable cause, for the filamentary superconductivity, than intercalated excess oxygen [156]. We now know that the origin of superconductivity was the oxidisation of samples during the annealing process, which was performed at high temperature and under high-pressure oxygen atmosphere. It is however very difficult, if not impossible, to obtain samples with a single superconducting phase using this technique. Fortunately, only a few years later electrochemical methods have been proven successful in creating single-phase superconducting La_2CuO_{4+y} (LCO+O) samples [159]. In this process, often referred to as superoxygenation, large LCO single crystals are grown inside a mirror furnace, using the travelling solvent floating zone (TSFZ) technique [160], and afterwards undergo an electrolysis process which introduces extra

oxygen inside the structure. During the latter phase, the crystal is immerged into an electrolyte bath (which can for example be a solution of water and NaOH [161, 162] or KOH [159]) and fulfils the role of the positive working electrode. The oxidation process of the crystal is then promoted by the passage of a constant voltage through the working electrode. This procedure is greatly influenced by the magnitude of the specific surface area[1] of the crystal and can last several months, in the case of a single crystal, due to the slow diffusion rate of oxygen atoms within the crystal structure [164].

The next posed question was of course what happens with the excess oxygen atoms, how do they arrange and influence the overall crystal structure of the doped compounds. If we turn our attention to the proposed phase diagram of LCO+O shown in Figure 6.1.1 we will immediately notice that it is composed of a number of discontinuous phases separated by so-called miscibility gaps[2] (in white), a trait which is quite uncommon across the cuprates family. It was observed early on that the addition of oxygen, through both annealing processes and electrochemical methods, can result in phase-separated samples containing oxygen-poor regions (which remain close to the undoped *Bmab* structure [165] shown in Figure 6.1.2(a)) and oxygen-rich ones (where the crystallographic space group symmetry can be either *Bmab* or *Fmmm* [166]). It should be noted that although the schematic phase diagram displays a number of miscibility gaps, only the one ranging from $y = 0.01$ to 0.055 oxygen doping has been explored and showcased in the literature up to this moment [166].
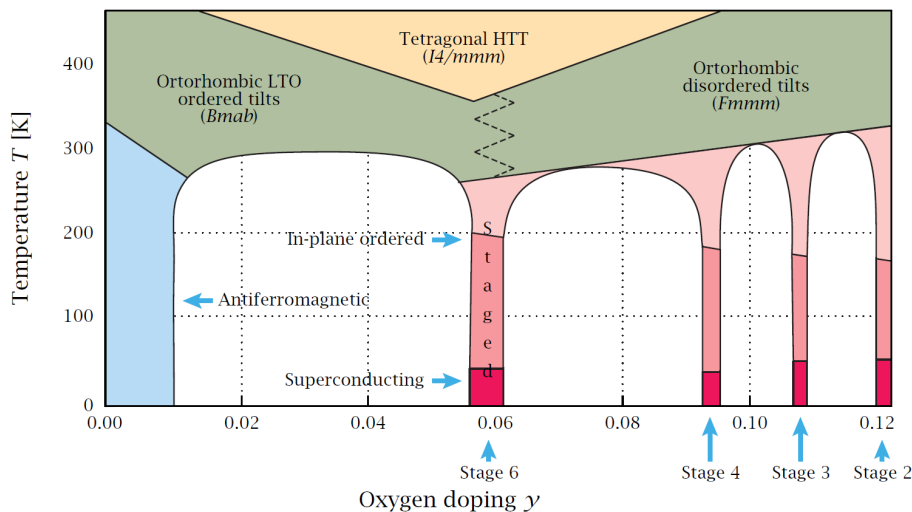
Figure 6.1.1: Temperature vs doping phase diagram of La_2CuO_{4+y}. The schematic representation includes the structural phase transitions from the high temperature tetragonal phase (yellow) to a low temperature orthorhombic one (green), the miscibility gaps (white), the parent antiferromagnetic phase (blue), the staged oxygen regions (different shades of pink) and the superconducting phase (the most intense shade of pink). Image adapted from [145] by P. Ray [14].

Above $y = 0.055$, certain doping levels can be achieved, without the significant segregation of charges that results in phase-separated samples. However, samples containing these specific dopant concentrations display a different type of oxygen aggregation visible as a superlattice structure along the c-axis. B. Wells *et al.* [161] proposed a staging model, previously used to

---

1 The specific surface area of solids is defined as the total area at the surface of the object per unit of mass [163].

2 The miscibility gap is defined as the region of the phase diagram in which the system exhibits two or more coexisting phases [163].

explain the superlattice structure observed in La_2NiO_{4+y} [167], to accommodate the extra atoms. It is well known that La-based cuprates can transition from a high temperature tetragonal phase (HTT) to a low temperature orthorhombic (LTO) one and this applies also to LCO+O as indicated in the phase diagram from Figure 6.1.1. This transition is induced by a slight tilting of the CuO_6 octahedra, shown in Figure 6.1.2(b), which in turn is caused by a different thermal expansion of the Cu-O and La-O bonds. Within the staging model, the tilt direction is reversed every n^{th} CuO_2 layer creating so-called antiphase domain boundaries which can accommodate ordered layers of interstitial oxygen [161]. Each type of structure is then defined by a staging number n which, as mentioned before, corresponds to the periodicity of interstitial oxygen layers (see Figure 6.1.2(c) for the graphical representation of the different staging patterns attainable in this system). Evidence supporting this model comes, for example, from neutron diffraction experiments where additional scattering has been measured around structural Bragg peaks [161]. More specifically, when performing scans along reciprocal space direction l (which is equivalent to the real space c direction) of one of the structural peaks allowed in the *Bmab* phase, such as $(0,1,4)$ or $(0,3,2)$, extra incommensurate peaks are observed. Their displacement from the Bragg position is inversely proportional to the staging number $\Delta l = 1/n$ [161].

It is thus the mobility of the intercalated oxygen atoms, that allows them to rearrange, to some extent, in order to minimise the free energy of the system, that gives rise to a rich phase diagram. In contrast with strontium doped $La_{2-x}Sr_xCuO_4$ (LSCO) superconductors, where doped Sr ions are immobile after crystallisation of the sample and therefore exhibit a "quenched" disorder under standard experimental conditions ($T < 500$ K), excess oxygen ions are able to diffuse down to $T \sim 200$ K [168] creating an "annealed"[3] type of disorder [145]. This difference in behaviour of the dopant species opens the door for determining and comparing the effect of annealed and quenched disorder on superconductivity in otherwise very similar systems. We will return to this aspect later in the this chapter.

Even though the LCO+O crystal structure exhibits some particularities, its magnetic order is not much different than that of other compounds of the family. Upon doping the parent antiferromagnetic compound, the newly introduced holes will arrange themselves so as to create a spin stripe order composed of antiferromagnetic domains separated by "rivers" of charge. The fact that LCO+O exhibits magnetic order in the superconducting phase is an intriguing feature since other compounds of the family, such as LSCO, with similar hole doping concentration and superconducting critical temperature do not display evidence for a magnetic order phase. The onset temperature of the static stripe signal (T_N) coincides with the superconducting critical temperature in LCO+O stage-4 samples ($T_N = T_c \sim 42$ K) [144], as also confirmed by local probe NMR [169] and μSR [170] studies. This parity of critical temperatures is still under debate when it comes to stage-6 LCO+O superconducting samples [171].

---

3 Anneled is used here to describe dopants that are mobile at high temperatures and occupy interstitial sites.
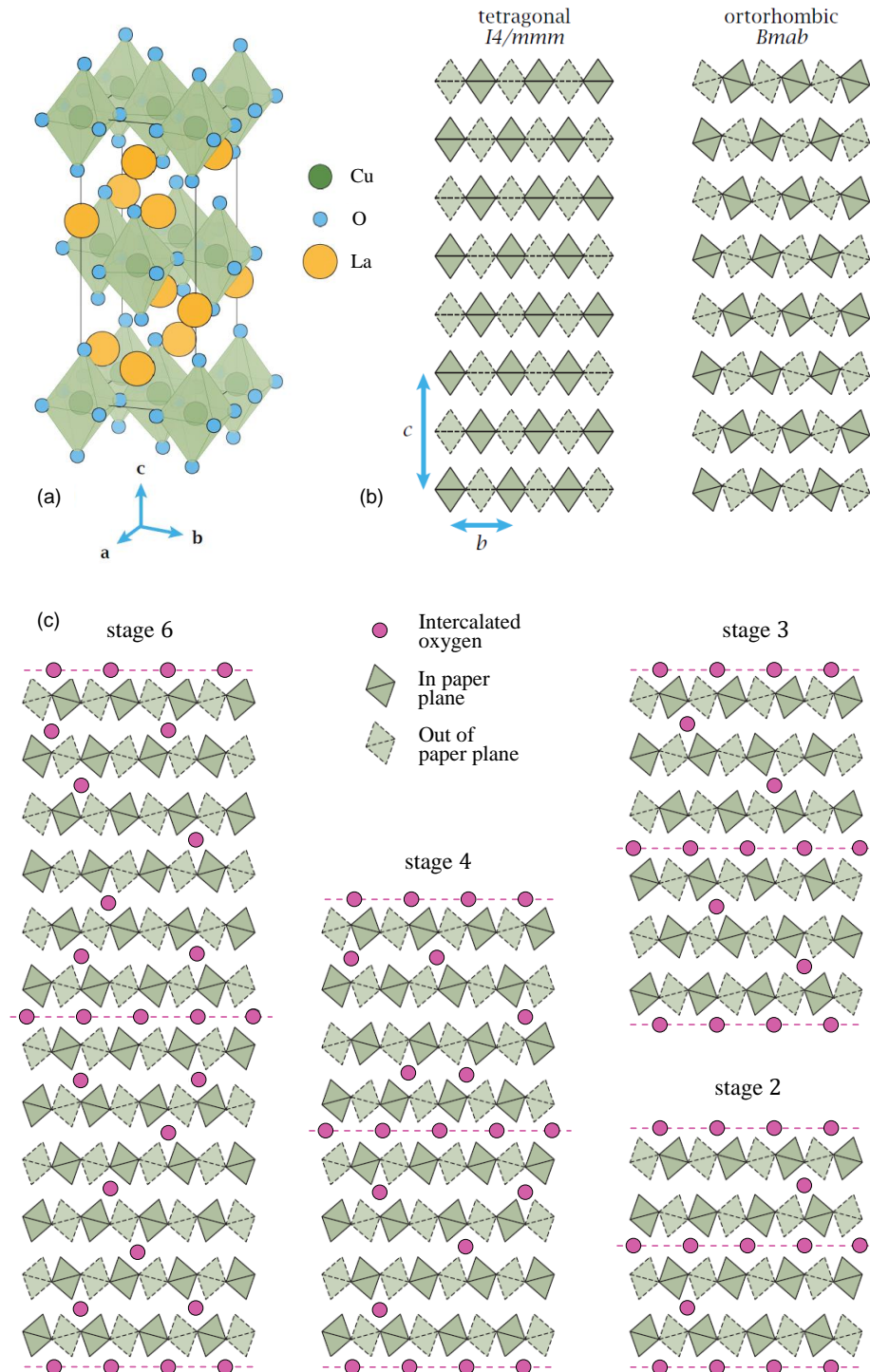
Figure 6.1.2: (a) Orthorhombic *Bmab* crystal structure of the La$_2$CuO$_4$ parent compound (eight conventional unit cells are depicted). Emphasis is put on the perovskite nature of the structure by highlighting the CuO$_6$ octahedra. **(b)** Tilting structure of the oxygen octahedra corresponding to the tetragonal and orthorhombic phases possible for this system. The Bmab is equivalent to the structure of the parent compound from sub-figure (a) with an exaggerated tilt for a better visualisation. Octahedra of different shades belong to antiphase tilt domains; while the dark green ones lay in the paper plane, the light green ones are displaced outside the paper plane by $a/2$ (a being one of the lattice parameters of the unit cell). At the same time the interstitial oxygen atoms are displaced outside the paper plane by $a/4$. **(c)** Schematic representation of the different staging patterns that are present in the phase diagram of LCO+O (see Figure 6.1.1). Images taken from [14].

As mentioned before, the mobility of the interstitial oxygen ions creates an excellent opportunity for studying the effect of dopant disorder on superconductivity. It was observed early on that varying the degree of dopant disorder, by controlling the cooling rate, can result in changes in the superconducting critical temperature of up to 5 K [136]. When the sample is quenched cooled, the thermally disordered oxygen lattice is conserved and manifests itself by a reduced critical temperature. On the other hand, if a slow cooling rate is applied the mobile oxygens have the necessary time to diffuse and create an electronic structure that favours optimal superconductivity. At the same time, disorder was shown to enhance the striped magnetic order signal in stage-4 LCO+O. As it can be observed in Figure 6.1.3(a), the magnitude of the enhancement is comparable to the effect of a relatively small[4] applied magnetic field (H). The origin of the magnetic field enhancement of the spin density wave (SDW) signal has been attributed to the non-magnetic phases of the crystals (meaning the ones harbouring superconductivity). Evidence for this interpretation comes from the linear increase of the SDW signal as a function of increased magnetic field, which was measured in both stage-4 and stage-6 samples (see Figure 6.1.3(b)), concomitant with the appearance of a field induced vortex lattice which is also proportional to $|H|$ [172]. Taking this into account, as well as the fact that both induced disorder and applied magnetic field are accompanied by a similar reduction of the superconducting critical temperature, ~ 5 K and ~ 10 K respectively, the data were interpreted within the model of repulsively coupled order parameters proposed by E. Demler *et al.* [97]. This model argues for repulsively coupled superconducting and SDW order parameters and predicts a variation of the magnetic order signal of the form $\Delta I = (H/H_{c2})\ln(\theta H_{c2}/H)$, where θ is a constant and H_{c2} is the upper critical field of the superconductor. As it can be observed in Figure 6.1.3(b) this formalism describes the data quite well, in both stage-4 and stage-6 samples. It is thus generally agreed that, due to the mobility of the doped oxygen ions, LCO+O superconductors exhibit an electronic phase separation into competing superconducting regions and others with static magnetism. Direct evidence for such a phase separation has been put forward in the form of μSR measurements performed on co-doped $La_{2-x}Sr_xCuO_{4+y}$ (LSCO+O) [173]. It should however be mentioned that similar measurements performed on LCO+O have not been as conclusive due to large systematic errors [170].

Low-energy incommensurate magnetic fluctuations have also been observed early on, through neutron scattering measurements, in LCO+O stage-6 samples by B. Wells *et al.* [145] and in stage-4 samples by Y. Lee *et al.* [144]. This early studies have demonstrated that the incommensurability and temperature dependence of the signal are remarkably similar to the ones known for Sr doped LSCO samples, confirming thus the universal character of the magnetic behaviour across the cuprate family. It was not until recent years that the origin of magnetic fluctuations, as Goldstone modes reflecting the broken symmetry of the static order [105], has been challenged. High resolution neutron experiments have revealed a significant mismatch in incommensurabilty between static and dynamic signals [61]. To explain the results, an electronic phase separation scenario was thus put forward consisting of one phase containing magnetic order and associated weak fluctuations, which is likely competing with superconductivity, and a second region harbouring the observed dynamic stripes.

---

4 In comparison with the upper critical field.
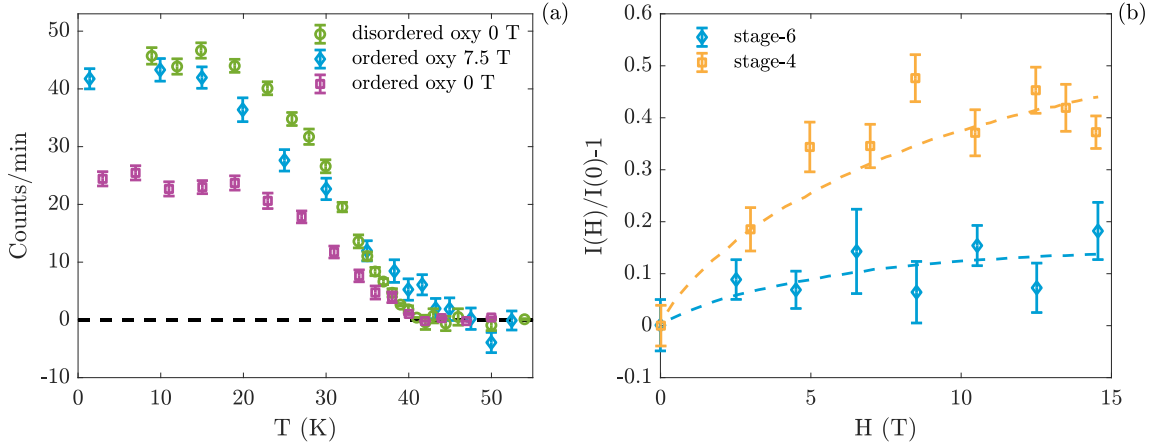
Figure 6.1.3: (a) Static stripe order measured on LCO+O stage-4 sample, as a function of temperature, under different conditions: slow cooling and no applied magnetic field (purple squares), slow cooling and 7.5 T applied magnetic field (blue diamonds) and quench cooling under no applied magnetic field (green circles). In order to allow for direct comparison the data taken in applied field have been normalised. Data from [136]. **(b)** Applied magnetic field dependence of static spin stripes measured in both stage-4 and stage-6 LCO+O samples. The incommensurate peak intensity is normalised to zero field amplitude (I(0)). The dashed lines are fits, which follow the competing order parameter model proposed by E. Demler *et al.* [97], of the form $(H/H_{c2})\ln(\theta H_{c2}/H)$ (where θ is a constant set to 1). The fits return the following values for the upper critical fields: $H_{c2} = 67$ T for the stage-4 sample and $H_{c2} = 49$ T for the stage-6 one, parameters which are in agreement with the ones of LSCO samples of similar doping concentration [174]. Data reproduced from [171].

In spite of the considerable amount of studies analysing the magnetism of LCO+O samples already published, a number of questions remained unanswered, such as what is the orientation of the spin stripes or the influence of an applied magnetic filled on magnetic fluctuations. For this reason, our group has decided to perform an extensive neutron scattering study of static and dynamic spin stripes in LCO+O revealing their orientation relative to the crystal lattice and behaviour as a function of varying energy, temperature and magnetic field.

6.2   THE SAMPLE

Our LCO+O crystals have been primarily prepared by Henrik Jacobsen. Large single crystals of the LCO parent compound have been grown Risø DTU National Laboratory for Sustainable Energy in a mirror furnace using the travelling solvent float zone (TSFZ) technique[5] [160]. X-ray Laue diffraction was then used to determine which parts of the rods were in a single crystal phase. These sections have then been superoxygenated in an aqueous bath at the University of Connecticut. Since the growth process resulted in several centimetric single crystals, different co-alignment combinations have been used throughout the neutron experiments depending on the experimental set-up requirements. The sample masses used in each bemtime are mentioned in the next section.

   The sample quality has been analysed using magnetic susceptibility and neutron Laue back-scattering measurements. The AC susceptibility data, shown in Figures 6.2.1(a) and (b), was acquired by Linda Udby and analysed by myself. A detailed description of the conversion from

---

5 A detailed step by step description of the method used in our laboratory can be found in my Master's Thesis [135]

magnetic moment measurements to magnetic susceptibility in SI units can be found in the Appendix C. AC magnetometry yields two quantities: the susceptibility (χ) and a phase shift (ϕ) relative to the applied AC field. Oftentimes, the measurement is decomposed into an in-phase term (the real part of the susceptibility χ') and an out-of-phase one (the imaginary part of the susceptibility χ''):

$$\chi' = \chi \cos(\phi)$$
$$\chi'' = \chi \sin(\phi).$$

(6.1)

From the real part one can extract the superconducting critical temperature of the compound and the superconducting volume fraction (SCVF). On the other hand, the imaginary part offers information about the state of the vortex lattice.

The sharpness of the diamagnetic response observed in the real part of the AC susceptibility (Figure 6.2.1(a)) is a clear indication that the sample is composed of a single superconducting phase, assuming that the small crystal pieces used are representative for the entire bulk of the sample. One single critical temperature of $T_c = 41.3 \pm 0.8$ K has been determined, where the uncertainty is given by the 10% - 90% criterion[6]. By comparing with other samples from the literature [136, 144, 172], this critical temperature indicates that our crystal most probably exhibits a stage-4 oxygen pattern. This has indeed been confirmed through neutron diffraction measurements by Pia Jensen Ray and described in great detail in her Master's thesis [14].

If a crystal is perfectly superconducting, the real part of the AC susceptibility (Figure 6.2.1(a)) would have the shape of a sigmoid function constrained in between 0 (corresponding to the antiferromagnetic state above T_c) and -1 (corresponding to the perfect diamagnetic response of the material below T_c). The deviation of the measured curve from the ideal limit, at the lowest temperature, is an indication of the fact that fractions of the sample are not superconducting, (SCVF $\neq$ 100%). Unlike T_c, the superconducting volume fraction is greatly influenced by the pre-measuring conditions (note that usually the measurements are performed during the heating process). If the sample is cooled in a small magnetic field (field cooled (FC)), the magnetic flux lines will be pinned by defects and impurities. This means that the Meissner effect is diminished, as the applied magnetic field is not completely expelled from the sample at temperatures lower than T_c, resulting in a lower SCVF in comparison with the case in which the sample is zero-field cooled (ZFC). The difference between data taken using the two methods (FC and ZFC) is thus a good indicator of sample quality. The smaller the difference the lower the amount of defects. Our measurements indicate a SCVF $\sim 20\%$[7]. This is a first hint of a phase separation of the sample. As we shall see later, a significant fraction of the crystal shows signs of the undoped AFM phase.

The peak temperature observed in the imaginary part of the AC susceptibility (Figure 6.2.1(b)) corresponds to the first order phase transition (T_{FOT}) from a vortex lattice phase to a unpinned vortex liquid one [82, 176]. A greater description of this transition and the nature/dimensionality of the vortex lattice can be achieved by performing measurements under various applied DC magnetic fields (H_{dc}). At low applied magnetic fields, as it is also our case, there is little to no difference between T_c and T_{FOT}. It would however be very interesting to perform the same

---

6 ΔT_c is defined as the temperature difference between the points corresponding to 10% and 90% of the normal state susceptibility.

7 At this moment, I am not aware if the measurements have been performed using the field cooling or the zero field cooling method. For this reason, I can not draw a detailed conclusion.
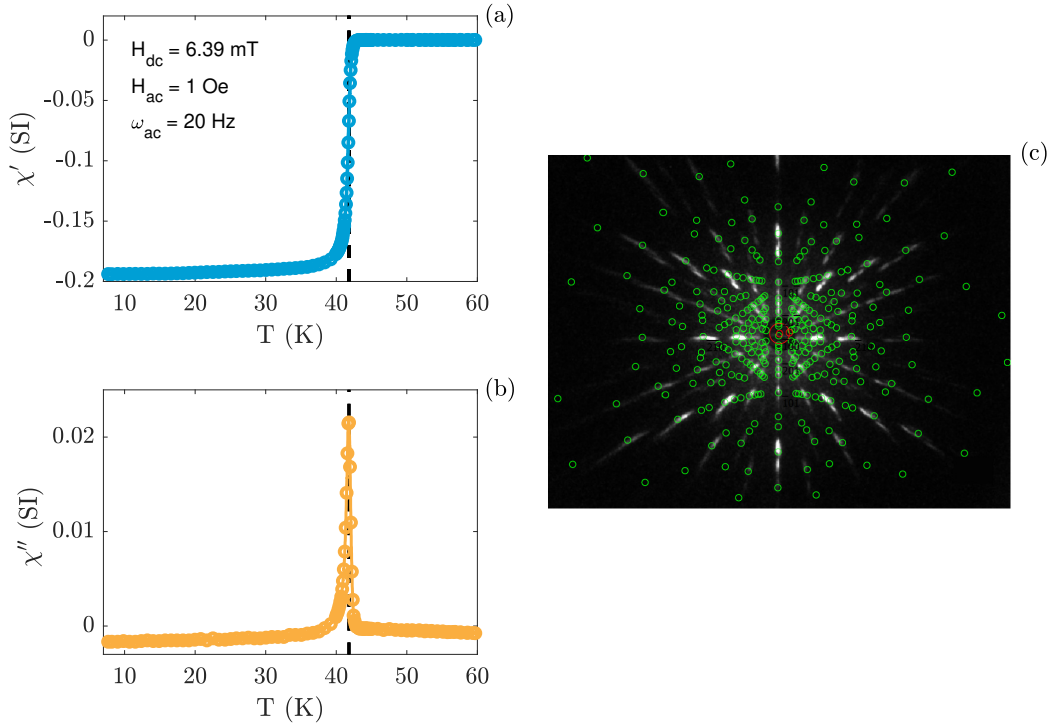
Figure 6.2.1: The **(a)** real and **(b)** imaginary parts of AC susceptibility measured as a function of temperature. The black dashed line indicates the peak position of χ'' (T) which marks the point of maximum slope in χ' (T). **(c)** Neutron Laue back-scattering images taken along a axis. The green circles show the calculated diffraction pattern corresponding to the LCO+O crystal structure. The image was obtained using the CLIP (Cologne Laue Indexation Program) software [175].

measurement under higher magnetic fields in order to be able to draw some conclusions about the anisotropy of the vortex lattice in comparison with other compounds of the cuprates family (for example LSCO of different doping presented in Ref. [82]).

Finally, the quality of the sample has also been tested by performing neutron Laue diffraction, on Orient Express [177] at the ILL, with the aim of aligning the single crystals in preparation for the triple-axis experiments. The measurements indicate that the samples are composed predominantly of one single crystal phase. Figure 6.2.1(c) shows a diffraction pattern, taken on one of the LCO+O crystals, superimposed on a simulated one. The sharpness of the peaks and the great agreement with the calculations point towards a high quality sample.

6.3   EXPERIMENTAL METHOD

Several neutron scattering experiments have been carried out on different instruments at different facilities. The focus in each beamtime was on one of the three main aspects studied: (1) temperature effects (two experiments performed on IN12 and another on ThALES, both cold neutron three-axis spectrometers at the ILL), (2) the influence of an applied magnetic field (one experiment performed on FLEXX at HZB and another on ThALES) and (3) polarisation analysis of magnetic signal (one experiment performed on ThALES). It should be noted that I did not participate in designing and performing all of the experiments, however I have done the data analysis presented in this chapter. The experiments in which I did not take part (the IN12, FLEXX

and first ThALES experiment) are explained in great detail in Henrik Jacobsen's PhD thesis [79]. In this section I will briefly mention the aim of each beamtime and the particularities of the experimental set-up. Similar to the following results and conclusions sections the experiments are grouped according to the above mentioned aim rather than chronologically.

Throughout this chapter two fitting routines ave been used. For the temperature dependence measured on IN12 and the first ThALES (TH1) experiment we implemented a so-called Sato-Maki function, first proposed as a model of describing antiferromagnetic correlations in chromium and its alloys [178]. This was later comprehensively explained and used by G. Aeppli *et al.* to fit neutron scattering measurements of magnetic fluctuations in optimally doped LSCO [179]. While G. Aeppli *et al.* used tetragonal notation, we have converted the formalism to the orthorhombic structure. The associated lattice parameters $a_o = b_o = 5.3$ Å have been used, since these are too close to distinguish from one another given the resolution of our inelastic neutron scattering experiments. The scattering amplitude is thus fitted to the function

$$S(Q, \omega) = \frac{[n(\omega) + 1] \chi''(\omega, T) \kappa^4(\omega, T)}{[\kappa^2(\omega, T) + R(Q)]^2}, \tag{6.2}$$

where

$$R(Q) = \frac{4[(Q - Q_{\text{AFM}})^2 - \delta^2]^2}{(2 a_o \delta)^2}. \tag{6.3}$$

Here $(n(\omega) + 1)$ is the thermal population factor for down-scattering (neutron energy loss), $\chi''(\omega, T)$ is the imaginary part of the dynamic susceptibility at the peak position, $\kappa(\omega, T)$ is the n inverse length scale (a measure of the peak width) and δ is the incommensurability of the signal measured around the antiferromagnetic point ($\mathbf{Q}_{\text{AFM}}$). Note that the possible differences in incommensurabilities δ_h and δ_k are small compared to the width of the resolution function [61] and we simply set $\delta_h = \delta_k = \delta$ henceforth. This routine imposes equal amplitude, width, and incommensurability for the two peaks that are scanned over during the measurement. The incommensurability is defined as the distance between the peak centre and $\mathbf{Q}_{\text{AFM}} = (1,0,0)$.

In terms of the field effect, the data collected at FLEXX was fitted with a Gaussian model with constrained equal widths and incommensurability, because part of the data were obtained by scanning over a single peak. The additional experimental data collected in the second ThALES experiment (TH2) was fitted using the Sato-Maki function described previously.

Finally, for the polarisation analysis data the above-mentioned Gaussian model has been used The appearance of additional parasitic scattering on top of one of the genuine incommensurate magnetic peaks made it impossible to use the Sato-Maki model which constrains the amplitude of the two peaks to equal values.

For all experiments, the sample was aligned in the a-b plane, enabling access to the $(h, k, 0)$ scattering plane. As in the rest of this thesis, the orthorhombic notation is used where the size of the unit cell is $a_o = 5.33$ Å, $b_o = 5.40$ Å, $c_o = 13.20$ Å and the antiferromagnetic reflection is found at $\mathbf{Q}_{\text{AFM}} = (1,0,0)$. However, due to twinning commonly present in these samples, each scattering point is a superposition of $(h,0,0)$ and $(0,k,0)$ reflections [161], meaning that antiferromagnetic scattering is also observed at $\mathbf{Q}_{\text{AFM}} = (0,1,0)$ without deviation of the spins from the orthorhombic b-axis [104].

During all experiments the sample was cooled slowly (1 K/min) in the temperature range 300 K to 100 K, in order to prevent unwanted effects arising from quenched oxygen disorder [136, 180]. Measurements were performed in the SC phase at 2 K and in the normal phase at 45 K. In the experimental setup, we resolve all four IC magnetic peaks at $\mathbf{Q}_{IC} = (1 \pm 0.125, 0 \pm \delta, 0)$ which are resolution limited and we obtain a lower bound for the correlation length of $\xi \sim 70$ Å, as exemplified later on in this section.

As mentioned above, the data were acquired through scanning over one or two of the four peaks with energy transfers between 0 and 10 meV. We furthermore followed the temperature dependence of the intensity of the peaks at 0 meV, 0.3 meV and 1.5 meV using one- and three-point measurements (on IN12).

- **IN12 experiments performed in 2013 by Henrik Jacobsen, Pia Jensen, Linda Udby, Wolfgang Schmidt and Kim Lefmann**

The aim of these two experiments, performed on IN12, has been to study the influence of temperature variations on dynamic stripes of different energies (0.3-10 meV). The instrument configuration has been the following:

VELOCITY SELECTOR - PYROLYTIC GRAPHITE MONOCHROMATOR - SLITS - ORANGE CRYOSTAT - SLITS - (BERYLLIUM FILTER) - PYROLYTIC GRAPHITE ANALYSER - ^{3}HELIUM NEUTRON DETECTOR.

Note that the Beryllium filter has only been used in the second IN12 experiment. The vertically and horizontally focusing pyrolytic graphite filters have been kept flat leading to a relaxed in-plane Q-resolution of about $0.02\,\text{Å}^{-1}$ (for $k_f = 1.5\,\text{Å}^{-1}$) and even broader resolution out of the scattering plane, where the stripe signal from cuprates is nearly constant [103, 180]. The energy resolution of the two experiments, determined by the full width at half maximum (FWHM) measured from incoherent scattering, is 0.186(1) and 0.239(2) meV, respectively. The total sample mass used was 15.79 g consisting of four cylindrical singe crystals co-aligned within 2°. For this particular study, where magnetic scattering is in focus, the use of greater sample mass allowed us to overcome the counting time restrictions imposed by the small cross section of inelastic magnetic scattering.

One particularity of these experiments was that, in order to obtain the best possible signal to noise ratio, which can be particularly difficult in the presence of spurious scattering or at very low energies because of the superposition of the elastic line, various outgoing wavevectors (k_f) have been used. Figure 6.3.1 summarises the measurements performed both inside and outside the superconducting phase employing different k_f values.

Overall, there is a good agreement between scans both in terms of dynamic susceptibility as well as intrinsic linewidth. In order to account for the different resolution volumes dictated by the k_f variation the data depicted in Figure 6.3.1(a) has been further normalised by a term proportional to the ratio between the resolution volume (V_f) corresponding to $k_f = 1.5\,\text{Å}^{-1}$ (at which most of the data was measured) and the ones corresponding to the different k_f' values at which each data set was taken (V_f'). See Appendix A for a detailed description of the absolute normalisation of magnetic cross section used throughout this study.
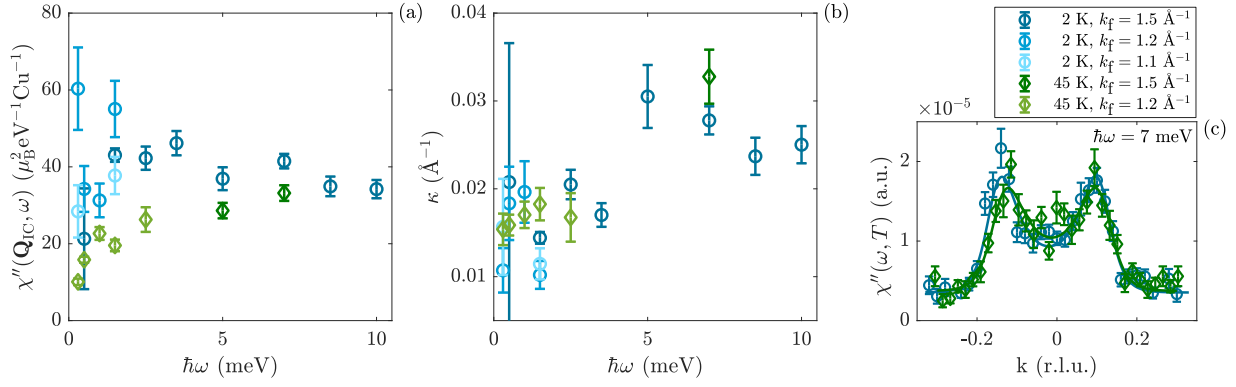
Figure 6.3.1: (a) Dynamic susceptibility $\chi''(\mathbf{Q}_{\mathrm{IC}}, \omega)$ measured at temperatures inside (2 K - circles in different shades of blue) and outside (45 K - diamonds in different shades of green) the superconducting dome employing different k_{f} values. **(b)** Inverse length scale (κ) as obtained from the Sato-Maki fitting routine explained in the text. **(c)** Representative Q-scan through the incommensurate peaks collected at 2 K (blue) and 45 K (green) and 7 meV energy transfer with fixed outgoing wavevector $k_{\mathrm{f}} = 1.5\,\text{Å}^{-1}$.

The inverse length scale (κ or the intrinsic linewidth, see Figure 6.3.1(c) for an example of fits), depicted in Figure 6.3.1(b), is inversely proportional to the dynamic spin correlation length (ξ). Following M. Kofu *et al.* [47], the jump from $\kappa \sim 0.015$ r.l.u. ($\xi \sim 67$ Å) to $\kappa \sim 0.028$ r.l.u ($\xi \sim 36$ Å) taking place at around 5 meV, could be seen as an indication for real space phase separation into two regions with different magnetic structures. However, the jump presented in the above-mentioned article is much more prominent than what we observed. At the same time, due to spurious scattering, the quality of our data is not high enough to provide very precise fits of the peaks width and thus we refrain from drawing any conclusions in the upcoming sections about variations in dynamic spin correlation length.

- **ThALES experiment performed in 2015 by Henrik Jacobsen, Sonja Holm-Dahlin, Linda Udby, Monica Lăcătușu, Paul Steffens, Martin Böhm and Kim Lefmann**

In order to improve the overall quality of the data taken on IN12, an additional experiment has been performed on Thales. Since the temperature variations seemed to have a greater impact on fluctuations of low energy (< 5 meV), this beamtime focused on studying fluctuations of energy $\hbar\omega < 4$ meV at temperatures both inside and outside the superconducting phase.

The instrument configuration was the same as at IN12 including the Beryllium filter. For this experiment only vertical focusing was employed, leading to an enhanced in-plane momentum resolution by a factor 2 ($0.01\,\text{Å}^{-1}$) and relatively loose resolution along the c-direction. The energy resolution has been improved as well down to $0.044(1)$ meV. The increased neutron flux at the sample position, compared to the IN12 instrument, allowed us to use a lower sample mass (a single 3.44 g crystal) and obtain better signal to noise ratio, since the size of the beam hitting both the cryostat and the sample can be significantly reduced.

- **FLEXX experiment performed in 2015 by Henrik Jacobsen, Monica Lăcătușu, Rasmus Toft-Petersen, Diana Quintero Castro and Kim Lefmann**

In continuation of the study on the properties of dynamic stripes, an experiment was performed at FLEXX employing a 12 T applied magnetic field. Its aim has been to study the behaviour

of both static and dynamic stripes under high applied magnetic field. The instrument configuration was very similar to that of the ILL instruments:

VELOCITY SELECTOR - PYROLYTIC GRAPHITE MONOCHROMATOR - SLITS - 15 T VERTICAL FIELD CRYOMAGNET - SLITS - PYROLYTIC GRAPHITE ANALYSER - ³HELIUM NEUTRON DETECTOR.

The energy resolution during this experiment has been $0.301(4)$ meV with outgoing wavevector $k_f = 1.55$ Å^{-1}. For this beamtime five single crystals have been co-aligned within $1.3°$ amounting to a total sample mass of 8.84 g.

- **ThALES experiment performed in 2016 by myself, Henrik Jacobsen, Sonja Holm-Dahlin, Tim Tejsner, Paul Steffens, Martin Böhm and Kim Lefmann**

Because the FLEXX experiment revealed a field suppression of low energy fluctuations which contradicts observations from the literature on similar compounds (for example on LSCO with Sr doping $x = 0.12$ [114], $x = 0.145$ [127], $x = 0.163$ [124], $x = 0.18$ [128]), a second experiment has been performed on ThALES in order to confirm the trend. The instrument configuration was the same as at FLEXX resulting in an energy resolution $0.070(1)$ meV.

Due to various technical issues, data at only three energy transfers have been acquired (0.5, 1 and 2 meV). At the same time, the measurements recorded outside the superconducting phase have confirmed temperature effects on magnetic fluctuations. Additionally, the influence of an applied magnetic field on excitations in the absence of superconductivity (at high temperatures), has been studied.

- **Two ThALES experiments performed in 2018 and 2020 by myself, Astrid Tranum Rømer, Tim Tejsner, Paul Steffens, Martin Böhm**

Previous experiments performed on this very same sample by H. Jacobsen *et al.* [61] have revealed a mismatch in incommensurability, between elastic and inelastic signals, which was speculated to be an indication of electronic phase separation. In this picture, the static stripes, and their associated Goldstone modes (which are not distinguishable during the measurement), reside in a different real space domain compared to the observed magnetic fluctuations. It is thus possible that the two magnetic structures could have different orientations. The aim of this polarisation analysis experiment has been to answer exactly this question, what is the orientations of the static and dynamic magnetic signals respectively.

In order to perform XYZ polarisation analysis (as described in Section 4.5), we used Heusler (111) monochromator and analyser crystals and a Cryopad [181] at the sample position in order to screen any stray magnetic field that might interfere with the measurement. We have however not made use of the full capabilities and sensitivity of the Cryopad in measuring the rotation of the neutron polarisation vector as we have only distinguished between the three main directions in space x, y and z.

The spin flip and non spin flip channels of the antiferromagnetic signal, incommensurate magnetic order as well as incommensurate magnetic fluctuations have been carefully measured.

This allowed us to (1) separate magnetic and nuclear contributions and (2) to determine the orientation in space of spin stripes.

Finally one additional measurement has been performed in which we determined the critical temperature of our sample by following, as a function of increased temperature, the depolarisation of the neutron beam induced by the trapped magnetic flux inside the superconductor. The experiment was performed as follows. The sample was slowly cooled down (with a cooling rate of 1 K/min) in a small applied vertical magnetic field ($\parallel z$-axis) such that at base temperature a number of vortex lines will be trapped inside the superconducting sample. At low temperature (6 K $< T_c$), the external magnetic field, which will guide the neutron polarisation in the following, was switched as to point along the x-direction (in the scattering plane). We have then proceeded to measure the intensity in the spin flip channel of a strong Bragg peak $(2,0,0)$ [8]. The $(2,0,0)$ is a purely nuclear reflection, meaning that it would not induce a flip of the neutron spin. However, by cooling inside a magnetic field we were able to trap vertical flux lines which will induce a non-adiabatic field change of the neutron spin. While the scattering remains purely nuclear, the depolarisation of the beam will increase the probability to observe spin flip scattering.

6.4 RESULTS

The sample exhibits a single and clean superconducting transition at $T_c = 42$ K, as seen from the temperature dependence of the diamagnetic signal shown in Figure 6.4.1(a) and confirmed by depolarisation measurements described further down in this section. This supports the presence of a single dominant staging structure which, given its critical temperature, was previously found to correspond to stage-4 samples [145, 161]. The temperature dependence of the magnetic order in Figure 6.4.1(b) unveils that the onset temperature of the elastic stripe signal coincides, within errors, with the onset of superconductivity, $T_c \approx T_N$.

The low-energy magnetic fluctuations have a much higher onset temperature than superconductivity ($T_{onset} > 70$ K $> T_c$) and do not show any dramatic signatures at T_N or T_c, see Figure 6.4.1(c). At the lowest energy $\hbar\omega = 0.3$ meV, a broad increase in intensity is observed around $T = 30$ K ($< T_c$). A similar temperature dependence of fluctuations of slightly higher energy ($\hbar\omega = 2$ meV) was observed by Y. Lee *et al.* [103] in a stage-4 LCO+O sample. These measurements showed an increase in intensity down to ~ 30 K, followed by a less pronounced suppression at lower temperatures. In stage-6 samples, the same temperature behaviour of low-energy magnetic fluctuations (2-4 meV) has been reported earlier [145]. In that work, the peak in intensity happened to coincide within errors with the critical temperature $T_c = 31$ K and to follow the same trend as underdoped ($x = 0.12$) LSCO samples of similar T_c [114]. The present data show that the increase in intensity of the low-energy fluctuations at temperatures close to 30 K is likely a universal feature of LCO+O and underdoped LSCO superconductors regardless of their corresponding superconducting critical temperatures.

As mentioned in the previous section we have also been interested in determining the behaviour of low-energy spectrum in the energy range $\hbar\omega = 0.3$-10 meV at different temper-

---

8 The choice of Bragg peak is arbitrary, in principle the experiment could be performed using the direct beam. The only requirement is a strong intensity
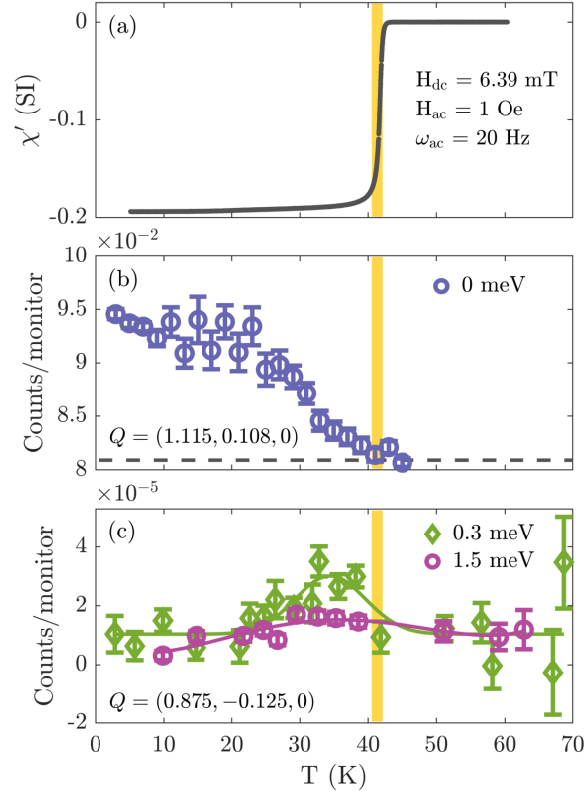
Figure 6.4.1: (a) The real part of AC magnetic susceptibility, χ', showing the sharp transition to a diamagnetic state upon cooling below the superconducting critical temperature. T_c is indicated by the yellow stripe which spans a temperature range 41.3 ± 0.8 K. The steps followed in the conversion from emu to SI units are presented in the Appendix C. **(b)** Temperature dependence of magnetic order measured as 1-point scans on top of one of the IC peaks $(1.115, 0.108, 0)$. The incoherent background has not been subtracted. The dashed line indicates the background level extracted from an energy scan taken away from the incommensurate peak position, at $(1.1, -0.24, 0)$. **c)** Temperature dependence of magnetic fluctuations with energy 0.3 meV and 1.5 meV. Data were measured as 3-points scans with $k_f = 1.2\,\text{Å}^{-1}$ ($\Delta E = 0.070(1)$ meV) and the intensity is obtained as the difference between the point on top of the peak, at $(0.875, 0.125, 0)$, and the average of the 2 background points.

atures, below and above T_c. Figures 6.4.2(a,b) show examples of representative scans taken at ThALES and IN12, respectively, at temperatures both inside (2 K) and outside (50 K or 45 K) the superconducting phase. The apparent increase in integrated intensity at the low energies as a function of increased temperature (Figure 6.4.2(a)) is merely an effect of the Bose occupation factor. Figure 6.4.2(c) depicts the imaginary part of the dynamical spin susceptibility $\chi''(\mathbf{Q}_{\text{IC}}, \omega)$, expressed in units of $(\mu_B^2 \text{eV}^{-1}\text{Cu}^{-1})$ [78, 138]. The data demonstrate that spin fluctuations with energy $\hbar\omega > 4$ meV are rather insensitive to the onset of superconductivity. At lower energies, cooling below T_c leads to an increase in the spin susceptibility at $\mathbf{Q}_{IC}$. This is unlikely to be a direct consequence of the onset of superconductivity, but clearly shows that there is no tendency towards a suppression of the low-energy magnetic spectrum in the superconducting phase. The sample thus shows no evidence of a spin gap, although a small partial gap at $\hbar\omega \sim 0.5$ meV cannot be excluded.

The current observations are in contrast to studies of optimally doped LSCO, with a similar high value of T_c, where the superconducting transition is accompanied by the opening of a clean spin gap in the low-energy magnetic spectrum [47, 124]. Subsequently, an increase in temperature
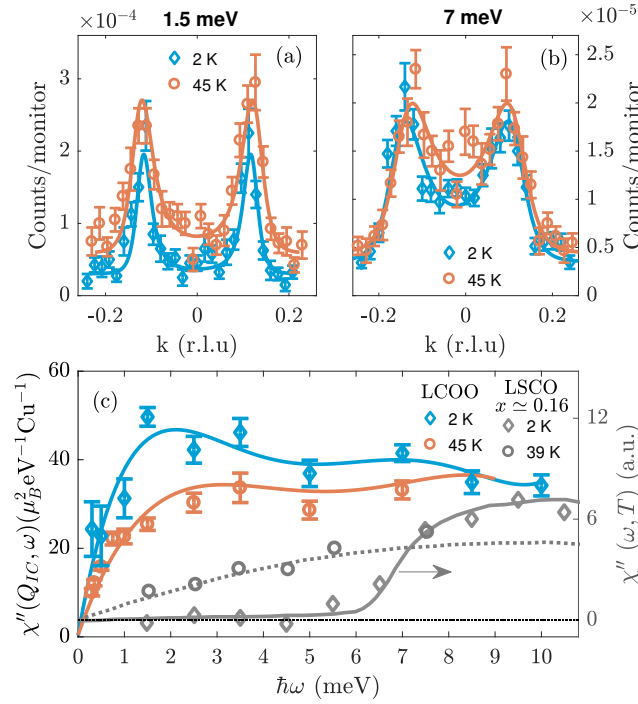
Figure 6.4.2: (a) and **(b)** Representative inelastic scans through the incommensurate positions $(\pm\delta, 1-\delta, 0)$ where $\delta = 0.125$, collected at 1.5 meV and 7 meV with fixed outgoing wavevectors $k_{\mathrm{f}} = 1.55$ Å^{-1} and $k_{\mathrm{f}} = 1.5$ Å^{-1}, respectively. The data were collected at ThALES (**(a)**) and IN12 (**(b)**) at two temperatures: blue diamonds show data in the superconducting state (2 K) and orange circles show data within the normal state (45 K). The solid lines are Sato-Maki function fits to the raw data as described in the text. **c)** Dynamic susceptibility $\chi''(\mathbf{Q}_{\mathrm{IC}}, \omega)$ measured inside (2 K - in blue) and outside (45 K - in orange) the superconducting dome. Solid lines are guides to the eye. Each data point represents an average of values obtained at different k_{f} values and on different instruments (ThALES and IN12). In grey symbols, we show for comparison the magnetic susceptibility measured inside and outside the superconducting state by B. Lake *et al.* [124] on a optimally doped $x = 0.163$ LSCO sample.

above T_{c} induces sub-gap states. To visualise this difference, Figure 6.4.2(c) shows the data obtained in this sample together with the data of LSCO $x = 0.163$ from Ref. [124]. On the other hand, the low-energy spectrum bear close resemblance to LBCO [64] and LSCO $x = 0.12$ [114] despite the higher T_{c} and the tendency towards phase separation not being observed in the latter compounds.

In order to gain a more comprehensive understanding of the magnetism of this oxygen-doped sample, the effect of an applied magnetic field has been studied on FLEXX and ThALES. In contrast with the temperature dependence presented above, were data from several experiments have been combined thanks to the absolute normalisation, no conversion to absolute units was carried out on the measurements taken in field at FLEXX due to the lack of a phonon measurement. This however poses no problems for the FLEXX data as the temperature was kept constant and the energy difference produces a negligible effect in this regime. The ThALES data on the other hand is presented in absolute units. In both experiments a $H = 12$ T (FLEXX) and $H = 10$ T (ThALES) magnetic field was applied along the c-axis. These values are much lower than the upper critical field $H_{c2} \sim 60$ T (see Ref. [174]). The data shown in Figure 6.4.3 illustrate the lack of response in the elastic channel and a small decrease with field in the low-energy inelastic channel.

The insensitivity of magnetic order to an applied magnetic field contradicts reports from the literature on LCO+O. A lengthier discussion on this aspect is included in the next section.
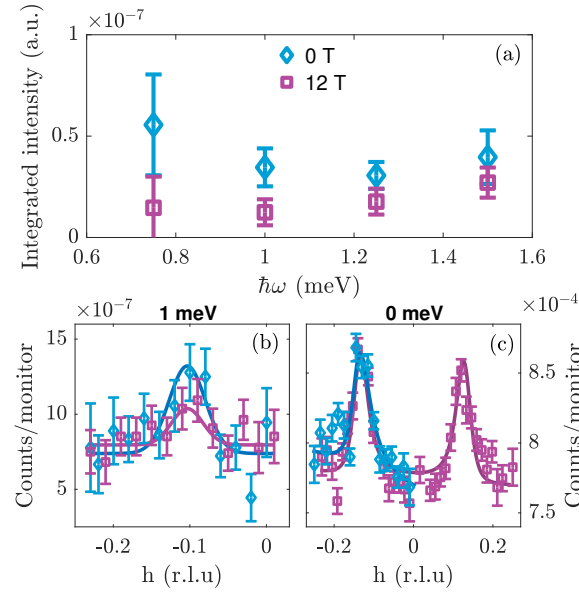
Figure 6.4.3: (a) Magnetic field dependence of low-energy spin excitations measured at 2 K on FLEXX. Representative **(b)** inelastic constant energy scan ($\hbar\omega = 1$ meV) used to create subfigure(a) and **c)** elastic scans collected in the superconducting phase (2 K) with and without applied magnetic field. The solid lines are Gaussian fits to the raw data.

Additional measurements performed on ThALES have confirmed the slight suppression, under 10 T applied magnetic field, of magnetic fluctuations with energies around $\hbar\omega = 1$ meV. (see Figures 6.4.4(a) and (c)). At the same time, the measurements recorded outside the superconducting phase (at 50 K) reveal a similar suppression of spin excitations. Interestingly enough, the magnitudes of the field and temperatures effects are comparable though it should be noted that data has been recorded at only one energy transfer.

Another finding of this experiment is the fact that the field effect is diminished outside the superconducting dome suggesting that, however small a field effect, it is correlated with the emergence of superconductivity. The intrinsic linewidth ($\kappa \sim 0.015$ r.l.u) extracted from the data (see Figure 6.4.4(b)) confirms the dynamic spin correlation length ($\xi \sim 67$ Å) previously observed on IN12 in this energy regime (< 5 meV).

Similar to the data presented in Ref. [61], we have started the polarisation experiments by mapping out, in diffraction mode, the area around the antiferromagnetic point at $(0, 1, 0)$. Keeping the neutron polarisation along x allows us to distinguish between magnetic (which will be visible in the SF channel) and nuclear (visible in the NSF channel) scattering. As it can be observed in Figure 6.4.5 the NSF channel contains increased intensity at $h = 0$ originating most probably from a double scattering event[9] as the $(0, 1, 0)$ is not an allowed nuclear reflection in the orthorhombic $Bmab$ space group of LCO+O. What is even more interesting is the presence of the same peak (of smaller magnitude) in the SF channel as well. This is a clear indication that our

---

9 This is supported by the observation that the signal at $h = 0$ in the NSF channel is dependent on the value of the outgoing wavevector k_f and implicitly on the size of the Ewald sphere. The data in Figure 6.4.5 recorded with $k_f = 1.5$ Å^{-1} clearly shows the spurious signal while the same scans performed with $k_f = 1.7$ Å^{-1}, and pictured in Figure 6.4.6(a), display no peaks in the NSF channel.
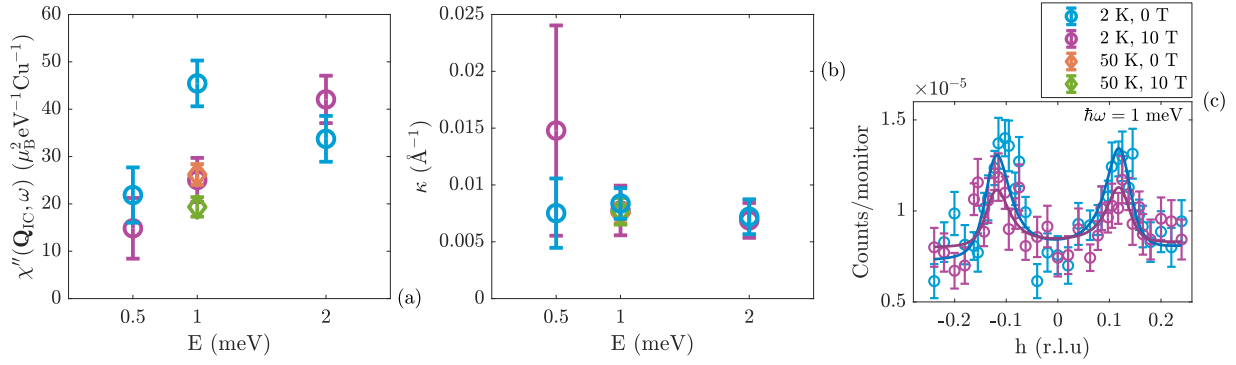
Figure 6.4.4: (a) Integrated intensity measured at temperatures inside (2 K - circles in blue (0 T) and purple (10 T)) and outside (50 K - diamonds in orange (0 T) and green (10 T)) the superconducting dome at ThALES. **(b)** Half width at half maximum as a function of energy transfer, varying temperature and applied magnetic field. The parameters are obtained from the Gaussian fits with constrained peaks positions and equal areas for the two measured peaks.

LCO+O sample contains an undoped antiferromagnetic phase (similar to other samples from the literature [145]). We further determined the orientation of the AFM phase by performing SF and NSF scans with the polarisation aligned along each of the three directions of the chosen coordinate system (where $\mathbf{Q} \parallel x$). The data is summarised in Figure 6.4.6.

With respect to the spin stripes signal, in Figure 6.4.5(b) one is able to distinguish purely magnetic signal appearing at incommensurate positions $(1.09, 0 \pm 0.125, 0)$. This is even more evident in the 1D representation of the scan (Figure 6.4.5(c)) where two clear incommensurate peaks can be distinguished in the SF channel, while the NSF only shows increased scattering at the $(0, 1.1, 0)$ position.
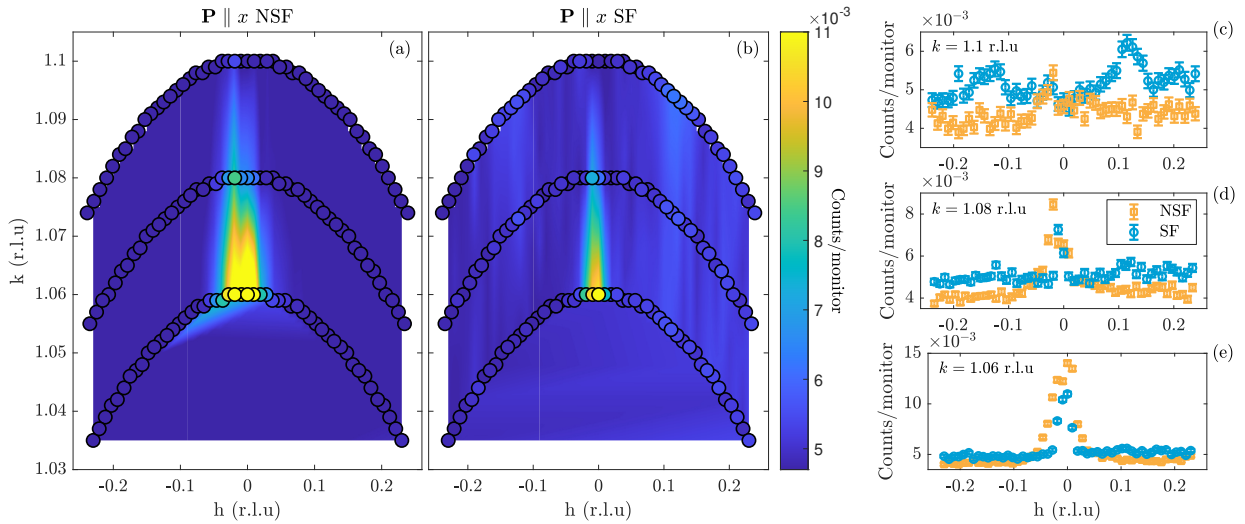
Figure 6.4.5: Elastic scans taken around the antiferromagnetic reflection at $(0, 1, 0)$ in the superconducting phase ($T = 1.5$ K) with neutron spin polarisation aligned along x. **(a)-(b)** 2D representation of the data corresponding to the non spin flip and spin flip channels respectively. The marked symbols are measured data points while the area surrounding them is a 2D interpolated map. **(c)-(e)** 1D representation of the three scans taken at different positions in reciprocal space. The inset of each graph indicates the average k value of the scan.

To access the precise orientation of the magnetic moments in static and dynamic magnetic stripes, further measurements have been performed in three different spin configurations of the
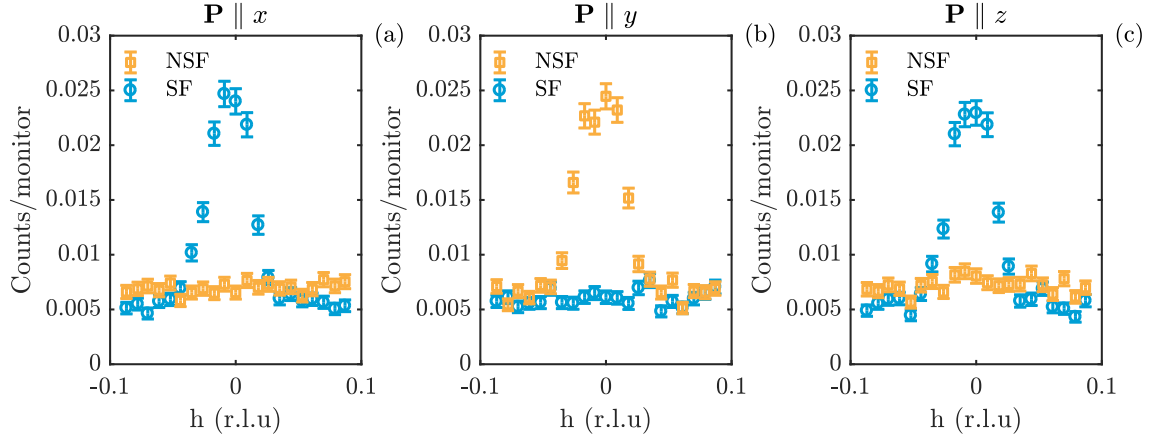
Figure 6.4.6: Elastic scans taken at the antiferromagnetic reflection $(0, 1, 0)$ in the superconducting phase ($T = 1.5$ K) with neutron spin polarisation aligned along x **(a)**, y **(b)** and z. **(c)**. In yellow squares the non spin flip channel is represented while blue circles denote the spin flip channel.

incoming neutron beam. First, the neutron polarisation was chosen parallel to the scattering vector **Q**, defined as the x-direction in the following. In this set-up, we performed scans in both the spin flip (SF) and the non-spin-flip (NSF) configurations. Afterwards, only the SF channel was measured with the neutron spin aligned along the y and z-direction, z being out of the scattering plane. This XYZ polarisation analysis allowed us to determine the contribution of different components of the magnetic order in the sample, as illustrated by the Equations 4.29.

In the elastic channel, Figure 6.4.7(b), we observe a lack of intensity in the $S \parallel y$ spin flip channel and equal intensity in the other two SF channels. Taking into account Equations 4.29, this provides definite evidence that M_z is (close to) zero and thus that the spin structure in the elastic channel resides in the a-b plane.

The inelastic polarised data of Figure 6.4.7(a) shows scattering intensity in all spin channels. This means that there is an out-of-plane spin component to the scattering signal, which is expected both in the case of isotropic spin fluctuations, and in the limit of purely transverse fluctuations connected to the static SDW signal. In the following section, the polarised measurements are discussed in further detail.

Finally, one additional measurement has been performed in which we determined the critical temperature of our sample by following, as a function of increased temperature, the depolarisation of the neutron beam induced by the trapped magnetic flux inside the superconductor. The motivation for such a measurement came from the fact that we were able to prove that part of the sample is undoped exhibiting a clear antiferromagnetic signal. Traditionally the superconducting critical temperature is determining by performing magnetic susceptibility measurement on small portions of the sample (as the ones presented in Figure 6.4.1(a)). Applying this method there is of course the risk that the properties of the small crystallites are not representative for the entire bulk of the sample. Alternatively, one can use polarised neutron imaging or tomography to accurately evaluate doping distributions throughout large single crystals [182] (as described in the next chapter). Here we have used the polarisation set-up in order to determine the onset of superconductivity.

The measurement is depicted in Figure 6.4.8 shows increased intensity at temperatures below 40 K corresponding to the depolarisation of the neutron beam by the vortex lattice. The
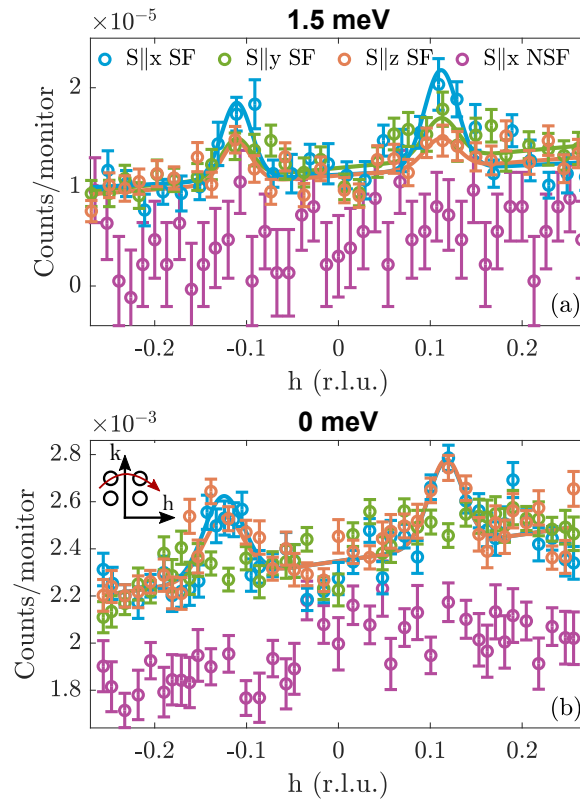
Figure 6.4.7: (a) Inelastic constant energy scan ($\hbar\omega = 1.5$ meV) and **(b)** elastic scans collected in the superconducting phase (30 K and 5 K respectively) in spin-flip (SF), with 3 spin configurations, and non-spin-flip (NSF) mode. The scan direction is represented in the inset of subplot (b). In panel (a) the NSF data are displaced by a factor -0.7×10^{-5} for better visualisation. S denotes the incoming neutron beam spin direction. The solid lines are Gaussian fits to the raw data.

observed intensity then drops to a constant low value which reflects the finite natural beam polarisation induced by the outer magnetic field that penetrates the sample homogeneously outside the superconducting phase. The fairly sharp transition at ~ 40 K is agreement with the critical temperature we have extracted from magnetic susceptibility data. The peculiar slight increase in intensity at around ~ 28 K is probably an indication of the phase transition from a vortex lattice to a vortex liquid phase [183].
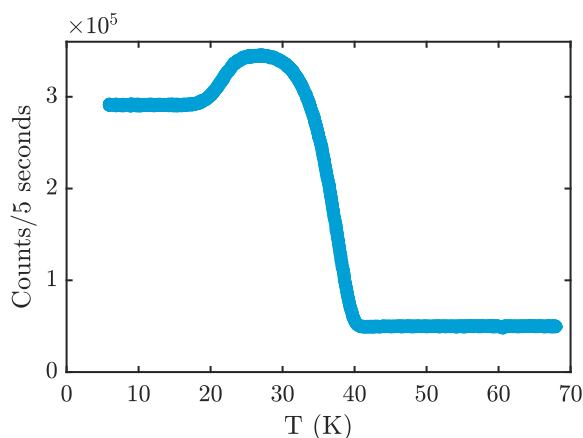
Figure 6.4.8: Measured intensity of the spin flip channel at $(2,0,0)$ Bragg position as a function of temperature.

6.5   DISCUSSION

6.5.1   *Phase separation and intertwined orders*

Figure 6.4.1 demonstrates that the sample exhibits similar critical temperatures for supercon-
ductivity and magnetic order, i.e. $T_c \simeq T_N$. This finding is supported by results from local probe
nuclear magnetic resonance (NMR) measurements [184] and was also found by neutron scatter-
ing [103, 136] in LCOO samples with the same critical temperature as the one used in this study.
While this could be interpreted as a microscopic coexistence of magnetic and superconducting
order [136], there is also the possibility of a microscopic phase separation of the crystal into dif-
ferent domains where each contains only one type of order, either magnetic or superconducting,
both phases with comparable free energy [170].

Evidence of phase separation was found in the local probe NMR and μSR studies of similar
systems [170, 184–186] and in a neutron scattering study of this very same sample [61]. Taking
this into account, H. Jacobsen *et al.* have previously advocated for a phase separation in which
one part of the crystal shows static magnetic order and associated Goldstone modes, while other
parts of the crystal display low-energy fluctuations without static order at a slightly different
incommensurability. The Goldstone modes associated with the static magnetic order are thought
to be too weak to be detected with neutrons when superimposed on the signal from the low-
energy fluctuations.

Another proposal of phase separation in the cuprate family was put forward in the case of
underdoped LSCO [47]. There, the electronic structure of the sample was interpreted as divided
into two phases; magnetic order with low-energy fluctuations (< 4 meV) in some parts of the
crystal and gapped higher energy fluctuations and superconductivity in other parts of the crystal.
Evidence for this phase separation was: (1) a dip in the energy spectrum at ~ 4 meV and (2) a
small change of linewidth of the signal at this energy. Our data does not show a dip in the energy
spectrum but exhibits a small variation of linewidth as a function of energy (see Figure 6.3.1).
However, it should be noted that such effects are very subtle and hard to detect, and we therefore
hesitate to draw definite conclusions based on our observations.

In the large number of studies performed on the $La_{2-x}M_xCuO_{4+y}$ family of superconductors,
two general types of magnetic behaviour in the superconducting state, have been observed: (1)
compounds that do not exhibit magnetic order and have gapped low-energy spin excitations
below T_c and (2) compounds where magnetic order is present concomitantly with a continuous
spectrum of spin fluctuations, albeit with reduced strength at low energies. Our stage-4 LCO+O
sample belongs to the latter category, exhibiting both static stripe order as shown in Figure 6.4.7(b)
and ungapped low-energy fluctuations as displayed in Figure 6.4.2(b). In our sample, fluctuations
appear insensitive to the onset of superconductivity. In fact there is a strengthening of the low-
energy spin susceptibility at the lowest temperatures. The suppression of the very low-energy
signal ($\hbar\omega < 4$ meV) with increasing temperature is likely a consequence of decreased spin
coherence. Figure 6.4.1(c) points to a complete destruction of spin coherence at $T \sim 70$ K. Our
sample is therefore different from optimally doped LSCO, which does not show static order and
in which low-energy spin fluctuations are gapped in the superconducting state and furthermore

persist up to 350 K. [179] The latter feature is depicted by the grey data points in Figure 6.4.2(b) which are reproduced from Refs. [55, 124]. At doping $x \simeq 0.16$, LSCO exhibits a spin gap of roughly $\Delta_{0.16} \sim$ 6-7 meV. This sample has a similar optimal value of $T_c \simeq 39$ K as found in LCO+O. In the event that LCO+O had a (magnetically) similar superconducting phase as in optimally doped LSCO, this would show up as an incomplete spin gap around $\Delta_{0.16}$ in our measurements. This is clearly not the case.

We can think of four scenarios that would be compatible with the lack of spin gap: (1) if super-conductivity arises in yet other parts of the crystal, where there are no low-energy spin fluctuations of $\hbar\omega < 7$ meV, (2) an increase in the low-energy fluctuations in the non-superconducting part of the sample exactly matches a decrease of the fluctuations in the superconducting regions, (3) a spin gap emerges at other wave vector not explored in this study or (4) superconductivity coexists with and does not compete with low-energy magnetic fluctuations. The two first scenarios seem unlikely, since (1) would imply regions with a very different low-energy electronic behaviour not observed in any other superconductors to date, (2) would seem like an improbable coincidence and (3) time of flight neutron measurements on similar samples [64, 99], which explored larger portions of the reciprocal space, have not shown any other contributions to magnetic scattering emerging at a different wave vectors. Thus, we are left with the fourth scenario, which points to a coexistence of low-energy fluctuations and superconductivity in LCO+O.

In underdoped LBCO, a lack of spin gap has also been observed and interpreted as evidence of a pair-density-wave (PDW) type of electronic structure with intertwined modulated supercon-ducting order and spin stripes. [64, 66] In our sample, we interpret the absence of any significant decrease in χ'' for $T < T_c$ at energies $\hbar\omega \leq 10$ meV, as an indication that superconductivity in LCO+O microscopically coexists with the low-energy magnetic fluctuations. However, because of additional evidence that the low-energy fluctuations do not occur in the same spatial regions as the static magnetic order [61], this proposed coexistence phase is different from the usual PDW phase: only low-energy fluctuations are intertwined with superconductivity, while magnetic order appears as a separate, probably competing, phase. In addition, by presenting our data on an absolute scale, we find that the magnetic spectral weight of low-energy fluctuations in LCO+O is approximately five times lower than that of LBCO or the parent compound, LCO (see the Appendix A). In LBCO, the strong magnetic response was taken as indication that magnetic order and fluctuations coexist locally with superconductivity in the entire bulk of the sample. The reduction of magnetic spectral weight in LCO+O found here points to the fact that there is a smaller volume fraction attributed to each of the different electronic phases. In particular, a fraction of the sample shows AFM order and the corresponding magnetic signatures as we have shown through polarised neuron measurements.

The temperature dependence of the magnetic susceptibility of LSCO with $x = 1/8$ dop-ing [114] is remarkably similar to our findings in LCO+O. This might indicate a similar coexistence of low-energy fluctuations and superconductivity in that system as well. Note that an additional similarity of LCO+O and LSCO $x = 0.12$ is the curious insensitivity to a magnetic field of the low-energy fluctuations, which could provide further support for a coexistence phase.

6.5.2 *Magnetic field effect*

A uniform d-wave superconductor is expected to show magnetic field-enhancement of the magnetic spectral weight at low energies since the destruction of superconductivity in the vortex cores paves the way for magnetic order [187]. This is opposite to our observations in LCO+O, see Figures 6.4.3(a) and 6.4.4(a) where we instead of a field-enhancement find a small suppression of the spectral weight at low energies in the range $\hbar\omega = 0.7\text{-}1.5$ meV. In optimally doped LSCO samples, the sub-gap field-induced states are thought to originate from a separate electronic phase most likely prevailing in the vicinity of the vortices [53, 124]. This explanation is similar to the previously-mentioned phase separation scenario proposed by M. Kofu *et al.* [47] where low-energy fluctuations, in underdoped LSCO samples, are thought to originate from a phase different from the superconducting one. In our sample, on the contrary, we argue that the low-energy magnetic fluctuations coexist with superconductivity without being in direct competition. For this reason, we do not expect a significant effect, on the magnetic excitations spectrum, induced by the appearance of a vortex lattice in the superconducting regions. This is in agreement with our observations of a weak suppression of the low-energy signal in a 10 T or 12 T applied magnetic field.

On the other hand, in terms of elastic stripes, in opposition to the lack of field effect in our sample (see Figure 6.4.3(c)), B. Khaykovich *et al.* [171, 172] and Y. Lee *et al.* [136] have previously reported a significant field enhancement of the elastic signal, comparable to the effect of electronic disorder induced by quenched cooling, in both stage-4 and stage-6 LCOO samples. Taking into account the high quality of our crystal, which exhibits a sharp single transition to superconductivity at 42 K (Figure 6.4.1(a)), we can think of two possible explanations for this discrepancy: (1) the slow cooling procedure we used in our experiments (with a cooling rate of 1 K/min) could differ from that used previously and result in a different arrangement of the excess oxygen, leading to a different electronic configuration at base temperature; (2) subtle differences in the oxygenation procedure could have created samples with different ground states containing various ratios of superconducting and magnetically ordered phases.

With respect to the first explanation, the exact cooling rate used during the field experiments is not stated in the literature. The only value we can compare against is the quench cooling rate of ~ 2.8 K/min [136] that creates a significant structural distortion which in turn induces an enhancement of the magnetic order. Only if our sample were to be in a highly disordered phase, following the cooling procedure, the effect of an applied magnetic field would be as insignificant as the one we have measured. This is highly unlikely, since our much lower cooling rate of 1 K/min is expected to give rise to an ordered oxygen lattice at low temperatures.

The second and more likely scenario is based on observations by J. Chang *et al.* [53], demonstrating that the effect of an applied magnetic field is to enhance the magnetic order in LSCO samples towards a common plateau level, which corresponds to the ground state of systems with 1/8 doping value. In this case, the initial fraction of the magnetically ordered phase in the sample dictates the magnitude of the impact of an applied magnetic field. Thus, the lack of a field effect which we have measured, indicates that our sample, in contrast with the ones used by B. Khaykovich *et al.* and Y. Lee *et al.*, exhibits a fully developed magnetic phase already in zero

applied magnetic field. We note that this does not prohibit the existence of a superconducting phase with similarly high T_c compared to samples with magnetic phases of different magnitudes.

6.5.3 *Stripe structure and twinning*

Through polarised neutron measurements we have been able to confirm the magnetic origin of the elastic intensity measured at the antiferromagnetic reflection. In a homogeneously doped sample, AFM order would not be expected. However, in oxygen doped samples, phase separation into oxygen-rich and oxygen-poor regions [145] might result in a remnant AFM order in small (presumably undoped) parts of the crystal. This is precisely what we observe in our crystal. The XYZ polarisation analysis allowed us to also determine the orientation of the AFM phase. As it can be deduced from Figure 6.4.6, by using Equations 4.29, the magnetisation of the AFM phase lies along the y-direction which is equivalent to the real space orthorhombic b-direction (see Figure 6.1.2). This is in agreement with measurements performed on the undoped parent compound of the family (LCO) [104].
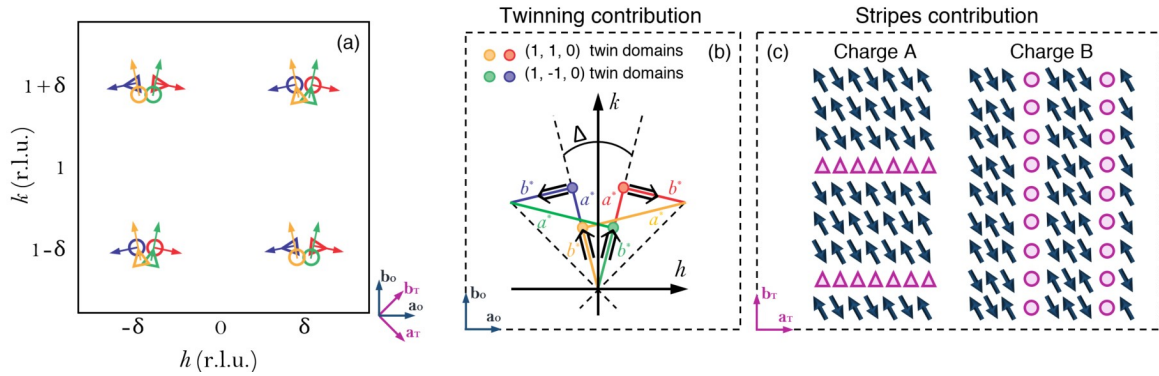
Figure 6.5.1: (a) A cartoon illustration of the neutron scattering signal generated by the incommensurate AFM spin structure including contributions from all four crystal twins. **(b)** Twinning of a structural peak into two domains each composed of a pair of twins. The direction of the orthorhombic b-axis, which corresponds to the spin direction, is shown by a double-arrow for each twin peak. Δ is the angular separation between two twin reflections [188] and in our orthorhombic system has a value $\Delta = 90° - 2\arctan\left(\frac{a}{b}\right) \sim 0.8°$, a splitting too small to be resolved given our Q-resolution. a^* and b^* are the reciprocal lattice constants in orthorhombic notation. Image adapted from the Supplemental Material of Ref. [61]. **c)** The stripe pattern arising from charge stripes running along the tetragonal a_T-axis (Charge A) and the tetragonal b_T-axis (Charge B). The triangles and circles indicate how the charge orientations corresponds to the incommensurate peak structures in (a) for the local coordinate system of each twin type, which are rotated by 90 degrees with respect to each other.

In terms of the incommensurate spin stripe modulation, in order to analyse its orientation we consider two arrangements of the charge stripes which are assumed to accompany the magnetic stripes as antiphase domain walls [189]. The two possible arrangements of charge stripes along the tetragonal axes are depicted in Figure 6.5.1(c). To access information about the structure of the spin stripe modulation we need to take into account all four possible twin orientations, which are naturally present in the system due to its weak orthorhombicity. We follow the detailed description of the twinning pattern presented in Ref. [188] (note that the tetragonal notation in the cited reference corresponds exactly to our orthorhombic cell). This twinning structure complicates the interpretation of the data significantly. We present a detailed discussion based

on the electronic stripe structure combined with the crystal twinning and illustrate the different contributions in Figure 6.5.1. The typical twinning pattern of peaks along the measured $(0, k, 0)$ direction is depicted in Figure 6.5.1(b), where the orthorhombicity is exaggerated for clarity. The spin direction is drawn along the orthorhombic b-axis of the local coordinate system for each of the four twin peaks.

The presence of magnetic stripes, which are in general incommensurate with respect to the crystal structure, is observed in neutron scattering experiments as a splitting of the antiferro-magnetic $(0, 1, 0)$ reflection into four peaks. Signals along one diagonal, *e.g.* $\mathbf{Q} = (\delta, 1 + \delta, 0)$ and $\mathbf{Q} = (-\delta, 1 - \delta, 0)$, belong to charge stripe patterns along the tetragonal a_T-axis, while the signals along the other diagonal arise due to stripe formation in the perpendicular direction, *i.e.* the b_T-axis. The orientation of the charge stripe patterns, either along the tetragonal a_T or b_T-axis, are illustrated in Figure 6.5.1(c). The commensurate structure shown here is the special case of a peak splitting of $\delta = 1/8$.

In the most general case, we expect the twinning structure to be present at all four peaks in the incommensurate peak quartet, as suggested by the colour coded symbols in Figure 6.5.1(a). This figure furthermore provides an illustration, through the two types of symbols, of the charge stripe orientation that underlies each peak structure. Charge stripes along the tetragonal a_T-axis are depicted by triangles, while charge stripes along the tetragonal b_T-axis are shown by circles with reference to Figure 6.5.1(c). Because each twin domain is composed of a pair of twins with interchanged a_O and b_O axes, we obtain two sets of twins with axes oriented in the same direction, namely red/blue and yellow/green. For the yellow/green domains, stripes along the a_T-axis (charge A) will give incommensurate magnetic peaks at positions $\mathbf{Q} = (\delta, 1 + \delta)$ and $\mathbf{Q} = (-\delta, 1 - \delta)$, while stripes along the b_T-axis (charge B) will cause incommensurate magnetic peaks along the other diagonal, i.e. at $\mathbf{Q} = (-\delta, 1 + \delta)$ and $\mathbf{Q} = (\delta, 1 - \delta)$. The situation is circumvent for the red/blue domains, because the a_T and b_T axes are interchanged in these twins compared to the green/yellow twin domains, as illustrated in Figure 6.5.1(b).

In this way, the underlying charge structure for each twin contribution to the incommensu-rate signal is shown as circles and triangles in Figure 6.5.1(a) with the colour code as defined in Figure 6.5.1(b). The spin directions for each peak is depicted by arrows, showing the direction of the orthorhombic b-axis of each domain.

In the experiment, we scanned over peaks belonging to both types of charge stripes by scanning through $\mathbf{Q} = (-\delta, 1 + \delta)$ and $\mathbf{Q} = (\delta, 1 + \delta)$. The scanning direction is shown in the inset of Figure 6.4.7(b). Since we only register signals where the scattering vector is perpendicular to the spins, we primarily pick up intensity due to the red/blue domains and only negligible weight from the yellow/green domains. Thus, we compare the relative strength of the charge types A and B of the red/blue twins and we can decide whether the system displays charge stripes along only one of the tetragonal axes or along both directions.

As shown in Figure 6.4.7(b), we find that the peaks at $\mathbf{Q} = (-\delta, 1 + \delta)$ and $\mathbf{Q} = (\delta, 1 + \delta)$ have similar amplitudes. From the equal signal amplitudes at both incommensurate positions, we conclude that charge stripes form along both the a_T- and b_T-direction and are equally present within the sample. In the event that charge stripes had a preferred direction (parallel or perpen-dicular to the b_T-axis), only one of the two IC peaks would have been visible. Our finding that the

system displays charge stripes along both tetragonal axes is similar to the observation in LBCO with $x = \frac{1}{8}$ [116].

We now turn to the inelastic polarised data of Figure 6.4.7(a). As opposed to the static signal, which shows that spins are purely in-plane, the inelastic scattering signal at $\hbar\omega = 1.5$ meV shows a clear out-of-plane spin component. First, we consider the expected outcome of the signal ratios in the case of isotropic spin fluctuations, where fluctuations along all three spin directions are equal in magnitude, *i.e.* where the transverse and longitudinal fluctuations are equally strong. Then we would expect to see the same signal strength in the spin channels $S \parallel y$ and $S \parallel z$ and double intensity strength in the spin channel $S \parallel x$, i.e. a signal ratio of $2/1/1$ for the spin channels $x/y/z$. At the opposite end, we consider isotropic transverse fluctuations with longitudinal fluctuations being negligible, i.e. transverse fluctuations of equal strength in all directions perpendicular to the spin direction, but no fluctuations in the direction of the ordered moment. In this case, we would expect a signal ratio of $3/2/1$ taking into account the twinning structure. To distinguish between these two limiting cases, we calculate the ratio between the measured peak areas of the three spin channels with the results shown in the third column of Table 3. These results are compared to the expected ratios in the case of isotropic and purely transverse fluctuations, see fourth and fifth columns of Table 3. This provides guidance to the dominating nature of the incommensurate spin fluctuations at 1.5 meV.

Neutron spin direction	Magnetic scattering	Area	Isotropic	Transverse
$\frac{S\parallel x}{S\parallel y}$	$\frac{M_y + M_z}{M_z}$	2.2 ± 0.7	$2/1$	$3/2$
$\frac{S\parallel x}{S\parallel z}$	$\frac{M_y + M_z}{M_y}$	2.5 ± 0.8	$2/1$	$3/1$
$\frac{S\parallel y}{S\parallel z}$	$\frac{M_z}{M_y}$	1.1 ± 0.4	$1/1$	$2/1$

Table 3: Comparison of the fitted intensity of the inelastic polarised neutron data. The ratio of intensity in the different spin channels is shown in terms of peak area. The values are obtained by adding the fitted parameters of the 2 peaks. For the fits, the peaks position and widths are fixed to the values obtained by fitting all the data (from all 3 channels) combined. The last two columns show the expected signal ratios in the case of isotropic fluctuations and purely transverse fluctuations.

The data indicates that the spin fluctuations are isotropic, in particular because the signals with polarisation along the y- and z-directions are almost equal. However, we have only taken into account the extreme cases. It should be noted that intermediate cases could lead to similar signal ratios. For example, anisotropic transverse fluctuations with a more pronounced in-plane component (in the x-y plane) than out-of-plane component could also result in a signal ratio of $2/1/1$ for the spin channels $x/y/z$ which would be compatible with the obtained signal ratios.

As mentioned before H. Jacobsen *et al.* [61] observed a difference in incommensurability between the static signal and low-energy spin fluctuations which led them to conclude that magnetic order and fluctuations likely originate from separate spatial domains within the crystal. If the nature of the low-energy spin fluctuations had been primarily transverse, i.e. spin-wave-like Goldstone modes of the static spin order, this would have contradicted the findings of Ref. [61]. The observation that the 1.5 meV fluctuations are more likely of isotropic character supports

the interpretation in Ref. [61] and re-affirms our hypothesis that the low-energy fluctuations reside in different parts of the crystal than the static order. This adds to our interpretation of a real space co-existence of superconductivity and low-energy fluctuations as discussed in the previous sections.

6.6 CONCLUSIONS AND OUTLOOK

This chapter presents an extensive neutron scattering study which characterises the magnetic order and fluctuations in the stage-4 oxygen doped $La_2CuO_{4+\delta}$ superconductor.

The lack of a spin gap together with a weak magnetic field induced suppression of the low-energy magnetic spectrum is interpreted as an indication that superconductivity and spin fluctuations co-exist microscopically in an intertwined phase with no sign of competition. Notably this happens in a single layer cuprate superconductor that exhibits a clean superconducting transition with one of the highest critical temperatures of $T_c = 42$ K. To further elucidate the nature of the superconducting state, it would be interesting to investigate the presence or absence of a magnetic resonance peak by inelastic neutron measurements of high energy spin excitations. One of the fingerprints of a pair-density-wave phase [10], as described in the literature [116], is the absence of the magnetic resonance peak [64, 66] otherwise observed, in standard d-wave SC, at $E_{cross} \approx 40$-50 meV [60, 190, 191]. Furthermore, a careful study of the spin correlation length across different energies has the potential to reveal new information about the magnetic spectrum and whether it is fluctuations of all energies that co-exist with superconductivity or only the low-energy ones.

On the other hand, we consider magnetic order to be a separate electronic phase competing with superconductivity, in agreement with previous interpretations from the literature [56]. The lack of a magnetic field effect on the elastic stripe signal, shows that our sample contains a fully developed magnetic phase. This observation contrasts previous reports of a magnetic field enhancement [136, 171, 172], and is possibly explained by discrepancies in the initial magnetic volume fraction of crystals which have been doped under different oxygenation procedures.

The XYZ polarisation analysis revealed the presence of equal fractions of static spin stripe modulations, induced by charge stripes, oriented along either of the tetragonal a_T-axis or b_T-axis. However, our data does not provide information about a possible orthogonal arrangement of stripes in adjacent CuO_2 planes, as discussed in the case of LBCO [57] and most likely, phase sensitive measurements are required to pursue this further.

In terms of dynamic spin stripes, our data, corroborated with the study by H. Jacobsen *et al.* [61] supports the hypothesis that the magnetic fluctuations in LCO+O are likely isotropic in nature, but further work is needed to confirm this. A detailed study of fluctuations, with measurements also along the l-direction in reciprocal space has the potential to shed light onto this matter. Due to long counting times, imposed by the polarisation set-up and the intrinsic weak magnetic inelastic signal, combined with the necessity to re-align the sample, we have not been able to further pursue this idea.

---

10 Another fingerprint is the lack of a spin gap similar to our observations on this sample.

Lastly, the polarisation analysis of the antiferromagnetic signal revealed the existence of an undoped AFM phase in our sample, similar to previous reports from the literature on other LCO+O crystals [145]. At the same time, we were able to confirm that the spin orientation along the orthorhombic b-axis of the parent LCO compound is conserved upon doping.

In conclusion, we propose a picture of electronic phase separation in LCO+O samples into two competing phases, where one exhibits magnetic stripe order while the other hosts superconductivity intertwined with low-energy spin fluctuations.

NON-DESTRUCTIVE CHARACTERISATION OF DOPANT SPATIAL DISTRIBUTION IN CUPRATE SUPERCONDUCTORS

This chapter is heavily based on our recently published manuscript [182]. The motivation for this research came after the discovery of a significant discrepancy in superconducting critical temperature, measured by magnetic susceptibility, of small crystal pieces originating from the two ends of our LSCO $x = 0.08$ single crystal. Proper characterisation of investigated samples is vital when studying superconductivity as impurities and doping inhomogeneities can affect the physical properties of the measured system. We have thus looked for a non-destructive method to characterise the doping distribution in our samples. Polarised neutron imaging, the technique used in this study, utilises the precession of spin-polarised neutrons in the presence of a trapped field in the superconducting sample to spatially map out the critical temperature for the phase transition between superconducting and non-superconducting states. Through this investigation we demonstrate this method on a superconducting crystal of the prototypical high-temperature superconductor $(La,Sr)_2CuO_4$. The results, which are backed up by complementary magnetic susceptibility measurements, show that the method is able to resolve minor variations in the transition temperature across the length of the LSCO crystal, caused by inhomogeneities in strontium doping.

7.1 LITERATURE REVIEW

As it has been pointed out numerous time throughout this thesis, in recent years, increasing amounts of evidence points to the interplay between magnetism and superconductivity as a key factor in the emergence of the latter [33]. One of the most widely used methods of studying highly correlated electron systems, and in particular intertwined electronic orders, is neutron scattering. Especially when investigating spin density wave order and the related fluctuations in cuprate superconductors, neutron scattering has played a major part in revealing the nature of their relationship with SC [61, 95, 192].

One of the many advantages of using neutrons as a probe is their charge neutrality, which makes them interact rather weakly with most matter [72], in contrast with, for example, X-rays. This allows the probing of the entire bulk of the sample in different environments such as magnets, pressure cells, cryostats or furnaces. However, the drawback is that, in order to measure weak

signals, samples of large masses are needed during experiments. When it comes to cuprate superconductors, the growth of large high-quality single crystals is not a trivial task. On top of that, due to the fact that the intrinsic properties of these materials are under scrutiny, the use of high quality and purity samples is a prerequisite as the analysed physical properties can be drastically affected by defects, impurities or inhomogeneities. This has increased the need for non-destructive characterisation methods which are able to accurately determine the physical properties of the entire bulk of the sample. One such property is the doping concentration, a parameter extremely important in defining the phase diagram of the compound, since it has direct impact on the superconducting properties [47].

Even though most neutron experiments have long ago taken advantage of the possibility to perform polarisation analysis to study magnetic structures, polarisation analysis for neutron imaging was only proposed a bit more than a decade ago [193]. Since then a number of studies have focused on proving the capabilities of the technique to map out magnetic fields, structures and phenomena [194–197]. Here, we propose and demonstrate the use of polarised neutron imaging as a non-destructive method for determining the distribution of the superconducting critical temperature (T_c) along the length of a HTSC sample, which is in turn related to the doping concentration distribution. Our sample is the prototypical cuprate HTSC $La_{2-x}Sr_xCuO_4$ (LSCO) of nominal doping $x = 0.08$. With this method we were able to detect an inhomogeneous distribution of the dopant throughout the sample. In contrast, when performing standard magnetic susceptibility measurements only small sample pieces are used, usually cut from only one side of the crystal, thus the result cannot be considered representative for the entire bulk. By measuring magnetic susceptibility on pieces originating from both ends of the main single crystal we were able to confirm the T_c difference, but the precise Sr concentration at each position in the sample went undetected.

7.2   THE SAMPLE

The sample used throughout this study is a cylindrically shaped (17.9 mm height, 4.75 mm diameter and ∼ 5 g mass) non-annealed LSCO sample with nominal Sr doping $x = 0.08$. The crystal has been grown using the Travelling Solvent Floating Zone technique (TSFZ) [198] at Department of Energy Conversion and Storage, Technical University of Denmark. In the field of cuprate superconductors the TSFZ method is preferred to other procedures, such as the flux method or the Czochralski method, for a number of reasons. Firstly, the crystallisation takes place inside a mirror furnace thus preventing contamination which might arise from the chemical reaction between crucibles and the melt [134]. As shown in Figure 7.2.1, the polycrystalline feed rod together with the solvent pill (which acts as a promoter of the molten zone) are vertically melted by very powerful halogen lamps. After a stable molten zone has been achieved, the lamps are being translated upwards (or the feed rod downwards) allowing the material to solidify and, if the right thermodynamic conditions are achieved, crystallise into a single crystal phase. At the same time, TSFZ is the only of the three above-mentioned techniques which permits the growth of centimeter-size single crystals of compounds that melt incongruently [199]. One of the disadvantages that might arise from using this method to synthesise LSCO samples in

particular is the lack of compositional homogeneity of the melt throughout the growth process. This combined with the fact that the Sr atoms are fixed at the end of the crystallisation, unlike compounds with a mobile dopant, such as oxygen doped La_2CuO_{4+y}, results in heterogeneous samples [200]. Because it is impossible to monitor or control the dopant concentration during the growth, it is important to characterise the entire bulk of the sample before proceeding to draw conclusions on the fundamental properties of this family of superconductors.
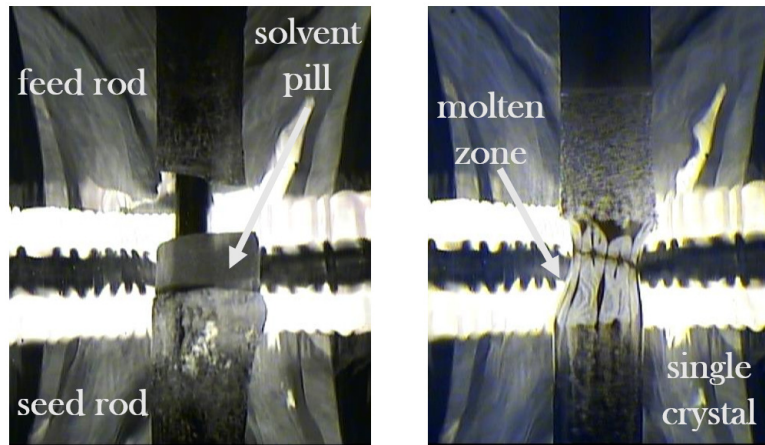
Figure 7.2.1: Images from inside the mirror furnace. *Left:* Initial configuration showing the three main components, the feed and seed rods, the solvent pill, and the bright light radiating from the halogen lamps. *Right:* Snapshot taken during a successful growth picturing the molten zone and the solidified single crystal material.

There are numerous ways to determine the doping concentration of a LSCO sample, some of the most widely used ones being measurements of magnetic susceptibility [201], electrical resistivity [202], heat capacity [203] and of the structural phase transition between the high temperature tetragonal phase and the low temperature orthorhombic one by means of elastic neutron scattering [92]. In order to test the doping homogeneity of our crystal, we have performed temperature dependent magnetic susceptibility measurements using a Quantum Design MPMS SQUID magnetometer. The set-up was used in DC magnetic measurements mode where the magnetic moment of the sample is determined from the local changes, induced by the movement of the sample, in the applied magnetic flux. Taking into account the sample volume, the magnitude of the applied magnetic field as well as demagnetising effects, the measured magnetic moment can be converted into units of susceptibility (χ) [204] (see also Appendix C). From the susceptibility as a function of temperature so obtained, it is possible to determine the critical superconducting temperature (T_c) at which the material abruptly transitions from a small positive susceptibility, corresponding to the antiferromagnetic state, to a diamagnetic phase characterised by negative susceptibility. T_c can be defined in various ways, the onset of the transition and the midpoint being the most popular ones. Throughout this chapter we define the magnetic susceptibility critical temperature (T_c^{χ}) as the diamagnetic saturation temperature obtained by fitting the data to a logistic function and following the slope at the inflection point down to the lower asymptote as it can be seen in Figure 7.2.2. This corresponds to the temperature at which a fully coherent superconducting state is established in the sample.
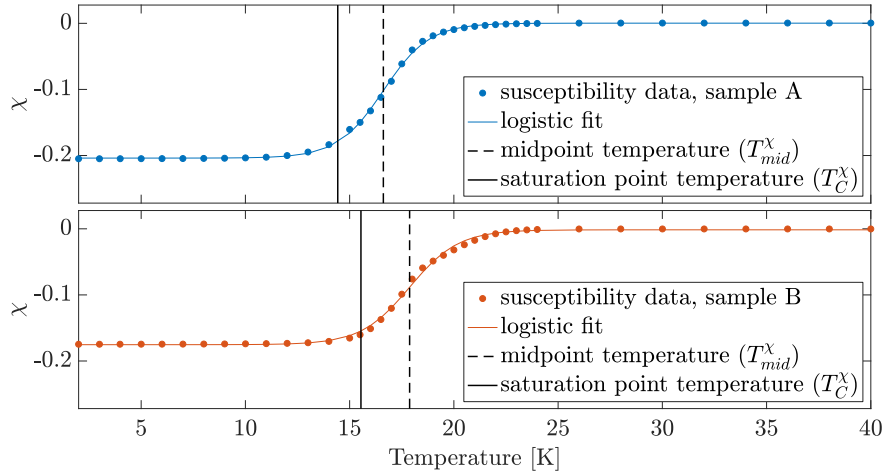
Figure 7.2.2: Magnetic susceptibility data of the two the cubes cut from each of the ends (A and B) of the single crystal sample. The deviation from $\chi = -1$ at low temperatures is due to magnetic flux trapping, which occurs when cooling the sample through the phase transition in an applied magnetic field $H = 800$ A/m (10 Oe). See Figure 7.4.2 and eq. 7.5 for fitting procedure.

Previous experimental studies have revealed a strong critical temperature anisotropy in LSCO superconductors. Measurements performed with applied magnetic field parallel to the (a, b)-plane show a higher critical temperature as well as an unexpected paramagnetic Meissner effect, recorded in the field cooled process under low applied magnetic fields [205]. To avoid this complication and in order to be able to directly compare our results with the ones from the literature [206] we chose to measure the magnetic susceptibility in the c-direction by using an applied magnetic field, $H = 800$ A/m (10 Oe), parallel to the c-axis ($H\|$c). For this reason the sample was aligned by hard X-ray diffraction, and small cubic pieces (~ 1 mm length) were cut from the two ends of the large single crystal, such that the c-axis was parallel to one of facets. The $\chi(T)$ measurements were performed using the field cooling (FC) protocol, where the sample is cooled from a temperature above T_c in a small static magnetic field ($H = 800$ A/m), while continuously recording data. Around the predicted critical temperature, from 24 K to 15 K, measurements have been taken every 0.5 K, while outside this range, larger temperature steps have been employed, 2 K steps from 40 K to 24 K and 1 K steps from 15 K down to 2 K. The measurements have revealed a mismatch in transition temperature between the two samples originating from the two ends of the main single crystal. One piece had a transition temperature $T_c^\chi = 14.43 \pm 0.09$ K and the other a $T_c^\chi = 15.54 \pm 0.18$ K (See Figure 7.2.2). This mismatch in critical temperature motivated the search for a non-destructive method that would be able to reveal doping variations in the entire bulk of the sample.

7.3   EXPERIMENTS

In order to probe the doping distribution along the entire length of the crystal in a non-destructive manner, we have performed polarised neutron imaging experiments at the PONTO-III (V21) instrument at the BER II nuclear reactor in Helmholtz-Zentrum Berlin. The instrumental set-up is shown in Figure 7.3.1. The instrument makes use of a cold neutron beam which, for this experiment, was monochromatized to 3.4 Å.
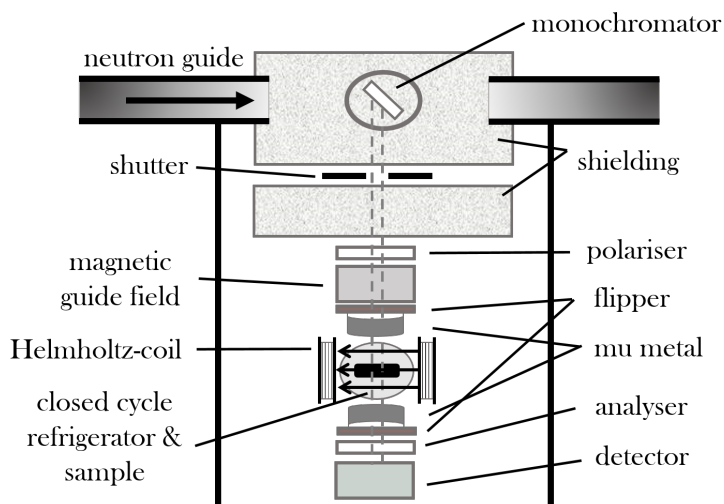
Figure 7.3.1: Sketch of the polarised neutron set-up used for the present measurements. Adapted from [207].

The control of the initial spin state of the neutrons as well as the analysis of their final spin state was done with the help of two super-mirror polarisers placed before and after the sample. A guide field was used to keep the neutron spin vertically aligned from the polariser up to the sample region and mu-metal shielding was used just before the sample as well as between the sample and the analyser. A single spin-flipper was used to select between spin-up and spin-down measurements.

In a polarised neutron imaging experiment there are two main methods of determining the superconducting critical temperature: by probing the Meissner transition or by imaging the trapped magnetic flux inside the superconductor as a function of temperature [193, 207]. In this study we employed the latter method. This requires cooling the superconductor through its critical temperature inside an applied magnetic field and performing the measurements while heating up the sample without applied field. This way, one is able to trap magnetic flux inside the superconductor and probe its release as the sample returns to the normal, non-superconducting state.

The single crystal used in this study was aligned in the (b, c)-plane and mounted on an aluminium sample holder inside a closed cycle refrigerator which was able to reach temperatures as low as 4.5 K. During the cooling procedure, a pair of Helmholtz coils were used to apply a horizontal magnetic field parallel to the c-axis of the sample and perpendicular to the neutron beam direction. The sample was slowly cooled from room temperature down to 100 K with a rate of 2 K/min followed by a higher cooling rate of 5 K/min down to 40 K. At this point, an external magnetic field was applied and the sample was further cooled below its superconducting critical temperature down to the base temperature of the closed cycle refrigerator, thus trapping the magnetic flux inside the sample. The external magnetic field was then switched off and radiographs were recorded, by a scintillator - CCD camera detection ensemble (camera: Andor DV 434-BV, effective pixel size: 77 m, ^{6}LiFZnS scintillator thickness: 400 m [208]), at various temperatures during the heating process. The horizontal divergence of the neutron beam was 0.34° and the vertical divergence was 1.28°.

Each image registers the polarisation of the neutron spin, defined by a precession angle calculated in modulo 360°, analysed by the second super-mirror polariser placed between the sample and the scintillator. As the neutron passes through the magnetic field trapped inside the superconducting material, the spin will undergo a so-called Larmor precession. The precession angle (ϕ) is dependent on the strength of the applied magnetic field and the time spent by the neutron inside it, which in turn is dependent on the neutron velocity (and thereby on its wavelength) as well as the length of the path through the magnetic field [207]:

$$\phi = \frac{\gamma_L m}{h} B L \lambda. \tag{7.1}$$

Here, $\gamma_L = -1.83247179(43) \times 10^8$ rad s^{-1} T^{-1} is the neutron's gyromagnetic ratio, $h = 6.62607015 \times 10^{-34}$ J s is Plank's constant, $m = 1.674927471(21) \times 10^{-27}$ kg is the mass of a neutron and B, L and λ are the strength of the applied magnetic field, the length of the neutron trajectory inside the field and the neutron wavelength respectively.

The magnitude of the applied magnetic field was of the order of a few milli-tesla, and was tuned to provide the most contrast while keeping the maximum precession angle below 180° in order to avoid ambiguity, as the measured polarisation is the cosine of the (ensemble average of the) neutron spin precession angle:

$$P = \langle \cos(\phi) \rangle. \tag{7.2}$$

In our experiment the maximum measured precession angle was $\sim 105°$.

Radiographs were recorded in two spin configurations: spin up and spin down, with the spin of the neutron in both being perpendicular to the beam direction. Spin down was selected by using an additional magnetic field to add a neutron spin precession angle of 180° before the analyser. For normalisation purposes, dark frame images (DF) without neutrons and in zero applied magnetic field were recorded at room temperature (which means no trapped field in the sample) so that noise in the detector systems could be corrected for. Open beam images (OB) were recorded as well at room temperature, in the absence of both the sample and the applied magnetic field, so that imperfections in the polarisation set-up could be corrected for.

The dark frame radiographs were subtracted from all the corresponding images, including the open beam ones. The measuring time was 10 minutes per image (composed of 4 exposures of 150 s combined after DF subtraction). The open beam polarisation was calculated as:

$$P_{OB} = \frac{\uparrow_{OB} - \downarrow_{OB}}{\uparrow_{OB} + \downarrow_{OB}}, \tag{7.3}$$

where $\uparrow$ and $\downarrow$ indicate the radiographs taken with spin up and down configuration, respectively. The uncorrected polarisation signal with sample, P_{UC}, was measured and calculated in the same way, whereafter the open beam corrected polarisation, P, was calculated as:

$$P = \frac{P_{UC}}{P_{OB}}. \tag{7.4}$$

7.4   RESULTS AND DISCUSSION

7.4.1   *The polarised imaging data*

Figure 7.4.1 shows an image of the polarisation of the beam transmitted through the sample, collected at six temperatures between 5 K and 20 K. In total, we collected data in temperature steps of 1 K between 5 K and 34 K. The direction of the field was along x, the neutrons were initially polarised along y, and the polarisation analysis was also performed along y. To improve counting statistics, the data was rebinned spatially by a factor of 6 along x and y to an effective pixel size of 0.462×0.462 mm^2. At the lowest temperature it can be seen that the entire LSCO sample causes a large deviation of the neutron beam polarisation vector (blue colour) with respect to the initial imposed direction. At the centre of the sample, the polarisation even reaches negative values, indicating a coherent rotation of the neutron polarisation inside the sample. This we interpret as the result of a trapped magnetic field. When the temperature is increased, the release of the trapped magnetic field is found to take place at different temperatures for different parts of the sample, as is evident from Figure 7.4.1. In particular, at 14 K only the left part of the sample depolarises the beam (i.e. is still in the superconducting state).
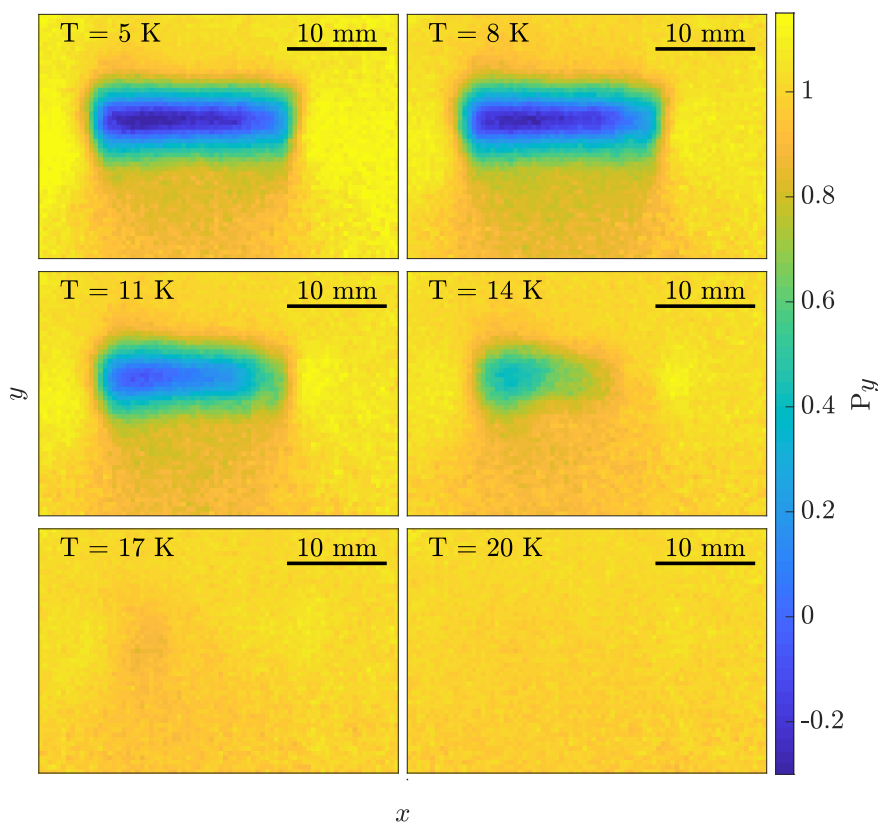
Figure 7.4.1: Polarisation transmission images as a function of temperature in the range 5 K to 20 K. The sample position (blue spot) can be seen in 5 K plot where neutrons passing through the trapped magnetic field in the sample undergo precession thereby moving the spin directions away from their initial polarisation along y. Neutrons were travelling along z and probing the trapped magnetic field, which was along x. As the temperature is raised the trapped field dissipates and no precession signal is observed. At 20 K the trapped field is completely gone. Notice how different ends of the sample lose their trapped field at different temperatures.

7.4.2 *Determining the distribution of T_c*

In order to quantitatively assess the superconducting transition temperature, T_C, for each pixel within the sample region, we first convert the polarisation data to spin precession angle through $\phi = \arccos(P)$, for each temperature, T. Values for pixel polarisations that due to noise were (slightly) larger than 1 were set to 1. Next, a logistic curve was fitted to the precession angle data, as the logistic function describes the sigmoidal nature of the phase transition between superconducting and non-superconducting states, such that values for the critical transition temperature can be extracted:

$$\phi = \phi_{\text{min}} + \frac{\phi_{\text{max}} - \phi_{\text{min}}}{1 + e^{-n_H(T - T_{\text{mid}})}}. \tag{7.5}$$

ϕ_{min} and ϕ_{max} are the low and high asymptotes, respectively, T_{mid} is the temperature at the inflection point of the slope, and n_H is Hill's coefficient, giving the steepness of the curve.

A fitting example for the centre-most pixel of the sample is shown in Figure 7.4.2. We define the critical temperature, T_c^{ϕ}, as the temperature where the trapped field is fully released. Within the logistics model, we approximate this by following the slope at the inflection point down to the lower asymptote as indicated by the dotted lines in the figure. The shaded area indicates the uncertainty interval of the estimated T_c^{ϕ}, where the error estimate was obtained from error propagation of the errors from the least square fit of the data, which was weighed using the error from the counting statistics of the measurement. Note that the low asymptote is non-zero, since a background magnetic field from the experimental set-up was present during the experiments at the given temperatures.
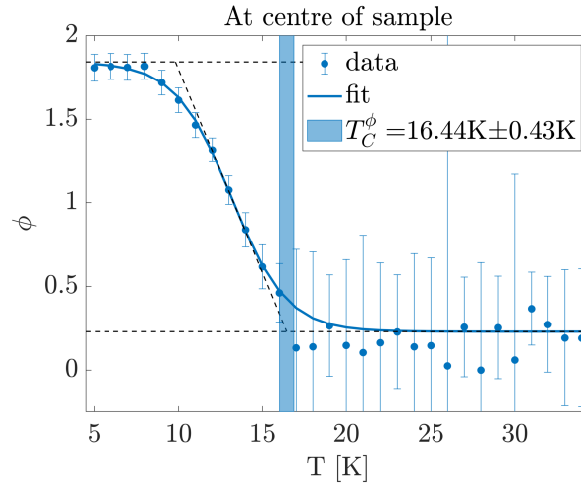
Figure 7.4.2: Example showing the fitting procedure for the central pixel of the sample using equation 7.5 to find the transition temperature, T_c, indicated by the shaded area.

The same fitting procedure was used to find T_c^{ϕ} for every pixel covered by the sample. The result is shown in Figure 7.4.3. A clear variation of T_c^{ϕ} is observed along the length of the sample, with a maximum T_c^{ϕ} of about 19 K at approximately 4 mm from one sample end. T_c^{ϕ} then drops to about 16 K at the end closest to the maximum and to 14 K at the opposite end. This corresponds to a strontium doping range $x \simeq 0.075 - 0.082$ [47, 201]. The doping range is in agreement with

the nominal doping of the crystal, its average value being exactly the intended doping value ($x = 0.080$) of the initial powder mixture. The variation across the length of the crystal can be explained as a slight accumulation of strontium atoms during one stage of the growth which in turn caused a deficiency of dopant at other stages. Furthermore, our results suggest that there is a radial variation of Sr distribution with more Sr at the sample surface. However, due to limited vertical resolution this result warrants further investigation. The required resolution is available at other neutron imaging instruments such as RADEN at J-PARC MLF [209].
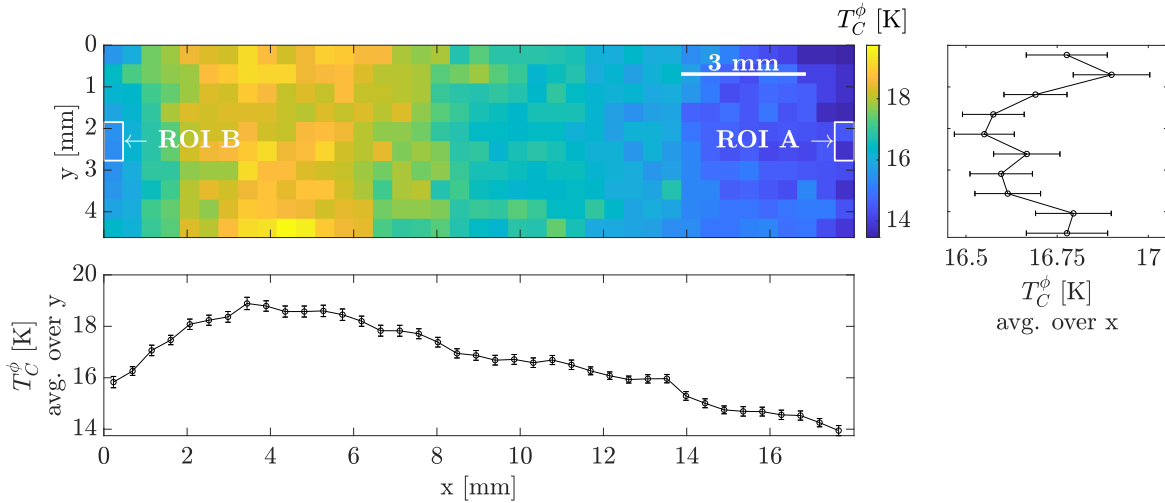
Figure 7.4.3: *Top left*: The transition temperature mapped out across the sample. Found using the method presented in Figure 7.4.2. The regions of interest (ROIs) indicated are used for comparing to susceptibility measurements on sample pieces that were adjacent to the ROIs (See Figure 7.4.4). *Bottom*: Transition temperature along the length of the sample, with data averaged over the width of the sample. *Top right*: Transition temperature along the width of the sample, with data averaged over the length of the sample. Note that, due to the vertical divergence, quantitative conclusions on the radial variation are limited.

In order to rule out a possible temperature gradient, the polarised imaging data was analysed to confirm that the temperature had stabilised before exposures and that no fluctuations were seen afterwards. Previous studies, with the same cryogenic set-up, mention temperature variations of maximum 0.01 K [193].

Using the polarised neutron imaging method we were able to identify the precise pattern of the critical temperature gradient, and implicitly the doping distribution, along the entire 17.9 mm length of the sample, in the growth direction. Considering that, within the TSFZ method, the molten zone is continually mixed and the material crystallises layer by layer, we do not expect a significant doping gradient in the radial direction. This can however be investigated using the tomography capabilities of a polarised imaging set-up. One of the advantages of using highly underdoped LSCO samples for this type of investigation is the fact that in this region of the phase diagram T_c varies steeply with doping, meaning that a small variation in Sr concentration corresponds to a significant critical temperature difference. However, using a high accuracy temperature control one would be able to determine the doping variation in samples across the entire superconducting dome, except the range $x = 0.14 - 0.18$, where T_c is essentially constant.

7.4.3 *Validation of the polarised imaging method*

We have also benchmarked our imaging results against magnetic susceptibility ($\chi(T)$) data. In Figure 7.4.4, we show, in comparison, the susceptibility data and the measurement of polarised neutron spin precession in trapped magnetic field for the two ends of the sample (shown as the two panels in the figure). As it can be observed, the results from the two measurements are in agreement, if we define T_c^χ, from the susceptibility data, to be the temperature where the negative susceptibility is saturated. Within errorbars, we find the same difference between the two sample ends for the two measurement methods. Due to the fact that the two methods are mapping different phenomena (one follows the diamagnetic response of the superconductor while the other images the expulsion of the trapped magnetic field as a function of temperature) a precise definition of T_c, to be applied to both measurements, is very hard, if not impossible, to formulate. However, the great agreement we are able to obtain by using the same fitting routine on the two data sets indicates that a fully developed superconducting state is a prerequisite for the formation of a vortex lattice and it proves that polarised neutron imaging is a reliable method of determining the spatial variation of the superconducting critical temperature and thus the doping level of superconducting crystals.
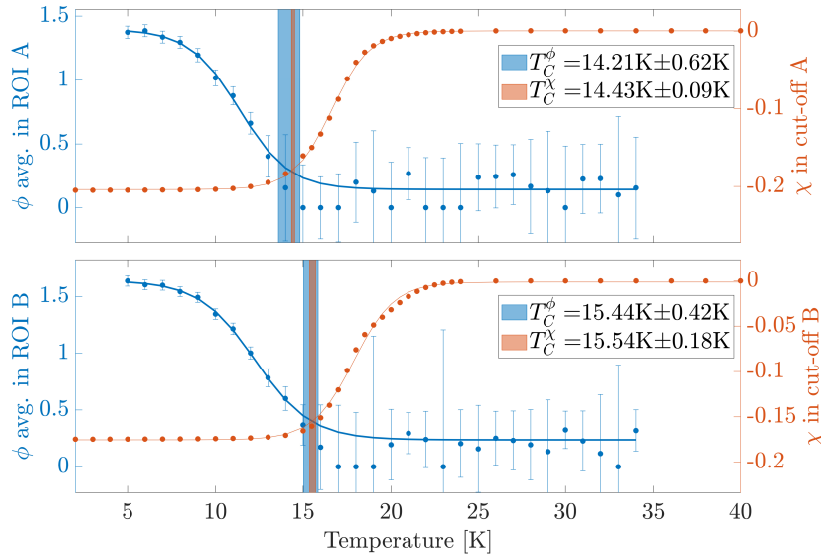
Figure 7.4.4: *Blue*: Fit of precession angle, ϕ, obtained by measuring polarised neutron spin precession in a trapped magnetic field as function of temperature. *Red*: Fit of magnetic susceptibility, χ, measured on cut off sample pieces that were adjacent to the two ROIs as indicated in Figure 7.4.3, ROI A (*Top*) and ROI B (*Bottom*).

Where the susceptibility method is more accurate (uncertainty around 0.1 K) than the polarised imaging method (uncertainty around 0.5 K), the latter method yields a complete picture of the sample and is furthermore non-destructive. For this reason, we can imagine polarised imaging to be an interesting alternative to susceptibility measurements for investigating the spatial variations in transition temperatures, and doping implicitly, in samples of centimetre sizes. Furthermore, by upgrading the instrumental components and extending the exposure time (and/or neutron flux) the precision of the measured transition temperature can be improved as

it is currently limited by counting statistics. The spatial resolution can be improved as well down to $100\,\mu m$ [194].

7.5 CONCLUSION

Homogeneity of a sample is important when investigating the superconducting properties, especially when performing bulk measurements. We have shown that through spin-polarised neutron imaging it is possible to directly map out the spatial distribution of the critical temperature thereby providing a characterisation method capable of eliminating uncertainties and sources of error related to – in this case – variations of the distribution of Sr doping in a $La_{2-x}Sr_xCuO_4$ high temperature superconductor. The results have been substantiated by magnetic susceptibility measurements showing the same trend for the T_c variation between the two ends of the sample.

Furthermore, as we are simply measuring a scalar property, our presented method for mapping the T_c distribution, can easily be expanded to three dimensional investigations using standard filtered backprojection methods for tomographic reconstructions.

8

MULTIPLE SCATTERING CAMOUFLAGED AS MAGNETIC STRIPES IN SINGLE CRYSTALS OF SUPERCONDUCTING (LA,SR)$_2$CUO$_4$

Neutron diffraction has been a very prominent tool to investigate high-temperature superconductors, in particular through the discovery of an incommensurate magnetic signal known as stripes. This chapter reports the findings of a neutron diffraction experiment on the LSCO superconductor with $x = 0.07$, where a spurious signal appeared to be magnetic stripes. The signal strength was found to be strongly dependent on the neutron energy, peaking at $E = 4.6$ meV. We therefore attribute the origin of this signal to be a combination of multiple scattering and crystal twinning. A forward calculation of the scattering intensity including these two effects almost completely recovers our experimental observations. We emphasise the need for employing such analysis when searching for ways to avoid spurious scattering signals.

Most of the material presented in this chapter has been included in our recently published article [210]. The data has been acquired during my Masters and presented there [135] as possibly originating from a multiple scattering event. The further analysis to prove this hypothesis has been performed during my PhD.

8.1 LITERATURE REVIEW

Since the initial discovery of cuprate superconductors [27], much like our work, numerous neutron scattering experiments have focused on characterising the static and dynamic spin correlations under different conditions in the attempt of determining their relationship with superconductivity. As it has probably become evident throughout this thesis, the interplay between superconductivity and magnetism is an extremely complex one which varies drastically as a function of type and amount of doping. For this reason it is utterly important to acquire high quality data on which future theories can be built upon.

From the early magnetic scattering studies performed on cuprates, multiple scattering was acknowledged as a possible contaminant of the stripe signal [50]. Here we present the results of a systematic neutron study aimed at determining the magnitude and origin of the double scattering events in a highly underdoped superconducting La$_{1.93}$Sr$_{0.07}$CuO$_4$ single crystal. The findings presented here can be taken into account as guidelines in the planning phase of

future experiments (i.e. by fine tuning the neutron beam energy) in order to obtain optimal measurements of magnetic stripes.

8.2 EXPERIMENTAL METHOD AND SAMPLE

The sample used throughout this study is a highly underdoped $La_{2-x}Sr_xCuO_4$ crystal with nominal doping $x = 0.07$. The large single crystal has been grown using the Traveling Solvent Floating Zone method and, later on, cut into two pieces, one annealed under oxygen gas flow as described in Ref. [100] (3.4 g) which is the main sample of this paper and a second which was kept as-grown. The true (average) doping has been determined, before annealing, in a neutron diffraction experiment [142] on the Morpheus diffractometer at the Paul Scherrer Institute (PSI), by following the temperature dependence of the strongly hole-doping dependent structural phase transition [92], from the high temperature tetragonal phase (*I4/mmm* space group number 139) to the low temperature orthorhombic one (*Bmab* space group number 64). The measurements revealed a transition temperature $T_s = 362 \pm 1$ K which corresponds to a doping of $x = 0.0753 \pm 0.0003$. The superconducting critical temperature of the as-grown and annealed crystals was established, through magnetic susceptibility measurements, to be $T_c^{onset} = 13.7 \pm 0.3$ K for both samples which is in agreement with measurements from literature on samples of similar doping [47].

Elastic neutron scattering investigations were carried out on the cold-neutron triple axis spectrometer RITA II at PSI [211]. The set-up contained a vertically focusing graphite monochromator, 80' horizontal collimation before the sample, a cooled beryllium filter after the sample in order to minimise the effects of higher order scattering contamination, followed by a graphite analyser consisting of 9 blades, each 25 mm wide, and a coarse cross-talk-avoiding radial collimator before a position-sensitive detector. The sample was aligned with the CuO_2 layers in the scattering plane, making it possible to access wavevectors in the $(h, k, 0)$-plane.

Throughout this chapter, as in the rest of the thesis, the orthorhombic notation is used, meaning that a commensurate antiferromagnetic reflection would be observed at $\boldsymbol{q} = (0, 1, 0)$, and crystallographically equivalent positions, and the stripe signal, due to its incommensurate magnetic modulation, should be visible at $(\pm\delta, 1 \pm \delta, 0)$, and equivalent positions, where $\delta \sim x$ in this low-doping regime [52]. In this notation, the 10 K lattice parameters of a $x = 0.0750$ doped crystal (a value very similar to the doping level of our crystal) were earlier reported as $a_o = 5.33$ Å, $b_o = 5.38$ Å, $c_o = 13.16$ Å [201].

To increase the efficiency of grid scanning around the antiferromagnetic reflection we made use of the monochromatic imaging mode of the multi-blade analyser. In this configuration, all 9 blades elastically scatter neutrons of the same energy, but due to the difference in scattering angle, each blade maps a slightly different portion of reciprocal space [212]. In this configuration, the effective collimation is determined by the width of the sample, the (narrow) analyser, and the distance between them. This leads to a collimation sequence of open – 80' – 40' – open. However, the results presented throughout the paper are not particular to this set-up. The same observations can be reproduced on a standard triple axis spectrometer with a single-blade analyser.

8.3 RESULTS

Initial neutron diffraction measurements were performed with incident and outgoing energies of 4.6 meV, corresponding to $k_i = k_f = 1.49 \text{ Å}^{-1}$, where k_i and k_f are the wave vectors of the initial and final neutron beams, respectively. This is a standard configuration of cold triple-axis instruments that allows for an optimal filtering of higher order scattering by cooled polycrystalline beryllium. The measurements revealed the presence of a peak at the antiferromagnetic position, which has previously not, to our knowledge, been reported in homogeneously doped systems of $x > 0.02$. In addition to this central peak, a number of satellite peaks at incommensurate positions $(\pm\delta_{obs}, 1\pm\delta_{obs}, 0)$ were also measured, as depicted in Figure 8.3.1(a), with incommensurability $\delta_{obs} = 0.023$, which is much smaller than the value expected from the dopant concentration: $\delta_x \sim x \sim 0.07$.
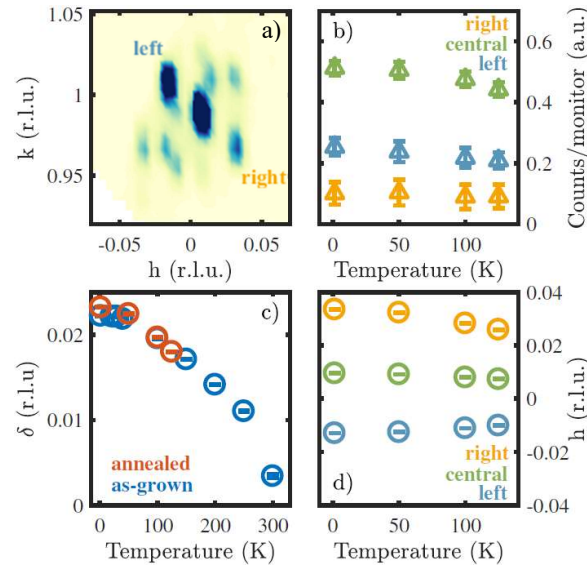
Figure 8.3.1: (a) Elastic scattering grid scan around the $(0,1,0)$ reflection taken at 2.5 K on LSCO with $x = 0.07$ (annealed crystal). Temperature dependence of the (b) peak intensity obtained from Gaussian fits, (c) incommensurability for both annealed and as-grown crystals of the same doping and (d) peaks position. The incommensurability is defined as half the distance between the two side peaks marked as 'left' and 'right' in sub-figure (a).

The temperature dependence of the signal, shown in Figure 8.3.1 was, however, significantly different from that of static magnetic stripes. First of all, the intensity persisted up to room temperature with only a slight decrease as a function of increased temperature in contrast with genuine spin stripes signal which, at this doping value, correlates with T_c [45, 47] within error-bars. Secondly, a decrease in incommensurability with increasing temperature was measured (Figures 8.3.1(c) and (d)), whereas the spin modulation in stripe signals was earlier found to be invariable to temperature variations. These two temperature effects were invariant to sample annealing (Figure 8.3.1(c)).

Because the temperature dependence of the peaks resembles that of the tetragonal-to-orthorhombic phase transition taking place at around 360 K, multiple scattering involving reflections allowed only in the orthorhombic phase was soon proposed as the origin of the signal. Following the textbook by G. Shirane, S. Shapiro, and J. Tranquada [213], the strict condition for

multiple scattering to occur is that more than one reciprocal lattice point lies on the surface of the Ewald sphere. Its presence can be tested by either rotating the crystal around the contaminated scattering vector or by changing the neutron energy of the diffraction experiment (*i.e.* changing the radius of the Ewald sphere). It should be mentioned that in a real experiment, where the incident beam is not perfectly monochromatized, the Ewald sphere should be seen rather as a spherical shell, the thickness of which corresponds to the spread in wave vectors of the neutron beam.

The method of changing wavelength of the diffraction experiment was employed in our experiments at RITA-II and the data is shown in Figure 8.3.2. Our findings clearly support the hypothesis of multiple scattering, since the incommensurate side peaks were only found at certain energies (4.5 meV to 4.7 meV) and the intensity of the central $(0,1,0)$ peak greatly decreased when the initial and final energies were modified. The more than one order of magnitude difference in intensity can be visualised in Figure 8.3.3 where 1 dimensional cuts thought the grids are plotted for two different energies.

Figure 8.3.2 also shows the result of a virtual experiment by the McStas ray-tracing simulation package [214, 215] of a hypothetical crystal showing single scattering at the $(0,1,0)$ reflection, in effect providing the resolution function of the instrument. Through the same McStas simulation it was found that the width of incoming energy, E_i, on the sample was 0.13 meV (FWHM). This value is the relevant number to determine the effective thickness of the Ewald sphere and is not equal to the energy resolution of the spectrometer (which is 0.20 meV FWHM), because the energy resolution of the secondary spectrometer is here not taken into account.
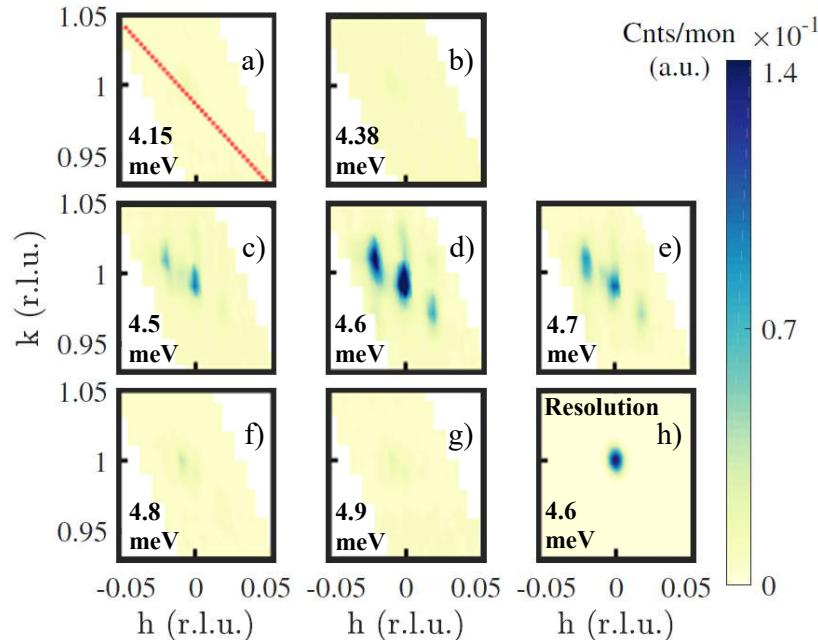
Figure 8.3.2: Diffraction measurements performed around the $(0,1,0)$ reflection at 125 K. The caption in each figure indicates the value of the initial and final energy of the neutron beam. Sub-figure (a) shows in red the direction of the two diagonal scans plotted in 2D in Figure 8.3.3. Panel (h) shows the simulated resolution of the instrument as presented in the text.
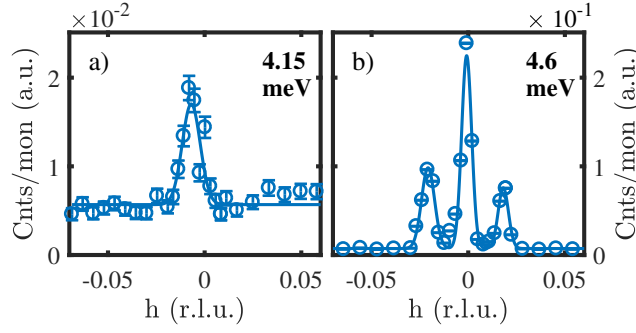
Figure 8.3.3: Elastic diagonal scans taken at different values of the initial and final energy, noted in the caption, in the direction exemplified in Figure 8.3.2(a). The solid lines represent a Gaussian fits to the data.

8.4   DISCUSSION

8.4.1   *Double scattering*

Due to the fact that the signal appears in a very narrow energy range and because we know the space groups of the crystallographic phases allowed in this sample, we were able to determine the reflections involved in a potential double scattering event. Following the treatment by G. Shirane, S. Shapiro, and J. Tranquada [213], we construct the Ewald sphere corresponding to our experiment as shown in Figure 8.4.1(a). In our particular case, the condition for double scattering is fulfilled if another allowed reflection of the low temperature orthorombic (LTO) phase lies on the surface of the sphere. This poses two requirements: (1) the existence of a secondary reflection wavevector k'_f of the same length as k_i; (2) the two scattering wavevectors q' and q'' should correspond to allowed reflections in the LTO phase (space group no. 64 in the unconventional *Bmab* setting [216]). k'_f is geometrically defined as:

$$k'_f = k_i - q'. \tag{8.1}$$

Using the scattering angle $\theta = \arcsin(q/2k_i)$ to calculate the angle $\varphi = 90° - \theta$ and knowing the lattice parameters corresponding to the LTO phase we are able to rewrite the components of k_i and q' as:

$$q'_x = h' \cdot \frac{2\pi}{a_o}, \qquad q'_y = k' \cdot \frac{2\pi}{b_o}, \qquad q'_z = l' \cdot \frac{2\pi}{c_o}, \tag{8.2}$$

$$k_{ix} = k_i \sin\varphi, \qquad k_{iy} = k_i \cos\varphi, \qquad k_{iz} = 0, \tag{8.3}$$

where h', k' and l' are the Miller indices of the allowed reflections in the LTO phase. We have investigated indices with values between -3 and 3. This decomposition allows us to calculate the corresponding k'_f in the energy range 4.5-4.6 meV for all the allowed reflections of the LTO phase:

$$k'_f = \sqrt{(k_{ix} - q'_x)^2 + (k_{iy} - q'_y)^2 + (k_{iz} - q'_z)^2}. \tag{8.4}$$

Checking the above mentioned condition (1), meaning comparing the values of k_i and k'_f, two pair of reflections appear to lie on the surface of the Ewald sphere $(0,2,-2)$ (equivalent to $(0,2,2)$) and $(1,1,-3)$ (equivalent to $(1,1,3)$). However, condition (2) is only fulfilled for the first pair since both $(1,1,-3)$ and $(1,1,3)$ require the disallowed q'' reflections $((-1,0,3)$ and $(-1,0,-3)$ respectively) in order to produce intensity at $q = q' + q'' = (0,1,0)$. In contrast, $(0,2,-2)$ and $(0,2,2)$ reflections pair with $q'' = (0,-1,2)$ and $(0,-1,-2)$ respectively, which are only allowed in the orthorombic phase and not in the tetragonal one. This explanation is thus in direct agreement with the specific temperature dependence of the signal as presented in Figure 8.3.1.

Figure 8.4.1(b) shows the excellent correlation between the fulfilment of condition (1) for the $(0,2,-2)$ reflection and the peak in integrated intensity of the measured data. The red symbols close to $y = 0$ correspond to the fulfilment of the first condition for multiple scattering: $k'_f \simeq k_i$ for the $(0,2,-2)$ which takes place in the same energy range as the observed increase in scattered intensity. The $(0,2,2)$ reflection behaves in an equivalent manner.
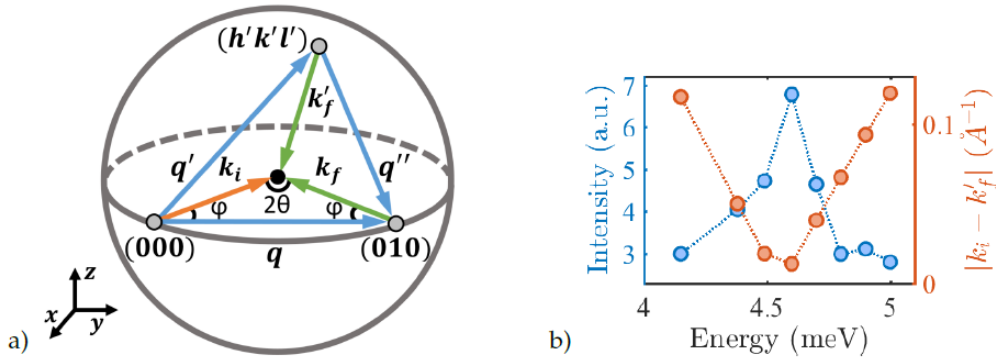
Figure 8.4.1: (a) Graphical representation of an instance of double scattering within the Ewald sphere. k_i and k_f define the incoming and outgoing neutron beam, q' and q'' denote the tested reflections allowed in the LTO phase and k'_f is the secondary reflection wavevector. (b) Blue symbols show the integrated intensity of the measured signal (see Figure 8.3.2) and follow the left side y-axis. The red symbols follow the right side y-axis and show the calculated difference between the magnitude of the two scattering wavevectors k_i and k'_f for the case $q' = (0,2,-2)$ and $q'' = (0,-1,2)$. The x-axis shows the incoming and outgoing energy of the neutron beam ($E_i = E_f$).

8.4.2   *The effect of twinning*

We attribute the complex pattern of multiple peaks around the $(0,1,0)$ reflection, as it can be observed in Figure 8.3.1(a), to a combination of the double scattering mechanism, presented above, and twinning of the reflections. It is well known that LSCO crystals in the low temperature orthorhombic phase are composed of two sets of two twin orientations sharing the $(1,1,0)$ or

$(1,-1,0)$ planes [188]. This co-existence of a 4-phase structure with equal lattice parameters but different orientations of the (a,b)-plane is observed in neutron scattering experiments as a peak splitting of the Bragg reflections along the h and k directions (as exemplified in Figure 1 from Ref. [188]).

Thus, if we consider all possible combinations of $\boldsymbol{q} = \boldsymbol{q'} + \boldsymbol{q''}$, where $\boldsymbol{q'}$ and $\boldsymbol{q''}$ are the wavevectors of the 4 satellite peaks around $(0,2,2)$ and $(0,-1,-2)$ respectively (i.e. $(\pm 2t, 2\pm 2t, 2)$ and $(\pm t, -1\pm t, -2)$), we obtain a total of 16 peaks appearing around the $(0,1,0)$ reflection (as depicted by the red circles in Figure 8.4.2). Note that the incommensurability (t) of the satellite peaks is related to the twin splitting ($\Delta = 90° - 2\arctan(b/a)$ [188]) as $t = \Delta/2$, in the small angle approximation, and it does not affect the l value since there is no splitting along the c-axis. In Figure 8.4.2(b) we plot the calculated pattern obtained as Gaussian distributions centred at the calculated peak positions and with tuned amplitudes as to match the measured data shown in Figure 8.4.2(a). The twin splitting used in the calculations corresponds to a lattice parameters ratio $b/a = 1.022$, a value slightly higher than the one from the literature $b_o/a_o = 1.009$ [201]. A similar figure could likely be produced from a true simulation of the scattering intensities by modifying the volume fractions of the 4 twin phases. However, we have chosen not to address this involved optimisation scheme, since we do not think is would add to the general understanding. The good agreement between the measured data and the calculated reconstruction implies that the observed multiple peaks pattern can be regarded as a superposition of the twinning patterns of all the reflections that simultaneously intersect the surface of the Ewald sphere.
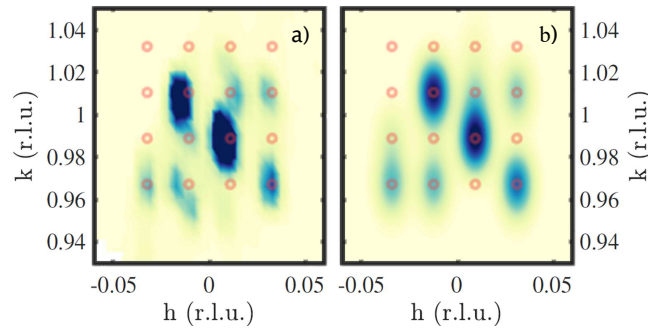
Figure 8.4.2: (a) Elastic scattering grid scan around the $(0,1,0)$ reflection taken at 2.5 K on LSCO with $x = 0.07$ annealed. (b) Calculated intensity patterns of the 16 peaks originating from the twinning of the sample. The red circles indicate the position of all reflections. The intensity of each Gaussian distribution around the calculated position is tuned as to match the measured data.

8.4.3 *Earlier studies of stripes in cuprates*

Although numerous studies from the literature follow the behaviour of static spin stripes in LSCO superconductors as a function of doping, temperature and applied magnetic field, this spurious process has not been addressed in any of the publications to our knowledge. There are two main ways in which the additional double scattering signal went unreported: (1) at higher doping ($x \sim 0.12$) the true magnetic signal appears at higher $\boldsymbol{q}$ values compared to the spurious one, thus, depending on the scanning direction, one is able to measure the stripe signal without detecting the spurion (for example by performing scans of the sample orientation, A3); (2) as we

have argued throughout this paper, by tuning the incoming and outgoing neutron beam energy, the contamination can easily be avoided. Indeed, many of the experiments presented in the literature have been carried out at energies outside the 4.5-4.7 meV regime [47, 53–55, 114].

That multiple scattering can make forbidden peaks appear was already mentioned by the first discovery of stripes [50], where J. Tranquada *et al.* reported a neutron energy (13.9 meV) of being almost free of spurious scattering at $(0,1,0)$. In this respect, not all findings in the present article are new as such. However, the effect of multiple scattering, and in particular the effect that twinning causes IC peaks to appear, is in our work thoroughly documented, as a warning and explanation to future experimentalists.

8.5 CONCLUSION

Our neutron diffraction measurements and calculations support the hypothesis of a double scattering event, originating from the $(0,2,-2)$- and $(0,-1,2)$-type reflections, corroborated with twinning of the crystal, as the cause for the observed varying intensity of the $(0,1,0)$ reflection and the appearance of incommensurate peaks around it.

Because the intensity of the static magnetic stripe signal is very low in cuprates in general and in LSCO in particular, the contribution of multiple scattering should always be carefully considered and the neutron energy should be tuned as to minimise this intrinsic effect, which could easily lead to detrimental pollution of the experimental data. In particular for cold-neutron experiment on the LSCO-family of compounds, energies around 4.6 meV should be avoided. As alternatives, energies of 3.7 meV (the BeO-filter edge) or 5.0 meV (the Be-filter edge) can be strongly recommended. Our findings explain why, historically, best diffraction results on stripes in cuprate superconductors were found for exactly these energies. Although the multiple scattering explanation of spurious signals was noted early by J. Tranquada *et al.*, we have here presented a comprehensive investigation of this effect that we now believe to be fully understood.

We emphasise the need for applying these considerations during the planning stages of neutron diffraction experiments on similar systems, in order to minimise contamination by spurious signals.

SUMMARY AND OUTLOOK

9.1 MAGNETISM OF UNDERDOPED LSCO

The comparative neutron scattering study performed on LSCO samples of different doping allowed us to observe the behaviour of both static and dynamic stripes across the phase transition from an insulator to a superconductor. Firstly, we have measured a drastic suppression, comparable in magnitude, of both magnetic order and low-energy fluctuations ($\hbar\omega < 2$ meV) signals at the onset of the superconducting dome. This indicates a competing relationship between the superconducting phase and a magnetic phase containing both types of magnetism. Secondly, all examined samples exhibited continuous ungapped magnetic spectra to the lowest energy measured. We interpret these two features as signatures of a pair density wave phase with intertwined magnetic and superconducting orders. We argue that, because the same effect is observed in the non-superconducting LSCO with $x = 0.05$, we are dealing with a two-dimensional phenomenon and that in-plane superconductivity, which is already present in LSCO5, cannot expand to bulk superconductivity in this sample due to the frustrated nature of the interlayer Josephson coupling. To this end we believe it would be valuable to determine the orientation of charge stripes by high-energy–photon diffraction for example. At the same time, a detailed study of both in-plane and out-of-plane resistivity has the potential to reveal signs of two-dimensional superconductivity. Another experiment which could shed light on the transition from 2D to 3D superconductivity is a study of pressure induced effects. Previous research performed on an underdoped LBCO crystal have revealed that, by applying stress, it is possible to obtain a phase in which the onset temperature of 2D SC will coincide with that of 3D SC.

The scenario we propose is a co-existence between a pair density wave phase and a second one with uniform d-wave superconductivity. The ratio between the two is tuned by adjusting the dopant concentration. In the non-superconducting LSCO5 the pair density wave is dominating. Upon entering the superconducting dome part of the electrons are claimed by the regions of classical uniform d-wave superconductivity.

The effect of an applied magnetic field provides additional information on the nature of the co-existence phase. In all samples we have measured a suppression of the low-energy ($\hbar\omega < 2$ meV) magnetic signal as a function of applied magnetic field. Similar to uniform d-wave superconductivity we argue that this is caused by local destruction of SC which in turn favours elastic and quasi-elastic magnetic order. A spectral weight shift towards the elastic and quasi-elastic signals has been confirmed in LSCO7. We suspect that the field effect we observe

originates primarily in the PDW regions as, contrary to d-wave SC where the onset of the field effect coincides with T_c, in our case the onset matches that of magnetic order (T_N). As a function of increased doping the balance will tip in favour of d-wave SC which exhibits gapped low-energy fluctuations and, as mentioned before, spectral weight shift towards the elastic line as a function of applied field. We speculate that the observed lack of a field effect at the anomalous $x = 0.12$ doping is the result of a particular balance between the sub-gap states induced in the uniform d-wave SC phase and the field suppression of low-energy excitations present in the pair density wave regions.

9.2   MAGNETISM OF OXYGEN DOPED LCO+O

Throughout Chapter 6 a detailed analysis of the purely oxygen doped compound of the family, La_2CuO_{4+y}, has been presented. Through numerous neutron scattering experiments, various properties have been analysed in great detail.

Measurements of the magnetic fluctuations with energy $0.35 \leq \hbar\omega \leq 10$ meV have revealed the absence of a spin gap which led to the conclusion that superconductivity and dynamic spin stripes co-exist microscopically in an intertwined phase. The lack of a temperature effect, with the exception of a small decrease of spectral weight as a result of decreasing spin coherence with increasing temperature up to ~ 70 K, is an indication that the two intertwined phases are not in direct electronic competition. To this end, the measurement of high energy magnetic fluctuations [1] (around the expected crossing energy of the hourglass dispersion $E_{cross} \simeq 40$ meV) has the potential to further confirm such an intertwined scenario. The absence of a magnetic resonance would tip the balance in favour of an intertwined pair density wave scenario, while its presence would favour a standard d-wave superconductivity approach. Moreover, some of the data collected on IN12 shows a small variation of the intrinsic linewidth as a function of varying energy. This points towards a phase separation into two distinct magnetic structures containing fluctuations above and below 5 meV respectively. It would be interesting to further investigate in greater detail and confirm with higher $\mathbf{Q}$-resolution the variation of the dynamic spin correlation length as a function of energy.

In contrast, the magnetically ordered stripe phase is a separate electronic region possibly competing with superconductivity as it has been previously speculated in the literature [56]. However, the lack of a significant magnetic field effect, in both the elastic and inelastic channels, which is commonly seen as an indication of competition between superconductivity and various other electronic phases, only revealed that our sample is composed of a fully developed magnetic phase in the absence of an applied magnetic field.

Lastly, through XYZ neutron polarisation analysis we have been able to identify the presence, in our sample, of a phase which behaves like the undoped antiferromagnetic one and confirm that the spin orientation, along the orthorhombic b-axis, of the parent compound (LCO) is conserved. What is probably even more remarkable is the fact that by measuring the modulation of the elastic spin stripes, in different neutron spin configurations, we were able to conclude that

---

1 It should be noted that we have attempted such a measurement on the thermal triple axis spectrometer IN8 at the ILL. Due to large spurious scattering, the quality of the data is not high enough to allow for any conclusive resolution on the matter.

equal fractions of charge stripes oriented along the tetragonal *a* and *b*-axis are present in the sample. With respect to the dynamic stripes, the polarisation analysis indicated that fluctuations are most probably isotropic in nature. In order to make this argument more compelling, further polarisation analysis of the magnetic fluctuations is necessary. To begin with, a thorough analysis of the out-of-plane component (in the reciprocal space *l*-direction or real space *c*-direction) of the fluctuations would be required.

9.3   POLARISED IMAGING

In Chapter 7 a study of the doping distribution inside a superconducting LSCO crystal by means of polarised neutron imaging is presented. In this experiment a magnetic field was trapped inside a superconducting crystal during the cooling process and its temperature dependence was then imaged while heating the sample. A superconducting critical temperature gradient, and implicitly doping, was observed along the growth direction of the crystal. This variation can be the result of a slight accumulation of strontium atoms during one phase of the growth which in turn caused a deficiency of dopant during later stages. Polarised neutron tomography with improved spacial resolution has the potential to reveal other interesting features such as the radial distribution of doping in the direction perpendicular to the growth one (basically during each stage of the growth process). Magnetic susceptibility measurements, performed on small crystallites collected from the two ends of the crystal have confirmed the variation in superconducting critical temperature.

What is remarkable about this experiment is the potential to determine the bulk properties of the entire sample in a non-destructive manner. Classical bulk measurements, such as magnetic susceptibility or resistivity, require the cutting of the crystal into smaller samples and risk to not be representative for the entire crystal as we have proven in this study.

9.4   DOUBLE SCATTERING PHENOMENA IN LSCO

Chapter 8 presents a *warning* type of study which aims to draw attention on the possibility to mistake a double scattering spurious signal for the genuine magnetic stripes one.

Neutron diffraction measurements performed at the expected position of static spin stripes revealed a surprising multiple peak structure. Additional scans performed as a function of simultaneously varying incoming and outgoing neutron energy uncovered the fact that the signal appeared only in a certain narrow neutron energy range (~ 4.5 to ~ 4.7 meV). This type of energy dependence is a clear indication that the origin of the signal might be a multiple scattering event. Indeed our calculations have confirmed this scenario and identified the precise reflections involved. Furthermore, we have also proved that the multi-peak structure could be reproduced if the twinning pattern of the compound is taken into account.

BIBLIOGRAPHY

[1] *Dimensions on The number of publications in the field of high temperature superconductivity*, shorturl.at/nuvPW, accessed February, 2021.

[2] M. Fowler, "Historical beginnings of theories of electricity and magnetism", *Recuperado el*, vol. 23, no. 5, p. 2012, 1997.

[3] W. Gilbert and S. P. Thompson, *On the magnet, magnetick bodies also, and on the great magnet the Earth: A New physiology, demonstrated by many arguments & experiments.* Imprinted at the Chiswick Press, 1900.

[4] R. Elliott, "The story of magnetism", *Physica A: Statistical Mechanics and its Applications*, vol. 384, no. 1, pp. 44–52, 2007.

[5] S. Blundell, *Magnetism in condensed matter*, 2003.

[6] S. L. Holm, "Neutron scattering investigations of correlated electron systems and neutron instrumentation", PhD thesis, Niels Bohr Institute, Faculty of Science, University of Copenhagen, 2016.

[7] M. F. Collins, *Magnetic critical scattering*. Oxford University Press, 1989.

[8] *Wikipedia on Quantum phase transitions*, https://en.wikipedia.org/wiki/Quantum_phase_transition, accessed February, 2021.

[9] K. H. Onnes, "Further experiments with liquid helium G. On the electrical resistance of pure metals etc. VI. On the sudden change in the rate at which the resistance of mercury disappears", *Koninklijke Nederlandse Akademie van Wetenschappen Proceedings Series B Physical Sciences*, vol. 14, pp. 818–821, 1912.

[10] D. van Delft, "History and significance of the discovery of superconductivity by Kamerlingh Onnes in 1911", *Physica C: Superconductivity*, vol. 479, pp. 30–35, 2012.

[11] J. F. Annett, *Superconductivity, superfluids and condensates*. Oxford University Press, 2004, vol. 5.

[12] C. Kittel, P. McEuen, and P. McEuen, *Introduction to solid state physics*. Wiley New York, 1996, vol. 8.

[13] A. P. Drozdov, M. I. Eremets, I. A. Troyan, V. Ksenofontov, and S. I. Shylin, "Conventional superconductivity at 203 kelvin at high pressures in the sulfur hydride system", *Nature*, vol. 525, no. 7567, pp. 73–76, 2015.

[14] P. Jensen Ray, "Structural investigation of $La_{2-x}Sr_xCuO_{4+y}$", Master's thesis, Niels Bohr Institute, Faculty of Science, University of Copenhagen, 2015.

[15] J. File and R. G. Mills, "Observation of persistent current in a superconducting solenoid", *Physical Review Letters*, vol. 10, no. 3, p. 93, 1963.

[16] W. Meissner and R. Ochsenfeld, "Meissner, walther, and robert ochsenfeld. "a new effect with the onset of superconductivity", *Natural Sciences*, vol. 21, no. 44, pp. 787–788, 1933.

[17] Akimitsu-Laboratory, *Characteristics of superconductivity*, http://www.phys.aoyama.ac.jp/~w3-jun/achievements/study_sc_chara_eng.html, accessed February, 2021.

[18] F. London and H. London, "The electromagnetic equations of the supraconductor", *Proceedings of the Royal Society of London. Series A-Mathematical and Physical Sciences*, vol. 149, no. 866, pp. 71–88, 1935.

[19] *Wikipedia on London penetration depth*, https://en.wikipedia.org/wiki/London_penetration_depth, accessed February, 2021.

[20] J. Bardeen, L. N. Cooper, and J. R. Schrieffer, "Theory of superconductivity", *Physical Review*, vol. 108, no. 5, p. 1175, 1957.

[21] E. Maxwell, "Isotope effect in the superconductivity of mercury", *Physical Review*, vol. 78, no. 4, p. 477, 1950.

[22] C. A. Reynolds, B. Serin, W. H. Wright, and L. B. Nesbitt, "Superconductivity of isotopes of mercury", *Physical Review*, vol. 78, no. 4, p. 487, 1950.

[23] A. A. Abrikosov, "The magnetic properties of superconducting alloys", *Journal of Physics and Chemistry of Solids*, vol. 2, no. 3, pp. 199–208, 1957.

[24] K. Tomimoto, I. Terasaki, A. I. Rykov, T. Mimura, and S. Tajima, "Impurity effects on the superconducting coherence length in Zn-or Ni-doped $YBa_2Cu_3O_{6.9}$ single crystals", *Physical Review B*, vol. 60, no. 1, p. 114, 1999.

[25] Y. Wang, S. Ono, Y. Onose, G. Gu, Y. Ando, Y. Tokura, S. Uchida, and N. P. Ong, "Dependence of upper critical field and pairing strength on doping in cuprates", *Science*, vol. 299, no. 5603, pp. 86–89, 2003.

[26] Suryadijaya, T. Sasagawa, and H. Takagi, "Oxygen isotope effect on charge/spin stripes in $La_{1.8-x}Eu_{0.2}Sr_xCuO_4$", *Physica C: Superconductivity*, vol. 426, pp. 402–406, 2005.

[27] J. G. Bednorz and K. A. Müller, "Possible high T_c superconductivity in the Ba-La-Cu-O system", in *Ten Years of Superconductivity: 1980–1990*, Springer, 1986, pp. 267–271.

[28] M.-K. Wu, J. R. Ashburn, C. J. Torng, P. H. Hor, R. L. Meng, L. Gao, Z. J. Huang, Y. Q. Wang, and C. W. Chu, "Superconductivity at 93 K in a new mixed-phase Y-Ba-Cu-O compound system at ambient pressure", *Physical Review Letters*, vol. 58, no. 9, p. 908, 1987.

[29] H. Kimura, K. Hirota, C.-H. Lee, K. Yamada, and G. Shirane, "Structural instability associated with the tilting of CuO_6 octahedra in $La_{2-x}Sr_xCuO_4$", *Journal of the Physical Society of Japan*, vol. 69, no. 3, pp. 851–857, 2000.

[30] M. Hücker, "Structural aspects of materials with static stripe order", *Physica C: Superconductivity*, vol. 481, pp. 3–14, 2012.

[31] T. Tejsner, "Oxygen dynamics in the high-temperature superconductor LSCO+O", Master's thesis, Niels Bohr Institute, Faculty of Science, University of Copenhagen, 2019.

[32] P. Fournier, E. Maiser, and R. L. Greene, "Current research issues for the electron-doped cuprates", in *The gap symmetry and fluctuations in high-T_c superconductors*, Springer, 2002, pp. 145–158.

[33] B. Keimer, S. A. Kivelson, M. R. Norman, S. Uchida, and J. Zaanen, "From quantum matter to high-temperature superconductivity in copper oxides", *Nature*, vol. 518, no. 7538, p. 179, 2015.

[34] K. Takenaka, J. Nohara, R. Shiozaki, and S. Sugai, "Incoherent charge dynamics of $La_{2-x}Sr_xCuO_4$: Dynamical localization and resistivity saturation", *Physical Review B*, vol. 68, no. 13, p. 134 501, 2003.

[35] S. Martin, A. T. Fiory, R. M. Fleming, L. F. Schneemeyer, and J. V. Waszczak, "Normal-state transport properties of $Bi_{2+x}Sr_{2-y}CuO_{6+\delta}$ crystals", *Physical Review B*, vol. 41, no. 1, p. 846, 1990.

[36] P. Curty and H. Beck, "Thermodynamics and phase diagram of high temperature super-conductors", *Physical Review Letters*, vol. 91, no. 25, p. 257 002, 2003.

[37] H. Ding, T. Yokoya, J. C. Campuzano, T. Takahashi, M. Randeria, M. R. Norman, T. Mochiku, K. Kadowaki, and J. Giapintzakis, "Spectroscopic evidence for a pseudogap in the normal state of underdoped high-T_c superconductors", *Nature*, vol. 382, no. 6586, pp. 51–54, 1996.

[38] D. Feng, A. Damascelli, K. Shen, N. Motoyama, D. Lu, H. Eisaki, K. Shimizu, J.-i. Shimoyama, K. Kishio, N. Kaneko, *et al.*, "Electronic structure of the trilayer cuprate superconductor $Bi_2Sr_2Ca_2Cu_3O_{10+\delta}$", *Physical review letters*, vol. 88, no. 10, p. 107 001, 2002.

[39] H. Alloul, T. Ohno, and P. Mendels, "89y nmr evidence for a fermi-liquid behavior in $YBa_2Cu_3O_{6+x}$", *Physical Review Letters*, vol. 63, no. 16, p. 1700, 1989.

[40] M. R. Norman, D. Pines, and C. Kallin, "The pseudogap: Friend or foe of high T_c?", *Advances in Physics*, vol. 54, no. 8, pp. 715–733, 2005.

[41] B. Batlogg, H. Y. Hwang, H. Takagi, R. J. Cava, H. L. Kao, and J. Kwo, "Normal state phase diagram of $(La,Sr)_2CuO_4$ from charge and spin dynamics", *Physica C: Superconductivity*, vol. 235, pp. 130–133, 1994.

[42] C. C. Homes, T. Timusk, R. Liang, D. A. Bonn, and W. N. Hardy, "Optical conductivity of c axis oriented $YBa_2Cu_3O_{6.70}$: Evidence for a pseudogap", *Physical Review Letters*, vol. 71, no. 10, p. 1645, 1993.

[43] J. W. Loram, K. A. Mirza, J. R. Cooper, and W. Y. Liang, "Electronic specific heat of $YBa_2Cu_3O_{6+x}$ from 1.8 to 300 K", *Physical Review Letters*, vol. 71, no. 11, p. 1740, 1993.

[44] B. Keimer, A. Aharony, A. Auerbach, R. J. Birgeneau, A. Cassanho, Y. Endoh, R. W. Erwin, M. A. Kastner, and G. Shirane, "Néel transition and sublattice magnetization of pure and doped La_2CuO_4", *Physical Review B*, vol. 45, no. 13, p. 7430, 1992.

[45] T. P. Croft, C. Lester, M. S. Senn, A. Bombardi, and S. M. Hayden, "Charge density wave fluctuations in $La_{2-x}Sr_xCuO_4$ and their competition with superconductivity", *Physical Review B*, vol. 89, no. 22, p. 224 513, 2014.

[46] N. E. Hussey, R. A. Cooper, X. Xu, Y. Wang, I. Mouzopoulou, B. Vignolle, and C. Proust, "Dichotomy in the T-linear resistivity in hole-doped cuprates", *Philosophical Transactions of the Royal Society A: Mathematical, Physical and Engineering Sciences*, vol. 369, no. 1941, pp. 1626–1639, 2011.

[47] M. Kofu, S.-H. Lee, M. Fujita, H.-J. Kang, H. Eisaki, and K. Yamada, "Hidden quantum spin-gap state in the static stripe phase of high-temperature $La_{2-x}Sr_xCuO_4$ Superconductors", *Physical Review Letters*, vol. 102, p. 047 001, 4 2009.

[48] L. Alff, Y. Krockenberger, B. Welter, M. Schonecke, R. Gross, D. Manske, and M. Naito, "A hidden pseudogap under the 'dome'of superconductivity in electron-doped high-temperature superconductors", *Nature*, vol. 422, no. 6933, pp. 698–701, 2003.

[49] D. C. Peets, J. D. F. Mottershead, B. Wu, I. S. Elfimov, R. Liang, W. N. Hardy, D. A. Bonn, M. Raudsepp, N. J. C. Ingle, and A. Damascelli, "$Tl_2Ba_2CuO_{6+\delta}$ brings spectroscopic probes deep into the overdoped regime of the high-T_c cuprates", *New Journal of Physics*, vol. 9, no. 2, p. 28, 2007.

[50] J. M. Tranquada, B. J. Sternlieb, J. D. Axe, Y. Nakamura, and S. Uchida, "Evidence for stripe correlations of spins and holes in copper oxide superconductors", *Nature*, vol. 375, no. 6532, p. 561, 1995.

[51] V. J. Emery, S. A. Kivelson, and O. Zachar, "Spin-gap proximity effect mechanism of high-temperature superconductivity", *Physical Review B*, vol. 56, no. 10, p. 6120, 1997.

[52] K. Yamada, C. H. Lee, K. Kurahashi, J. Wada, S. Wakimoto, S. Ueki, H. Kimura, Y. Endoh, S. Hosoya, G. Shirane, R. J. Birgeneau, M. Greven, M. A. Kastner, and Y. J. Kim, "Doping dependence of the spatially modulated dynamical spin correlations and the superconducting-transition temperature in $La_{2-x}Sr_xCuO_4$", *Physical Review B*, vol. 57, no. 10, p. 6165, 1998.

[53] J. Chang, C. Niedermayer, R. Gilardi, N. B. Christensen, H. M. Rønnow, D. F. McMorrow, M. Ay, J. Stahn, O. Sobolev, A. Hiess, S. Pailhes, C. Baines, N. Momono, M. Oda, M. Ido, and J. Mesot, "Tuning competing orders in $La_{2-x}Sr_xCuO_4$ cuprate superconductors by the application of an external magnetic field", *Physical Review B*, vol. 78, no. 10, p. 104 525, 2008.

[54] B. Khaykovich, S. Wakimoto, R. J. Birgeneau, M. A. Kastner, Y. S. Lee, P. Smeibidl, P. Vorderwisch, and K. Yamada, "Field-induced transition between magnetically disordered and ordered phases in underdoped $La_{2-x}Sr_xCuO_4$", *Physical Review B*, vol. 71, no. 22, p. 220 508, 2005.

[55] B. Lake, H. M. Rønnow, N. B. Christensen, G. Aeppli, K. Lefmann, D. F. McMorrow, P. Vorderwisch, P. Smeibidl, N. Mangkorntong, T. Sasagawa, M. Nohara, H. Takagi, and T. E. Mason, "Antiferromagnetic order induced by an applied magnetic field in a high-temperature superconductor", *Nature*, vol. 415, no. 6869, pp. 299–302, 2002.

[56] M.-H. Julien, "Magnetic order and superconductivity in $La_{2-x}Sr_xCuO_4$: A review", *Physica B: Condensed Matter*, vol. 329, pp. 693–696, 2003.

[57] M. Hucker, Z. M. v, G. D. Gu, Z. J. Xu, J. S. Wen, G. Xu, H. J. Kang, A. Zheludev, and J. M. Tranquada, "Stripe order in superconducting $La_{2-x}Ba_xCuO_4$ ($0.095 \leqslant x \leqslant 0.155$)", *Physical Review B*, vol. 83, p. 104 506, 10 Mar. 2011.

[58] B. Lake, G. Aeppli, T. E. Mason, A. Schröder, D. F. McMorrow, K. Lefmann, M. Isshiki, M. Nohara, H. Takagi, and S. M. Hayden, "Spin gap and magnetic coherence in a clean high-temperature superconductor", *Nature*, vol. 400, no. 6739, pp. 43–46, 1999.

[59] K. Yamada, S. Wakimoto, G. Shirane, C. H. Lee, M. A. Kastner, S. Hosoya, M. Greven, Y. Endoh, and R. J. Birgeneau, "Direct observation of a magnetic gap in superconducting $La_{1.85}Sr_{0.15}CuO_4$ ($T_c = 37.3$ K)", *Physical Review Letters*, vol. 75, no. 8, p. 1626, 1995.

[60] B. Vignolle, S. M. Hayden, D. F. McMorrow, H. M. Rønnow, B. Lake, C. D. Frost, and T. G. Perring, "Two energy scales in the spin excitations of the high-temperature superconductor $La_{2-x}Sr_xCuO_4$", *Nature Physics*, vol. 3, no. 3, pp. 163–167, 2007.

[61] H. Jacobsen, S. Holm-Dahlin, M.-E. Lăcătuşu, A. T. Rømer, M. Bertelsen, M. Boehm, R. Toft-Petersen, J.-C. Grivel, S. B. Emery, L. Udby, B. O. Wells, and K. Lefmann, "Distinct nature of static and dynamic magnetic stripes in cuprate superconductors", *Physical Review Letters*, vol. 120, no. 3, p. 037 003, 2018.

[62] J. J. Wagman, D. Parshall, M. B. Stone, A. T. Savici, Y. Zhao, H. A. Dabkowska, and B. D. Gaulin, "Quasi-two-dimensional spin and phonon excitations in $La_{1.965}Ba_{0.035}CuO_4$", *Physical Review B*, vol. 91, no. 22, p. 224 404, 2015.

[63] J. J. Wagman, J. P. Carlo, J. Gaudet, G. Van Gastel, D. L. Abernathy, M. B. Stone, G. E. Granroth, A. I. Kolesnikov, A. T. Savici, Y.-J. Kim, H. Zhang, D. Ellis, Y. Zhao, L. Clark, A. B. Kallin, E. Mazurek, H. A. Dabkowska, and B. D. Gaulin, "Neutron scattering studies of spin-phonon hybridization and superconducting spin gaps in the high-temperature superconductor $La_{2-x}(Sr, Ba)_xCuO_4$", *Physical Review B*, vol. 93, no. 9, p. 094 416, 2016.

[64] Z. Xu, C. Stock, S. Chi, A. I. Kolesnikov, G. Xu, G. Gu, and J. M. Tranquada, "Neutron-scattering evidence for a periodically modulated superconducting phase in the underdoped cuprate $La_{1.905}Ba_{0.095}CuO_4$", *Physical Review Letters*, vol. 113, no. 17, p. 177 002, 2014.

[65] P. Choubey, S. H. Joo, K. Fujita, Z. Du, S. D. Edkins, M. H. Hamidian, H. Eisaki, S. Uchida, A. P. Mackenzie, J. Lee, J. C. Seamus Davis, and P. J. Hirschfeld, "Atomic-scale electronic structure of the cuprate pair density wave state coexisting with superconductivity", *Proceedings of the National Academy of Sciences*, vol. 117, no. 26, pp. 14 805–14 811, 2020.

[66] M. H. Christensen, H. Jacobsen, T. A. Maier, and B. M. Andersen, "Magnetic fluctuations in pair-density-wave superconductors", *Physical Review Letters*, vol. 116, no. 16, p. 167 001, 2016.

[67] T. E. Mason, T. J. Gawne, S. E. Nagler, M. B. Nestor, and J. M. Carpenter, "The early development of neutron diffraction: Science in the wings of the Manhattan Project", *Acta Crystallographica Section A: Foundations of Crystallography*, vol. 69, no. 1, pp. 37–44, 2013.

[68] K. Lefmann, *Lecture notes on Neutron scattering: Theory, instrumentation and simulation*, 2019.

[69] C. Hartnig and I. Manke, "Measurement methods | structural properties: Neutron and synchrotron imaging, in-situ for water visualization", in *Encyclopedia of Electrochemical Power Sources*, Amsterdam: Elsevier, 2009, pp. 738–757, ISBN: 978-0-444-52745-5.

[70] R. M. Moon, T. Riste, and W. C. Koehler, "Polarization analysis of thermal-neutron scattering", *Physical Review*, vol. 181, no. 2, p. 920, 1969.

[71] A. Boothroyd, *Principles of Neutron Scattering from Condensed Matter*. Oxford University Press, USA, 2020.

[72] G. L. Squires, *Introduction to the theory of thermal neutron scattering (3rd ed.)* Cambridge University Press, 2012.

[73] *Wikipedia on Spallation*, https://en.wikipedia.org/wiki/Spallation, accessed February, 2021.

[74] E. Fermi, "High energy nuclear events", *Progress of Theoretical Physics*, vol. 5, no. 4, pp. 570–583, 1950.

[75] *University of Groningen on Magnon spintronics*, https://www.rug.nl/research/zernike/physics-of-nanodevices/research/magnonspintronics?lang=en, accessed February, 2021.

[76] G. Ehlers, J. R. Stewart, A. R. Wildes, P. P. Deen, and K. H. Andersen, "Generalization of the classical xyz-polarization analysis technique to out-of-plane and inelastic scattering", *Review of Scientific Instruments*, vol. 84, no. 9, p. 093 901, 2013.

[77] A. Wildes and L. Mangin-Thro, *D7 - Diffuse scattering spectrometer*, https://www.ill.eu/users/instruments/instruments-list/d7/description/instrument-layout.

[78] G. Shirane, S. M. Shapiro, and J. M. Tranquada, *Neutron Scattering with a Triple-Axis Spectrometer*. Cambridge: Cambridge University Press, 2002.

[79] H. Jacobsen, "Complex magnetic systems studied with neutron scattering", PhD thesis, Niels Bohr Institute, Faculty of Science, University of Copenhagen, 2016.

[80] M. Boehm and P. Steffens, *ThALES — three axis instrument for low energy spectrometry*, https://www.ill.eu/users/instruments/instruments-list/thales/characteristics.

[81] N. Kardjilov, A. Hilger, I. Manke, R. Woracek, and J. Banhart, "CONRAD-2: the new neutron imaging instrument at the Helmholtz-Zentrum Berlin", *Journal of Applied Crystallography*, vol. 49, no. 1, pp. 195–202, 2016.

[82] J. Chang, "Magnetic and electronic properties of the high-temperature superconductor $La_{2-x}Sr_xCuO_4$", PhD thesis, Swiss Federal Institute of Technology Zürich, 2008.

[83] S. Wakimoto, S. Ueki, Y. Endoh, and K. Yamada, "Systematic study of short-range antiferromagnetic order and the spin-glass state in lightly doped $La_{2-x}Sr_xCuO_4$", *Physical Review B*, vol. 62, no. 5, p. 3547, 2000.

[84] K. Binder and A. P. Young, "Spin glasses: Experimental facts, theoretical concepts, and open questions", *Reviews of Modern physics*, vol. 58, no. 4, p. 801, 1986.

[85] F. C. Chou, N. R. Belk, M. A. Kastner, R. J. Birgeneau, and A. Aharony, "Spin-glass behavior in $La_{1.96}Sr_{0.04}CuO_4$", *Physical Review Letters*, vol. 75, no. 11, p. 2204, 1995.

[86] M. E. Filipkowski, J. I. Budnick, and Z. Tan, "Observation of a low temperature magnetic phase transition in nonsuperconducting $La_{2-x}Sr_xCuO_{4+y}$ by macroscopic magnetization and electron spin resonance", *Physica C: Superconductivity*, vol. 167, no. 1-2, pp. 35–41, 1990.

[87] A. N. Lavrov, Y. Ando, S. Komiya, and I. Tsukada, "Unusual magnetic susceptibility anisotropy in untwinned $La_{2-x}Sr_xCuO_4$ single crystals in the lightly doped region", *Physical Review Letters*, vol. 87, no. 1, p. 017 007, 2001.

[88] J. H. Cho, F. Borsa, D. C. Johnston, and D. R. Torgeson, "Spin dynamics in $La_{2-x}Sr_xCuO_4$ ($0.02 \leqslant x \leqslant 0.08$) from ^{139}La NQR relaxation: Fluctuations in a finite-length-scale system", *Physical Review B*, vol. 46, no. 5, p. 3179, 1992.

[89] V. J. Emery and S. A. Kivelson, "Frustrated electronic phase separation and high-temperature superconductors", *Physica C: Superconductivity*, vol. 209, no. 4, pp. 597–621, 1993.

[90] M. Hücker, M. Zimmermann, G. D. Gu, Z. J. Xu, J. S. Wen, G. Xu, H. J. Kang, A. Zheludev, and J. M. Tranquada, "Stripe order in superconducting $La_{2-x}Ba_xCuO_4$ ($0.095 \leqslant x \leqslant 0.155$)", *Physical Review B*, vol. 83, no. 10, p. 104 506, 2011.

[91] Z. Guguchia, D. Das, C. N. Wang, T. Adachi, N. Kitajima, M. Elender, F. Brückner, S. Ghosh, V. Grinenko, T. Shiroka, M. Müller, C. Mudry, C. Baines, M. Bartkowiak, Y. Koike, A. Amato, J. M. Tranquada, C. W. Klauss H.-H.and Hicks, and H. Luetkens, "Using uniaxial stress to probe the relationship between competing superconducting states in a cuprate with spin-stripe order", *Physical Review Letters*, vol. 125, no. 9, p. 097 005, 2020.

[92] S. Wakimoto, S. Lee, M. P. Gehring, R. J. Birgeneau, and G. Shirane, "Neutron scattering study of soft phonons and diffuse scattering in insulating $La_{1.95}Sr_{0.05}CuO_4$", *Journal of the Physical Society of Japan*, vol. 73, no. 12, pp. 3413–3417, 2004.

[93] T. B. Tejsner, "Oxygen dynamics in the high-temperature superconductor LSCO+O", PhD thesis, Niels Bohr Institute, Faculty of Science, University of Copenhagen, 2020.

[94] C. Panagopoulos, J. L. Tallon, B. D. Rainford, T. Xiang, J. R. Cooper, and C. A. Scott, "Evidence for a generic quantum transition in high-tc cuprates", *Physical Review B*, vol. 66, no. 6, p. 064 501, 2002.

[95] J. M. Tranquada, "Neutron scattering studies of antiferromagnetic correlations in cuprates", in *Handbook of High-Temperature Superconductivity*, Springer, 2007, pp. 257–298.

[96] S. Wakimoto, R. J. Birgeneau, Y. S. Lee, and G. Shirane, "Hole concentration dependence of the magnetic moment in superconducting and insulating $La_{2-x}Sr_xCuO_4$", *Physical Review B*, vol. 63, no. 17, p. 172 501, 2001.

[97] E. Demler, S. Sachdev, and Y. Zhang, "Spin-ordering quantum transitions of superconductors in a magnetic field", *Physical Review Letters*, vol. 87, no. 6, p. 067 202, 2001.

[98] J. Chang, J. S. White, M. Laver, C. J. Bowell, S. P. Brown, A. T. Holmes, L. Maechler, S. Strässle, R. Gilardi, S. Gerber, T. Kurosawa, N. Momono, M. Oda, M. Ido, O. J. Lipscombe, S. M. Hayden, C. D. Dewhurst, R. Vavrin, J. Gavilano, J. Kohlbrecher, E. M. Forgan, and J. Mesot, "Spin density wave induced disordering of the vortex lattice in superconducting $La_{2-x}Sr_xCuO_4$", *Physical Review B*, vol. 85, no. 13, p. 134 520, 2012.

[99]   H. Jacobsen, I. A. Zaliznyak, A. T. Savici, B. L. Winn, S. Chang, M. Hücker, G. D. Gu, and J. M. Tranquada, "Neutron scattering study of spin ordering and stripe pinning in super-conducting $La_{1.93}Sr_{0.07}CuO_4$", *Physical Review B*, vol. 92, no. 17, p. 174 525, 2015.

[100] M. Fujita, K. Yamada, H. Hiraka, P. M. Gehring, S. H. Lee, S. Wakimoto, and G. Shirane, "Static magnetic correlations near the insulating-superconducting phase boundary in $La_{2-x}Sr_xCuO_4$", *Physical Review B*, vol. 65, no. 6, p. 064 505, 2002.

[101] H. Hiraka, Y. Endoh, M. Fujita, Y. S. Lee, J. Kulda, A. Ivanov, and R. J. Birgeneau, "Spin fluctuations in the underdoped high-T_c cuprate $La_{1.93}Sr_{0.07}CuO_4$", *Journal of the Physical Society of Japan*, vol. 70, no. 3, pp. 853–858, 2001.

[102] O. J. Lipscombe, B. Vignolle, T. G. Perring, C. D. Frost, and S. M. Hayden, "Emergence of coherent magnetic excitations in the high temperature underdoped $La_{2-x}Sr_xCuO_4$ superconductor at low temperatures", *Physical Review Letters*, vol. 102, no. 16, p. 167 002, 2009.

[103] Y. S. Lee, R. J. Birgeneau, M. A. Kastner, Y. Endoh, S. Wakimoto, K. Yamada, R. W. Erwin, S.-H. Lee, and G. Shirane, "Neutron-scattering study of spin-density wave order in the superconducting state of excess-oxygen-doped La_2CuO_{4+y}", *Physical Review B*, vol. 60, p. 3643, 1999.

[104] D. Vaknin, S. K. Sinha, D. E. Moncton, D. C. Johnston, J. M. Newsam, C. R. Safinya, and J. H. E. Kin, "Antiferromagnetism in La_2Cu_{4-y}", *Physical Review Letters*, vol. 58, no. 26, p. 2802, 1987.

[105] M. Vojta, "Lattice symmetry breaking in cuprate superconductors: Stripes, nematics, and superconductivity", *Advances in Physics*, vol. 58, no. 6, pp. 699–820, 2009.

[106] M. Kato, K. Machida, H. Nakanishi, and M. Fujita, "Soliton lattice modulation of incom-mensurate spin density wave in two dimensional Hubbard model: A mean field study", *Journal of the Physical Society of Japan*, vol. 59, no. 3, pp. 1047–1058, 1990.

[107] H. J. Schulz, "Domain walls in a doped antiferromagnet", *Journal de Physique*, vol. 50, no. 18, pp. 2833–2849, 1989.

[108] S. Wakimoto, G. Shirane, Y. Endoh, K. Hirota, S. Ueki, K. Yamada, R. J. Birgeneau, M. A. Kastner, Y. S. Lee, P. M. Gehring, and S. H. Lee, "Observation of incommensurate magnetic correlations at the lower critical concentration for superconductivity in $La_{2-x}Sr_xCuO_4$ ($x = 0.05$)", *Physical Review B*, vol. 60, no. 2, R769, 1999.

[109] S. Wakimoto, R. J. Birgeneau, M. A. Kastner, Y. S. Lee, R. Erwin, P. M. Gehring, S. H. Lee, M. Fujita, K. Yamada, Y. Endoh, K. Hirota, and G. Shirane, "Direct observation of a one-dimensional static spin modulation in insulating $La_{1.95}Sr_{0.05}CuO_4$", *Physical Review B*, vol. 61, no. 5, p. 3699, 2000.

[110] M. Matsuda, M. Fujita, K. Yamada, R. J. Birgeneau, M. A. Kastner, H. Hiraka, Y. Endoh, S. Wakimoto, and G. Shirane, "Static and dynamic spin correlations in the spin-glass phase of slightly doped $La_{2-x}Sr_xCuO_4$", *Physical Review B*, vol. 62, no. 13, p. 9148, 2000.

[111]   N. B. Christensen, J. Chang, J. Larsen, M. Fujita, M. Oda, M. Ido, N. Momono, E. M. For-gan, A. T. Holmes, J. Mesot, M. Hücker, and M. Zimmermann, "Bulk charge stripe order competing with superconductivity in La$_{2-x}$Sr$_x$CuO$_4$ ($x = 0.12$)", *arXiv preprint*, 2014. [Online]. Available: https://arxiv.org/abs/1404.3192.

[112]   H. Kimura, H. Matsushita, K. Hirota, Y. Endoh, K. Yamada, G. Shirane, Y. S. Lee, M. A. Kastner, and R. J. Birgeneau, "Incommensurate geometry of the elastic magnetic peaks in superconducting La$_{1.88}$Sr$_{0.12}$CuO$_4$", *Physical Review B*, vol. 61, no. 21, p. 14 366, 2000.

[113]   V. Thampy, M. P. M. Dean, N. B. Christensen, L. Steinke, Z. Islam, M. Oda, M. Ido, N. Momono, S. B. Wilkins, and J. P. Hill, "Rotated stripe order and its competition with superconductivity in La$_{1.88}$Sr$_{0.12}$CuO$_4$", *Physical Review B*, vol. 90, no. 10, p. 100 510, 2014.

[114]   A. T. Rømer, J. Chang, N. B. Christensen, B. M. Andersen, K. Lefmann, L. Mähler, J. Gavilano, R. Gilardi, C. Niedermayer, H. M. Rønnow, and A. Schneidewind, "Glassy low-energy spin fluctuations and anisotropy gap in La$_{1.88}$Sr$_{0.12}$CuO$_4$", *Physical Review B*, vol. 87, no. 14, p. 144 513, 2013.

[115]   J. M. Tranquada, "Exploring intertwined orders in cuprate superconductors", *Physica B: Condensed Matter*, vol. 460, pp. 136–140, 2015.

[116]   D. F. Agterberg, J. C. S. Davis, S. D. Edkins, E. Fradkin, D. J. Van Harlingen, S. A. Kivelson, P. A. Lee, L. Radzihovsky, J. M. Tranquada, and Y. Wang, "The physics of pair-density waves: Cuprate superconductors and beyond", *Annual Review of Condensed Matter Physics*, vol. 11, pp. 231–270, 2020.

[117]   J. M. Tranquada, H. Woo, T. G. Perring, H. Goka, G. D. Gu, G. Xu, M. Fujita, and K. Yamada, "Universal magnetic excitation spectrum in cuprates", *Journal of Physics and Chemistry of Solids*, vol. 67, no. 1-3, pp. 511–515, 2006.

[118]   M. Fujita, H. Hiraka, M. Matsuda, M. Matsuura, J. M. Tranquada, S. Wakimoto, G. Xu, and K. Yamada, "Progress in neutron scattering studies of spin excitations in high-T_c cuprates", *Journal of the Physical Society of Japan*, vol. 81, no. 1, p. 011 007, 2011.

[119]   F. Krüger and S. Scheidl, "Spin dynamics of stripes", *Physical Review B*, vol. 67, no. 13, p. 134 512, 2003.

[120]   C. D. Batista, G. Ortiz, and A. V. Balatsky, "Unified description of the resonance peak and incommensuration in high-T_c superconductors", *Physical Review B*, vol. 64, no. 17, p. 172 508, 2001.

[121]   R. J. Birgeneau, C. Stock, J. M. Tranquada, and K. Yamada, "Magnetic neutron scattering in hole-doped cuprate superconductors", *Journal of the Physical Society of Japan*, vol. 75, no. 11, p. 111 003, 2006.

[122]   C. Stock, R. A. Cowley, W. J. L. Buyers, C. D. Frost, J. W. Taylor, D. Peets, R. Liang, D. Bonn, and W. N. Hardy, "Effect of the pseudogap on suppressing high energy inelastic neutron scattering in superconducting YBa$_2$Cu$_3$O$_{6.5}$", *Physical Review B*, vol. 82, no. 17, p. 174 505, 2010.

[123]   M. Kofu, T. Yokoo, F. Trouw, and K. Yamada, "Dispersion and energy spectrum of spin excitations in an underdoped La$_{1.90}$Sr$_{0.10}$CuO$_4$", *arXiv preprint arXiv:0710.5766*, 2007.

[124]   B. Lake, G. Aeppli, K. N. Clausen, D. F. McMorrow, K. Lefmann, N. E. Hussey, N. Mangko-rntong, M. Nohara, H. Takagi, T. E. Mason, and A. Schröder, "Spins in the vortices of a high-temperature superconductor", *Science*, vol. 291, no. 5509, pp. 1759–1762, 2001.

[125]   S. Petit, A. H. Moudden, B. Hennion, A. Vietkin, and A. Revcolevschi, "Spin dynamics study of $La_{2-x}Sr_xCuO_4$ by inelastic neutron scattering", *Physica B: Condensed Matter*, vol. 234, pp. 800–802, 1997.

[126]   C.-H. Lee, K. Yamada, Y. Endoh, G. Shirane, R. J. Birgeneau, M. A. Kastner, M. Greven, and Y. J. Kim, "Energy spectrum of spin fluctuations in superconducting $La_{2-x}Sr_xCuO_4$ $(0.10 \leqslant x \leqslant 0.25)$", *Journal of the Physical Society of Japan*, vol. 69, no. 4, pp. 1170–1176, 2000.

[127]   J. Chang, N. B. Christensen, C. Niedermayer, K. Lefmann, H. M. Rønnow, D. F. McMorrow, A. Schneidewind, P. Link, A. Hiess, M. Boehm, and R. Mottl, "Magnetic-field-induced soft-mode quantum phase transition in the high-temperature superconductor $La_{1.855}Sr_{0.145}CuO_4$: An inelastic neutron-scattering study", *Physical Review Letters*, vol. 102, no. 17, p. 177006, 2009.

[128]   J. M. Tranquada, C. H. Lee, K. Yamada, Y. S. Lee, L. P. Regnault, and H. M. Rønnow, "Evidence for an incommensurate magnetic resonance in $La_{2-x}Sr_xCuO_4$", *Physical Review B*, vol. 69, no. 17, p. 174507, 2004.

[129]   T. E. Mason, G. Aeppli, S. M. Hayden, A. P. Ramirez, and H. A. Mook, "Magnetic fluctuations in superconducting $La_{2-x}Sr_xCuO_4$", *Physica B: Condensed Matter*, vol. 199, pp. 284–287, 1994.

[130]   J. Chang, A. P. Schnyder, R. Gilardi, H. M. Rønnow, S. Pailhes, N. B. Christensen, C. Niedermayer, D. F. McMorrow, A. Hiess, A. Stunault, M. Enderle, B. Lake, O. Sobolev, N. Momono, M. Oda, M. Ido, C. Mudry, and J. Mesot, "Magnetic-field-induced spin excitations and renormalized spin gap of the underdoped $La_{1.895}Sr_{0.105}CuO_4$ superconductor", *Physical Review Letters*, vol. 98, no. 7, p. 077004, 2007.

[131]   B. M. Andersen, S. Graser, and P. J. Hirschfeld, "Disorder-induced freezing of dynamical spin fluctuations in underdoped cuprate superconductors", *Physical Review Letters*, vol. 105, no. 14, p. 147002, 2010.

[132]   S. Wakimoto, H. Zhang, K. Yamada, I. Swainson, H. Kim, and R. J. Birgeneau, "Direct relation between the low-energy spin excitations and superconductivity of overdoped high-T_c superconductors", *Physical Review Letters*, vol. 92, no. 21, p. 217004, 2004.

[133]   B. Keimer, N. Belk, R. J. Birgeneau, A. Cassanho, C. Y. Chen, M. Greven, M. A. Kastner, A. Aharony, Y. Endoh, R. W. Erwin, and G. Shirane, "Magnetic excitations in pure, lightly doped, and weakly metallic La_2CuO_4", *Physical Review B*, vol. 46, no. 21, p. 14034, 1992.

[134]   H. L. Bhat, *Introduction to crystal growth: principles and practice*. CRC Press, 2014.

[135]   A. E. Țuțueanu, "Growth and characterization of superconducting $La_{2-x}Sr_xCuO_4$ single crystals", Master's thesis, University of Copenhagen, 2017.

[136] Y. S. Lee, F. C. Chou, A. Tewary, M. A. Kastner, S. H. Lee, and R. J. Birgeneau, "Neutron scattering study of the effects of dopant disorder on the superconductivity and magnetic order in stage-4 $La_2CuO_{4+\delta}$", *Physical Review B*, vol. 69, no. 2, p. 020 502, 2004.

[137] M. Boehm, P. Steffens, J. Kulda, M. Klicpera, S. Roux, P. Courtois, P. Svoboda, J. Saroun, and V. Sechovsky, "ThALES—three axis low energy spectroscopy for highly correlated electron systems", *Neutron News*, vol. 26, no. 3, pp. 18–21, 2015.

[138] G. Xu, Z. Xu, and J. M. Tranquada, "Absolute cross-section normalization of magnetic neutron scattering data", *Review of Scientific Instruments*, vol. 84, no. 8, p. 083 906, 2013.

[139] J. Kulda and J. Šaroun, "Elastically bent silicon monochromator and analyzer on a TAS instrument", *Nuclear Instruments and Methods in Physics Research Section A: Accelerators, Spectrometers, Detectors and Associated Equipment*, vol. 379, no. 1, pp. 155–166, 1996.

[140] A. Hiess, M. Jimenez-Ruiz, P. Courtois, R. Currat, J. Kulda, and F. J. Bermejo, "ILL's renewed thermal three-axis spectrometer IN8: A review of its first three years on duty", *Physica B: Condensed Matter*, vol. 385, pp. 1077–1079, 2006.

[141] Y. Wang and H.-H. Wen, "Doping dependence of the upper critical field in $La_{2-x}Sr_xCuO_4$ from specific heat", *Europhysics Letters*, vol. 81, no. 5, p. 57 007, 2008.

[142] M.-E. Lăcătuşu, "Magnetic stripes and structural transition in the high temperature superconductor $La_{2-x}Sr_xCuO_4$", Master's thesis, University of Copenhagen, 2015.

[143] Y. Zhang, W. Liu, X. Zhu, H. Zhao, Z. Hu, C. He, and H.-H. Wen, "Unprecedented high irreversibility line in the nontoxic cuprate superconductor $(Cu,C)Ba_2Ca_3Cu_4O_{11+\delta}$", *Science advances*, vol. 4, no. 9, 2018.

[144] Y. S. Lee, R. J. Birgeneau, M. A. Kastner, Y. Endoh, S. Wakimoto, K. Yamada, R. W. Erwin, S.-H. Lee, and G. Shirane, "Neutron-scattering study of spin-density wave order in the superconducting state of excess-oxygen-doped La_2CuO_{4+y}", *Physical Review B*, vol. 60, no. 5, p. 3643, 1999.

[145] B. O. Wells, Y. S. Lee, M. A. Kastner, R. J. Christianson, R. J. Birgeneau, K. Yamada, Y. Endoh, and G. Shirane, "Incommensurate spin fluctuations in high-transition temperature superconductors", *Science*, vol. 277, no. 5329, pp. 1067–1071, 1997.

[146] T. Dahm and D. J. Scalapino, "Dependence of tc on the $q-\omega$ structure of the spin-fluctuation spectrum", *Physical Review B*, vol. 97, no. 18, p. 184 504, 2018.

[147] J. M. Tranquada, G. D. Gu, M. Hücker, Q. Jie, H.-J. Kang, R. Klingeler, Q. Li, N. Tristan, J. S. Wen, G. Y. Xu, Z. J. Xu, J. Zhou, and M. v. Zimmermann, "Evidence for unusual superconducting correlations coexisting with stripe order in $La_{1.875}Ba_{0.125}CuO_4$", *Physical Review B*, vol. 78, no. 17, p. 174 529, 2008.

[148] M. v. Zimmermann, A. Vigliante, T. Niemöller, N. Ichikawa, T. Frello, J. Madsen, P. Wochner, S. Uchida, N. H. Andersen, J. M. Tranquada, D. Gibbs, and J. R. Schneider, "Hard-X-ray diffraction study of charge stripe order in $La_{1.48}Nd_{0.4}Sr_{0.12}CuO_4$", *EPL (Europhysics Letters)*, vol. 41, no. 6, p. 629, 1998.

[149] Y. Wang, D. F. Agterberg, and A. Chubukov, "Coexistence of charge-density-wave and pair-density-wave orders in underdoped cuprates", *Physical Review Letters*, vol. 114, no. 19, p. 197 001, 2015.

[150] J. Wen, Z. Xu, G. Xu, J. M. Tranquada, G. Gu, S. Chang, and H. J. Kang, "Magnetic field induced enhancement of spin-order peak intensity in $La_{1.875}Ba_{0.125}CuO_4$", *Physical Review B*, vol. 78, no. 21, p. 212 506, 2008.

[151] Z. Du, H. Li, S. H. Joo, E. P. Donoway, J. Lee, J. C. Séamus Davis, G. Gu, P. D. Johnson, and K. Fujita, "Imaging the energy gap modulations of the cuprate pair-density-wave state", *Nature*, vol. 580, no. 7801, pp. 65–70, 2020.

[152] M. H. Hamidian, S. D. Edkins, S. H. Joo, A. Kostin, H. Eisaki, S. Uchida, M. J. Lawler, E.-A. Kim, A. P. Mackenzie, K. Fujita, J. Lee, and J. Séamus Davis, "Detection of a Cooper-pair density wave in $Bi_2Sr_2CaCu_2O_{8+x}$", *Nature*, vol. 532, no. 7599, pp. 343–347, 2016.

[153] M. Enoki, M. Fujita, T. Nishizaki, S. Iikubo, D. K. Singh, S. Chang, J. M. Tranquada, and K. Yamada, "Spin-stripe density varies linearly with the hole content in single-layer $Bi_{2+x}Sr_{2-x}CuO_{6+y}$ cuprate superconductors", *Physical Review Letters*, vol. 110, no. 1, p. 017 004, 2013.

[154] A. E. Țuțueanu, H. Jacobsen, P. Jensen Ray, S. Holm-Dahlin, M.-E. Lăcătușu, T. B. Tejsner, J.-C. Grivel, W. Schmidt, R. Toft-Petersen, P. Steffens, M. Böhm, L. Udby, K. Lefmann, and A. Tranum Rømer, "Nature of the magnetic stripes in fully oxygenated La_2CuO_{4+y}", *Physical Review B*, vol. 103, no. 4, p. 045 138, 2021.

[155] P. A. Lee, N. Nagaosa, and X. G. Wen, "Doping a Mott insulator: Physics of high-temperature superconductivity", *Reviews of Modern Physics*, vol. 78, no. 1, p. 17, 2006.

[156] P. M. Grant, S. S. P. Parkin, V. Y. Lee, E. M. Engler, M. L. Ramirez, J. E. Vazquez, G. Lim, R. D. Jacowitz, and R. L. Greene, "Evidence for superconductivity in La_2CuO_4", *Physical Review Letters*, vol. 58, no. 23, p. 2482, 1987.

[157] J. Beille, R. Cabanel, C. Chaillout, B. Chevalier, and G. Demazeau, "Superconductivity below 40 K in orthorhombic La_2CuO_4", *CRASM*, vol. 304, no. 18, pp. 1097–1101, 1987.

[158] K. Sekizawa, Y. Takano, H. Takigami, S. Tasaki, and T. Inaba, "Superconductivity in the La-Cu-O system", *Japanese Journal of Applied Physics*, vol. 26, no. 5A, p. L840, 1987.

[159] J. C. Grenier, A. Wattiaux, N. Lagueyte, J. C. Park, E. Marquestaut, J. Etourneau, and M. Pouchard, "A new superconductor obtained by electrochemical oxidation of La_2CuO_4", *Physica C: Superconductivity*, vol. 173, no. 3-4, pp. 139–144, 1991.

[160] S. Kimura and I. Shindo, "Single crystal growth of YIG by the floating zone method", *Journal of Crystal Growth*, vol. 41, no. 2, pp. 192–198, 1977.

[161] B. O. Wells, R. J. Birgeneau, F. C. Chou, Y. Endoh, D. C. Johnston, M. A. Kastner, Y. S. Lee, G. Shirane, J. M. Tranquada, and K. Yamada, "Intercalation and staging behavior in super-oxygenated $La_2CuO_{4+\delta}$", *Zeitschrift für Physik B Condensed Matter*, vol. 100, no. 4, pp. 535–545, 1996.

[162] F. C. Chou, J. H. Cho, and D. C. Johnston, "Synthesis, characterization, and superconducting and magnetic properties of electrochemically oxidized $La_2CuO_{4+\delta}$ and $La_{2-x}Sr_xCuO_{4+\delta}$ $(0.01 \leq x \leq 0.33, 0.01 \leq \delta \leq 0.36)$", *Physica C: Superconductivity*, vol. 197, no. 3-4, pp. 303–314, 1992.

[163] A. D. McNaught and A. Wilkinson, *Compendium of chemical terminology*. Blackwell Science Oxford, 1997, vol. 1669, Online version (2019-) created by S. J. Chalk.

[164] C. Ling, H. Yu-Zhen, Z. Fang, D. Cheng, C. Guang-Can, and Z. Zhong-Xian, "Electrochemical oxidation of La_2CuO_4 single crystals", *Chinese Physics*, vol. 9, no. 8, p. 624, 2000.

[165] T. Roy and T. E. Mitchell, "On the space group of $La_2CuO_{4-\delta}$", *Materials Letters*, vol. 6, no. 10, pp. 336–341, 1988.

[166] P. G. Radaelli, J. D. Jorgensen, R. Kleb, B. A. Hunter, F. C. Chou, and D. C. Johnston, "Miscibility gap in electrochemically oxygenated $La_2CuO_{4+\delta}$", *Physical Review B*, vol. 49, no. 9, p. 6239, 1994.

[167] J. M. Tranquada, Y. Kong, J. E. Lorenzo, D. J. Buttrey, D. E. Rice, and V. Sachan, "Oxygen intercalation, stage ordering, and phase separation in $La_2NiO_{4+\delta}$ with $0.05 \lesssim \delta \lesssim 0.11$", *Physical Review B*, vol. 50, no. 9, p. 6340, 1994.

[168] F. C. Chou and D. C. Johnston, "Phase separation and oxygen diffusion in electrochemically oxidized $La_2CuO_{4+\delta}$: A static magnetic susceptibility study", *Physical Review B*, vol. 54, no. 1, p. 572, 1996.

[169] T. Imai and Y. S. Lee, "139La and 63Cu NMR investigation of charge order in La_2CuO_{4+y} ($T_c = 42$ K)", *Physical Review B*, vol. 97, no. 10, p. 104 506, 2018.

[170] A. T. Savici, Y. Fudamoto, T. I. I. M. Gat, M. I. Larkin, Y. J. Uemura, G. M. Luke, K. M. Kojima, Y. S. Lee, M. A. Kastner, R. J. Birgeneau, and K. Yamada, "Muon spin relaxation studies of incommensurate magnetism and superconductivity in stage-4 $La_2CuO_{4.11}$ and $La_{1.88}Sr_{0.12}CuO_4$", *Physical Review B*, vol. 66, p. 014 524, 2002.

[171] B. Khaykovich, R. J. Birgeneau, F. C. Chou, R. W. Erwin, M. A. Kastner, S.-H. Lee, Y. S. Lee, P. Smeibidl, P. Vorderwisch, and S. Wakimoto, "Effect of a magnetic field on long-range magnetic order in stage-4 and stage-6 superconducting La_2CuO_{4+y}", *Physical Review B*, vol. 67, no. 5, p. 054 501, 2003.

[172] B. Khaykovich, Y. S. Lee, R. W. Erwin, S.-H. Lee, S. Wakimoto, K. J. Thomas, M. A. Kastner, and R. J. Birgeneau, "Enhancement of long-range magnetic order by magnetic field in superconducting La_2CuO_{4+y}", *Physical Review B*, vol. 66, no. 1, p. 014 528, 2002.

[173] H. E. Mohottala, B. O. Wells, J. I. Budnick, W. A. Hines, C. Niedermayer, L. Udby, C. Bernhard, A. R. Moodenbaugh, and F.-C. Chou, "Phase separation in superoxygenated $La_{2-x}Sr_xCuO_{4+y}$", *Nature Materials*, vol. 5, no. 5, pp. 377–382, 2006.

[174] Y. Ando, G. S. Boebinger, A. Passner, L. F. Schneemeyer, T. Kimura, M. Okuya, S. Watauchi, J. Shimoyama, K. Kishio, K. Tamasaku, N. Ichikawa, and S. Uchida, "Resistive upper critical fields and irreversibility lines of optimally doped high-T_c cuprates", *Physical Review B*, vol. 60, no. 17, p. 12 475, 1999.

[175] J. S. Olaf, *Clip user manual*, 2009. [Online]. Available: http://clip4.sourceforge.net/.

[176]   R. Gilardi, S. Streule, N. Momono, M. Oda, and J. Mesot, "Doping dependence of the vortex glass and sublimation transitions in the high-T_c superconductor $La_{2-x}Sr_xCuO_4$ as determined from macroscopic measurements", *The European Physical Journal B-Condensed Matter and Complex Systems*, vol. 47, no. 2, pp. 231–237, 2005.

[177]   B. Ouladdiaf, J. Archer, G. J. McIntyre, A. W. Hewat, D. Brau, and S. York, "OrientExpress: A new system for Laue neutron diffraction", *Physica B: Condensed Matter*, vol. 385, pp. 1052–1054, 2006.

[178]   H. Sato and K. Maki, "Theory of inelastic neutron scattering from Cr and its alloys near the Neel temperature", *International Journal of Magnetism*, vol. 6, no. 3-4, p. 183, 1974.

[179]   G. Aeppli, T. E. Mason, S. M. Hayden, H. A. Mook, and J. Kulda, "Nearly singular magnetic fluctuations in the normal state of a high-T_c cuprate superconductor", *Science*, vol. 278, no. 5342, pp. 1432–1435, 1997.

[180]   A. T. Rømer, P. J. Ray, H. Jacobsen, L. Udby, B. M. Andersen, M. Bertelsen, S. L. Holm, N. B. Christensen, R. Toft-Petersen, M. Skoulatos, M. Laver, A. Schneidewind, P. Link, M. Oda, M. Ido, N. Momono, and K. Lefmann, "Field-induced interplanar magnetic correlations in the high-temperature superconductor $La_{1.88}Sr_{0.12}CuO_4$", *Physical Review B*, vol. 91, no. 17, p. 174 507, 2015.

[181]   E. Lelièvre-Berna, E. Bourgeat-Lami, P. Fouilloux, B. Geffray, Y. Gibert, K. Kakurai, N. Kernavanois, B. Longuet, F. Mantegezza, M. Nakamura, S. Pujol, F. Regnault L.-P.and Tasset, M. Takeda, M. Thomas, and X. Tonon, "Advances in spherical neutron polarimetry with Cryopad", *Physica B: Condensed Matter*, vol. 356, no. 1-4, pp. 131–135, 2005.

[182]   A.-E. Ţuţueanu, M. Sales, K. L. Eliasen, M.-E. Lăcătuşu, J.-C. Grivel, N. Kardjilov, I. Manke, M. Krzyzagorski, Y. Sassa, M. S. Andersson, S. S., and K. Lefmann, "Non-destructive characterisation of dopant spatial distribution in cuprate superconductors", *Physica C: Superconductivity and its Applications*, vol. 575, p. 1 353 691, 2020.

[183]   J. E. Sonier, J. H. Brewer, and R. F. Kiefl, "μSR studies of the vortex state in type-II super-conductors", *Reviews of Modern Physics*, vol. 72, no. 3, p. 769, 2000.

[184]   T. Imai and Y. S. Lee, "^{139}La and ^{63}Cu NMR investigation of charge order in La_2CuO_{4+y} ($T_c = 42$ K)", *Physical Review B*, vol. 97, p. 104 506, 10 Mar. 2018. [Online]. Available: https://link.aps.org/doi/10.1103/PhysRevB.97.104506.

[185]   H. E. Mohottala, B. O. Wells, J. I. Budnick, W. A. Hines, C. Niedermayer, L. Udby, C. Bernhard, A. R. Moodenbaugh, and F. Chou, "Phase separation in superoxygenated $La_{2-x}Sr_xCuO_{4+y}$.", *Nature Materials*, vol. 5, no. 5, pp. 377–382, May 2006, ISSN: 1476-1122. [Online]. Available: http://www.ncbi.nlm.nih.gov/pubmed/16617346.

[186]   L. Udby, J. Larsen, N. B. Christensen, M. Boehm, C. Niedermayer, H. E. Mohottala, T. B. S. Jensen, R. Toft-Petersen, F. C. Chou, N. H. Andersen, K. Lefmann, and B. O. Wells, "Measurement of Unique Magnetic and Superconducting Phases in Oxygen-Doped High-Temperature Superconductors $La_{2-x}Sr_xCuO_{4+y}$", *Physical Review Letters*, vol. 111, p. 227 001, 2013.

[187] B. M. Andersen, M. Schmid, S. Graser, P. J. Hirschfeld, and A. P. Kampf, "Effects of impurities and vortices on the low-energy spin excitations in high-T_c materials", *Journal of Physics and Chemistry of Solids*, vol. 72, no. 5, pp. 358–361, 2011.

[188] M. Braden, G. Heger, P. Schweiss, Z. Fisk, K. Gamayunov, I. Tanaka, and H. Kojima, "Characterization and structural analysis of twinned $La_{2-x}Sr_xCuO_{4\pm\delta}$ crystals by neutron diffraction", *Physica C: Superconductivity*, vol. 191, no. 3-4, pp. 455–468, 1992.

[189] Z. Zhang, R. Sutarto, F. He, F. C. Chou, L. Udby, S. L. Holm, Z. H. Zhu, W. A. Hines, J. I. Budnick, and B. O. Wells, "Nematicity and charge order in superoxygenated $La_{2-x}Sr_xCuO_{4+y}$", *Physical Review Letters*, vol. 121, p. 067 602, 6 Aug. 2018.

[190] N. B. Christensen, D. F. McMorrow, H. M. Rønnow, B. Lake, S. M. Hayden, G. Aeppli, T. G. Perring, M. Mangkorntong, M. Nohara, and H. Takagi, "Dispersive excitations in the high-temperature superconductor $La_{2-x}Sr_xCuO_4$", *Physical Review Letters*, vol. 93, no. 14, p. 147 002, 2004.

[191] M. Fujita, H. Hiraka, M. Matsuda, M. Matsuura, T. J. M, S. Wakimoto, G. Xu, and K. Yamada, "Progress in neutron scattering studies of spin excitations in high-T_c cuprates", *Journal of the Physical Society of Japan*, vol. 81, no. 1, p. 011 007, 2012.

[192] J. M. Tranquada, "Spins, stripes, and superconductivity in hole-doped cuprates", in *AIP Conference Proceedings*, American Institute of Physics, vol. 1550, 2013, pp. 114–187.

[193] N. Kardjilov, I. Manke, M. Strobl, A. Hilger, W. Treimer, M. Meissner, T. Krist, and J. Banhart, "Three-dimensional imaging of magnetic fields with polarized neutrons", *Nature Physics*, vol. 4, no. 5, p. 399, 2008.

[194] M. Strobl, H. Heimonen, S. Schmidt, M. Sales, N. Kardjilov, A. Hilger, I. Manke, T. Shinohara, and J. Valsecchi, "Polarization measurements in neutron imaging", *Journal of Physics D - Applied Physics*, vol. 52, no. 12, p. 123 001, 2019.

[195] M. Strobl, H. Heimonen, S. Schmidt, M. Sales, N. Kardjilov, A. Hilger, I. Manke, T. Shinohara, and Valsecchi, "Topical review: Polarisation measurements in neutron imaging", *Journal of Physics D: Applied Physics*, vol. 52, no. 12, p. 123 001, 2018.

[196] M. Dawson, I. Manke, N. Kardjilov, A. Hilger, M. Strobl, and J. Banhart, "Imaging with polarized neutrons", *New Journal of Physics*, vol. 11, no. 4, p. 043 013, 2009.

[197] N. Kardjilov, I. Manke, R. Woracek, A. Hilger, and J. Banhart, "Advances in neutron imaging", *Materials Today*, vol. 21, no. 6, pp. 652–672, 2018.

[198] I. Tanaka, K. Yamane, and H. Kojima, "Single crystal growth of superconducting $La_{2-x}Sr_xCuO_4$ by the TSFZ method", *Journal of Crystal Growth*, vol. 96, no. 3, pp. 711–715, 1989.

[199] L. Le Dréau, "Phase transitions and oxygen ordering in $La_2CoO_{4+\delta}$ and (T, T') - La_2CuO_4: single crystal growth and structural studies using synchrotron and neutron diffraction methods", PhD thesis, University of Rennes, 2011.

[200] K. Oka, M. J. V. Menken, Z. Tarnawski, A. A. Menovsky, A. M. Moe, T. S. Han, H. Unoki, T. Ito, and Y. Ohashi, "Crystal growth of $La_{2-x}Sr_xCuO_{4-\delta}$ by the travelling-solvent floating-zone method", *Journal of Crystal Growth*, vol. 137, no. 3-4, pp. 479–486, 1994.

[201] P. G. Radaelli, D. G. Hinks, A. W. Mitchell, B. A. Hunter, J. L. Wagner, B. Dabrowski, K. G. Vandervoort, H. K. Viswanathan, and J. D. Jorgensen, "Structural and superconducting properties of $La_{2-x}Sr_xCuO_4$ as a function of Sr content", *Physical Review B*, vol. 49, no. 6, p. 4163, 1994.

[202] Y. Ando, S. Komiya, K. Segawa, S. Ono, and Y. Kurita, "Electronic phase diagram of high-T_c cuprate superconductors from a mapping of the in-plane resistivity curvature", *Physical Review Letters*, vol. 93, no. 26, p. 267 001, 2004.

[203] N. Momono, M. Ido, T. Nakano, M. Oda, Y. Okajima, and K. Yamaya, "Low-temperature electronic specific heat of $La_{2-x}Sr_xCuO_4$ and $La_{2-x}Sr_xCu_{1-y}Zn_yO_4$. evidence for a d-wave superconductor", *Physica C: Superconductivity*, vol. 233, no. 3-4, pp. 395–401, 1994.

[204] M. McElfresh, "Fundamentals of magnetism and magnetic measurements featuring Quantum Design's magnetic property system.", Purdue University, Tech. Rep., 1994.

[205] I. Felner, M. I. Tsindlekht, G. Drachuck, and A. Keren, "Anisotropy of the upper critical fields and the paramagnetic Meissner effect in $La_{1.85}Sr_{0.15}CuO_4$ single crystals", *Journal of Physics: Condensed Matter*, vol. 25, no. 6, p. 065 702, 2013.

[206] T. Adachi, K. Omori, Y. Tanabe, and Y. Koike, "Magnetic-susceptibility and specific-heat studies on the inhomogeneity of superconductivity in the underdoped $La_{2-x}Sr_xCuO_4$", *Journal of the Physical Society of Japan*, vol. 78, no. 11, pp. 114 707–114 707, 2009.

[207] W. Treimer, "Radiography and tomography with polarized neutrons", *Journal of Magnetism and Magnetic Materials*, vol. 350, pp. 188–198, 2014.

[208] N. Kardjilov, M. Dawson, A. Hilger, I. Manke, M. Strobl, D. Penumadu, F. H. Kim, F. Garcia-Moreno, and J. Banhart, "A highly adaptive detector system for high resolution neutron imaging", *Nuclear Instruments and Methods in Physics Research Section A: Accelerators, Spectrometers, Detectors and Associated Equipment*, vol. 651, no. 1, pp. 95–99, 2011.

[209] T. Shinohara, T. Kai, K. Oikawa, T. Nakatani, M. Segawa, K. Hiroi, Y. Su, M. Ooi, M. Harada, H. Iikura, H. Hayashida, J. D. Parker, Y. Matsumoto, T. Kamiyama, H. Sato, and Y. Kiyanagi, "The energy-resolved neutron imaging system, RADEN", *Review of Scientific Instruments*, vol. 91, no. 4, p. 043 302, 2020.

[210] A. E. Ţuţueanu, T. B. Tejsner, M. E. Lăcătuşu, H. W. Hansen, K. L. Eliasen, M. Böhm, P. Steffens, C. Niedermayer, and K. Lefmann, "Multiple scattering camouflaged as magnetic stripes in single crystals of superconducting $(La, Sr)_2CuO_4$", *Journal of Neutron Research*, no. Preprint, pp. 1–8, 2020.

[211] K. Lefmann, C. Niedemayer, A. B. Abrahamsen, C. R. H. Bahl, N. B. Christensen, H. S. Jacobsen, T. L. Larsen, P. Hafliger, U. Filges, and H. M. Rønnow, "Realizing the full potential of a rita spectrometer", *Physica B*, vol. 385-386, pp. 1083–1085, 2006.

[212] C. R. H. Bahl, K. Lefmann, A. B. Abrahamsen, H. M. Rønnow, F. Saxild, T. B. S. Jensen, L. Udby, N. H. Andersen, N. B. Christensen, H. S. Jakobsen, T. L. Larsen, P. S. Hafliger, S. Streule, and C. Niedemayer, "Inelastic neutron scattering experiments with the monochromatic imaging mode of the RITA-II spectrometer", *Nuclear Instruments and Methods B*, vol. 246, no. 2, pp. 452–462, 2006.

[213]   G. Shirane, S. M. Shapiro, and J. M. Tranquada, *Neutron scattering with a triple-axis spectrometer: basic techniques*. Cambridge University Press, 2002.

[214]   K. Lefmann, P. K. Willendrup, L. Udby, B. Lebech, K. Mortensen, J. O. Birk, K. Klenø, E. Knudsen, P. Christiansen, J. Saroun, J. Kulda, U. Filges, M. Konnecke, P. Tregenna-Piggott, K. Peters J. Lieutenant, G. Zsigmond, P. Bentley, and E. Farhi, "Virtual experiments: The ultimate aim of neutron ray-tracing simulations", *Journal of Neutron Research*, vol. 16, no. 3-4, pp. 97–111, 2008.

[215]   P. K. Willendrup and K. Lefmann, "McStas (i): Introduction, use, and basic principles for ray-tracing simulations", *Journal of Neutron Research*, no. Preprint, pp. 1–16, 2019.

[216]   J. K. Cockcroft, *Crystallographic space group diagrams and tables*, http://img.chem.ucl.ac.uk/sgp/large/064dz2.htm. (visited on 07/25/2019).

[217]   K. Momma and F. Izumi, "VESTA: A three-dimensional visualization system for electronic and structural analysis", *Journal of Applied Crystallography*, vol. 41, no. 3, pp. 653–658, 2008.

[218]   P. J. Brown, *Form factors for 3d transition elements and their ions*, https://www.ill.eu/sites/ccsl/ffacts/ffactnode5.html, accessed June, 2020.

[219]   P. Radaelli, J. Jorgensen, A. Schultz, B. Hunter, J. Wagner, F. Chou, and D. Johnston, "Structure of the superconducting $La_2CuO_{4+\delta}$ phases ($\delta \simeq 0.08$, 0.12) prepared by electrochemical oxidation", *Physical Review B*, vol. 48, no. 1, p. 499, 1993.

Part III

APPENDICES

ABSOLUTE NORMALISATION OF MAGNETIC CROSS SECTION

This section is based heavily on the explanations provided by G. Xu *et al.* [138] and the text of our manuscript [154].

Throughout this thesis two main physical properties are used to describe the magnetic structure of our samples: (1) dynamic spin correlation function (S) and (2) the dynamic susceptibility (χ''). The latter is nothing but the first normalised to the Bose factor as we shall see.

The dynamic susceptibility is defined as:

$$\chi''(\mathbf{Q},\omega) = \frac{\pi}{2}\mu_B^2(1-e^{-\hbar\omega/k_BT})\frac{13.77(b^{-1})\tilde{I}(\mathbf{Q},E)}{|f(\mathbf{Q})|^2e^{-2W}Nk_fR_0}, \tag{A.1}$$

while the dynamic spin correlation function has the following form:

$$S(\mathbf{Q},\omega) = \frac{13.77(b^{-1})\tilde{I}(\mathbf{Q},E)}{g^2|f(\mathbf{Q})|^2e^{-2W}Nk_fR_0}. \tag{A.2}$$

As it is important to pay extra attention to the units used, each term will be illustrated individually using as example the data recorded on IN12 on our oxygen doped LCO+O sample described in Chapter 6.

- Nk_fR_0 - the resolution volume

The resolution volume is obtained from the sample phonon scattering measured as a constant energy scan:

$$Nk_fR_0 = \frac{\int \tilde{I}(\mathbf{Q},E)d\mathbf{q}}{e^{-2W}|F_N(\mathbf{G})|^2\cos^2(\beta)\frac{m}{M}\frac{(\hbar\mathbf{Q})^2}{2m}\frac{n}{\hbar\omega}\frac{1}{d\omega/dq}}, \tag{A.3}$$

where $\int \tilde{I}(\mathbf{Q},E)d\mathbf{q}$ is the average integrated intensity of the two phonon branches. e^{-2W} is the Debye-Waller factor and β is the angle between $\mathbf{Q}$ and the polarization of the phonon. Both e^{-2W} and $\cos^2(\beta)$ are assumed 1. $F_N(\mathbf{G})$ is the structure factor of the phonon, it can easily be obtained from VESTA [217] and should be used in units of barns. m is the neutron mass and M is the is the mass of all the atoms in the unit cell (see Table 4). $n = 1/(1-e^{-E/k_BT})$ is the Bose factor of the phonon, where E is the energy at which the phonon was measured, k_B is the Boltzmann constant and T is the temperature at which the phonon was measured. $d\omega/dq$ is the phonon velocity where ω is the energy at which the phonon was measured and q is obtained

as half the distance between the two phonon branches in reciprocal lattice units. The term $\frac{(\hbar \mathbf{Q})^2}{2m}$ should be calculated in units of meV.

Element	Atom's mass (m) [g]	No. of atoms/unit cell (n)
La	$2.31 \cdot 10^{-22}$	8
Cu	$1.05 \cdot 10^{-22}$	4
O	$2.66 \cdot 10^{-23}$	16.32

Table 4: The mass of one atom was calculated as the ratio between the atomic mass and Avogadro's number. The number of atoms is presented for a conventional unit cell of LCO+O with oxygen doping $\delta = 0.08$.

In the case of our acoustic phonon measured on IN12 at $(2,0,0)$, 3 meV and 280 K, we obtain the numerical values shown in Table 5. For the LSCO experiments presented in Chapter 5, the same acoustic phonon was measured each time at 2 meV energy transfer and ~ 100 K.

Term	$F_N(\mathbf{G})$	m/M	$\frac{(\hbar \mathbf{Q})^2}{2m}$	$\frac{n_q}{\hbar\omega}$	$d\omega/dq$	$N k_f R_0$
Unit	barns	-	meV	meV^{-1}	meV/ r.l.u.	meV/ barns
Value	91	$\frac{1}{1617}$	11.57	2.85	35.76	0.0025

Table 5: Parameters corresponding to the acoustic phonon measured on IN12.

- $f(\mathbf{Q})$ - the form factor

In the case of LCO+O and LSCO it is sufficient to use the Cu form factor since it is the only atom that is responsible for the magnetic scattering:

$$f(\mathbf{Q}) = A e^{-a(\frac{\mathbf{Q}}{4\pi})^2} + B e^{-b(\frac{\mathbf{Q}}{4\pi})^2} + C e^{-c(\frac{\mathbf{Q}}{4\pi})^2} + D, \tag{A.4}$$

where the coefficients A, a, B, b, C, c and D can easily be found tabulated [218] for Cu^{2+}.

The other remaining factors in Eq. (A.1) are the Bose factor of the measured magnetic signal $1/(1 - e^{-E/k_B T})$, the Debye-Waller factor e^{-2W} assumed 1, the Bohr magneton μ_B. The amplitude of one of the incommensurate magnetic peaks $\tilde{I}(\mathbf{Q}, E)$ is obtained from fitting each scan to an appropriate model. Before fitting the raw data counts are normalised to the monitor count which is inversely proportional to the incoming wave vector (k_i). Taking into account that the scattering cross section is also proportional to $1/k_i$, we obtain a scattering signal per monitor, where the dependence of k_i is normalised out [78].

Furthermore, in order to obtain the $\mathbf{Q}$-integrated local susceptibility ($\chi''(\omega)$), as presented in Ref. [64] for an underdoped LBCO sample, an additional integration over all the peaks in the Brillouin Zone (BZ) is needed:

$$\chi''(\omega) = \frac{2\pi \sigma_h \sigma_k n_{peaks}}{a^* b^*} \chi''(\mathbf{Q}, \omega), \tag{A.5}$$

where σ_h and σ_k are the widths of the Gaussian fits to the peaks in h- and k-directions, n_{peaks} is the number of peaks in the BZ and a^*, b^* are the reciprocal lattice parameters. In our orthorhombic notation there are 2 peaks in the BZ. $\chi''(\omega)$ does not depend on the choice of unit

cell (tetragonal or orthorhombic), meaning that all variations of the parameters (such as the number of Cu per unit cell or the lattice parameters) eventually cancel out. One can thus make a direct comparison, as shown in Figure A.0.1, between the magnetic spectral weight of different compounds such as our LCO+O sample and an underdoped LBCO crystal presented in the literature. It should however be noted that, unless all measurements are performed and analysed in the exact same manner, there is a rather large uncertainty in the normalisation procedure. Some of the causes are the multiple assumptions about the shape of the signal and, in the case of one dimensional scans through the peaks, the fact that the scan direction might not pass through the top of the peak.
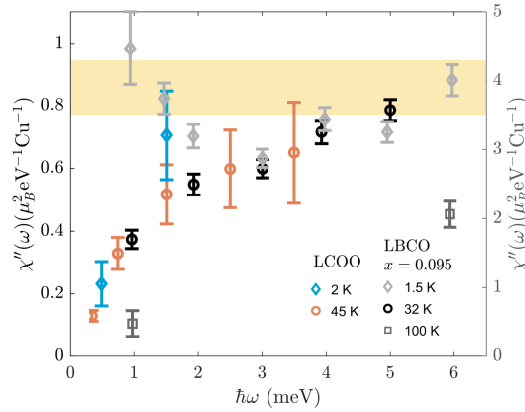

Figure A.0.1: Dynamic susceptibility $\chi''(\omega)$ measured at temperatures inside (2 K) and outside (45 K) the superconducting dome. All data has been measured at Thales (Th1) with constant $k_{\mathrm{f}} = 1.55\,\text{Å}^{-1}$. In grey and black symbols, we show the magnetic susceptibility measured inside and outside the superconducting state by Z. Xu *et al.* [64] on an underdoped $x = 0.095$ LSBCO sample with $T_{\mathrm{c}} = 32$ K. The shaded area indicates the magnitude of the spin waves in the parent compound LCO, as presented by Z. Xu *et al.* [64], and is connected to the right hand side axis.

Additionally, if data is recorded using different outgoing wavevectors, as it is the case of the experiments performed on IN12, it is possible to correct for the change in resolution volume [78] using a factor proportional to the ratio between the different resolution volumes. We have used the following simplified ratio where we assumed constant reflectivity of the analyser for the various outgoing wave vectors:

$$\frac{V_{\mathrm{f}}}{V_{\mathrm{f}}'} = \frac{k_{\mathrm{f}}^3}{\tan(\theta_A)} \frac{\tan(\theta_A')}{k_{\mathrm{f}}'^3}, \tag{A.6}$$

where θ_{A} and θ_{A}' are the Bragg angles of the analyser for the two k_{f} values considered.

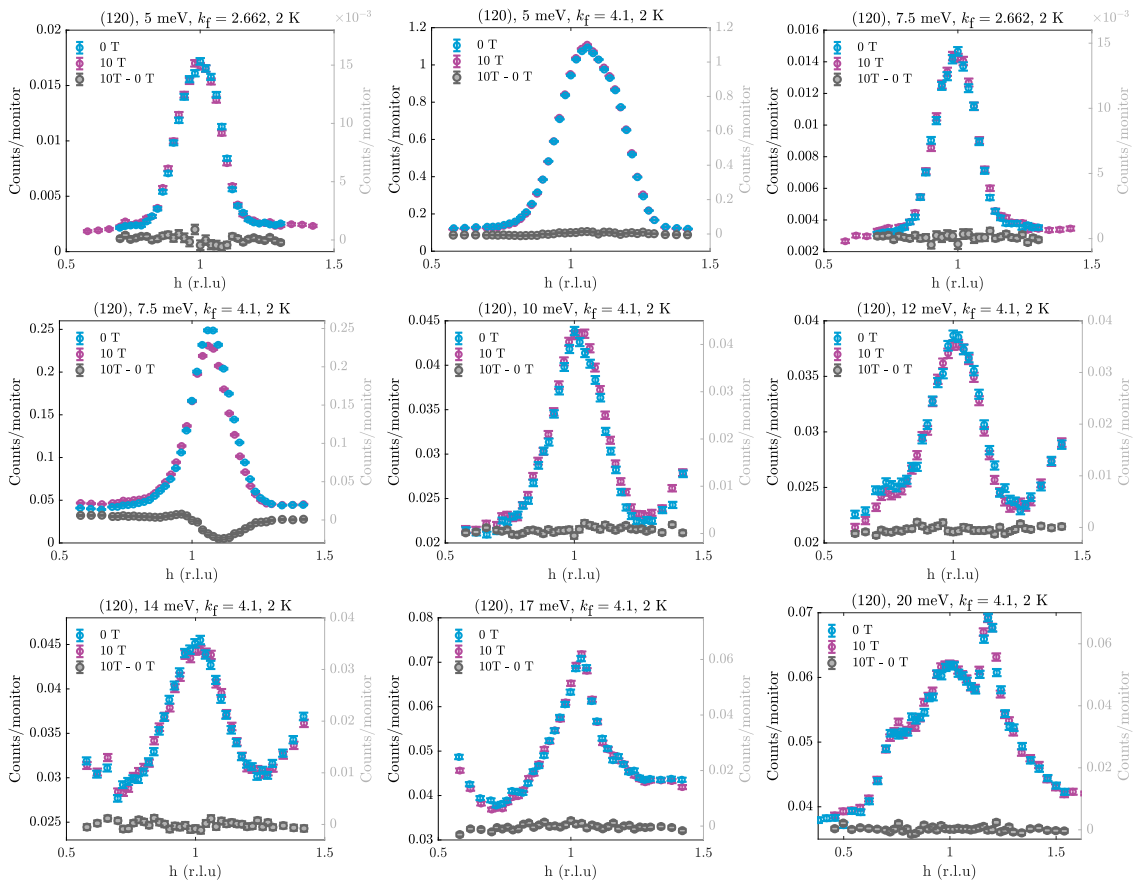# HIGH ENERGY FLUCTUATIONS IN LSCO5, ADDITIONAL PLOTS

Figure B.0.1: Inelastic scans as a function of applied magnetic field taken in the second Brillouin zone at 2 K. The title of each plot indicated the value of the energy transfer as well as the outgoing wavevector k_f used. In grey a point by point subtraction of the data taken under 10 T field and in zero applied magnetic field is shown.

Figure B.0.2: Inelastic scans as a function of applied magnetic field taken in the second Brillouin zone at 2 K. The title of each plot indicated the value of the energy transfer as well as the outgoing wavevector k_f used. In grey a point by point subtraction of the data taken under 10 T field and in zero applied magnetic field is shown.
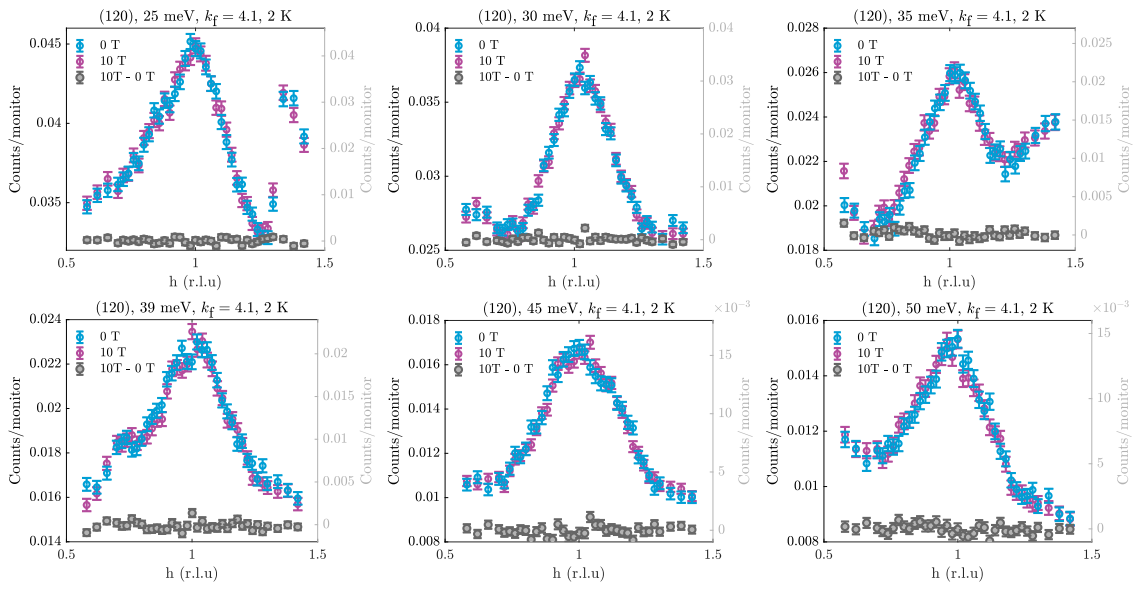
MAGNETIC SUSCEPTIBILITY CONVERSION TO SI UNITS

A significant part of text of this section has been reproduced in the Supplementary Material of our manuscript [154]. For this reason the conversion is exemplified on the specific case of the measurements performed on our LCO+O crystal. The same procedure has however been employed when analysing all magnetic susceptibility spectra presented throughout this thesis.

The output of standard vibrating sample magnetometry experiments is the measured magnetic moment of the sample. When studying superconducting sample there is important value in converting the magnetic moment measurements into magnetic (volume) susceptibility of the sample in SI units. For example the value of the magnetic susceptibility extrapolated to $T = 0$ K is a direct indication of the superconducting volume fraction of the sample. We have thus to start with the following formula:

$$\chi = 4\pi \frac{\mu}{V \cdot H_{internal}}, \tag{C.1}$$

where μ is the measured magnetic moment in electromagnetic units (emu), V is the sample's volume in cm^3 and $H_{internal}$ is the strength of the internal magnetic field. It should be noted that the internal magnetic field differs from the applied one ($H_{applied}$) by a demagnetising factor (N):

$$H_{internal} = \frac{1}{1-N} H_{applied}, \tag{C.2}$$

which is valid only in the Meissner state, i.e. for very small applied magnetic fields. Our measurements were performed under $H_{applied} = 6.4$ mT (in the case of the underdoped LSCO samples presented in Chapter 5 the valued of the applied magnetic field is always indicated in the insert of the plot).

If we treat our cubic samples as spheres, in which case the demagnetising factor has the value N = 1/3, we obtain:

$$H_{internal} = 1.5 \times H_{applied}, \tag{C.3}$$

For an accurate measure of the sample's volume, the density (ρ) of LCOO is used in the calculations as follows:

$$\rho = \frac{m_{UnitCell}}{V_{UnitCell}}. \tag{C.4}$$

where $V_{UnitCell}$ is the unit cell volume calculated with the lattice parameters taken from Ref. [219] for oxygen doping $\delta = 0.08$ at a temperature of 10 K (and from Ref. [201] for LSCO samples):

$$
\begin{aligned}
V_{UnitCell} = a \times b \times c &= 5.33\text{Å} \times 5.39\text{Å} \times 13.16\text{Å} \\
&= 378.07\text{Å}^3 = 378.07 \cdot 10^{-24}\,\text{cm}^3.
\end{aligned}
\tag{C.5}
$$

The number of atoms per unit cell and the atomic masses of the 3 components of LCOO (shown in Table 4 of Appendix A) are used to determine the mass of the unit cell:

$$
\begin{aligned}
m_{UnitCell} &= m_{La} \cdot n_{La} + m_{Sr} \cdot n_{Sr} + m_{Cu} \cdot n_{Cu} + m_O \cdot n_O \\
&= 2.70 \cdot 10^{-21}\text{g}.
\end{aligned}
\tag{C.6}
$$

Finally, following equation C.4, the density of LCOO with doping $x = 0.08$ is $\boldsymbol{\rho = 7.14\,\text{g/cm}^3}$. This value is afterwards used as the division factor of the mass in order to obtain an accurate estimation of the sample's volume.

The calculated susceptibility is then plotted against the temperature as it can be observed in numerous figures throughout this thesis. In an ideal case, the graph will have the shape of a sigmoid function constrained in between 0 (corresponding to the antiferromagnetic state above T_c) and -1 (corresponding to the perfect diamagnetic response of the material below T_c).

LIST OF PUBLICATIONS

This section contains a list of all publications that I have been part of during my time as a PhD student including a brief explanation of my contribution.

Published

- A.-E. Ţuţueanu, H. Jacobsen, P. J. Ray, S. Holm-Dahlin, M.-E. Lăcătuşu, T. Tejsner, J.-C. Grivel, W. Schmidt, R. Toft-Petersen, P. Steffens, M. Boehm, B. Wells, L. Udby, K. Lefmann, and A. Tranum Rømer, "Nature of the magnetic stripes in fully oxygenated La_2CuO_{4+y}", *Physical Review B*, vol. 103, no. 4, p. 045138, 2021.

  Conceived, planned and carried out the polarisation experiments, processed all the experimental data, designed the figures and drafted the manuscript.

- A.-E. Ţuţueanu, T. Tejsner, M.-E. Lăcătuşu, H. W. Hansen, K. L. Eliasen, M. Boehm, P. Steffens, C. Niedermayer and K. Lefmann, "Multiple scattering camouflaged as magnetic stripes in single crystals of superconducting $(La, Sr)_2CuO_4$", *Journal of Neutron Research*, (Preprint), p. 1, 2020.

  Took part in the sample fabrication, designed and performed the experiments, processed all the experimental data, designed the figures and drafted the manuscript.

- A.-E. Ţuţueanu, M. Sales, K.L. Eliasen, M.-E. Lăcătuşu, J.-C. Grivel, N. Kardjilov, I. Manke, M. Krzyzagorski, Y. Sassa, M. S. Andersson, S. Schmidt and K. Lefmann, "Non-destructive characterisation of dopant spatial distribution in cuprate superconductors". *Physica C: Superconductivity and its Applications*, vol. 575, p. 1353691, 2020.

  Took part in the sample fabrication, performed the experiments, processed part of the experimental data, designed part of the figures and drafted the manuscript.

- T. Tejsner, A. Piovano, A.-E. Țuțueanu, A. T. Rømer, B. O. Wells, J.-C. Grivel, M. Boehm and L. Udby, "Anomalous dispersion of longitudinal optical phonons in oxygen-doped $La_{2-x}Sr_xCuO_{4+\delta}$", *Physical Review B*, vol. 101, no. 10, p. 100504, 2020.

  Took part in most of the neutron scattering experiments, provided my input to the final version of the manuscript.

- S. Janas, J. Lass, A.-E. Țuțueanu, M. L. Haubro, C. Niedermayer, U. Stuhr, G. Xu, D. Prabhakaran, P. Deen, S. Holm-Dahlin, and K. Lefmann, "Classical spin liquid or extended critical range in h-YMnO3?", Accepted for publication in *Physical Review Letters* on 13 January 2021.

  Took part in some of the neutron scattering experiments, provided my input to the final version of the manuscript.

Future publications

- S. Holm-Dahlin, J. Larsen, H. Jacobsen, A. T. Rømer, A.-E. Țuțueanu, M. Ahmad, J.-C. Grivel, R. Scheuermann, M. V. Zimmermann, M. Boehm, P. Steffens, C. Niedermayer, K. S. Pedersen, N. B. Christensen, B. O. Wells, K. Lefmann and L. Udby, "Field-induced electronic phase separation in a cuprat high temperature superconductor", Submitted for publication in *Physical Review Letters* on 3 February 2021.

  Took part in some of the neutron scattering experiments, provided my input to the final version of the manuscript.

- A.-E. Țuțueanu, T. Tejsner, Y. Sassa, N. B. Christensen, M. E. Kamminga, H. W. Hansen, M.-E. Lăcătușu, J.-C. Grivel, K. L. Eliasen, P. Steffens, M. Boehm, A. T. Rømer and K. Lefmann, "Coexistence of pair-density-wave order and uniform d-wave superconductivity in underdoped $La_{2-x}Sr_xCuO_4$", Manuscript in preparation.

  Took part in the sample fabrication, designed and performed the experiments, processed all the experimental data. I plan to design the figures and draft the manuscript.